Shervin Shahriari, MSc

Numerical Modelling of the Approach Flow of Run-of-River Plants

DOCTORAL THESIS

to achieve the university degree of
Doktor der technischen Wissenschaften
submitted to

Graz University of Technology

Adviser:

Univ.-Prof. Dipl.-Ing. Dr.techn. Gerald Zenz
Institute of Hydraulic Engineering and Water Resources Management

Reviewers:

Prof. Dr. George S. Constantinescu
College of Engineering, IIHR-Hydroscience & Engineering
University of Iowa

Prof. Dr.-Ing. Jürgen Stamm
Institute of Hydraulic Engineering and Technical Hydromechanics
Dresden University of Technology

ABSTRACT

Exponential growth of computational power in the past decade on one hand and the success of numerical models in studying turbulent flows on the other hand lead to an increasing usage of this technique in hydraulic engineering problems. In particular, three-dimensional numerical models are becoming the industry standard, especially in problems where capturing three-dimensional flow characteristics are important. Additionally, with availability of open-source computational fluid dynamic codes (CFD), this type of modelling is more accessible. The main aims of this thesis are to evaluate the application of such modelling techniques in predicting the Run-of-River (ROR) plant approach flow with focus on the role of the turbulence models. Additionally, the numerical model is used to provide insight into the complex hydrodynamic processes involved in this type of flows. The investigation is carried out using a case study. This particular case study is selected due to its similarity to several other ROR plants. All the numerical simulations are carried out using an open-source CFD code OpenFOAM. This monograph is divided into four main parts. In the first part, a brief overview of the different parts and design aspects of ROR plants are presented. More specifically the emphasis is on the intakes and their important design considerations. In the second part, the case study along with the experimental investigation, which is carried out by the author, are described. The measurement is carried out using Acoustic Doppler Velocimetry device inside the intake structure. In this part, the results from the experiment are presented and briefly discussed.

Reynolds-averaged Navier-Stokes (RANS) is considered a pragmatic choice in studying hydraulic engineering problems, hence, in the third part of this monograph the results from series of parameter studies employing RANS are presented. The focus of the study is to evaluate the impact of different parameters in predicting the flow inside the intake structure. It is shown that grid refinement, wall roughness and location of the model's inlet do not significantly impact the results. On the other hand, it is found that the turbulence model is the most important parameter and Shear Stress Transport (SST) model performed relatively better compared to other one- and two-equations models. Additionally, it is recommended to perform the flow evaluation further downstream where the flow is more developed. In the final part, a novel turbulence modelling approach known as Improved Delayed Detached Eddy Simulation (IDDES) is employed to model the approach flow. These types of simulations are computationally expensive, hence, in order to reduce the computation time a solver is implemented in OpenFOAM based on explicit Runge-Kutta and fractional step method. The solver is validated by two classical turbulent flow cases. In the first case, fully developed turbulent channel flow is modelled and compared to the DNS and theoretical values. In the second case, flow over two-dimensional dune is modelled and the results are compared to experimental as well as Large Eddy Simulation (LES) studies. It is shown that utilizing such solver can significantly reduce the computation time. Using this solver and IDDES, the simulation of the ROR approach

flow is carried out and the results are presented in two sections. In the first section the time-averaged results are presented and compared to the experiment in terms of velocity and turbulence parameters. In the second section, the instantaneous flow field is studied. It is shown that this technique is relatively more accurate than RANS approach and instantaneous flow field is able to provide valuable insight into the hydrodynamic processes which are in some instances not available in the time-averaged results.

KURZFASSUNG

Das exponentielle Wachstum der Rechenleistung im letzten Jahrzehnt einerseits und der erfolgreiche Einsatz numerischer Modelle bei der Untersuchung turbulenter Strömungen andererseits führen zu einer zunehmenden Verwendung von numerischen Methoden für Problemstellungen im Wasserbau. Dabei gewinnen insbesondere dreidimensionale numerische Modelle an Bedeutung, insbesondere für jene Problemstellungen, bei denen die Erfassung dreidimensionaler Strömungseigenschaften von Bedeutung ist. Diese Art der Modellierung wird aufgrund der erhöhten Verfügbarkeit von Open Source CFD (Computational Fluid Dynamic) Software leichter zugänglich. Ziel dieser Arbeit ist es, die Anwendbarkeit solcher numerischer Methoden für die Untersuchung der Anströmung bei Laufkraftwerken zu evaluieren. Der Fokus liegt dabei vor allem auf der Rolle von Turbulenzmodellen. Die angewandten numerischen Methoden erlauben einen detaillierten Einblick in die komplexen hydrodynamischen Vorgänge für diese Art der Strömung. Die Untersuchungen werden dabei anhand einer Fallstudie durchgeführt. Das Fallbeispiel wird wegen dessen ähnlichkeit zu einer Vielzahl von anderen Laufkraftwerken gewählt. Die numerischen Simulationen werden mit dem Open Source CFD Code OpenFOAM durchgeführt. Vorliegende Arbeit ist in vier Teile unterteilt. Im ersten Teil wird ein kurzer überblick über die jeweiligen Komponenten eines Flusskraftwerks sowie deren Entwurfs- und Bemessungsüberlegungen gegeben. Der zweite Teil gibt einen überblick über das ausgewählte Fallbeispiel und beschreibt die vom Autor durchgeführten Messungen im Laborversuch. Die Messungen werden mithilfe eines ADV-Messgerätes (Acoustic Doppler Velocimeter) im Einlauf des Modells getätigt. Die Messergebnisse werden präsentiert und diskutiert.
Ansätze, die auf den Reynolds-averaged Navier-Stokes (RANS) Gleichungen basieren, gelten als eine pragmatische Wahl für die Untersuchung von hydraulischen Problemstellungen. Aus diesem Grund befasst sich der dritte Teil dieser Arbeit mit auf RANS Modellierungen basierenden Parameterstudien. Ziel dieser Studie ist es, den Einfluss verschiedener Parameter auf die Strömung im Turbineneinlaufbereich des Laufkraftwerks zu bewerten. Es kann vorweggenommen werden, dass die Auflösung des Berechnungsnetzes, die Wandrauheit sowie die Position der Einlaufrandbedingung die Ergebnisse nicht maßgeblich beeinflussen. Hingegen beeinflusst die Wahl des Turbulenzmodells die Ergebnisse signifikant, wobei das SST (Shear Stress Transport) Modell die Realität am besten widerspiegeln konnte. Es wird empfohlen, die Strömungsparameter weiter stromab des Einlasses zu evaluieren, um eine vollkommen ausgebildete Strömungsverhältnisse zu gewährleisten. Im vierten und damit letzten Teil wird ein neuartiger Ansatz für die Modellierung der Turbulenz, das IDDES (Improved Delayed Detached Eddy Simulation) Modell, für die numerische Simulierung der Zuströmung angewendet. Diese Art der Modellierung ist sehr rechenintensiv. Um die Rechenzeiten zu verringern, wurde ein auf einem expliziten Runge-Kutta (mit Zwischenschritt „fractional step method“) Ver-

fahren basierender Solver implementiert. Der Solver wird anhand von zwei in der Literatur sehr präsenten Fallbeispielen validiert. Im Rahmen des ersten Fallbeispiels wird ein Trapezgerinne mit turbulenter Strömung modelliert und mit Ergebnissen aus DNS (Direct Numerical Simulation) sowie theoretischen Betrachtungen verglichen. Im zweiten Beispiel wird die Strömung über eine zweidimensionale Dune modelliert. Die Ergebnisse werden anschließend mit Messungen und LES (Large Eddy Simulation) Simulationen verglichen. Die Studien zeigten, dass die Rechenzeiten durch die Anwendung des implementierten Solvers erheblich verringert werden konnten. Anschließend wird das gewählte Fallbeispiel mithilfe des implementierten Solvers und IDDES simuliert. Die Ergebnisse werden in zwei Kapiteln präsentiert. Im ersten Kapitel werden die zeitlich gemittelten Geschwindigkeiten und Turbulenzparameter ausgewertet und mit den Ergebnissen der Messung verglichen. Im zweiten Kapitel wird das veränderliche, derzeitige Strömungsfeld untersucht. Es zeigt sich, dass die hier angewandten Methoden im Vergleich zu RANS eine höhere Genauigkeit aufweisen und der daraus berechnete Jetztzustand der Strömung eine genaue Einsicht in die hydrodynamischen Prozesse erlaubt.

ACKNOWLEDGEMENTS

I would like to express my gratitude to the Graz University of Technology for providing me a possibility of gaining the necessary knowledge and experience to accomplish my work. My greatest words of appreciation go to my adviser Professor Gerald Zenz, whose professional support and guidance has been essential to this work. I would like to thank Professor George Constantinescu, whose outstanding academic expertise and advice helped me find my way through several challenges in the course of this research. I am grateful to Professor Josef Schneider for his support and advice during the laboratory study. To my colleagues at the Institute of Hydraulic Engineering and Water Resources Management for your friendship and support. I feel blessed to have been surrounded by such fabulous people.

Last but not the least, to my beautiful family, my wife Vestina and my lovely daughter Milda, thank you for your patience, support, encouragement and most importantly your unconditional love.

STATUTORY DECLARATION

I declare that I have authored this thesis independently, that I have not used other than the declared sources / resources, and that I have explicitly marked all material which has been quoted either literally or by content from the used sources. The text document uploaded to TUGRAZonline is identical to the present doctoral thesis.

August 5, 2020

. . . . . .

Date

. . . . . .

Signature

CONTENTS

NOMENCLATURE

Upper-case Roman

$\hat{S_{ij}}$	large-scale strain rate tensor
$\tilde{P_k}$	Turbulence kinetic energy's production term
$\tilde{S}$	function in the turbulent production term of SA turbulence model
A	Area
A_i	Area of a quadrant, where i represents quadrant's number
A_p	Area of a part
A_t	Sum of areas
C_μ	Turbulent viscosity constant in $k-\varepsilon$ turbulence model
$C_{\varepsilon 1}$	constant in $k-\varepsilon$ turbulence model
$C_{\varepsilon 2}$	constant in $k-\varepsilon$ turbulence model
C_{b1}	constant in SA turbulence model
C_{b2}	constant in SA turbulence model
C_{DES}	constant in SA-DES turbulence model
C_d	function in DDES turbulence model
D	Diameter
F	mass flux through the face
F_1	blending function in Shear Stress Transport turbulence model
F_2	blending function in Shear Stress Transport turbulence model
G	filter function
H	height of a section
L_x	streamwise length of periodic channel
L_z	spanwise length of periodic channel
N	centroid of a neighbour cell in FVM
P	centroid of a cell in FVM
P_k	Turbulence production term in $k-\varepsilon$ turbulence model
Q_i	Discharge of quadrant, where i represents quadrant's number
Q_t	Sum of discharges
R	Radius

Re	Reynolds number
Re_τ	friction Reynolds number
Re_b	Reynold number based on bulk velocity
S	invariant measure of the strain rate
S_ϕ	source term of ϕ
S_f	surface vector in FVM
S_{ij}	Stress rate tensor
U_b	bulk velocity

Lower-case Roman

$\bar{u}_p$	Mean axial velocity of a part
$\bar{u}_{rf}$	Mean axial reference velocity for the entire reference section
$\boldsymbol{u}$	velocity vector
$\boldsymbol{u}^*$	intermediate velocity
$\boldsymbol{u}^{n+1}$	velocity at $n+1$th time step
$\boldsymbol{u}^n$	velocity at nth time step
$\hat{p}$	filtered pressure
$\hat{u_i}$	filtered velocity
$\overline{u_i}$	Time or ensemble averaged velocity vector
$\overline{f}$	resolved part of the flow variable
$\overline{u_i^{'}u_j^{'}}$	Reynolds stress tensor
$\tilde{d_{DDES}}$	modified DDES turbulence model length scale
$\tilde{d}$	DES length scale
$\tilde{f_d}$	blending function in IDDES model
a_1	constant in Shear Stress Transport turbulence models
c_l	constant in IDDES model
c_{t3}	constant in IDDES model
c_{t4}	constant in IDDES model
c_t	constant in IDDES model
c_{v1}	constant in SA turbulence model
c_{w1}	constant in SA turbulence model
c_{w2}	constant in SA turbulence model
c_{w3}	constant in SA turbulence model
c_w	constant in IDDES's subgrid length scale function
d	turbulent length scale in SA turbulence model or a vector in FVM
d_{DDES}	DDES turbulence model length scale

d_{hyb} IDDES length scale

d_{LES} LES length scale in DDES turbulence model

d_{RANS} RANS length scale in DDES turbulence model

d_{WMLES} blended RANS-LES length scale in WMLES branch of IDDES model

d_w wall normal distance

f flow variable or a face in FVM

$f^{'}$ deviation of the flow variable

f_B function in WMLES branch of IDDES model

f_{dt} blending function in IDDES model

f_d function in DDES turbulence model

f_{e1} function in WMLES branch of IDDES model

f_{e2} function in WMLES branch of IDDES model

f_e function in WMLES branch of IDDES model

f_l function in WMLES branch of IDDES model

f_{t2} constant in IDDES model

f_t function in WMLES branch of IDDES model

f_{v1} function in SA turbulence model

f_{v2} function in SA turbulence model

f_w function in SA turbulence model

f_w^* constant in IDDES model

g function in SA turbulence model

k Turbulent kinetic energy

k height of a dune

k_s equivalent sand grain roughness

l length

l_t Turbulent length scale

p Pressure

r function in SA turbulence model

r_{dl} function in WMLES branch of IDDES model

r_{dt} function in WMLES branch of IDDES model

s_M Momentum source terms

t time

u x-component of velocity

u_τ friction velocity

u_i Velocity vector

$u_i^{'}$ Fluctuation of velocity vector

u_t Turbulent velocity scale

v y-component of velocity

w weight factor in CD scheme

w z-component of velocity

Upper-case Greek

Δt Time step size

Δ LES filter width

Δ_{free} subgrid length scale in IDDES model away from the walls

Δ_{max} local maximum subgrid length scale in IDDES model

Δ_{wall} subgrid length scale in IDDES model close to the walls

Γ_ϕ diffusivity coefficient of ϕ

Ψ function in DDES branch of IDDES model

Lower-case Greek

α Kinetic energy flux coefficient or a function in WMLES branch of IDDES

α_1 constant in Shear Stress Transport turbulence models

α_2 constant in Shear Stress Transport turbulence models

α_3 constant in Shear Stress Transport turbulence models

β^* constant in Shear Stress Transport turbulence model

β_1 constant in Shear Stress Transport turbulence models

β_2 constant in Shear Stress Transport turbulence models

β_3 constant in Shear Stress Transport turbulence models

δ channel half-height

δ_{ij} Kronecker delta

κ von karman constant

λ wave length

μ Dynamic viscosity

μ_t Turbulent/eddy (dynamic) viscosity

ν Kinematic viscosity

ν_t Turbulent/eddy (kinematic) viscosity

ω turbulent frequency

ω vorticity

ϕ generic conserved flow quantity

ρ Density

σ constant in SA turbulence model

$\sigma_{\omega 1}$ constant in Shear Stress Transport turbulence models

$\sigma_{\omega 2}$ constant in Shear Stress Transport turbulence models

$\sigma_{\omega 3}$ constant in Shear Stress Transport turbulence models

σ_{ε} constant in $k-\varepsilon$ turbulence model

σ_{k1} constant in Shear Stress Transport turbulence models

σ_{k2} constant in Shear Stress Transport turbulence models

σ_{k3} constant in Shear Stress Transport turbulence models

σ_{k} constant in $k-\varepsilon$ turbulence models

τ_{ij} Stress tensor

τ_{ij}^{SGS} sub-grid-scale stress tensor

τ_{w} wall shear stress

θ_{XY} Local deviation angle of velocity with respect to local axial velocity

θ_{XZ} Local deviation angle of velocity with respect to local axial velocity

$\tilde{\nu}$ modified viscosity in SA turbulence model

ε Rate of dissipation of k

Superscripts

$+$ quantity normalised in frictional wall units

sgs sub-grid scale

Subscripts

ave average value of the section

DES flow variable computed by DES

exp flow variable computed by experiment

n normalized

$RANS$ flow variable computed by RANS

Symbols

$< x >$ time average of x

$\bar{x}$ time average of x

$\hat{x}$ filtered x

$\overrightarrow{x}$ vector x

$\star$ any tensor product

$x^{'}$ fluctuation of flow variable (x)

1 INTRODUCTION

Hydropower, a true engineering accomplishment. Over the past few centuries it is refined and transformed to a low cost, reliable, sustainable and renewable energy source. In fact, according to International Energy Association (IEA), it is estimated that more than 16% of the world's electricity is generated by hydroelectric sources in 2015. According to Hydropower Status Report published by International Hydropower Association (IHR), in 2018, electricity generation from hydropower projects reached a record 4200 TWh, significantly more than all other renewable energies combined. Furthermore, hydropower supports growth of variable renewables such as wind and solar through its flexibility in operation, storage capacity and meeting energy demand when these sources are not available. This is especially important as we stepped into the new era where the world is slowly moving away from burning fossil fuels toward more sustainable and environmentally friendly sources of energy.

Although small-scale hydropower plants compared to their large-scale dam based counterparts have higher investment costs (EU/kW), these types require lower initial investment. Therefore, this makes them suitable option for decentralization of power and providing energy to rural areas. This is especially important for instance in less-developed countries or in Europe where most of its capacity for large-scale hydropower plants are exploited and it is moving toward an energy production with less environmental footprint. In Europe (EU-27), approximately 21800 small hydropower plants are in operation with average sizes of 0.6 to 0.7 MW. Additionally several projects are planned or under construction. Furthermore, IEA estimated that only 5% of the world's small-scale (note that the definition of small-scale varies from literature to literature) potential is currently being exploited. These demonstrate the importance of small-scale hydropower projects and their potential to become a viable and vital solution to ever increasing energy demand.

Hydropower is an important source of energy in Austria. The country's alpine topography along with high precipitation and numerous rivers offer considerable water resources. In fact 76% of the country's electricity is generated by renewable resources in which hydropower generates more than 60% (see Figure 1.1). Austria's hydropower industry blossomed in early 20th century and continued to become one of the world's leaders in harvesting renewable energy, in particular hydropower. A significant portion of the electricity is produced by small-scale hydroelectric plants with approximately 41% of the electricity is generated using run-of-river (ROR) type plants. This figure is expected to increase as new ROR plants are planned or under construction.

ROR, as the name suggests, typically located on a river and it operates by diverting up to 95% of the river directly through the intakes and the turbines or by the diversion channel to the powerhouse away from the river. The water then returns to the river downstream. Because the power generation depends on the river discharge, it may fluctuate dramati-

cally between days, months and seasons. Despite this, ROR plants have numerous advantages over large-scale projects where large reservoirs are needed to be constructed. These include but not limited to low construction costs, shorter construction period, low environmental impact on the local ecosystem, less greenhouse gas emission (in certain conditions), flexible operation and localization of the energy productions.

Design and operation of ROR is far from straightforward. The design must be flexible and robust to maximize the electricity production in a highly dynamic environment. This requires detailed and comprehensive study of the flow. Among many aspects, an optimum design of the approach channel and intake structure are especially important. The design procedure must consider elimination of unfavourable flow at the intakes and reduction of energy losses to minimum level. The investigations are usually carried out using physical model test and more recently by numerical models. Physical model tests are well established and refined over decades. However, numerical models are relatively new in modelling a complex approach flow. Hence, it is necessary to evaluate its performance and identify suitable key parameters involved in the modelling process. This study is focusing on this aspect.

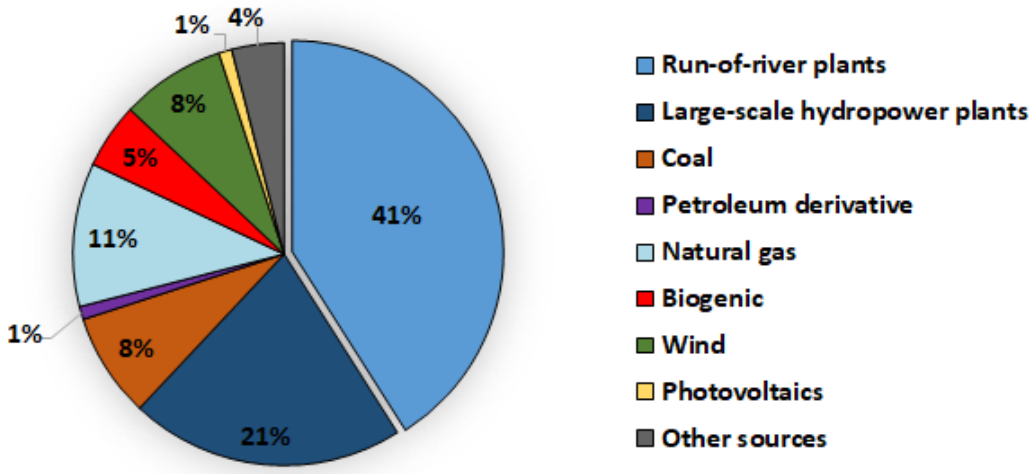

Figure 1.1: *Share of energy sources for the production of electricity in Austria (E-Control, 2016)*

1.1 Motivation

Several physical model tests have been carried to investigate flow problems at the intakes of run-of-river plants. In fact, until a few decades ago, physical models were the only way to study and optimise the designs of run-of-river plants. Example of such investigation can be found in Pugh et al. (1983) where different entrance shapes are tested, Mosonyi (1987) presented several laboratory tests and recommendations. Recent examples of such studies can be found in Zenz et al. (2015) and Zenz et al. (2016b) where the approach flows are investigated and optimised. Although physical model tests are the cornerstones of these type of investigation, past few decades experienced a rapid rise of the numerical models due to increase in computational power and development of advanced numerical algorithms. As the numerical simulations become more affordable, more studies are

carried out using this method. The numerical models are typically performed along the physical model tests where the numerical model is validated via physical model tests and then optimization of the approach flow can be carried out using the numerical model. Later the optimised solution can be put into test by the physical model test of the optimised solution for further tests. In the context of approach flow study and optimization, numerical models can offer a few advantages over the physical model study:

- Low costs of setting up and modification of the model.
- Availability of the results for the entire domain.
- The possibility of performing the simulation in prototype scale.

Examples of such investigation can be found in Demny et al. (1998), Khan et al. (2004), Zenz and Shahriari (2014), Benigni et al. (2018), Zenz and Shahriari (2019).

Despite recent popularity of numerical models in modelling approach flow of run-of-rivers, not many studies have been performed in which detailed investigation of hydrodynamical processes are carried out. Typically these types of investigations are limited to individual projects and the focus is on the prediction of the velocity distribution close to turbines rather than discussion of the hydrodynamical processes which, in some cases, hinder achievement of optimum flows. Hence, it seems essential to carry out such studies. This study, therefore, attempts to address some of the questions surrounding this topic.

1.2 Objectives

In practical hydraulic engineering problems, RANS is still considered a pragmatic choice. This is due to its robustness, efficiency and ease of use. Hence it is important to evaluate the suitability of this tool in modelling the approach flow. Furthermore, it is important to identify the parameters that affecting the outcome of the computation. The objective of this part can be summarized as follows:

1. Evaluation of the RANS accuracy using physical model tests results.
2. Determination of appropriate setup and boundary conditions.
3. Determination of appropriate grid size.
4. Effect of RANS turbulence models and a suitable choice.
5. Applicability of flow evaluation guidelines and identification of an appropriate location where the flow criteria are applied to.

Hybrid RANS-LES approaches are considered promising in modelling engineering problems. Among these, DES and improved versions of DES in particular have been successfully applied to complex hydraulic problems with high Reynolds number. On the other hand, RANS shown to have its drawbacks in modelling complex flows especially those which are based on eddy viscosity hypothesis. Therefore, a DES study is performed to achieve the following objectives:

1. Determination of suitable boundary condition. This includes generation of accurate inlet boundary values.
2. Evaluation of the accuracy of the method in comparison with RANS using the physical model test results.
3. Determination of computational requirement for such simulations.
4. Analysis of hydrodynamical processes occur in approach flows.

Furthermore, modelling a large domain at high Reynolds number result in high computational time. Hence, another objective of the study is to implement and validate an explicit solver based on Runge-Kutta and fractional step. This solver expected to speed up the computation in LES and DES cases.

1.3 Methodology

In order to realise the objectives of the study, the thesis is divided into seven chapters as follows.

1. Chapter 2 provides review of key components and aspects which are important in design and operation of run-of-river plants with specific focus on the intake structure and the approach flow.
2. Chapter 3 briefly describes the numerical algorithm used to perform the present numerical simulations.
3. Chapter 4 describes explicit solver based on Runge-Kutta and fractional step methods. It is validated via two numerical test cases. This solver later is used for Eddy-resolving computation.
4. Chapter 5 presents the physical model study, the measurement method and the results.
5. Chapter 6 presents RANS parameter study where key parameters affecting the results are identified. Additionally, the flow is evaluated according to the guideline and a brief flow analysis carried out.
6. Chapter 7 presents and discusses the results from the DES study. The hydrodynamical processes in approach flow are then investigated.
7. Chapter 8 summarizes the main outcomes and offers recommendations for future studies.

2 INTAKES OF LOW HEAD HYDRO POWER PLANTS

Hydroelectric plants are complex systems with several components. Design and operation of such complex systems require interdisciplinary collaboration of several engineering fields. Among these, civil engineering plays an essential role in design of such systems. Beside the design of the structures, optimum flow conditions into and out of the plants, operation of the weirs, sedimentation and several other aspects must be considered. These require careful consideration and design to maximize energy output and, more importantly, fail proof hydraulic systems. A failure in the system can have catastrophic consequences. Therefore, a significant amount of research has been carried out since the beginning of the last century.

In this study, the focus is on the approach flow to run-of-river plants and the flow conditions in and upstream of the intakes. In order to obtain an optimum flow to the turbine(s), several aspects have to be considered. There are general guidelines and books available to assist engineers in the design phase and during the operation of the plants. Among these, the book by Mosonyi (1987) is dedicated to low-head hydro power plants. The author comprehensively discusses different aspects of this type of hydropower plants including machinery equipments. Another important guideline is also available from American Society of Civil Engineers (ASCE) which focuses only on the intake's structures (Ott, 1995). In this Chapter a brief overview is provided over the different parts and design aspects for run-of-river. More specifically the focus is on the intake and the parts which affects the approach flow to the turbines.

2.1 Types

In general, the run-of-river plants can be divided into three types. For the first type is where the weirs and the intakes are located directly in the river. These types are shown in Figure 2.1a to d. In this type, several different arrangements of the weirs and powerhouse can be considered:

1. The powerhouse and the intakes are located at one side of the channel while the weirs are on the other side (Figure 2.1a). Examples of such hydroelectric plants are Rothleiten (Figure 2.2) and Graz-Puntigam (also know as Mur power plant) located south of Graz on the river Mur (Figure 2.3). The total capacity of the plant is 17.7 MW with design discharge of 200 m^3/s.

2. The other variant of this design is when the weirs are located at the center of the channel and the powerhouses are on the sides (Figure 2.1b).

3. In a larger rivers, it is possible to have the turbines and weirs arranged in alternating order where the turbines are placed in the piers (Figure 2.1c). This type is known as pier hydro power plants. Example of this type is Villach HPP with capacity of 24.6 MW on the river Drava in Austria. (4) is when the powerhouse is submerged and a portion of the flow is passing above the powerhouse (Figure 2.1d).

The second type of run-of-river is a special case of type 1 where the river is widened to accommodate the intakes. This is shown in Figure 2.1e. This type is very common and several example of these type can be found in river Mur in Austria. One of the advantages of this type is that the river cross section is not altered in contrast to the type 1, thus, during high flooding event, the water can be safely pass through the system and dissipate. The cost associated with the widening of the river is compensated by the simplified and flood-proof construction of the powerhouse in a dry excavation pit. Finally, In case where there is a bend upstream of the powerhouse, the widened part of the channel is located on outer side of the river bend due to sedimentation (see Section 2.6).

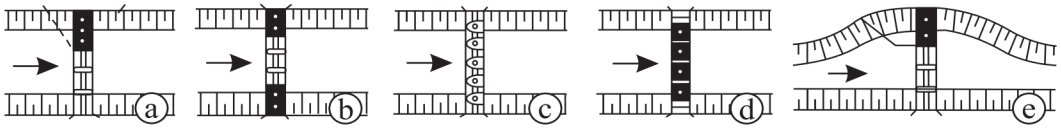

Figure 2.1: *Types of ROR where the powerhouse is located directly at the river Giesecke et al. (2014).*

Figure 2.2: *A ROR with forebay under-construction (Source: Institute of Hydraulic Engineering and Water Resources Management, TU Graz).*

The third type is different from the other two in a way that the powerhouse is constructed further downstream of the weirs and connected by a diversion channel to the main river.

Figure 2.3: *Three-dimensional visualization of Graz ROR located at river Mur (Source: murkraftwerkgraz.at).*

This type is usually constructed in highly meandering rivers with a small inclination of the river bed. Example of such power plant is Kirchbichl on Inn river. Figure 2.4 shows an aerial picture of this power plant. Total design flow of the plant is 499 m^3/s with total capacity of approximately 38 MW. The weirs are located directly on Inn river and a water channel is constructed on the right bank of the river. This channel is extended approximately one kilometre downstream to the powerhouse and connected to the main river afterwards.

2.2 Forebay

In this study, the focus is on the approach flow of type 2 hydroelectric plants (see Section 2.1). Therefore, all the aspects corresponds to this type is discussed. Previously it is discussed that in this type of plants, the river is widened to accommodate the powerhouse. This widening must be carried out in a way that no adverse effect on the flow is generated. Figure 2.5 shows a dimensioning of the forebay. In general a smooth transition is desirable, however, if the length of the forebay is too long it leads to increased costs (Figure 2.5a). On the other hand, when the transition is too short (Figure 2.5b), flow is separated and it leads to increase in head losses. Mosonyi (1987) proposed a design based on his experience which results in an optimum flow condition at the forebay. The design is based on 30 degrees expansion with a side pier. Figure 2.5c shows this design and corresponding dimensions.

The above design suggests a pier on the left side of the intakes with width and length of $1/6$ and $1/3$ to $1/4$ of the intake's width respectively. Mosonyi (1987) carried out a series of physical model tests in the laboratory to determine the optimum shape of the pier. Figure 2.7 shows four different shapes of the separation pier. The flow is visualised using streamlines. It is found that the set-up in Figure 2.7d is the optimum dimension for the pier followed by the set-up where the pier is completely removed (Figure 2.7a). Also it is observed that the excessive length of the pier leads to unfavourable separation immediately after the tip of the pier toward the intakes (Figure 2.7b). It is also suggested

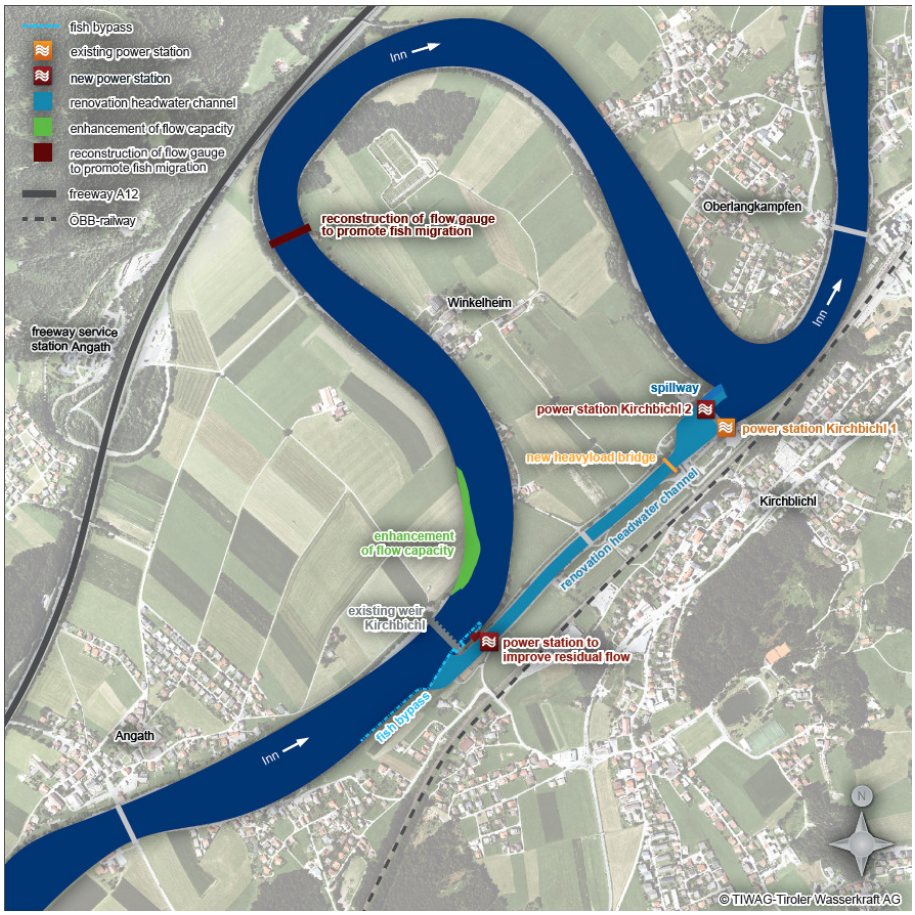

Figure 2.4: *Third type of ROR where the powerhouse is located outside of the river and connected via a channel (Source: tiwag.at).*

that the shape of the pier, beside the length, is important. Fore example it is found that a shape similar to Figure 2.7d is much more effective than the shape in Figure 2.7c. Based on these investigations, it is suggested that the shape of the pier must follow Figure 2.6. This is also confirmed by another study where numerical model is used to find the optimum shape of the pier. Fošumpaur and Čihák (2005) tested five different shapes and lengths. Their conclusion is very similar to Mosonyi (1987), however, the shape is slightly different and it follows an elliptical shape.

In general, the design without the pier is common (Figure 2.7a). This is due to the extra costs of a separation pier and more importantly maintenance issues. During a flood, when the weirs are in operation to pass the large debris downstream, some large debris can accumulate at the intake and detained especially when, during this time, turbines are in operation. The possible solution to this problem is a submerged pier. This type of piers are tested in the physical as well as the numerical models (see for examples Zenz and Shahriari (2014) and Zenz et al. (2016a)). It is shown that it can improve the velocity distribution inside the intakes.

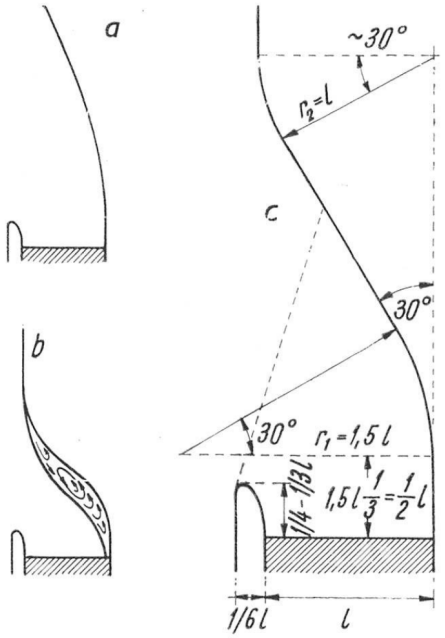

Figure 2.5: *Dimensioning of the forebay proposed by Mosonyi (1987).*

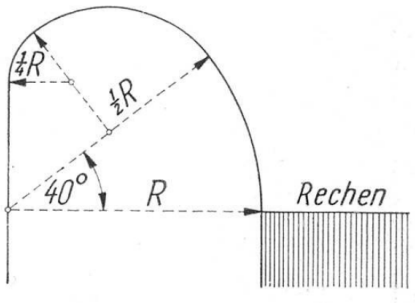

Figure 2.6: *Dimensioning of the separation pier proposed by Mosonyi (1987).*

2.3 Entrance shape

Entrance shape of the intake in low head hydro power plant is highly important. Although, the losses are relatively small in the intake section due to low velocity, irregular flow as well as flow separation in the intake section have unfavourable effect on the turbine's hydraulic behaviour. Therefore, an optimum design of entrance shape is essential in order to utilize full turbine performance as well as reduction of constructional costs.

General guidelines such as Ott (1995) provides some insight into the design of the entrance structure, however, a more specific and important study has been carried out by Pugh et al. (1983) on bulb turbine intakes. In a series of physical model tests, four different intake shapes have been investigated. The velocities were measured immediately upstream from the bulb using a hot-wire, constant-temperature anemometer. Moreover, pressure drops as well as discharges were measured to determine the head loss associated with each intake shape. The author concluded that significant simplifications and size reductions can be made in the intakes without increasing losses or adversely affecting flow distribution. This simplification can reduce the structural cost by 10 percent in

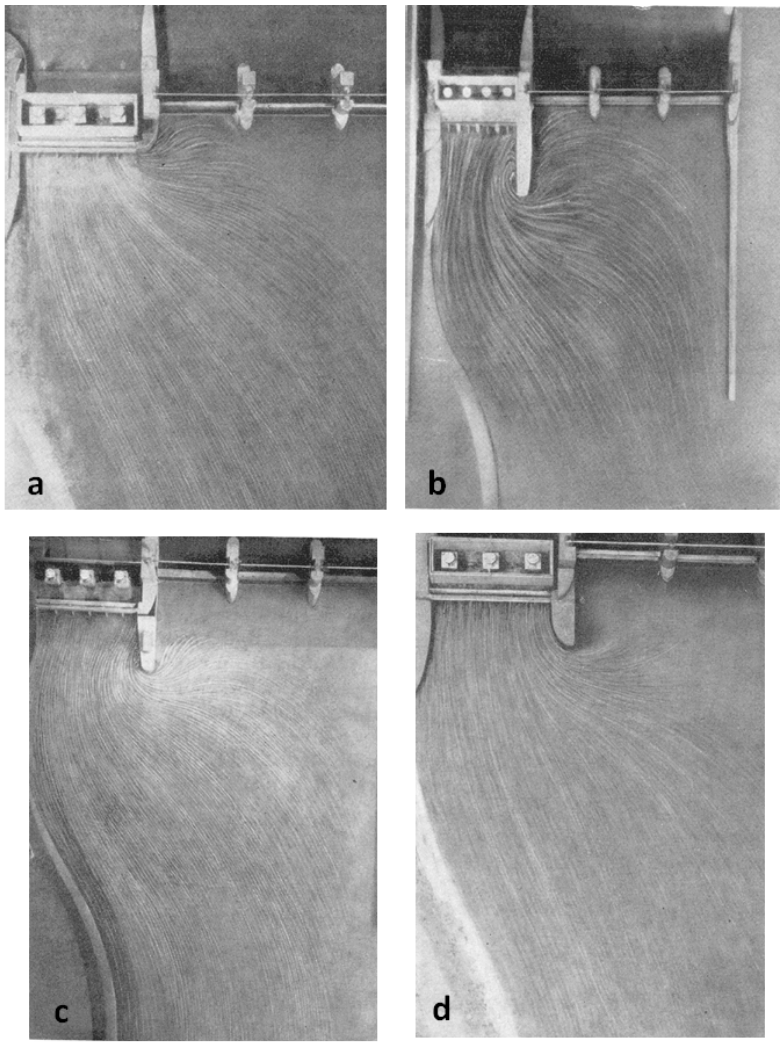

Figure 2.7: *Physical model tests to determine the optimum shape and length of the separation pier (Mosonyi, 1987).*

comparison with the original design. Figure 2.8 shows the conventional and the shortened designs. A numerical investigation has been carried out by Kostic (2016) based on these physical model tests and the results found to be in good agreement with the experimental results of Pugh et al. (1983).

2.4 Trashrack

Trashrack is an indispensable part of any low head hydroelectric plants. They usually placed at the forebay or the intake structure. The purpose of such a structure is to prevent the floating as well as submerged debris to enter the intakes and damage the intake structure, powerplant, and the equipments. Moreover, they can be used as a device to prevent fish from entering the intakes and subsequently reducing the rate of fish injuries. Trashracks are usually consists of parallel vertical bars, spaced in a way to minimize the head losses and, at the same time, perform their main tasks. The trashracks are usually constructed from square edged elements. The reason behind this is that it is found that streamlined rackbars are subjected to higher vibrations specially when the angle of inci-

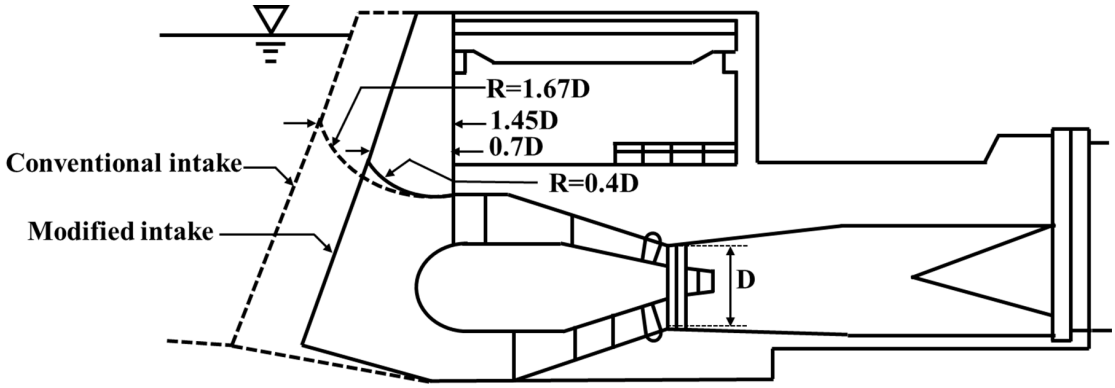

Figure 2.8: *Typical intake for bulb turbine illustrating conventional and modified (shortened) design adopted from Ott (1995).*

dent is greater than 10 degrees (Nguyen and Naudascher, 1991; Naudascher and Wang, 1993), although usually these streamlined bars are reducing head losses. It is common that the vertical bars are assembled using horizontal structural members to complete the overall trashrack structure. In run-of-river plants, trashracks are usually inclined vertically with slope of 1 horizontal to 4 vertical (as an example). This set up facilitates cleaning (or raking) operation of the trashrack and it provides a safer condition for the swimmers and the operating staff. Figure 2.9 shows the construction of the trashrack strcuture at Rothleithen hydroelectic plant.

In addition to the trashrack, trashracking system is also presents in order to remove the trash and prevent accumulation of debris. Figure 2.10 and 2.11 show automatic trashraking systems in two run-of-river plants. The racking procedure is carried out using hydraulically articulating arm that swings down over the trashrack and rakes the trash. In a survey conducted by Bureau of Reclamation (Wahl, 1992) on 85 different sites, the most common problems found to be raking and sediment problems.

One of the design aspects which must be considered is the structural safety of the trashracks. These structures are designed for static and dynamic loads. The loads on the structure are usually variable due to the different operating conditions of the plants and with wide range of flow velocities. Furthermore, change in loading can occur when clogging of the trashrack is expected (debris, aquatic plants and driftwoods). However, this can be avoided by regularly raking the trashracks. Beside static loads, dynamic loads are highly important when high approach velocity is present. One of the main concern in such circumstances is structural failure of the system due to vibrations induced by the fluid. Studies show that these vibrations are due to Karman vortices or impinging leading-edge vortices. These vibrations can have catastrophic consequences. For example, Design Standard of USBR (USBR, 2016) stated that trashracks should be analysed for vibration when the approach velocities are greater than 1.5 m/s. In this context, several authors investigated the fluid-structure interaction of the trashracks (Crandall et al., 1975; Nguyen and Naudascher, 1991; Matsumoto et al., 1998; Nascimento et al., 2006; Naudascher, 2017).

Above, it is discussed that the fluid flow through bars induce vibration. This cannot be studied without understanding the underlying hydrodynamic processes. Furthermore, the effects of the trashrack on the flow are highly important. This in return enables optimisa-

tion of this structures to reduce costs and minimize head losses. There are several studies on a single plate with different angles (see for example Nakamura et al. (1991), Ohya et al. (1992), Matsumoto et al. (1998) and Blazewicz et al. (2007)). Similarly there are several experimental studies on the trash rack like group of bars with different shapes and sizes. These studies are reviewed by Tsitaka et al. (2007), Tsikata et al. (2009a),Tsikata et al. (2009b) and Clark et al. (2010). However, there are not many numerical studies on this topic especially with more advanced turbulence models (LES) and for three-dimensional geometry. The most notable studies are from Hermann et al. (1998), Meusburger et al. (2001), Meusburger (2002), Ghamry and Katopodis (2012), Raynal et al. (2013) and Åkerstedt et al. (2017). The general outcomes of the studies that authors agree upon can be summarised as follows:

1. Larger aspect ratios of the bar increased the head losses.
2. Different flow regimes have been observed depend on the aspect ratios.
3. Reduction of the spacing leads to increase in head losses and change in flow regimes.

Finally, for the design of trashrack, reader can find more information in several guidelines and text books e.g. USBR (2016), Mosonyi (1987). Other problems which may arise related to the trashrack such as Ice and sediment problems are discussed in its relevant sections.

Figure 2.9: *Construction of a trashrack structure at a ROR (Source: Institute of Hydraulic Engineering and Water Resources Management, TU Graz).*

2.5 Free surface vortices

In general, two type of vortices are present in the approach flow of the run-of-river plants. The first type is located under the water surface, typically, near the bed and the walls. The

Figure 2.10: *Trashraking system using hydraulically articulating arm at a ROR (Source: Institute of Hydraulic Engineering and Water Resources Management, TU Graz).*

second type is the free surface vortices. These are located, as the name suggest, at the water surface and in close proximity to the intakes where the flow changes from a free surface flow to the pressurized system. These types are not uncommon in run-of-river plants especially in block types where the intakes are located on the either sides of the approach channel. However, the intensities of these vortices are usually low and do not lead to air entrainment into the pressurized systems.

In principle, the ideal condition is a single phase water only flow to the turbines due to negative consequences of air in pressurized system. Presence of air in the system can affect the operation, safety and efficiency of the hydropower plants. It is found that air in the system can cause:

1. Significant reduction in the turbine and pump intakes efficiency (Denny and Young (1957); Papillon et al. (2000)).
2. Unsteady flow situations (i.e. pulsation and pressure surges)
3. Reduction of the cross section and consequently reduction of discharge along with corrosion damages.

In cases where air entrainment is expected, de-aeration methods can be used to reduce the adverse effects (see for example Wickenhäuser (2008)).

Studies on this topic include wide range of problems from intakes of hydropower to pump sump intakes. Therefore, vast numbers of experimental studies have been carried out on

Figure 2.11: *Alternative trashraking system at ROR (Source: Institute of Hydraulic Engineering and Water Resources Management, TU Graz).*

intake vortices. These investigations are ranging from simple tests such as basic cylinder experiments (Einstein and Li (1951)) to more complex set up where large-scale physical model tests along with velocity and air entrainment rates have been measured (Möller et al., 2015). In general, vortex prevention measures are performed using increase in submergence of the intake, improvements to the approach conditions and anti-vortex devices. There are several experimental studies where anti-vortex devices are tested and proposed. For example Taghvaei et al. (2012) tested 13 different anti-vortex devices and found the best performance is achieved by a submerged horizontal slab extended out from the top of the intakes. Studies on this topic is not limited to experimental studies only, several numerical studies also carried out. However, numerical studies are mostly limited to simple set ups (see for examples Constantinescu and Patel (2000); Tokyay and Constantinescu (2006); Suerich-Gulick et al. (2006)). Möller (2013) provided a comprehensive review over the studies on this topic.

The source of free surface vortices in run-of-river plants are the eccentricity of the approach flow relative to the intakes. In the block type run-of-river plants where the intakes are located at one side of the river (Figure 2.1e), the flow are divided into two groups. The first group is the flow which is flowing in the direction of the intakes. The second group is almost perpendicular to the first and approaches from the side. This last group in particular is the cause of the free surface vortices. As the high velocity from the side joins the main flow, the separated water generates a transient, unsteady and shallow vortices. This is illustrated in Figure 7.50. In general, vortices are classified by their types (VT). These types are illustrated in Figure 2.12. These classification simply describe different phases on vortex formation from type VT1 with a coherent surface swirl to type VT6 where a full air core swirl extended all the way to the intake is present. Typically, two methods are used to identify and classify the vortices in the physical model test. One rely on the measurement of some quantities directly or indirectly. For example, changes in entrance loss coefficient, the magnitude of inlet pipe swirl or determination of the ingested air (Knauss, 2017). The second approach relies on visual techniques. Although

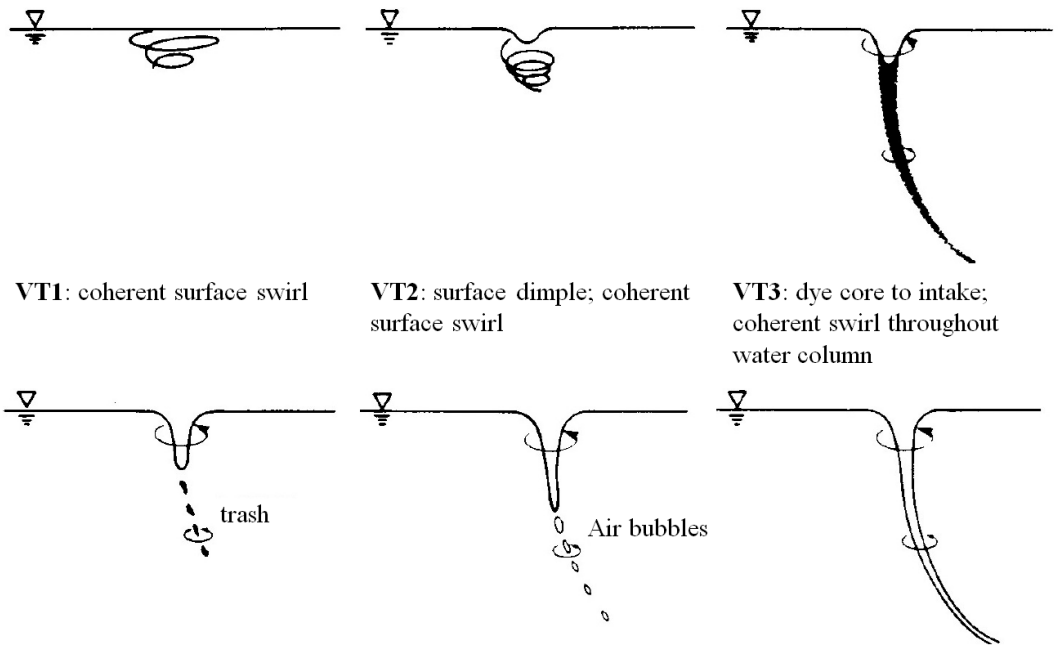

Figure 2.12: *Classification of free surface vortices based on their types adopted from Knauss (2017)*

it is highly objective, it is very common in physical model tests of run-of-river plants (see Figure 7.50). This techniques requires injection of dye and visually classification of the vortex type by Figure 2.12. In run-of-river intakes, types VT1 and VT2 are common and they are changing phases from one to another during the test. In numerical models, these can be easily achived by visualization of iso-surface of vortex related parameters such as Q-criterion, Lambda2 and vorticity (see Holmén (2012) for description of the aforementioned methods).

In and after the design process, it is important for an engineer to identify possible problems related to free surface vortices at the intakes. One of the criteria is the critical submergence. The critical condition is defined as the situation where the vortex core reaches the intakes and the air bubbles continuously enters the pressurized system. Hence, critical submergence is the hight where critical condition is occurring. Several authors proposed formulas to identify the critical submergence based on basic flow parameters (i.e. intake diameter, velocity head and Froude number) or rotational parameters. A comprehensive list of these formulas can be found in Suerich-Gulick et al. (2013), Ott (1995), Möller (2013) and Knauss (2017).

In conclusion, free surface vortices are present at run-of-river intakes due to its design and set up, however, these vortices are of type VT1 and VT2 according to the classical classification. In this study, the origin of these vortices are investigated via numerical studies in Section 7.4.3.

2.6 Sedimentation

Reservoir sedimentation is one of the major challenges in large or small reservoirs. It is estimated that about 1% of the storage capacity of the reservoirs are being reduced worldwide per year. However, this number can be higher depended on the region. For example it is reported that due to sedimentation, in average, more than 2% of the China's reservoir storage capacity is lost (Batuca and Jordaan Jr, 2000; Morris and Fan, 1998) or measurements in India showed that the annual loss rate is reaching 0.8% (Basson, 2008, 2009). Another example is the survey which has been carried out in the United States and reported in Dendy et al. (1973). The report showed that annual sedimentation rate are from 2.0 to more than 3.0% for small initial storage volumes. These studies indicating the importance of development of sediment management strategies and tools to address this issue. Only a general outline of this topic is discussed here due to the fact that this topic covers a wide range of scientific fields.

In ROR plants, sedimentation is a major challenge when rivers carry significant amount of sediment. The deposition of sediment in reservoirs not only impacts the storage capacity but also it may increase the flood risk, blockage of the intakes and injection of particles into the turbines and consequently decrease of machine's life time. For example Figure 2.13 shows a significant deposition of sediment in front of the intakes. In rivers, the amount of sediment can vary significantly. Figure 2.14 summarized the mean annual sedimentation rate of selected reservoirs at Austrian rivers (Figure 2.14). It is shown that significant amount of sedimentation has been observed depended on the river. This figure alone shows the importance of the sediment management in RORs.

Figure 2.13: *Sedimentation in front of the intakes (Source:TIWAG).*

One of the first measure to reduce sedimentation, specifically at the intakes of ROR plants, is a selection of the intake's location where less sediment deposition is expected. In rivers, secondary currents play an important role in sediment deposition and erosion. Specially in meandering rivers, due to secondary currents, the sediment is being deposited and eroded in the interior and exterior of the bend respectively. Therefore, it is appropriate to place the intake at the exterior of the river bend where scour is expected. Figure 2.15 shows this process and the best locations for the intakes of a ROR.

In order to establish a sustainable sediment management system, several strategies must be considered. These can be combined or changed to achieve a viable solution. Annandale et al. (2016) summarized these techniques as

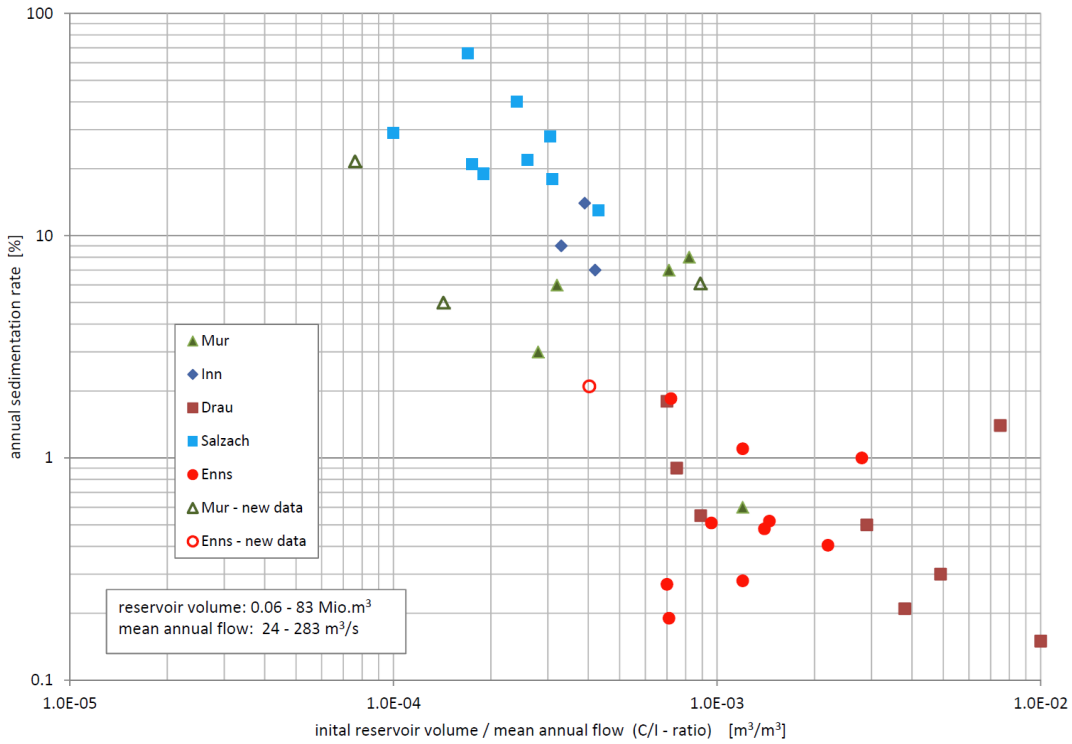

Figure 2.14: *Mean annual sedimentation rate of selected reservoirs of ROR plants at Austrian rivers in relation to the initial reservoir volume to mean annual flow ratio of the reservoirs (Harb, 2013).*

1. Upstream measures to reduce the inflow of sediment by controlling soil and channel erosion at its source and/or trapping eroded material upstream of the reservoir
2. Flushing the reservoir through the system
3. Redistribute or remove the deposited sediment by dredging
4. Techniques to adopt to sedimentation

Morris and Fan (1998) discussed the sediment management options in detail and provided several case studies.

From the design phase of a run-of-river to the reconfiguration of existing projects, sediment modelling plays an important role. Typically physical model study and/or numerical modelling is performed to investigate and refine the design parameters. These modelling approaches allow significant reduction in constructional and long-term operational costs. For example, several physical model studies have been performed at the Institute of Hydraulic Engineering and Water Resources Management of Graz University of Technology where the design is optimised for sediment management. These projects are ranging from new run-of-river plants (Schneider et al., 2012) to existing ones where the configurations altered until the optimized condition is achieved (Schneider et al., 2018) and general sediment management projects (Schneider et al., 2009, 2011; Harb et al., 2014). Figure 2.16 shows an example of such projects. In this study, a new set of weir systems planned to be constructed with the old one remained in place. The function of the old weirs as well

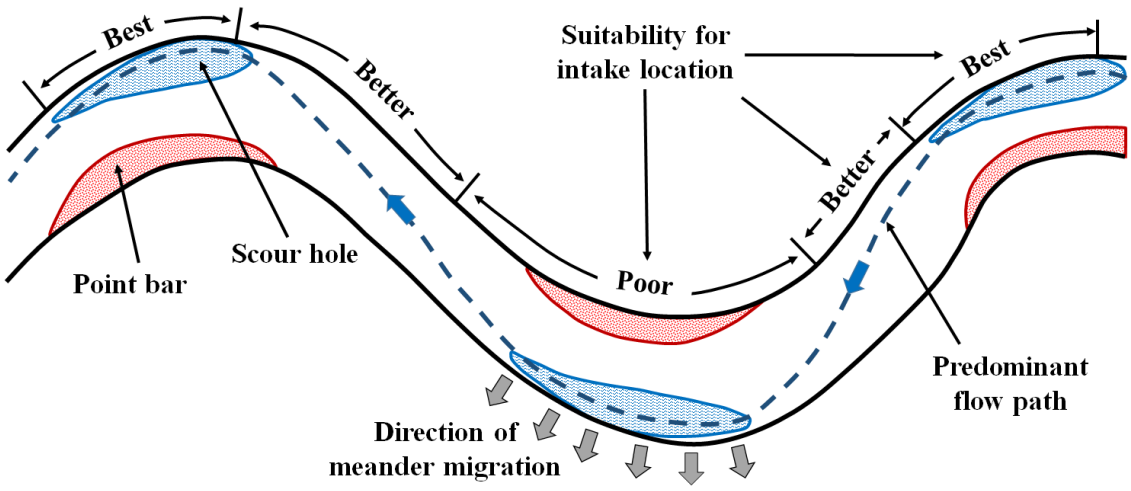

Figure 2.15: *Suitable locations of the ROR intakes in terms of sedimentation (Adopted from Annandale et al. (2016)).*

as the sediment process are then investigated during the construction phase where part of the downstream channel is blocked by the construction pit.

In recent decades, due to increase in computational power and development of numerical tools for sediment modelling, numerical models have become an inseparable part of the design and optimization of the run-of-river plants. Typically, numerical models relies on the empirical formulas to model the erosion and sedimentation processes. This includes suspended sediment as well. They may performed in 1, 2 or 3 Dimensional depends on the size and characteristics of the project. Although these tools are constantly being validated with measurement data and improved, they have their own drawbacks and limitations however. The main problems here is not the numerical techniques themselves, but from insufficient knowledge about the sedimentation processes especially for cohesive materials (Teisson, 1991). Despite that, examples of successful application of the numerical tools are numerous and several examples can be found in Harb et al. (2011), Dorfmann et al. (2012), Haun et al. (2012), Harb et al. (2012), Harb et al. (2013) and Dorfmann et al. (2015).

2.7 Ice

In cold regions where the ambient air temperature reaches well below zero in winter, engineers must consider the effect of ice on the design and operation of hydroelectric facilities and the intakes. The primary concern is the effect of ice on the hydraulic structures (i.e. trashracks and weirs) and the passage of water through the system. The main strategy when the formation of ice is expected is the avoidance, or in other word, minimizing the amount of ice building up at or reaching the intakes. This is usually done by selecting an appropriate location for the plants and the intakes. Despite this, many hydroelectric plants may encounter ice problems during their operation. These problems, in general, can be grouped into three:

1. Blocking of intakes by active or passive frazil ice

Figure 2.16: *Investigation of the sediment transport via physical model study; top: initial state, bottom: final state (Source:Institute of Hydraulic Engineering and Water Resources Management, TU Graz).*

2. Blocking of intakes by surface ice blocks

3. Freezing of gates and rack guide rails and seals

Frazil ice is regularly affects intakes structures especially trashracks. This is due to the fact that they are made of steel with high heat conductivity. Additionally, frazil ice tends to accumulate on surfaces that interrupt the flow streamlines. Most notable study on the formation of frazil ice on the trashrack and its effects on the flow is done by Andersson and Daly (1992). It is shown that frazil ice accumulates first on the upstream side of the trashrack bars independent of the shape of the bars. The accumulated frazil ice then grows and bridges between individual bars first near the water surface and then proceeds downward. This led to blockage of the trashrack. Furthermore, the flow is found to be highly nonuniform as the frazil ice accumulates and bridges across the bars. The porosity of accumulated frazil ice is found to be around 0.67. Finally, it is shown that for rectangular bars with different spacing, the head losses are increasing during frazil ice formation with the rate of head loss increase is significantly higher when the bars are closer together. Daly (1991) described the frazil ice formation and presented several ways to deal with this issue. These methods include suppressing frazil ice production by stable ice cover, using heat by addition of warmer water upstream or heated trashracks, mechanical removal, back flushing, different coating for trashracks, vibration and removal of trashracks. Furthermore, Daly (1991) proposed several measures for operating under frazil conditions.

Frazil ice is not the only problem which an intake may encounter. Blockage of intakes by surface ice is another issue. Due to intermittent thaws and break-ups during spring, large quantity of ice may accumulate at the intakes. Detection and avoidance of this problem is easier than the frazil ice problems. In the design phase by avoiding a narrow, shallow approach channel along with adequate submergence on intakes this problem can be minimized. Furthermore, the location of the intakes can be chosen in a way that the risk of ice accumulation at the intakes are low. From the operational point of view, ice removal facilities can be organized to remove surface ice.

In alpine regions, usually ice does not have significant influence on the ROR plants and hydropower system. Therefore, this topic is not discussed further. Reader can refer to a recent study by Gebre et al. (2013) where authors reviewed the ice-related effects on hydropower systems and given a comprehensive overview on the available literatures.

2.8 Open channel surge

Another design aspect which must be accounted for is open channel surge waves. In hydropower, low- or high-head, rapid starting or stopping of the turbines or pumps can generate significant surge waves. In a high-head system, there are measures to deal with this issue (i.e. surge tanks), however, in run-of-rivers ,the surge wave, if ignored, can lead to flooding of powerplant as well as the overtopping of the dams. Hence, accurate estimation of the surge wave is crucial. This is usually done by analytical formulas (see for example Chanson (2004)) or numerical models. In some cases a physical model may carried out to estimate the surge and evaluate the design (common for high-head power-plants).

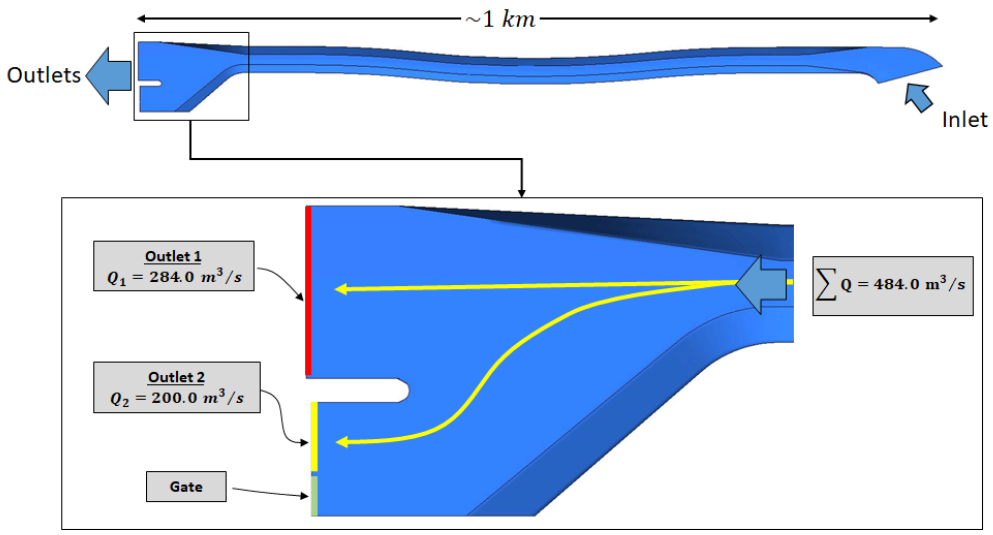

Figure 2.17: *Computational domain and boundary conditions of Kirchbichl HPP (Zenz and Shahriari, 2019).*

In headwater channels of RORs, the surge wave is generated when there is a rapid stopping of the turbines. It is shown that depends on the discharge and channel characteristics, the height of the surge wave can be estimated by analytical and numerical models to avoid problems. Example of such investigation can be found in Zenz and Shahriari (2019). The layout of this project is illustrated in Figure 2.4. As part of the renovation, expansion and upgrading plan, several additions as well as modifications have been planned. One of the major part is the addition of a new turbine with 200 m^3/s discharge, increasing total discharge from 284 to 484 m^3/s. Additionally a weir is designed to be located at the left side of the powerhouse. A series of investigation has been carried out to determine the height of the surge wave during a rapid shutdown of the turbines and possible reduction of the initial surge height by utilizing the automatically operated weir during the event. The flap of the weir is designed to open by 1 m/min, in the vertical direction, immediately after the shutdown. Initially the investigation carried out using analytical approach with simplification and without the weir. Additionally, a series of 3D CFD simulations have been carried out to determine the height of the surge wave and its evolution over time. Figure 2.17 shows the computational domain and boundary conditions. The most challenging part of the simulation was the operation and integration of the gate in the simulation. This is done via additional script where at each time step the water level along with position of the flap are evaluated. Then the discharge through the weir is computed using weir flow expression and it imposed on the boundary as a new value. Figure 2.18 shows the computed water level along with the discharge through the gate. It is shown that in a case where the gate is not in operation, the surge starts to rise and reaches more than 2 meters higher than the initial water level at approximately 170 s post shutdown. On the other hand, when the operation of the weir is considered, the water level rises to the same value as the first case until approximately 50 s, however, at this point, due to the operation of the gate, the rate of increase of water level decreases and it levels off at approximately 100 s.

The case study which described briefly above shows that estimation of the height and characteristic of a surge wave is important to avoid any risk for flooding the powerplant,

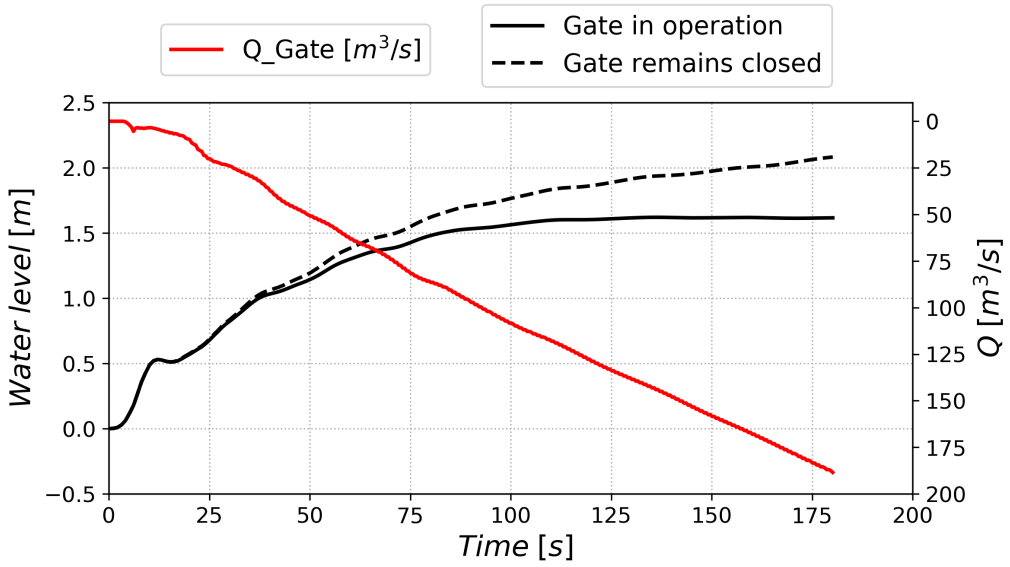

Figure 2.18: *Estimation of the surge-wave heights by numerical models in a long head-water channel due to rapid turbine shutdown (Zenz and Shahriari, 2019). 0 water level represent initial or operating water level.*

surrounding facilities, operators and more importantly to avoiding human loss. This is particularly important when high discharge in combination with a narrow channel is present. Furthermore, it is shown that by opening a gate after shutdown, the height of the surge wave can be reduced significantly.

2.9 Design criteria for low head intakes

In principal, the turbines are designed to work in their full capacity for the uniform flow or ideal intake condition. However, in reality an ideal flow condition is hardly achieved. In high head HPPs, The intake structure is far away from the turbines and usually flow to the turbines are well developed, on the other hand, in the low head HPPs the intake structure is short and flow condition becomes important. A highly non-uniform flow condition can lead to vibration-induced damages and reduction of energy production (Fisher and Franke, 1987). Therefore, early detection of possible flow problems and optimization of the intake is crucial in the design phase.

Typically each turbine manufacturer have their own set of criteria for acceptable flow condition. Nevertheless, Fisher and Franke (1987) proposed a set of guidelines based on their own experiences and three turbine manufactures known as Fisher-Franke guideline. Later, Godde (1994) carried out experimental investigations on the bulb turbines intake and the author applied and compared excising criteria to the physical models. The flow is typically evaluated at a control section. The control section is typically located after the trash-rack and upstream of the turbine due to its accessibility for measurement in the physical model tests. Based on Fisher and Franke (1987) and Godde (1994) recommendations, these criteria for a reference cross section can be summarized as follows

- **C1**: The flow must be free from air-entraining vortices.

- **C2**: The magnitude of the cross flow velocity components $\bar{v}$ and $\bar{w}$ must not exceed $\pm 5\%$ of the axial or streamwise velocity for the entire reference section, $\bar{u}_{rf}$. This can be shown as a histogram of the normalized velocities in each direction using following expression:

$$\bar{v}_n = |(\bar{v} \times 100)/\bar{u}_{rf}|, \text{ and } \bar{w}_n = |(\bar{w} \times 100)/\bar{u}_{rf}| \tag{2.1}$$

- **C3**: Typically the reference section is divided into quadrants Q_1, Q_2, Q_3 and Q_4 (Figure 2.19) and flow rate is computed for each quadrant. Then the volumetric flow deviation is computed from the ideal condition. The maximum deviation must be within $\pm 10\%$ of the total flow rate. Figure 2.19 shows the quadrants and the corresponding parameters for arbitrary control section.

- **C4**: The deviation angle of flow velocity from the axial direction must be below $5°$. This condition is checked by plotting the histograms of deviations angles using Equation below:

$$\theta_{XY} = tan^{-1}|\bar{v}/\bar{u}|, \text{ and } \theta_{XZ} = tan^{-1}|\bar{w}/\bar{u}| \tag{2.2}$$

  where θ_{XY} and θ_{XZ} are the deviation angle in XY and XZ directions respectively.

- **C5**: The mean velocity of the part ($\bar{u}_p$) is normalised by the global mean velocity ($\bar{u}_{ref}$). This value must be between the upper and lower boundaries which they depend on the testing section area (A_p) to the total area (A_t) ratio. These boundary values are summarized in Table 2.1. Additionally, Figure 2.20 shows a graphical representation of these upper and lower boundaries. Any points inside the boundaries are fulfilling the criterion.

A_p/A_t	0	0.2	0.5	1.0
Upper values	1.25	1.1	1.05	1.05
Lower values	0.75	0.9	0.95	0.95

Table 2.1: *Upper and lower boundaries for condition 5 (Godde, 1994).*

- **C6**: The kinetic energy flux coefficient α is calculated for the control section. This value is simply the ratio of the kinetic energy of the control section to the theoretical value using the following expression:

$$\alpha = \frac{1}{A} \cdot \int_A \left(\frac{\bar{u}}{\bar{u}_{rf}}\right)^3 \mathrm{d}A \tag{2.3}$$

In the conditions above $\bar{u}$, $\bar{v}$ and $\bar{w}$ corresponds to local mean velocities in X, Y and Z directions respectively. Furthermore, subscript $\bar{u}_{rf}$ is the mean axial velocity perpendicular to the control section (X direction).

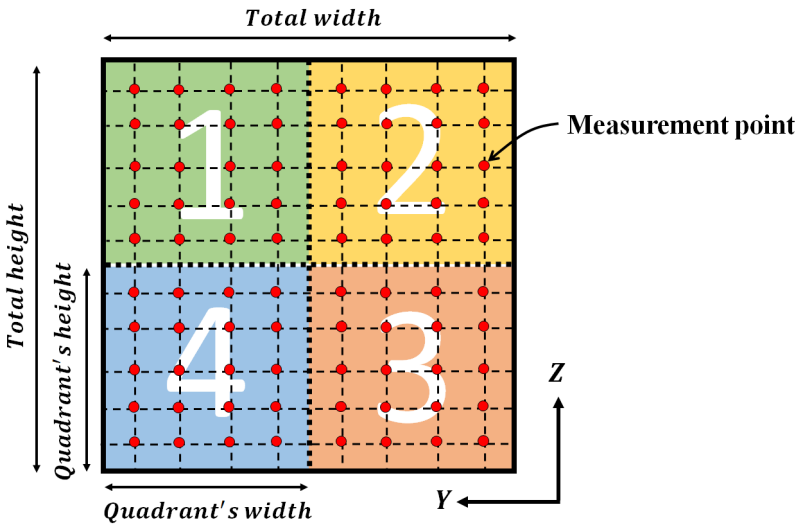

Figure 2.19: *Arbitrary control section with relevant parameters and the coordinate system.*

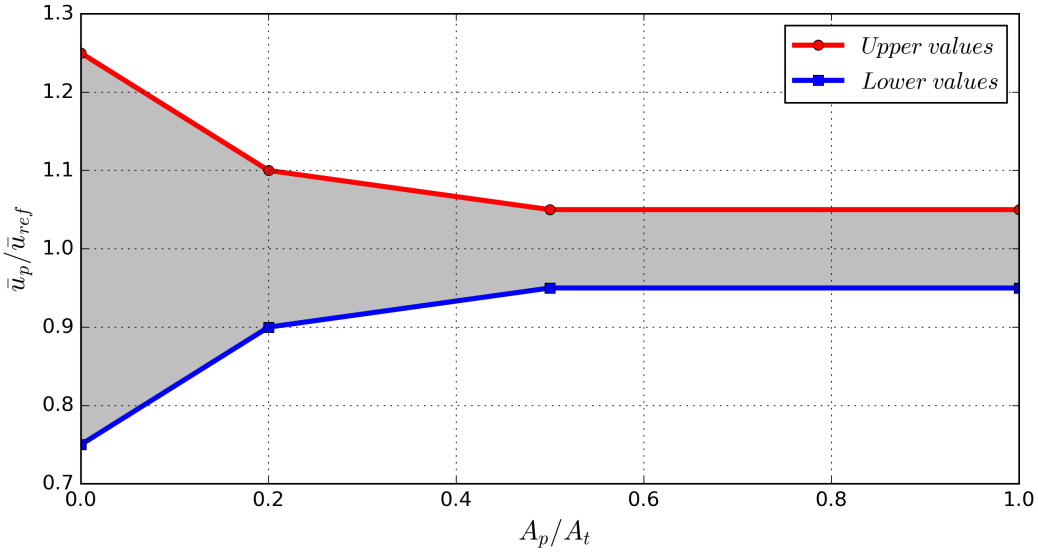

Figure 2.20: *Graphical representation of condition 5. Any point inside the boundaries (Grey area) is fulfilling the criterion (Godde, 1994).*

Recently, Gabl et al. (2018) reviewed these criteria and proposed a modification to the condition 5. He argued that evaluation of the flow near the trash-rack is not enough due to negligible wall influence. Rather the flow must be evaluated close to the turbines where the cross section is circular. The modified criterion which was originally used for rectangular control sections is then applicable to the circular section. Furthermore, he concluded that the kinetic energy flux coefficient in combination with the modified criterion are recommended for the geometry optimization of the intake. However, in the physical model test it is not easily possible to measure the velocity at that section due to limited accessibility and this modified criterion is only can be used in the CFD simulations.

2.10 Other aspects

Until now, several important aspects related to the design of intake and head water channel are discussed. Many other important aspects are also must be considered. however, these factors are beyond the scope of this work and they cover a wide range of topics. Ecological and fish protection for instance is highly important and must be considered. According to the European Union Water Framework Directive (2000/60/EC), the member states must achieve good qualitative and quantitative status of all water bodies until 2027 including the free passage of the fish in the rivers. Although significant progress has been made for upstream migration of fishes, downstream migration remains challenging. The fish injury and mortality rate is highly depends on the intake structure, the fish species, fish size, turbine types and several more conditions (Ott, 1995). In particular, the most challenging aspect is the guidance of the fish to the bypass system due to incomplete knowledge of fish behaviour. Hence, studying of fish behaviour is important and requires a close collaboration between engineers and ecologists. In this context, Cuchet (2014) provided an overview of the studies in this field and carried out a laboratory experiment to investigate fish behaviour at hydropower intakes.

Several other aspects are also crucially important in the operation of run-of-river plants. The instrumentation and gauges, operation of the gates and many more are the examples. Reader must refer to the relevant literatures, text books (i.e. Giesecke et al. (2014)) and guidelines (i.e. Ott (1995)) for further information.

3 COMPUTATIONAL METHODOLOGY

In this chapter, a brief description of the numerical methods are presented. Firstly, the governing equations of incompressible fluid flow is described. This is followed by a general description of turbulent flows and its modelling approaches. In this part, emphasis is given to Reynolds Averaged Navier-Stokes, Large Eddy Simulation and Improved Delayed Detached Eddy Simulation methods. In the final section, solution method for the flow equations via Finite Volume Method is presented. The descriptions are provided in respect to the methods used by OpenFOAM.

3.1 Governing equations

The bedrock of computational fluid dynamics is the fundamental equations of motion for fluid particles. They are the mathematical statements of following conservation laws of physics:

- Conservation of mass: It states that the amount of mass remains constant within the domain (matter cannot be created or destroyed)
- Conservation of momentum: It follows the Newton's second law of motion and it states that the amount of momentum remains constant within the domain; or in other word, momentum is neither destroyed or created but it changes through the action of forces.
- Conservation of energy: It is based on the first law of thermodynamics and it states that the rate of change of energy equals the sum of rate of heat addition to and the work done on fluid particle.

For the Analysis of the fluid flows, the fluid is treated as a continuous medium, thus, at macroscopic length scale (e.g. larger than $1\mu m$) the molecular structure of the fluid and molecular motions may be ignored. This assumption allows to describe the fluid in terms of pressure, velocity, density and temperature, and their time and space derivatives. These sets of equations can be simplified by assuming that the flow is incompressible and the temperature do not have influences on the flow field dynamics. Therefore, these equations can be reduced to four equations; continuity and momentum equations. subsequently, the number of unknowns also will reduce to four; pressure, and three velocity components in Cartesian coordinate system.

The first step in the derivation of mass conservation (continuity) equation is to write the mass balance for the fluid element. The mass balance states that the rate of increase of

mass in fluid element is equal to net rate of flow of mass into fluid element. Using this principle and assuming an incompressible flow, the mass continuity (or simply continuity) equation can be written as

$$\frac{\partial u_i}{\partial x_i} = 0 \tag{3.1}$$

In order to derive the equation of motion (momentum equation) for a fluid, Newton's second law of motion can be applied to the fluid particle. It states that the rate of change of momentum of a fluid particle equals to the sum of the forces on the particle. By assuming that the forces on the particle are due to pressure, viscous stresses and body forces, the momentum equation can be written in differential form for incompressible Newtonian fluid as

$$\frac{\partial u_i}{\partial t} + \frac{\partial u_i u_j}{\partial x_j} = -\frac{1}{\rho}\frac{\partial p}{\partial x_i} + \nu \frac{\partial^2 u_i}{\partial x_j \partial x_j} + s_M \tag{3.2}$$

where ν is the kinematic viscosity of the fluid and ρ is the fluid density. In Equation 3.2, the first term on the right hand side is the forces due to pressure, the second term is due to viscosity and the last term is the body force (i.e. gravity).

To summarize, Equation 3.1 and Equations 3.2 form a set of coupled differential equations for incompressible Newtonian fluids. There are four unknowns (pressure and velocities) and four equations which they can be solved simultaneously for a problem domain by numerical techniques to compute these unknowns.

3.2 Turbulence Modelling

In hydraulic engineering the majority of flows from simple cases like two dimensional pipe flow to more complex three dimensional free surface flows are having high Reynolds numbers (Re) due to significant inertia forces over viscous forces. At low Reynolds number, the flow is laminar and the adjacent layers of fluid slide past each other with no disruption. This type of flow regime is characterized by high momentum diffusion over momentum convection. Figure 3.1a shows a laminar flow regime in a pipe where water flows in parallel layers. On the other hand, as suggested by the appearance of the dye in Figure 3.1b, when the Reynolds number of the flow is higher than a particular value (Re_{cr}) it becomes unstable and chaotic and the flow parameters, pressure and velocity, fluctuate continuously with time. Due to the chaotic and unpredictable nature of turbulent flow, it represents one of the great scientific challenges. In fact, Nobel Laureate and theoretical physicist Richard Feynman (Feynman, 1964) described turbulence as 'the most important unsolved problem of classical physics'.

Because of the importance of the turbulence in engineering applications and engineer's need for a suitable tools capable of capturing the effects of turbulence, significant amount of researches are dedicated to the development of numerical methods to model the turbulence effects. These methods can be categorized into the following three groups:

- Direct Numerical Simulation (DNS): The instantaneous continuity and momentum equations (3.1 and 3.2) for an incompressible turbulent flow are solved on a fine

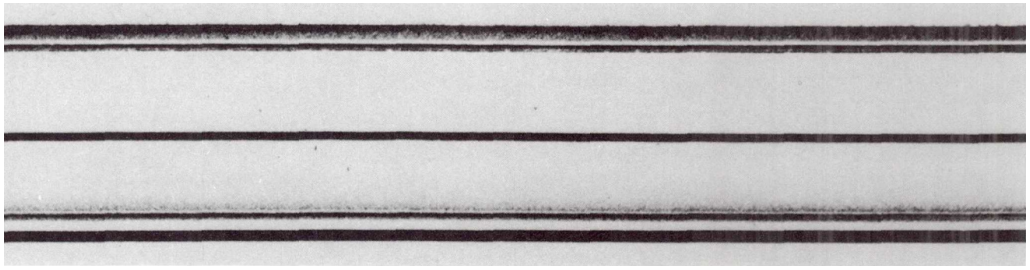

(a)

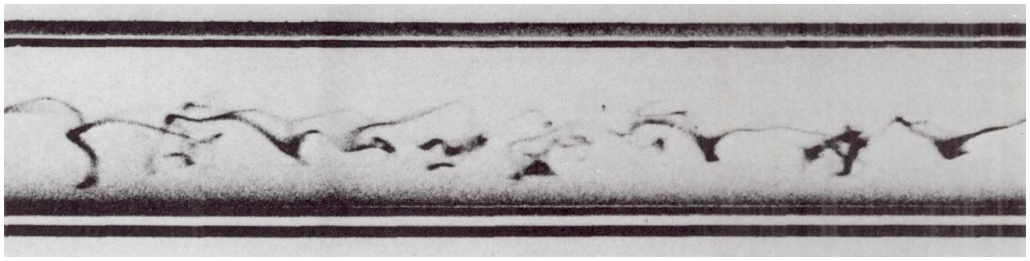

(b)

Figure 3.1: *Effect of Reynolds number on ribbon of dye in water flowing through a glass tube (Van Dyke, 1982); (a) Low Reynolds number ($Re < 2000$), (b) High Reynolds number.*

spatial grids with sufficiently small time steps to resolve all scales of the turbulence. Because of the wide range of time and length scales, the direct simulation of the turbulent flow is not feasible for engineering applications due to high computational costs of the method.

- Large Eddy Simulation (LES): applies a spatial filtering operation on the time-dependent flow equations, prior to the application of numerical methods, to separate the large eddies which are bigger than the grid size from the smaller eddies. During the filtering operation, information relating to the smaller eddies which are filtered-out is destroyed.Furthermore, the interaction effects between the large (resolved) eddies and the smaller, unresolved ones result in sub-grid-scale or SGS stresses. The effect of these stresses on the resolved flow are considered by an SGS model. The inherent unsteady nature of LES leads to larger computational requirements than those of classical turbulence models such as k-epsilon (KE) and k-omega (KO) models.

- Reynolds Averaged Navier-Stokes (RANS) turbulence models: The main focus of this approach is on the mean flow and the effect of the turbulence on the mean flow properties. This is done by time averaging or ensemble averaging (when the boundary conditions are time dependent) the flow equations. The time averaged Navier-Stokes Equations contains extra terms, known as Reynolds stresses, due to the interaction between various turbulent fluctuations. Then the Classical turbulence models are used to model these extra terms. This approach has been one of the the main tools for engineering flow calculations over the last four decades because of it's reasonable accuracy and the computing resources that is required.

Due to the success of LES turbulence models in modelling hydraulic engineering flow

problems in recent years (see i.e. Rodi et al. (2013)) and increase in computational power, LES became an excellent tool to study flow problems with complex geometry. Additionally, development of hybrid models, i.e LES-RANS, reduce the computational requirements of classical LES. These techniques make modelling problems with higher Reynolds number possible. In the following sections principle of RANS and LES will be discussed followed by description of a Hybrid LES-RANS model.

3.2.1 Reynolds Average Navier-Stokes

The cornerstone of the classical turbulence models is Reynolds Average Navier-Stokes (RANS) equations. The idea is based on Reynolds decomposition through which an instantaneous flow quantities, velocity and pressure, are decomposed by a mathematical technique into its time-averaged and fluctuating quantities. This approach first proposed by Osborne Reynolds (Reynolds, 1895).

Random nature of the turbulent flow can be seen in figure 3.2. It is showing a typical point measurement of the flow velocity. Assuming that the velocity can be divided into an average, $\overline{u_i}^{RANS}$, and a time varying components, u'_{iRANS} :

$$u_i(x_i,t) = \overline{u_i}^{RANS}(x_i,t) + u'_{iRANS}(x_i,t) \tag{3.3}$$

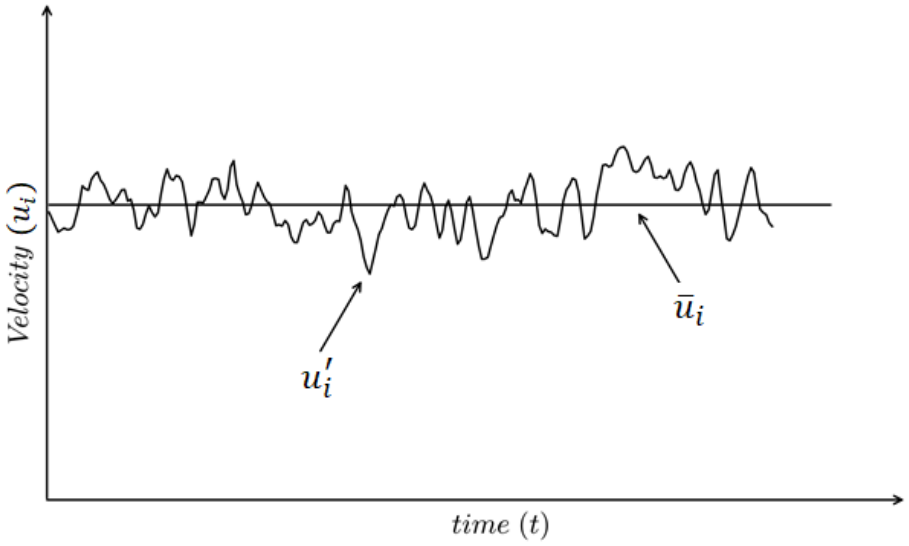

Figure 3.2: *velocity fluctuation at a point in turbulent flow*

Then the average component can be defined by integrating the velocity over a time scale, Δt:

$$\overline{u_i}^{RANS} = \frac{1}{\Delta t}\int_t^{t+\Delta t} u_i \mathrm{d}t \tag{3.4}$$

In the average procedure above, the time step, Δt, is large compared to the turbulence fluctuations, but relatively small compared to the timescale of which the equations are being solved.

By applying the Reynolds decomposition (equation 3.3) and substituting the average components into the equations 3.1 and 3.1, RANS equations for incompressible fluid can be obtained. These equations are similar to equations 3.1 and 3.2, however, when the procedure is applied to the non-linear term $\partial u_i u_j / \partial x_j$ of the momentum equation, it leads to the introduction of six Reynolds stresses, $-\rho < u'_{iRANS} u'_{jRANS} >$ or in short $-\rho \overline{u'_i u'_j}$, in addition to the viscous stresses. It is the main task of turbulence modelling to develop computational procedures of sufficient accuracy and generality to predict these Reynolds stresses.

In a Newtonian fluid, the viscous stresses are proportional to the rate of deformation of fluid elements and by assuming incompressible fluid and dropping over bar and $RANS$ symbols from the equations, the viscous stresses are given by equation:

$$\tau_{ij} = 2\mu S_{ij} = \mu(\frac{\partial u_i}{\partial x_j} + \frac{\partial u_j}{\partial x_i}) \tag{3.5}$$

Experimental evidence showed that the turbulence decays unless there is shear in in isothermal incompressible flows. Furthermore, it has been found that when the rate of deformation increases, the turbulent stresses are also increases. Based on these evidences, Boussinesq proposed that the Reynolds stresses might be proportinal to the mean velocity gradient. According to boussinesq hypothesis, the Reynolds stresses can be given by :

$$-\rho \overline{u'_i u'_j} = \mu_t(\frac{\partial u_i}{\partial x_j} + \frac{\partial u_j}{\partial x_i}) - \frac{2}{3}\rho k \delta_{ij} \tag{3.6}$$

Where k is the turbulent kinetic energy per unit mass.

The first term on the right hand side of the equation 3.6 is similar to the equation 3.5 except the molecular viscosity has been replaced by the parameter μ_t which is the turbulent or eddy viscosity with the dimensions of Pas. The second term on the right hand side of the equation 3.6 includes the Kronecker delta, δ_{ij}, which equals to one for $i = j$ and it is zero for $i \neq j$.

Based on this hypothesis, several turbulence models are developed. In this study, three RANS turbulence models are used: Spalart-Allmaras (SA), Standard k-epsilon (SKE) and Shear Stress Transport (SST). In the following sections these models are discussed briefly.

3.2.1.1 Standard k-epsilon Model

One of most commonly used RANS turbulence model is the SKE model (Launder and Spalding, 1974). In addition to solving an equation for turbulence kinetic energy and hence for the turbulent velocity scale, this model employs another equation for dissipation rate (ε) of the turbulent kinetic energy for the length-scale determination.

This model states that the velocity and length scale which are representative of the large scale turbulence can be defined by turbulent kinetic energy, k, and the rate of dissipation of turbulent kinetic energy, ε as follows:

$$u_t = k^{1/2} \tag{3.7}$$

$$l_t = \frac{k^{2/3}}{\varepsilon} \tag{3.8}$$

and by applying dimensional analysis and using the relations in equations 3.14 and 3.16 for velocity and length scale, the eddy viscosity, μ_t, can be determined by equation 3.9.

$$\mu_t = \rho\nu_t = C_\mu \rho \frac{k^2}{\epsilon} \tag{3.9}$$

where C_μ is a dimensionless constant.

The SKE model uses the following(semi-empirical) transport equations for turbulent kinetic energy (k) and it's rate of dissipation (ε):

$$\frac{\partial k}{\partial t} + u_j \frac{\partial k}{\partial x_j} = \frac{\partial}{\partial x_j}[(\nu + \frac{\nu_t}{\sigma_k})\frac{\partial k}{\partial x_j}] + P_k - \varepsilon \tag{3.10}$$

$$\frac{\partial \varepsilon}{\partial t} + u_j \frac{\partial \varepsilon}{\partial x_j} = \frac{\partial}{\partial x_j}[(\nu + \frac{\nu_t}{\sigma_\varepsilon})\frac{\partial \varepsilon}{\partial x_j}] + C_{\varepsilon 1}\frac{\varepsilon}{k}P_k\frac{\partial u_i}{\partial x_j} - C_{\varepsilon 2}\frac{\varepsilon^2}{k} \tag{3.11}$$

where P_k is the turbulence production due to viscous forces and it is given by equation :

$$P_k = \nu_t(\frac{\partial u_i}{\partial x_j} + \frac{\partial u_j}{\partial x_i})\frac{\partial u_i}{\partial x_j} \tag{3.12}$$

On the right hand side of the equations 3.10 and 3.11, the first term is the rate of change of k or ε and the second term is the transport by convection of k or ε. On the left hand side, the first term is the transport of k or ε by diffusion, the second term is the rate of production of k or ε and the last term is the rate of destruction of k or ε.

The production term in the $k-$equation were obtained by substituting the production term of the exact $k-$equation by equation 3.6. On the right hand side, a modeled form of the principal transport process appears in the both equations of the model. Using the gradient diffusion idea, the turbulent transport terms are represented and to connect the diffisivities of k and ε to the eddy viscosity μ_t, Prandtl numbers σ_k and σ_ε have been introduced into the model. Furthermore, it is not possible to measure directly the pressure term of the

turbulent kinetic energy exact equation, however, its effect is accounted for in equation 3.10 within the gradient diffusion term.

The model equation (3.11) for dissipation rate , ε, assumes that its production and destruction terms are proportional to the production and destruction terms of the kinetic energy equation (3.10). This assumption, ensures that when kinetic energy increases, the dissipation rate will also increase and that when the kinetic energy decreases, the dissipation rate decreases sufficiently fast to prevent nonphysical (negative) values for the kinetic energy. In order to production and destruction terms dimensionally be correct, in the dissipation rate equation (3.11), these terms were multiplied by the factor ε/k and the constants $C_{\varepsilon 1}$ and $C_{\varepsilon 2}$ allow for the correct proportionality between the terms in $k-$ and $\varepsilon-$equations.

Constant	$C_{\varepsilon 1}$	$C_{\varepsilon 2}$	C_{μ}	σ_k	σ_{ε}
Value	1.44	1.92	0.09	1.0	1.3

Table 3.1: *Standard k-epsilon turbulence model constants*

The equations above contain five constants that are determined by comprehensive data fitting for wide range of flows. these constants are given in Table 3.1 for SKE model.

Finally, in order to compute Reynolds stresses, the boussinesq relationship (Equation 3.6) can be used.

3.2.1.2 Shear Stress Transport (SST) Model

There are other variables that can be employed to determine the length scale instead of the rate of dissipation of turbulence kinetic energy. In fact, several other two-equation turbulence models have been proposed. One of the notable alternatives to the KE model is the KO model proposed by Wilcox et al. (1998). In the Wilcox's KO model, the first transported variable is the turbulence kinetic energy, k , similar to the KE model. On the other hand, instead of the rate of dissipation of turbulent kinetic energy as the second variable, the model uses the turbulence frequency , ω, to define the length scale ($l_t = \sqrt{k}/\omega$). Using k and ω, the eddy viscosity can be computed by equation 3.13 below.

$$\mu_t = \rho k/\omega \tag{3.13}$$

The KO model has an advantage over the KE model because integration to the solid boundary is not required damping functions in low Reynolds number applications. However, Practical application of the KO model has shown that the results are highly sensitive to assumed free stream conditions for ω at the inlet (Menter, 1993). On the other hand, the results of the KE model has shown to be much less sensitive to the assumed values in the free stream. Menter (1994) developed a hybrid turbulence model to take advantage of the KO near the wall and the SKE in the outer region by introducing a blending function and transforming the ε-equation into an ω-equation by substituting $\varepsilon = k\omega$. Finally, The two transport equations for k and ω for incompressible turbulent flows at high Reynolds number are as follows:

$$\frac{\partial k}{\partial t} + u_j \frac{\partial k}{\partial x_j} = \frac{\partial}{\partial x_j}[(\nu + \sigma_{k3}\nu_t)\frac{\partial k}{\partial x_j}] + \tilde{P}_k - \beta^* k\omega \tag{3.14}$$

where

$$\tilde{P}_k = \min(\tau_{ij}\frac{\partial u_i}{\partial x_j}, 10\beta^* k\omega) \tag{3.15}$$

is the rate of turbulent kinetic energy's production and

$$\frac{\partial \omega}{\partial t} + u_j\frac{\partial \omega}{\partial x_j} = \frac{\partial}{\partial x_j}[(\nu + \sigma_{\omega 3}\nu_t)\frac{\partial \omega}{\partial x_j}] + \alpha_3 S^2 - \beta_3\omega^2 + 2(1-F_1)\sigma_{\omega 2}\frac{1}{\omega}\frac{\partial k}{\partial x_j}\frac{\partial \omega}{\partial x_j} \tag{3.16}$$

is the equation for ω.

Menter et al. (2003) introduced a number of modifications to improve the performance of the SST $k-\omega$ model based on two decades of experience from broad range of computations with the model. The main modifications can be summarized as follows:

- Modified model constants: The model constants have been revised for better performance of the SST model. These values are given in table 3.2.

Constant	α_1	α_2	β_1	β_2	β^*	σ_{k1}	σ_{k2}	$\sigma_{\omega 1}$	$\sigma_{\omega 2}$	a_1
Value	0.55	0.44	0.075	0.083	0.09	0.85	1.0	0.5	0.856	0.31

Table 3.2: *Shear Stress Transport turbulence model constants*

- Blending functions: Due to numerical instabilities which may arise because of the different computed values of the eddy viscosity with the transformed $k-\varepsilon$ model near the wall and the standard $k-\varepsilon$ model in the free shear region outside of the boundary layer, blending functions are used to obtain a smooth transition between the two models. Blending function, F_1, is added to the cross-diffusion term on the right hand side of the equation 3.16 and it is given by:

$$F_1 = \tanh\left\{\left\{\min\left[\max\left(\frac{k^{1/2}}{\beta^*\omega y}, \frac{500\nu}{y^2\omega}\right), \frac{4\sigma_{\omega 2}k}{CD_{k\omega}y^2}\right]\right\}^4\right\} \tag{3.17}$$

where

$$CD_{k\omega} = \max\left(2\rho\sigma_{\omega 2}\frac{1}{\omega}\frac{\partial k}{\partial x_j}\frac{\partial \omega}{\partial x_j}, 10^{-10}\right) \tag{3.18}$$

Furthermore, the function (F_1) is used by equation 3.19 for the model constants, ϕ_3. F_1 is one near the wall and hence it takes the original $k-\omega$ model constants. on the other hand, outside of the boundary layer, F_1 reduces to zero and it gives the constants for the Menter's transformed $k-\varepsilon$ model.

$$\phi_3 = \phi_1 F_1 + \phi_2(1-F_1) \tag{3.19}$$

- Limiters: the model's performance is increased by taking into account the transport of the turbulent shear stress. This is done by introducing a limiter to the formulation of the eddy viscosity:

$$\nu_t = \frac{a_1 k}{\max(a_1\omega, SF_2)} \tag{3.20}$$

where a_1 is a constant, $S = \sqrt{2S_{ij}S_{ij}}$ is an invariant measure of the strain rate and F_2 is a blending function similar to $F1$ and it is given by:

$$F_2 = \tanh\left[\left\{\max\left(\frac{2k^{1/2}}{\beta^*\omega y}, \frac{500\nu}{y^2\omega}\right)\right\}^2\right] \tag{3.21}$$

Moreover, the turbulent kinetic energy production is limited by equation 3.15 to prevent accumulation of turbulence in stagnation regions.

3.2.2 Large Eddy Simulation

Turbulent flows contain wide range of scales of the fluid motion. The fundamental idea behind LES is to compute directly the motion of large scales (eddies) by solving the governing three-dimensional time-dependent equations and to model the motions of the small scales. The large scales contain the most of the energy and the transport process. They are depend on geometry and boundaries. Moreover, they are inhomogeneous, anisotropic and diffusive. On the other hand, small scales are produced by large eddies, homogeneous, isotropic and dissipative, thus easier to model (Rodi et al., 2013). Figure 3.3 illustrates the concept of LES by showing the energy flux in turbulent flow. In the energy cascade, the large eddies extract energy from the mean flow and transfer energy to the smaller scales. On the other side of the spectrum, the kinetic energy is withdrawn by the dissipation mechanism.

The first step in LES is to separate the turbulence motion into large and small scales. This is done by a filtering process in which small-scale motion is removed from the flow field. In this process, one of the important parameters is a characteristic length-scale or filtering width Δ. Basically, scales larger than Δ will be retained and computed directly, on the other hand, scales smaller than Δ, usually referred to as SGS, are modelled. In the following, the pricipale of filtering process is briefly described.

In principle, any flow variable, f, is split into the resolved part, $\overline{f}$, and the deviation, f', from that as follows:

$$f = \hat{f} + f' \tag{3.22}$$

In order to extract the resolved components $\hat{f}$ a filtering operation is applied, in its general form its formulated as

$$\hat{f}(\boldsymbol{r}, t) = \int_D G(\boldsymbol{r}, \boldsymbol{r'}, \Delta) f(\boldsymbol{r'}, t) \mathrm{d}V' \tag{3.23}$$

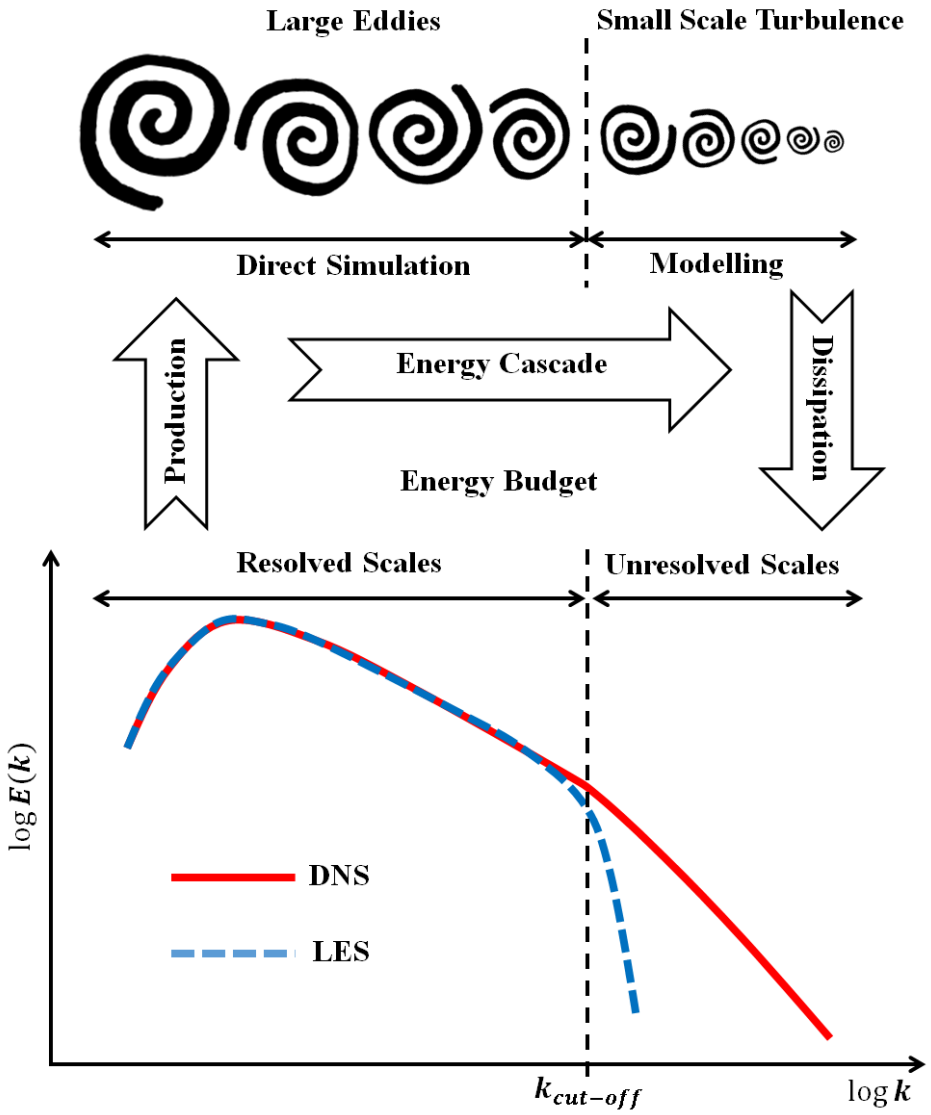

Figure 3.3: *Concept of Large Eddy Simulation in relation to energy flux and energy spectrum (adopted from Rodi et al. (2013)).*

where $\boldsymbol{r}$ is the location where $\hat{f}$ is to be computed and $\boldsymbol{r'}$ is the location where f is considered in the spatial integration, D is the flow domain and finally G, is the filter function. The filter function is compactly supported with filter width Δ and it satisfies the condition:

$$\int_D G(\boldsymbol{r}, \boldsymbol{r'}, \Delta) V' = 1 \tag{3.24}$$

In one spatial direction Equation 3.23 can be written as:

$$\hat{f}(x_i, t) = \int_D G(x_i, x_i', \Delta) f(x_i', t) \mathrm{d}x_i' \tag{3.25}$$

The most commonly used filter function is the top-hat filter especially for finite volume methods. Primarily reason behind the popularity of this filter function for Finite Volume

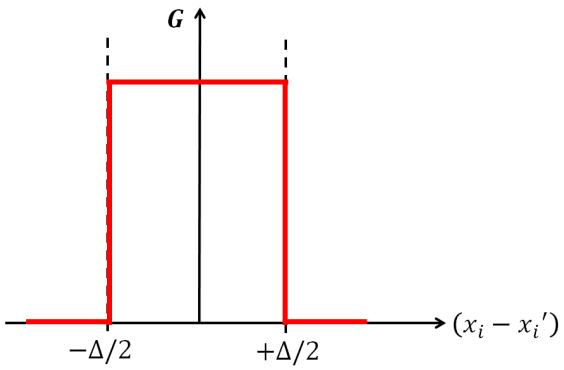

Figure 3.4: *Top-hat filter function used in LES*

Methods (FVM) is that the average is over a grid volume of the finite volume mesh where the flow quantities are a piecewise linear function of x. suppose that the filter width Δ is equal to the grid-spacing the top-hat filter function reads

$$G = \begin{cases} \frac{1}{\Delta}, & \text{if } |x - x_i| \leq \frac{\Delta}{2}. \\ 0, & \text{otherwise.} \end{cases} \tag{3.26}$$

Figure 3.4 is a graphical representation of the top-hat filter function. OpenFOAM uses this filter function for LES.

3.2.2.1 Filtered governing equations

The governing equations of incompressible flow, Equation 3.1 and 3.1, are described in Section 3.1. Applying the filtering operation to these equations leads to the filtered equations governing the resolved variables in LES:

$$\frac{\partial \hat{u}_i}{\partial x_i} = 0 \tag{3.27}$$

$$\frac{\partial \hat{u}_i}{\partial t} + \frac{\partial}{\partial x_j}(\hat{u}_i \hat{u}_j) = -\frac{1}{\rho}\frac{\partial \hat{p}}{\partial x_i} + \frac{\partial}{\partial x_j}\left(\nu \frac{\partial \hat{u}_i}{\partial x_j}\right) - \frac{\partial \tau_{ij}^{SGS}}{\partial x_j} \tag{3.28}$$

For clarity these equations are written in tensor notations. In Equation 3.28), τ_{ij}^{SGS} is the subgrid-scale stress tensor and it represents the effect of the unresolved fluctuation on the resolved motion. this stress tensor further can be split into a isotropic and an anisotropic component as follows:

$$\tau_{ij}^{SGS} = \tau_{ij} + \frac{1}{3}\tau_{kk}^{SGS}\delta_{ij} \tag{3.29}$$

This separation is convenient since the anisotropic component τ_{ij} can be modelled using eddy viscosity approach

$$\tau_{ij} = -2\nu_t \hat{S}_{ij} \tag{3.30}$$

where ν_t is the subgrid-scale turbulent viscosity or eddy viscosity and $\bar{S}_{ij}$ is the large-scale strain rate tensor.

As for the isotropic component $1/3\tau_{kk}^{SGS}\delta_{ij}$, this term can be added to the filtered pressure or simply neglected (Erlebacher et al., 1992).

Finally the filtered momentum equation 3.28 can be written as

$$\frac{\partial \hat{u}_i}{\partial t} + \frac{\partial}{\partial x_j}(\hat{u}_i\hat{u}_j) = -\frac{1}{\rho}\frac{\partial \hat{p}}{\partial x_i} + 2\frac{\partial}{\partial x_j}\left[(\nu + \nu_t)\hat{S}_{ij}\right] \tag{3.31}$$

Equation 3.31 contains additional variable ν_t which must be modelled similar to RANS. However, unlike RANS which this variable must model the entire turbulence spectrum, here, much smaller portion of the turbulence spectrum is modelled, hence smaller potential for errors.

3.2.3 Hybrid RANS-LES models

Hybrid RANS-LES approaches are considered promising in modelling engineering problems. Among these, DES and improved versions of DES in particular have been successfully applied to complex hydraulic problems with high Reynolds number. for example, Constantinescu et al. (2011) applied DES to investigate the structure of turbulent flow in an open channel bend of strong curvature with deformed bed. Constantinescu and Squires (2003), investigated the flow around and over a sphere using LES and DES and concluded that both techniques predict well the drag, position of laminar separation,and the mean pressure and skin-friction distributions along the sphere. Koken and Constantinescu (2009) studied the dynamics of coherent structures in a turbulent channel flow with a vertical side-wall obstruction. Finally, Constantinescu et al. (2012) used DES to investigate the effect of momentum ratio on the dynamics and sediment-entrainment capacity of coherent flow structures at a stream confluence.

3.2.3.1 Detached Eddy Simulation (DES)

The general idea behind DES is to combine RANS and LES. The model works in RANS mode in the boundary layer and switches to LES mode in the separated flow regions. In general, there are two DES models; one based on the Spalart-Allmaras (SA) RANS model which was originally proposed by Spalart et al. (1997) and one based on the $k-\omega$ Shear-Stress-Transport (SST) model proposed by Strelets (2001). In this study improved version of SA-DES is used due to its success in modelling hydraulic problems (i.e. Chang et al. (2007) and Constantinescu et al. (2012)) in comparison with SST-DES approach.

The base model for the SA-DES is the RANS model of Spalart-Allmaras or SA in short. This model is relatively simple and it solves a transport equation for the modified eddy viscosity $\tilde{\nu}$ given by

$$\frac{\partial \tilde{\nu}}{\partial t} + u_j\frac{\partial \tilde{\nu}}{\partial x_j} = c_{b1}\tilde{S}\tilde{\nu} + \frac{1}{\sigma}\left[\nabla\cdot((\nu+\tilde{\nu})\nabla\tilde{\nu}) + c_{b2}(\nabla\tilde{\nu})^2\right] - c_{w1}f_w\left[\frac{\tilde{\nu}}{d}\right]^2 \tag{3.32}$$

Then the eddy viscosity ν_t is computed from

$$\nu_t = \tilde{\nu} f_{v1} \text{ with } f_{v1} = \frac{\chi^3}{\chi^3 + c_{v1}^3} \text{ and } \chi = \frac{\tilde{\nu}}{\nu} \tag{3.33}$$

Equation 3.32 contains the turbulent length scale , d, in the destruction term (last term on the RHS). It is equal to the distance to the nearest wall. The rest of the parameters in Equation 3.32 is given by:

$$\begin{gathered} \tilde{S} = \bar{S} + (\tilde{\nu}/\kappa^2 d^2) f_{v2},\ f_{v2} = 1 - (\tilde{\nu}/\nu)/(1 + \chi f_{v1}),\ f_w = g\left[\frac{1 + c_{w3}^6}{g^3 + c_{w3}^6}\right]^{\frac{1}{6}} \\ g = r + c_{w2}(r^6 - r),\ r = \frac{\tilde{\nu}}{\tilde{S}\kappa^2 d^2} \end{gathered} \tag{3.34}$$

The model contains several constants. these constants are $c_{b1} = 135$, $c_{b2} = 0.622$, $\sigma = 0.67$, $\kappa = 0.41$, $c_{v1} = 7.1$, $c_{w2} = 0.3$, $c_{w3} = 2.0$ and $c_{w1} = c_{b1}/\kappa^2 + (1 + c_{b2})/\sigma$.

Finally, in order to switch to LES mode, the RANS length scale,d, in Equation 3.32 is replaced with the new parameter, $\tilde{d}$, which is defined by:

$$\tilde{d} = min(d, c_{DES}\Delta) \tag{3.35}$$

In Equation 3.35, d is the distance to the nearest wall, c_{DES} is an empirical constant equal to 0.65 and Δ is the local maximum grid spacing in the three directions ($\Delta = max(\Delta_x, \Delta_y, \Delta_z)$). Basically, expression 3.35 states that when d, the distance to the wall, is smaller than $c_{DES}\Delta$, the model runs in RANS mode, however, when $d < c_{DES}\Delta$, the model acts as SGS model in LES mode.

3.2.3.2 Delayed Detached Eddy Simulation (DDES)

The original DES model showed encouraging success. However, this model encountered a few drawbacks. In the presence of ambiguous grids with wall-parallel grid spacing of the order of the boundary layer thickness, Modelled Stress Depletion (MSD) and Grid-Induced Separation (GIS) can occur (Spalart et al., 2006). In order to address these issues with the original SA based DES model, Spalart et al. (2006), following the ideas of Menter and Kuntz (2004), proposed several modification to the original model. The basic idea behind these modification is to introduce a blending function. This is done by replacing r in Equation 3.34 with a new parameter r_d as follows:

$$r_d = \frac{\nu + \nu_t}{\kappa^2 d^2 \cdot max\left[\sqrt{\frac{\partial \bar{u_i}}{\partial x_j}\frac{\partial \bar{u_i}}{\partial x_j}}, 10^{-10}\right]} \tag{3.36}$$

Then this new variable is used to define a smooth function f_d:

$$f_d = 1 - tanh\Big([8r_d]^3\Big) \tag{3.37}$$

This function returns 1 in LES region where $r_d << 1$ and zero everywhere else. Finally, a new model length scale d_{DDES} is defined based on the new function as follows:

$$d_{DDES} = d_{RANS} - f_d \cdot max(0, d_{RANS} - d_{LES}) \tag{3.38}$$

where d_{LES} is equal to $c_{DES}\Delta$. This new definition of the model length scale prevent a early switch of the model to LES mode which is encountered in the original SA-DES model. The new version is called Delayed DES (DDES) due to this effect.

3.2.3.3 Improved Delayed Detached Eddy Simulation (IDDES)

Recently a new hybrid RANS-LES model is proposed. The aim of the model was to develop a universal model to perform well in problems with complex geometry and high Reynolds number. The basic idea behind the model is to combine the advantages of the wall-modelled LES (WMLES) with the DDES capabilities. The combined model is called Improved DDES (IDDES) and developed by Shur et al. (2008) based on SA model. Gritskevich et al. (2012) proposed a similar model based on $k - \omega$ SST model. In this study IDDES model based on SA (SA-IDDES) is used, thus, in the following sections this model's formulation will be briefly described via four aspects of the model; Midification of the subgrid length scale, the DDES branch of the IDDES, WMLES branch of the IDDES and finally hybridization of DDES and WMLES.

1. **Subgrid length scale:** The most widely used subgrid length scale in the classical LES is based on the cube root of a cell volume ($\Delta = \sqrt{(\Delta x)^2 + (\Delta y)^2 + (\Delta z)^2}$). Furthermore, in DES, the subgrid length scale is taken as the largest local grid spacing ($\Delta = max(\Delta_x, \Delta_y, \Delta_z)$). However, neither of these definitions is successful due to the problem in determination of SGS model constants (Shur et al. (2008)). For instance, a set of constants which work for wall-bounded flows (like turbulent channel flow) are different from the optimal values for Decaying Isotropic Homogeneous Turbulence (DIHT). Therefore, a new formulation of the subgrid length scale is defined based not only on the cell sizes but including a wall distance dependency:

   $$\Delta = f(\Delta_x, \Delta_y, \Delta_z, d_w) \tag{3.39}$$

   where Δ is the subgrid length scale, Δ_x, Δ_y and Δ_z are the local streamwise, wall-normal and spanwise (spanwise) cell sizes respectively.

   In order to formulate the subgrid length scale in IDDES, flow regions subdivided into three regions:

   - Region away from the wall where grid is mostly isotropic and is set similar to classical DES:

     $$\Delta_{free} = \Delta_{max} \equiv max(\Delta_x, \Delta_y, \Delta_z) \tag{3.40}$$

- Region in the vicinity of the wall where the subgrid length scale is defined by the wall-parallel grid:

$$\Delta_{wall} = f(\Delta_x, \Delta_z) \tag{3.41}$$

- Region between the above limiting cases where the subgrid length scale is a linear function of d_w and it varies within the range $\Delta_{min} \leq \Delta \leq \Delta_{max}$.

then the subgrid length scale is defined considering all the above conditions as follows:

$$\Delta = min(max[c_w d_w, c_w \Delta_{max}, \Delta_{wn}], \Delta_{max}) \tag{3.42}$$

where Δ_{wn} is the grid step in the wall-normal direction and c_w is an empirical constants and it is equal to 0.15 based on a wall-resolved LES of channel flow using Smagorinsky SGS model (for Smagorinsky SGS model see Smagorinsky (1963)).

2. **DDES branch of IDDES:**

The IDDES model consists of two branches. The first branch has DDES-like functionality and it is intended to be activated only when the inflow conditions do not have any turbulent content. Considering the definition of the DDES length scale in Equation 3.38, in IDDES, $d_{LES} = c_{DES}\Psi\Delta$. It contains additional low-Reynolds number correction Ψ compared to the DDES model. This correction is introduced in order to compensate the activation of the low-Reynolds number terms of SA-RANS model in LES mode. For SA model this function is as follows:

$$\Psi^2 = min\left[10^2, \frac{1 - \frac{c_{b1}}{c_{w1}\kappa f_w^*}[f_{t2} + (1 - f_{t2})f_{v2})}{f_{v1} max(10^{-10}, 1 - f_{ft2})}\right] \tag{3.43}$$

where all the notations are following the SA-RANS model except f_w^* which is equal to 0.424 and f_{t2} which is defined by:

$$f_{t2} = c_{t3} e^{-c_{t4}\chi^2} \tag{3.44}$$

where $c_{t3} = 1.2$ and $c_{t4} = 0.5$ are constants. It is clear from Equation 3.43 that the correction value is inactive when the subgrid eddy viscosity is higher than ten times the molecular viscosity and its contribution becomes higher for lower values.

3. **WMLES branch of IDDES:**

The second branch of IDDES, in contrast to the DDES branch, is activated when the inflow conditions are unsteady with turbulent content and the grid sufficiently fine to resolve boundary-layer turbulent eddies.In this case, the coupling between the RANS and LES is obtained by the introduction of a new blended RANS-LES length scale:

$$d_{WMLES} = f_B(1 + f_e)d_{RANS} + (1 - f_B)d_{LES} \tag{3.45}$$

This new definition contains two new empirical functions f_B and f_e. In order to achieve rapid switching between RANS and LES modes within the range of wall distance $0.5\Delta_{max} < d_w < \Delta_{max}$, the empirical blending function f_B is defined as

$$f_B = min\big[2 \cdot e^{-9\alpha^2}, 1.0\big] \tag{3.46}$$

where $\alpha = 0.25 - d_w/\Delta_{max}$.

The other empirical function in Equation 3.45 is f_e. It has been observed that in the vicinity of the RANS-LES interface, RANS Reynolds stresses are excursively reduced. The aim of this function to remedy this problem and to avoid log-layer mismatch (LLM). This function defined as:

$$f_e = max\big[(f_{e1} - 1), 0\big]\Psi f_{e2} \tag{3.47}$$

It is defined in a way that it is close to zero, in other word it is passive, in two cases; first, when the grid is sufficiently fine for a wall-resolved LES and second, when the final IDDES model in Equation 3.53 effectively performs as the background RANS model.

The function f_{e1} in Equation 3.47 is formulated as:

$$f_{e1} = \begin{cases} 2 \cdot e^{-11.09\alpha^2}, & \text{if } \alpha \geq 0. \\ 2 \cdot e^{-9.0\alpha^2}, & \text{if } \alpha < 0. \end{cases} \tag{3.48}$$

and the function f_{e2} reads:

$$f_{e2} = 1.0 - max\big[f_t, f_l\big] \tag{3.49}$$

where

$$f_t = tanh\big[(c_t^2 r_{dt})^3\big],\ f_l = tanh\big[(c_l^2 r_{dl})^{10}\big] \tag{3.50}$$

In expression 3.50, c_t and c_l are the constants depends on the background RANS model and their values are 3.55 and 1.63 for SA-IDDES model respectively. Furthermore, the quantities r_{dl} and r_{dt} are the laminar and turbulent analogues of r_d in 3.36 by simply replacing $\nu + \nu_t$ with ν for r_{dl} and ν_t for r_{dt}. Comprehenssive explanation of the model and the functions are described in Shur et al. (2008).

4. **Blending of DDES and WMLES branches:**

   The final step in the IDDES model is to blend the DDES length scale (Equation 3.38) and that of the WMLES branch (Equation 3.45). In order to achieve this, the original DDES formulation for the length scale is modified as follows:

$$\tilde{d}_{DDES} = \tilde{f}_d d_{RANS} + (1 - \tilde{f}_d) d_{LES} \tag{3.51}$$

   where the blending function is defined as:

$$\tilde{f}_d = max\big[(1 - f_{dt}), f_B\big] \text{ with } f_{dt} = 1 - tanh\big[(8r_{dt})^3\big] \tag{3.52}$$

   Finally, with the new expression for DDES length scale and combining this with Equation 3.45, final expression for the IDDES length scale is formulated as:

$$d_{hyb} = \tilde{f}_d(1 + f_e) d_{RANS} + (1 - \tilde{f}_d) d_{LES} \tag{3.53}$$

   This formulation of the length scale works in two modes. When the turbulent content inflow, the quantity $r_{dt} \ll 1$ and as a results of that f_{dt} is close to 1. Consequently, $\tilde{f}_d$ function returns f_B and the expression 3.53 reduces to $d_{hyb} = d_{WMLES}$. On the other hand, when the inflow does not have turbulent content, the quantity f_e becomes zero and the the expression 3.53 reduces to $d_{hyb} = \tilde{d}_{DDES}$.

3.3 Finite Volume Method (FVM)

The governing equation of fluid flow (3.1 and 3.2) which discussed in previous chapters are nonlinear second order partial differential equations. These equations can be analytically solved only for simple cases with significant simplifications. Therefore numerical techniques must be used to transform these equations to solvable forms. Several numerical techniques such as finite volume method (FVM), finite element method (FEM) and finite difference method (FDM) are available to tackle this problem. Among these methods, finite volume method is one of the preferred method in computational fluid dynamics due it's characteristics. In finite element method, first step is to subdivide the geometric domain into finite number of non-overlapping control volumes (CVs). Next, the partial differential equations are descretized and transformed into algebraic equations by integrating them over each cell. Finally, the system of algebraic equations will be solved to compute the values of the flow parameters for each elements.

As mentioned earlier finite volume method has a few specific features that makes it suitable for computational fluid dynamic simulations. The first feature of the method is that some of the terms in the conservation equation are transformed into face fluxes and evaluated at the cell faces. Because the flux entering a volume is identical to the flux which is leaving the adjacent volume, the FVM is conservative and this characteristic makes it the preferred method in computational fluid dynamics. Another important features of the

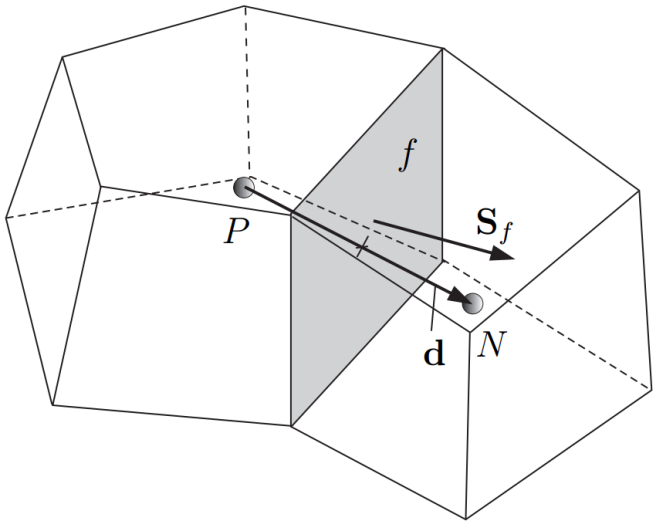

Figure 3.5: *Parameters in finite volume discretisation (Greenshields, 2015)*

FVM is that it can be used in the three dimensional physical space on unstructured polygonal cells. Finally in finite volume method it is simple to implement various boundary conditions because the unknown variables are evaluated at the center of the element and not at their boundary faces.

These features have made the finite volume method suitable for the numerical simulation of numerous engineering applications involving fluid flow and mass transfer. OpenFOAM uses this numerical technique to solve the partial differential equations. The control volumes and the notations which OpenFOAM uses are shown in Figure 3.5. Dependent variables are stored at the centroides of the cells P and N, although they may be stored on faces or nodes. Each cell is bounded by a group of faces f and each face is owned by one adjacent cell (neighboring cell) except for the boundary faces. Furthermore each face has an area $|S_f|$ and a unit normal vector n pointing toward the neighboring cell as shown in Figure 3.5, therefore a surface vector can be defines as $S_f = |S_f|n$. Additionally a vector d is defined from the centroide of the owner cell towards the centroide of the neighbor cell $d = \vec{PN}$. Finally, the volume of the cell is donated as V_P. OpenFOAM allows using an arbitrarily unstructured grids with no restriction on the shape of the cells nor on the alignment of the faces. This provides grid generation flexibility particularly for complex geometries.

3.3.1 Equation Discretization

It can be seen from the previous sections that there are significant similarities between the equations. If we introduce a general variable ϕ the governing equations for conservation of mass, momentum and transport of scalar quantities (e.g. temperature and salt concentration), can be generalized by the generic transport equation for property ϕ and it can be written in the following form:

$$\frac{\partial \phi}{\partial t} + \nabla \cdot (\boldsymbol{u}\phi) = \nabla \cdot (\Gamma_\phi \nabla \phi) + \boldsymbol{S_\phi} \tag{3.54}$$

The key step in the finite volume method that distinguishes it from all other techniques is the control volume integration of equation 3.54. This leads to the integral form of the transport equation and it can be written as follows:

$$\overbrace{\int_V \frac{\partial \phi}{\partial t} dV}^{\text{time derivative}} + \overbrace{\int_V \nabla \cdot (\boldsymbol{u}\phi) dV}^{\text{convection}} = \overbrace{\int_V \nabla \cdot (\Gamma_\phi \nabla \phi) dV}^{\text{diffusion}} + \overbrace{\int_V \boldsymbol{S_\phi} dV}^{\text{source}} \tag{3.55}$$

Equation above must be discritisize in space and time for a control volume. In the following sections, the discretization techniques which have been used in this study will be presented.

In the general transport equation 3.55, the volume integrals in the second term on the left side, the convective term, and in the first term on the right side, the diffusive term, can be written as integrals over the bounding surfaces of the control volume by using Gauss's theorem. In its most general form, Gauss's theorem states that

$$\int_V \nabla \star \phi dV = \int_S \phi \star dS \tag{3.56}$$

where S is the surface area vector, ϕ represents any tensor field and $\star$ is represent any tensor product, i.e., gradient ($\nabla\phi$), divergence ($\nabla \cdot \phi$) and curl ($\nabla \times \phi$).

In the following sections the Gauss's theorem will be applied to the convective and diffusive terms of the equation 3.55. The volume and surface integrals are then linearized using numerical schemes. A detailed derivation is provided in Jasak (1996).

3.3.1.1 Convection term

The convective term on the left hand side of the equation 3.55 is one of most important term. Using Gauss's theorem the volume integral of the convective term can be transformed to surface integral. The surface integral then linearized as follows:

$$\int_V \nabla \cdot (\boldsymbol{u}\phi) dv = \int_S dS \cdot (\boldsymbol{u}\phi) \approx \sum_f S_f \cdot (\boldsymbol{u})_f \phi_f \approx \sum_f F \phi_f \tag{3.57}$$

In equation above the face value ϕ_f is needed and it can be evaluated by various numerical scheme including Upwind, Central and Blended differencing. OpenFOAM provides several interpolation schemes for ϕ_f, among these schemes, `upwind` is one of the simplest. This scheme is first-order accurate and bounded. Depends on the direction of the face flux it can be written as

$$\phi_f = \begin{cases} \phi_P, & \text{for F} > 0. \\ \phi_N, & \text{for F} \leqq 0. \end{cases} \tag{3.58}$$

Although it is known that `upwind` scheme is introducing significant diffusion into the computation and thus smooths out any sharp changes in the value ϕ (Ferziger and Peric, 2012), this scheme can be used for preliminary simulations and creating initial condition for more accurate computation.

In order to improve accuracy and overcome shortcoming of the upwind scheme, it is possible to use another upwinding scheme `LinearUpwind`. This scheme is an extension of `upwind` to second-order by introducing a corrector. Assuming that the sign of the face flux is positive, the general formulation of the scheme can be written as

$$\phi_f = \phi_P + \boldsymbol{r} \cdot \nabla \phi_{\text{upstream}} \tag{3.59}$$

where ϕ_P is the value of ϕ at the upstream cell center, $\nabla \phi_{\text{upstream}}$ is the gradient of ϕ at the upstream face and $\boldsymbol{r}$ is a vector from the upstream cell center to the center of the face which ϕ_f is being evaluated.

Another second-order scheme which is available in OpenFOAM is central or `linear` differencing scheme (CD). In central differencing the value of ϕ at the control volume face f is interpolated by weighting the two adjacent cell center values by the distances to the face. The central diffecrencing scheme can be written as follows:

$$\phi_f = \omega \phi_P + (1 - \omega)\phi_N \tag{3.60}$$

where ω is the weight factor and it is computed as the ratio of the distance of the neighboring cell center to the face $\overline{fN}$ and the distance between the centroids of the owner cells $\overline{PN}$

$$\omega = \frac{\overline{fN}}{\overline{PN}} \tag{3.61}$$

Although it can be shown by Taylor series expansion that CD is second-order accurate, i.e., the leading term of the truncation error is proportional to the square of the grid spacing, the method is unbounded and it may lead to oscillatory solution and unstable computations.

Scheme	Numerical behavior
`linear`	Unbounded second-order
`upwind`	bounded first-order
`linearUpwind`	bounded first/second order

Table 3.3: *Behaviour of the interpolation schemes*

Finally, the mass flux $\boldsymbol{F}$ in equation 3.57 is computed from interpolated values of $\boldsymbol{U}$. Similar to interpolation of ϕ_f, $\boldsymbol{F}$ can be evaluated using various schemes including the schemes that described above. All interpolation schemes which were used in this study for convective term and their behavior are summarized in table 3.3.

Comprehensive details about the first- and second-order upwinds and the central differencing schemes can be found in Versteeg and Malalasekera (2007) and Ferziger and Peric (2012).

3.3.1.2 Laplacian term

The diffusive or Laplacian term in equation 3.55 is integrated over a control volume and it can be linearized as follows:

$$\int_V \nabla \cdot (\Gamma_\phi \nabla \phi) dV = \int_S dS \cdot (\Gamma_\phi \nabla \phi) \approx \sum_f \Gamma_f S_f \cdot (\nabla \phi)_f \tag{3.62}$$

In the equation above, the discritization of the face gradient is implicit when the length vector $\boldsymbol{d}$ between the centroid of the cell of interest $\boldsymbol{P}$ and the centroid of the neighbouring cell $\boldsymbol{N}$ is orthogonal to the face plane. In the case were $\boldsymbol{d}$ is parallel to $\boldsymbol{S_f}$:

$$\boldsymbol{S_f} \cdot (\nabla \phi)_f = |S_f| \frac{\phi_N - \phi_P}{|\boldsymbol{d}|} \tag{3.63}$$

In the case of non-orthogonal meshes, an additional explicit term is introduced. It is evaluated by interpolating cell center gradients which themselves computed by central differencing cell center values. Comprehensive details about the treatment of the Laplacian term is provided in Jasak (1996).

4 EXPLICIT HIGH-ORDER RUNGE-KUTTA SOLVER

This chapter describes the implementation and validation of the explicit high-order Runge-Kutta solver in OpenFOAM. The main objective is to speed-up the computation especially when LES and DES methods are used. The chapter starts off by presenting the motivation behind using such solver. This is followed by the mathematical description of Runge-Kutta and fractional step method. Finally, via two classical turbulent flow cases, the implemented solver is validated. In the first case, a relatively simple study of turbulent channel flow is modelled and the results are compared to the DNS data. In the second case, a flow over two-dimensional dune is modelled using IDDES. The results are then compared to the experiment and reference LES studies. In both cases it is found that the explicit third-order Runge-Kutta method in combination with the fractional step method can decrease the computational time by approximately 40% compared to PISO algorithm.

4.1 Introduction

In LES the Courant number (or CFL) must be low in every time step (usually between 0.5 and 1.0) for accuracy. Furthermore, low order methods in time are too diffusive. In OpenFOAM, for transient problems, several implicit first or second order time integration schemes are available in conjunction with PISO solver. However, Vuorinen et al. (2014) showed that using RK family of methods in combination with the fractional-step method (see Section 4.3) can not only increase the accuracy but more importantly the speed of the solver. Vuorinen et al. (2014) through two turbulent flow cases has shown that the RK method have low numerical dissipation and computational speed up of up to $60 - 70\%$ for accelerated version of third order RK method compared to PISO solver of OpenFOAM. Therefore, in this study following Vuorinen et al. (2014) and Vuorinen et al. (2015), explicit third (RK3) and fourth (RK4) order RK methods with fractional step method implemented in OpenFOAM with some changes. Both versions tested by two turbulent flow problems in this chapter. Indeed, it is found that when computational speed-up is concern, RK4 is atleast as fast as PISO solver with second order backward time discretization scheme. Furthermore, it is found that the classical third order version is 40% faster than the standard PISO solver.

4.2 Runge-Kutta methods

RK methods are numerical methods for solving equations of $dy/dt = f(t, y)$ form. It is widely used for incompressible and compressible flows as well as internal and external flows (Hirsch, 2007). The solution for y_{n+1} is then approximated using

$$y_{n+1} = y_n + h \sum_{i=1}^{s} b_i k_i \tag{4.1}$$

with

$$\begin{aligned} k_1 &= f(t_n, y_n), \\ k_2 &= f(t_n + c_2 h, y_n + h(a_{21} k_1)), \\ k_3 &= f(t_n + c_3 h, y_n + h(a_{31} k_1 + a_{32} k_2)), \\ &\vdots \\ k_i &= f(t_n + c_i h, y_n + h \sum_{j=1}^{i-1} a_{ij} k_j) \end{aligned} \tag{4.2}$$

In the Equation 4.1, s is the number of stages and h is the step size. Moreover, the coefficients in the above expressions can be summarized in tabular form (also known as Butcher tableau):

$$\begin{array}{c|cccc} c_1 & a_{11} & a_{12} & \dots & a_{1s} \\ c_2 & a_{21} & a_{22} & \dots & a_{2s} \\ \vdots & \vdots & \vdots & \ddots & \vdots \\ c_s & a_{s1} & a_{s2} & \dots & a_{ss} \\ \hline & b_1 & b_2 & \dots & b_s \end{array}$$

These coefficients for explicit third order RK (also known as Kutta's third-order method) is

$$\begin{array}{c|ccc} 0 & 0 & 0 & 0 \\ 1/2 & 1/2 & 0 & 0 \\ 1 & -1 & 2 & 0 \\ \hline & 1/6 & 2/3 & 1/6 \end{array}$$

and for explicit fourth order RK is

$$\begin{array}{c|cccc} 0 & 0 & 0 & 0 & 0 \\ 1/2 & 1/2 & 0 & 0 & 0 \\ 1/2 & 0 & 1/2 & 0 & 0 \\ 1 & 0 & 0 & 1 & 0 \\ \hline & 1/6 & 1/3 & 1/3 & 1/6 \end{array}$$

Finally, RK3 and RK4 combined with the fractional step which is described in Section 4.3 to formulate and implement the solver in OpenFOAM environment.

4.3 Projection method

In general there are two solvers available for solving the incompressible flow equations (Equations 3.1 and 3.1) in OpenFOAM. The Semi-Implicit Method for Pressure-Linked Equations or SIMPLE for steady-state problems (Patankar, 1980) and Pressure-Implicit with Splitting of Operators or PISO (Issa, 1986) for transient problems. Clearly because LES is inherently transient, such simulations in OpenFOAM are usually performed using the standard PISO solver along with implicit time integration. PISO algorithm consists of two main steps; in the first step or predictor step, an intermediate velocity field is solved using pressure from the previous time step. In the second step consisting of corrector steps, the intermediate and final velocity and pressure fields are computed iteratively. The number of corrector steps impact the accuracy of the results and at least two corrector steps are necessary. As an alternative to PISO, fractional-step or projection method are also used in LES. This method is first introduced by Chorin (1968) and does not require a corrector loop. Instead, in a single projection step the velocity field is projected onto its solenoidal counter part using the pressure gradient. The projection method in combination with high order explicit time integration methods (Canuto et al., 2007; Hirsch, 2007) and FVM (Vuorinen et al., 2012; Jameson et al., 1981) have been employed before successfully.

In order to briefly describe the method, lets consider the momentum Equation 3.2 in more general form:

$$\frac{\partial \boldsymbol{u}}{\partial t} + (\boldsymbol{u} \cdot \nabla)\boldsymbol{u} = -\frac{1}{\rho}\nabla p + \nu \nabla^2 \boldsymbol{u} \tag{4.3}$$

Chorin's projection method consists of two steps. In the first step, the pressure gradient term in Equation 4.3 is ignored and an intermediate velocity u^* is computed

$$\frac{\boldsymbol{u}^* - \boldsymbol{u}^n}{\Delta t} = -(\boldsymbol{u}^n \cdot \nabla)\boldsymbol{u}^n + \nu \nabla^2 \boldsymbol{u}^n \tag{4.4}$$

where $\boldsymbol{u}^n$ is the velocity at nth time step. Then in the second step, the projection step, the intermediate velocity is corrected to obtain the final value of velocity field using

$$\frac{\boldsymbol{u}^{n+1} - \boldsymbol{u}^*}{\Delta t} = -\frac{1}{\rho}\nabla p^{n+1} \tag{4.5}$$

However in the projection step (Equation 4.5), pressure at $n+1$ time is required. Considering that $\nabla \cdot \boldsymbol{u}^{n+1} = 0$, the pressure can be obtained by taking divergence from both sides of Equation 4.3 leading to Poisson equation for p^{n+1}:

$$\nabla^2 p^{n+1} = \frac{\rho}{\Delta t}\nabla \cdot \boldsymbol{u}^* \tag{4.6}$$

In projection method in combination with explicit RK time integration, the projection is carried out between the integration sub-steps in order to retain the time accuracy.

4.4 Validation and verification

The explicit fractional-step solver is implemented in OpenFOAM according to the description in the previous sections. The high-level programming syntax of OpenFOAM allows a user to write the code as close as possible to the partial differential equations and their notations. This makes the coding straightforward and reasonably quick. However, before employing the solver to model the main case (Chapter 7), a series of numerical tests have been carried out to verify and validate the code. This chapter, presents two relatively simple numerical test cases; fully developed turbulent channel flow and flow over two-dimensional dunes.

4.4.1 Turbulent Channel Flow

Fully developed turbulent channel flow is a classical case in wall-bounded turbulent flows. The basic idea behind this numerical test is a flow between two infinity long plates. Moreover, the flow is driven by a constant pressure gradient. This case is extensively studied numerically as well as experimentally (see for example Pope (2001) and Kim et al. (1987)). Moreover, due to simplicity of the model and the geometry, it is modelled by numerical techniques with high accuracy for example DNS using spectral methods ,Moin and Kim (1982),Kim et al. (1987), Moser et al. (1999), Iwamoto et al. (2005) and Jiménez Sendín et al. (2010). The results from these analyses provide valuable reference values for verification of the other techniques, in this case, the implemented code. Additionally, this case is used to compare the computational speed of the solver with the one which is based on PISO algorithm and it is readily available in OpenFOAM. In this section, the channel flow which is investigated by Moser et al. (1999) are modelled at $Re_\tau = 395$ and $Re_\tau = 590$. The friction Reynolds number, Re_τ, is defined as the ratio of the channel half-height to the friction length scale:

$$Re_\tau = \frac{u_\tau \cdot \delta}{\nu} \tag{4.7}$$

where u_τ is the friction velocity and δ is the channel half-width. The friction velocity, u_τ, is defined in terms of the wall shear stress, τ_w, and the density, ρ, according to

$$u_\tau = \sqrt{\frac{\tau_w}{\rho}} \tag{4.8}$$

4.4.1.1 Computational setup

The channel domain is illustrated in Figure 4.1. The x-direction is representing the main flow direction and here refers to as streamwise direction. The y-direction is assumed to be normal to the walls (plates). Furthermore, The distance between the walls are assumed to be $2m$ and consequently channel half-height $\delta = 1m$. In the following section, this direction will be referred to as wall-normal direction. Finally, z-direction is representing the spanwise direction.

The length of the domain in stream and spanwise direction must be large enough to accommodate the largest existing turbulent structures. In several studies (i.e. Moser et al. (1999)) on the channel flow, the size of the computational domain is chosen to

Parameter	Notation	Value	Unit	Expression
Channel width	h	2.0	m	2δ
Streamwise length	L_x	5.0	m	-
Spanwise Length	L_z	2.0	m	-
Kinematic viscosity	ν	2×10^{-5}	m^2/s	-
Bulk velocity	U_b	0.1335	m/s	-
Bulk Reynolds number	Re_b	6675	-	$U_b\delta/\nu$

Table 4.1: *Physical and geometrical parameters for* $Re_\tau = 395$.

be $2\pi\delta \times 2h \times \pi\delta$ in the streamwise, wall-normal and spanwise directions respectively. However, in order to reduce the computational costs, the domain is reduced to somewhat minimum based on studies from Fureby et al. (1997), De Villiers (2007) and Mukha and Liefvendahl (2015) on the same channel at moderate friction Reynolds numbers. Finally, the computational domain is chosen to be $5\delta \times 2\delta \times 2\delta$ in the streamwise, wall-normal and spanwise directions respectively. The flow is assumed to be incompressible, hence, two physical parameters are adequate to define the model; the kinematic viscosity of the fluid, ν and the driving pressure gradient. As stated in Pope (2001), the pressure gradient and the wall shear stress are related as follows:

$$-\frac{d\tilde{p}}{dx} = \frac{\tau_w}{\delta} \tag{4.9}$$

Expression above indicates that by defining a pressure gradient, appropriate friction Reynolds number, Re_τ, can be achieved. On the other hand, in OpenFOAM a tool is available through which a user can define a mean velocity, U_b for a particular bulk Reynolds number Re_b. This bulk Reynolds number must be defined in a way that it leads to the desired friction Reynolds number. Considering the practical aspects and the fact that this study must fit in a short time frame, the latter approach is used. The geometrical and physical parameters for a case with $Re_\tau = 395$ is summarized in Table 4.1. The parameters for $Re_\tau = 590$ is identical except that the bulk velocity $U_b = 0.2187m/s$ and consequently, bulk Reynolds number based on channel half width of $Re_b = 10935$.

Simplicity of this case allows to generate high quality hexahedral elements. The grid is generated using `blockMesh` utility of OpenFOAM. In the streamwise and spanwise directions, uniform grid spacings are used. The non-dimentional grid spacings in the streamwise and spanwise directions are respectively $\Delta x^+ \approx 20$ and $\Delta z^+ \approx 14$ in wall units for $Re_\tau = 395$ and $\Delta x^+ \approx 30$ and $\Delta z^+ \approx 15$ for $Re_\tau = 590$. The grid spacings are graded in y-direction in order to resolve the turbulent structures and the large velocity gradient near the walls. In `blockMesh` utility, this was done by setting the ratio of the largest and the smallest elements in y-direction. This ratio is set to 10 for $Re_\tau = 395$ and 20 for $Re_\tau = 590$ to have $y^+ < 1.0$. Figure 4.2 shows the computational grid for $Re_\tau = 395$ with every second grid line is shown. Finally, Table 4.2 and 4.3 are summarizing the grid information and gives a comparison between the grid and simulation parameters which are used in this study with the ones from the DNS of Moser et al. (1999). In both cases, the grids are three times coarser than the DNS study.

The computational domain, as stated before, represents a domain with infinite lengths.

Study	L_x	L_z	$N_x \times N_y \times N_z$	Δx^+	Δz^+	y^+
Current	5δ	2δ	$100 \times 100 \times 60$	20.0	14.0	0.96
DNS	$2\pi\delta$	$\pi\delta$	$256 \times 193 \times 192$	10.0	6.5	-

Table 4.2: *Computational grid information for $Re_\tau = 395$ of this study compared with the DNS study of Moser et al. (1999).*

Study	L_x	L_z	$N_x \times N_y \times N_z$	Δx^+	Δz^+	y^+
Current	5δ	2δ	$100 \times 160 \times 80$	30.0	15.0	0.60
DNS	$2\pi\delta$	$\pi\delta$	$384 \times 257 \times 384$	9.7	4.8	-

Table 4.3: *Computational grid information for $Re_\tau = 590$ of this study compared with the DNS study of Moser et al. (1999).*

In order to achieve this, cyclic boundary conditions are imposed in streawise and spanwise directions. additionally, the no-slip condition is assumed for the walls (Figure 4.1). Finally, a bulk velocity is defined to reach the desired friction velocity. The pressure gradient is necessary to drive the flow since there is no inlet and outlet in this model. This is done by adding an external force to the momentum equation and computing the magnitude of this force from the bulk velocity. This external force is being updated at each time step by recomputing U_b. In the absence of any obstacle, walls are the only source of turbulence in a flow. In reality, imperfection of the walls or small perturbations can trigger the transition process to turbulence flow. However, in this numerical case, very little if any imperfection exist. Therefore, an artificial perturbation is necessary to initiate the process. Here, this is done by adding a random perturbation (random noise) to the domain. This and the numerical noise and round off errors led to the fully turbulent flow. The simulations are carried out in two phases. In the first or preliminary phase the domain initialized as described above and the flow is simulated for 100 flow passes to reach fully turbulent flow. This allows all the transient process related to the initial conditions to pass away. Then velocity and pressure averaged for additional 1000 flow passes. The time step is adjusted at each time step to have the maximum Courant number under 0.5.

The interpolation and spatial discretization scheme of the convective as well as the diffusive terms are all set to second-order central differencing scheme for higher accuracy. Finally, all the simulations of the channel flow are performed using LES technique with The Wall-adapting local eddy-viscosity (WALE) SGS model. The description of this SGS model can be found in Nicoud and Ducros (1999). Later in this section, however, the results from LES and SA-IDDES are compared for $Re_\tau = 395$ for a coarser mesh.

4.4.1.2 Results

The results are divided into three main categories. In the first section the results from LES are presented and compared with DNS data. The models computational setup are according to what described in Section 4.4.1.1. Next, the results from the LES which is computed usng `RK3FracStep` solver will be compared with the PISO solver of OpenFOAM. Finally, channel with $Re_\tau = 395$ is modelled using LES and SA-IDDES on a coarse grid and the results are briefly compared.

4.4.1.3 Large Eddy Simulation

The discussion of the results begin with the comparison of computed values of the friction Reynolds number and the target values from DNS. The target friction Reynolds number value in the first analysis is 395. The computed value of Re_τ from LES analysis is slightly underestimated and it is $Re_\tau = 380$. On the other hand, the computed Re_τ value for the second case is 592, very close to the target value of 590. This is also true, of course, for the computed friction velocities. Moving on to the average velocities, Figure 4.3 and 4.4 show streamwise average velocity of cases with $Re_\tau = 395$ and $Re_\tau = 590$ respectively. In both graphs, on the right hand side, the profiles are presented in global coordinate system with velocities scaled by the bulk velocity U_b. However, in order to have a closer look at the profiles, they illustrated at the left hand side in logarithmic scale. The velocities and the distance to the wall are scaled with friction velocity u_τ. It is clear that in both cases the average streamwise velocities are accurately predicted and they are in good agreement with DNS data. Furthermore, both profiles are following precisely the theoretical lines.

One of the important quantities in a turbulent flow is the Reynolds stress tensor and its components. These components describing the turbulent fluctuations. Figure 4.5 to 4.10 show the diagonal components of the Reynolds stress tensor in terms of the standard deviation of the three components of velocity in the wall-normal direction. Furthermore, these values are made dimensionless using the friction velocity u_τ.

In general, there is a good agreement between computed values and DNS data. Figure 4.5 and 4.6 show the normalized standard deviation of the streamwise component of velocity, u'^+. In regions close to the wall where $y^+ < 7$, the computed values are accurately estimated. Furthermore, in both cases, the location of the peak is located approximately at $y^+ = 15$. Although the location of the peak is accurately predicted, however, the magnitude of the peak is slightly overestimated in both cases. Further away from the wall toward the middle of the channel, computed values showing the same trend with little underestimation of u'^+ from $y/\delta = 0.2$ to the channel center line.

In the wall-normal direction,The overall estimation of the values are good. Figure 4.7 and 4.8 show the normalized standard deviation of the wall-normal component of velocity, v'^+. The peak values are estimated accurately although the location of the peak is slightly shifted to higher y^+ values. The largest differences are located from $y/\delta = 0.2$ to $y/\delta = 0.7$. These differences are more pronounced for $Re_\tau = 590$ (Figure 4.8).

The profiles of the computed normalized standard deviation of the spanwise component of velocity, w'^+ are shown in Figure 4.9 and 4.10. It can be seen in Figure 4.9 that the computed values for w'^+ in a case with $Re_\tau = 395$ are in a good agreements with DNS data. The location and the value of the peak computed accurately. On the other hand, it is evident from Figure 4.10 that for $Re_\tau = 590$ case, the computed profile lies on the DNS data except near the peak. Although the location of the peak is accurately predicted, the value is underestimated. Perhaps this is due to short length of the domain in spanwise direction.

The comparison of results are finalized in this section by studying the off-diagonal components of the Reynolds stress tensor, also known as Reynolds shear stresses. The xz and yz components are zero due to the symmetry of the channel. Therefore, the xy components of the Reynolds stress tensor is analysed. Figure 4.11 and 4.12 show the computed

turbulent shear stress for $Re_\tau = 395$ and $Re_\tau = 590$ respectively. It is apparent from these figures that the computed values are lying exactly on the DNS data. Furthermore, the graphs follows the analytical profile of total shear stress which implies that the sum of the viscous and turbulent shear stresses varies linearly across the channel (Pope, 2001).

4.4.1.4 RK3FracStep Versus PIMPLE

It is shown previously that the new solver's performance is satisfactory. However, it is compelling to test the performance of this new solver against the standard transient solver of OpenFOAM for incompressible flow. This solver is based on PISO algorithm (in OpenFOAM `pisoFoam`) for solving the equations. Furthermore, it is tested several times by the community. Full description of the algorithm is beyond the scope of this work. More information can be found in Versteeg and Malalasekera (2007) and Jasak (1996).

The computational setup of both cases follows the description in Section 4.4.1.1 for $Re_\tau = 395$ with a few adjustments. The goal of the the analyses is to compare the performance of the two and not to predict the values accurately. Therefore, in order to reduce computational time, the number of elements are reduced to $50 \times 50 \times 30$. The non-dimensional grid spacings in the streamwise and spanwise directions are respectively $\Delta x^+ \approx 40$ and $\Delta z^+ \approx 27$ in wall units for $Re_\tau = 395$. Also the grids graded from wall toward the channel center line with setting the ratio of the largest to the smallest elements to 10. This led to $y^+ = 1.90$ for $Re_\tau = 395$. Moreover, in the analysis using PISO solver, the time integration scheme is set to second-order backward and the spatial schemes are set to central differencing schemes. Since OpenFOAM package comes with sets of tutorials and one of these tutorial is the channel flow at $Re_\tau = 395$, all other numerical settings related to `pisoFoam` are according to the tutorial and remained unchanged. In the following paragraphs, the results obtained using both solvers are briefly presented and discussed.

The computed mean velocity profiles are shown in Figure 4.13. the values computed using both solvers, RK3FracStep and `pisoFoam`, are very close, almost indistinguishable, although they are not following the DNS data in the logarithmic layer due to the coarse meshes. The computed values, however, deemed accurate enough for engineering applications. The difference between the results are more pronounced when other turbulence quantities are compared. Figure 4.14 shows the diagonal components of the Reynolds stress tensor. In Figure 4.14 markers represents DNS data, solid lines, represents the results obtained from RK3FracStep and the dashed lines are the results from `pisoFoam`. In the streamwise direction the computed values are close. However, in spanwise and wall-normal directions, values obtained from the `pisoFoam` are under predicted in comparison with the values form `RK3FracStepFoam`. Interestingly, when the Reynolds shear stress is compared in Figure 4.15, `pisoFoam` performed better.

Another purpose of this analysis is to evaluate the performance of the new solver, more precisely, the speed up which was expected from an explicit solver against an implicit one. In general, the results are encouraging. The new solver is 30 to 40 percent faster than `pisoFoam`. However, this speed up is only valid in this particular case with the particular settings which are used.

4.4.1.5 LES Versus SA-IDDES

The analysis of the $Re_\tau = 395$ channel is finalized by briefly comparing the results obtained using LES with WALE SGS from one hand and utilizing SA-IDDES approach for modelling turbulence on the other hand. In Section 4.4.2 a more complex numerical tests carried out to evaluate the capability of IDDES thenique.

The computational setup follows the description in Section 4.4.1.1. However, the computational grid is slightly different. The grid used in this analysis is moderately fine with $75 \times 75 \times 45$ elements in the streamwise, wall-normal and spanwise respectively. These corresponds to $\Delta x^+ \approx 27$ and $\Delta z^+ \approx 18$ in wall units. In the wall-normal direction, however, two different grid parameters adopted. First with grading toward the channel's center line and one domain with uniform grid. The latter is used to test the capability of SA-IDDES for a case when the y^+ is higher than the customary value of 1 for IDDES computations.

The profiles of the computed mean streamwise velocities are illustrated in Figure 4.16. It is evident that switching from WALE model to SA-IDDES improved the accuracy, even in the case where uniform grid is used and y^+ is approximately equal to 5. The streamwise velocity profile accurately predicted when it is compared to DNS data although the refinement at the boundary certainly can improve the prediction.

4.4.1.6 Summary

Through out a series of numerical tests on a classical turbulent channel flow, the performance of the new solver is evaluated. This is done in three steps; first, the LES simulation of the channel carried out with relatively fine mesh. The results shown a good agreements with the DNS data. Furthermore, the performance of the solver is evaluated in comparison with the standard solver of OpenFOAM for transient simulation for incompressible flow, `pisoFoam`. It is observed that the results are comparable and even computational time reduced by at least 30 percent. Finally, the same channel at $Re_\tau = 395$ on a coarse computational grid modelled with SA-IDDES and the results improved compared to the LES results. Even in the case where uniform computational grid used in wall-normal direction the velocities accurately predicted.

4.4.2 Flow over Two-Dimensional Dunes

In this Section, a classical case in Hydraulic engineering is modelled to evaluate the performance of `RK3FracStepFoam` solver in combination with the DES turbulence modelling approach. The case which is investigated is the flow over two-dimensional dunes. Bed forms such as two- and three-dimentional dunes are naturally presents in the rivers. They have a large impact on the sediment loads and the discharge capacity of a river. Therefore, several experimental as well as numerical studies have been carried out to understand the effect of these forms on the flow.

In the presence of steady unidirectional flows, it is known that the dunes reaching a periodic equilibrium shape (see i.e. Jackson (1976) and Balachandar et al. (2007)) with height, k, equal to $1/4$ of the flow depth, h, and a wavelength, λ, equal to 5-6 times the flow depth. Thus, here, the dune shape which is investigated experimentally by Polatel (2006) and numerically modelled by Stoesser et al. (2008) and Omidyeganeh (2013) is

modelled for evaluation of the numerical performance of the solver and the DES technique.

4.4.2.1 Computational setup

The computational domain is illustrated in Figure 4.18 and 4.17. The geomrtry is following Polatel (2006) laboratory experiment in which 22 two-dimensional fixed dunes placed at the bottom of a flume. A two-component laser Doppler velocimetry (LDV) system was used for the measurements. The velocity in streamwise and vertical directions were collected at six vertical locations along the $17th$ dune. Figure 4.18 shows the locations of these verticals. The computational domain is selected to represent the computational domain of Stoesser et al. (2008). Hence, dune height is $k = 20\,mm$ and the dune wavelength is $20k$. In the spanwise direction, the domain is extended to $8k$. Several water depths have been investigated in the previous studies, however, in this study, only the water depth $h = 4k$ is modelled. Finally, The bulk Reynolds number Re_b is equal to 2.5×10^4 based on the average bulk velocity $U_b = 0.3\,m/s$ and the maximum flow depth.

The computational grid is generated using `blockMesh` utility of OpenFOAM. It is consisted of $207 \times 80 \times 60$ grid points in the streamwise, spanwise, and wall-normal directions, respectively. In the wall-normal direction, The grid spacings are stretched with the ratio of largest elements to the smallest equal to 10. The number of grid points in this study are approximately 10 times coarser than the one used in Stoesser et al. (2008). The same case is studied also at length by Omidyeganeh (2013) and the author used a grid similar to Stoesser et al. (2008), however, the computational domain was twice larger in spanwise direction.

The rigid-lid condition is imposed for the free surface. This condition has been used by Yue et al. (2006) and Stoesser et al. (2008) for LES of flow over dunes. It has been shown that it successfully represents the free surface, since, according to Stoesser et al. (2008), the maximum mean surface deviation was equal to 3% and the maximum fluctuating deviations were 0.5% of the water depth. In the streamwise and spanwise directions, periodic boundary condition was applied. Although, according to Calhoun (1998) , at least two periodic segments are necessary in streamwise direction for wavy-wall problems, here, only one used. Stoesser et al. (2008) stated that due to large intercrestdistance-to-water-depth ratio, use of one segment only is justified. This is backed by previous work of Temmerman (2004) in which the author used one and two segments in the periodic hill simulations and reported that only a small differences have been observed. Moreover, Fröhlich et al. (2005) discussed this problem at length in the same flow and used one segment.

The simulation is performed with OpenFOAM using `RK3FracStep` solver and SA-IDDES turbulence model. Second-order central differences are employed for the convective as well as for the diffusive terms. The maximum Courant number is set to 0.5 and the simulation is performed for approximately $20\lambda/U_b$ time units to remove any effects associated with initial conditions. In the second phase or averaging phase, the flow is simulated for $500\lambda/U_b$ time units until the sampling time interval is large enough to make statistical errors insignificant.

4.4.2.2 Results

The aim of this study is to validate both the solver and SA-IDDES turbulence model performance, hence, only selected results are presented here. Stoesser et al. (2008) and Omidyeganeh (2013) studied and discussed this problem at length. In this section, first the mean streamwise velocities are compared with the laboratory results of Polatel (2006) and numerical results of Stoesser et al. (2008) followed by the turbulence intensities and turbulence shear stress.

Figure 4.19 shows mean velocities in streamwise and spanwise directions along with flow streamlines. The velocities are normalized using bulk velocity. It is shown that the flow separates at the crest and reattaches downstream at $x/k \approx 5.6$ leading to a large separation zone. The computed reattachment point is close to the value reported by Stoesser et al. (2008), $x/k \approx 5$, and Omidyeganeh (2013), $x/k \approx 5.7$. Moreover, the computed reattachment point is within the range of the similar experimental (Kadota and Nezu, 1999) and numerical (Grigoriadis et al., 2009) flow investigations on dunes.

Figure 4.20 shows the comparison between the computed mean streamwise velocities with LES and experimental results. Again, the velocities are normalized using the bulk velocity. Overall, the computed values are in a very good agreement with the LES data. Similarly, the overall agreements between the predicted values using SA-IDDES and the measured values are good. However, as Stoesser et al. (2008) reported, the experimental data show a continuity defect at locations L3 and L4 due to the secondary circulations which have been observed during the experiment in the flume.

The diagonal components of Reynolds stress tensor is representing the turbulent fluctuations in streamwise, spanwise and wall-normal direction. Figure 4.21a to 4.21c show the turbulence intensities by plotting the root-mean-square of u', v' and w' in a longitudinal plane. As it can be seen, high turbulence intensity present at the separation zone and the separated shear layer. The peak of the stress-intensity is extended to the locations where bottom elevation starts to rise.

Additionally, Figure 4.23, 4.24 and 4.25 shows the computed values of the turbulence intensities along the six measurement vertical lines $L1$ to $L6$. In the streamwise direction (Figure 4.23), excellent agreements can be seen for all the vertical lines. Similarly, in spanwise (Figure 4.24) and wall-normal direction (Figure 4.25) the computed values are in a good agreement with the LES and experimental results. However, at the first vertical line, $L1$, computed v' and w' from the SA-IDDES simulation are under-predicted from $x/k = 0$ to 1.5. Although, the differences between the results extended to vertical lines $L2$ and $L3$, especially for normal-normal turbulence intensities in Figure 4.25, they are less pronounced than at vertical line $L1$.

Figure 4.22 shows the distribution of the mean turbulent shear stress, $u'w'$ in a longitudinal plan. In general, four regions can be identified on the plot; the separated shear layer located at the recirculation zone, the wake layer immediately after the recirculation zone which extends to the top of the (next) dune, the developing boundary layer underneath the wake layer and finally, the layer near the free surface which the shear stress is the lowest. Stoesser et al. (2008) described this thoroughly and here the contour plot of the turbulence shear stress is provided for completeness. On the other hand, what is more important here is the comparison of the computed shear stress values with the LES data.

Figure 4.26 shows this comparison by plotting the values for six vertical lines. As can be seen, the agreements between the computed values with the LES data is very good, however, similar to v' and w', The peak value of the shear stress is slightly underestimated at the first vertical line $L1$.

4.4.2.3 Summary

The aim of this study was to model the flow over two-dimensional dune using `RK3FracStep` solver and SA-IDDES model. In general the agreement with the experimental and especially LES data from Stoesser et al. (2008) is good, although the number of elements of this study is 10 and 20 times coarser than Stoesser et al. (2008) and Omidyeganeh (2013) studies respectively. The comparison showed that the solver as well as the turbulence model perform as expected and it has the capability to predict the velocity and turbulence parameters accurately in a more complex problem than the case of turbulent channel flow in Section 4.4.1.

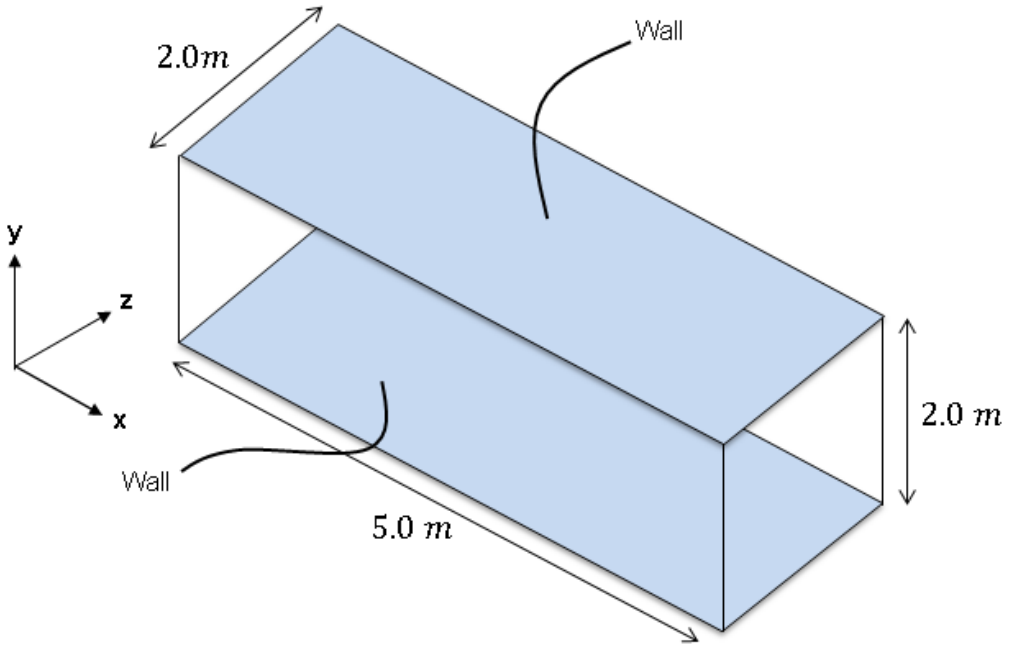

Figure 4.1: *The Channel configuration, the computational domain and the coordinate system for LES computation.*

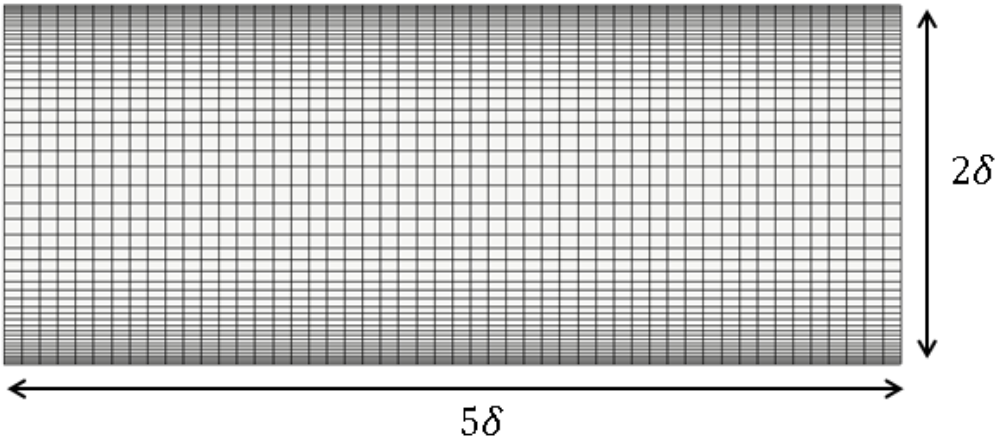

Figure 4.2: *Computational grid for* $Re_\tau = 395$ *(Every second grid line is shown).*

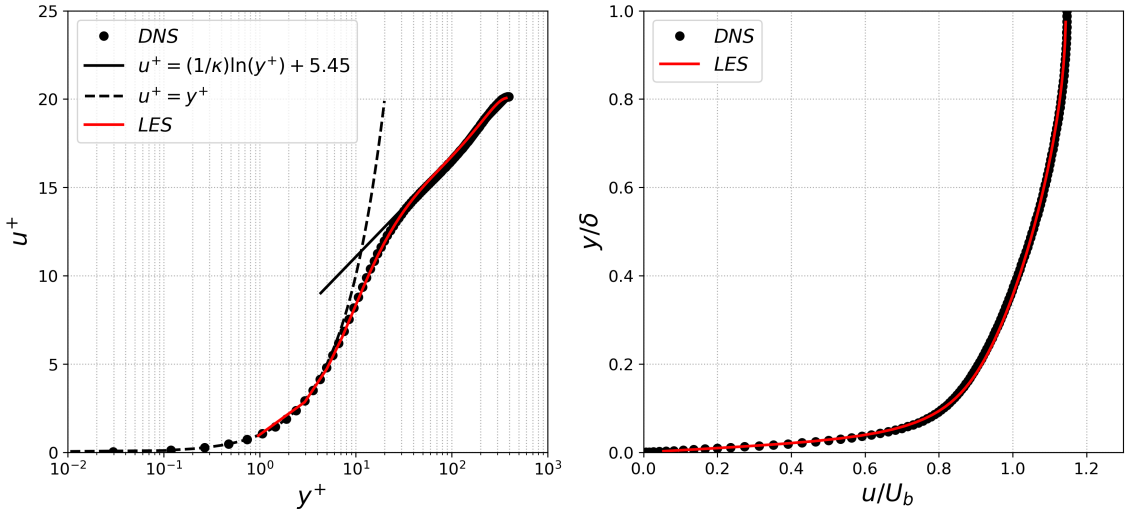

Figure 4.3: *Computed mean streamwise velocity profiles using LES compared with DNS data by Moser et al. (1999) for fully developed channel flow at $Re_\tau = 395$.*

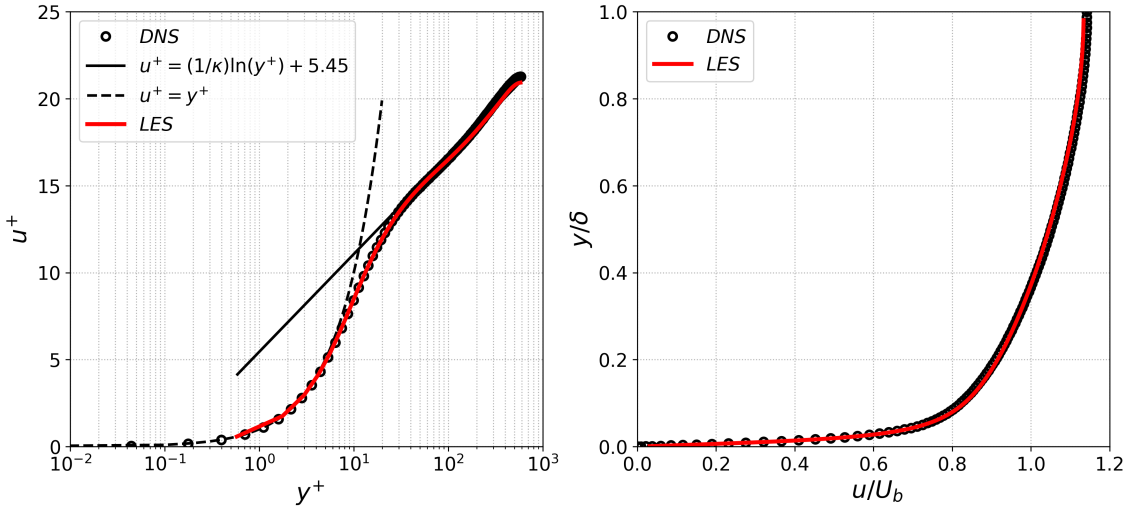

Figure 4.4: *Computed mean streamwise velocity profiles using LES compared with DNS data by Moser et al. (1999) for fully developed channel flow at $Re_\tau = 590$.*

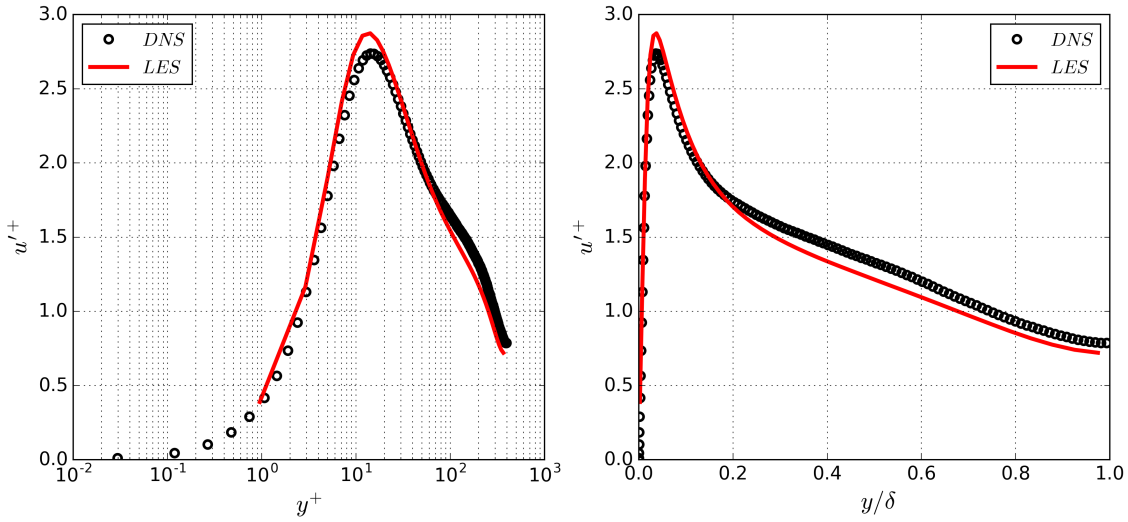

Figure 4.5: *Profiles of the normalized standard deviation of the streamwise component of velocity (u'^+) using LES compared with DNS data by Moser et al. (1999) for fully developed channel flow at $Re_\tau = 395$.*

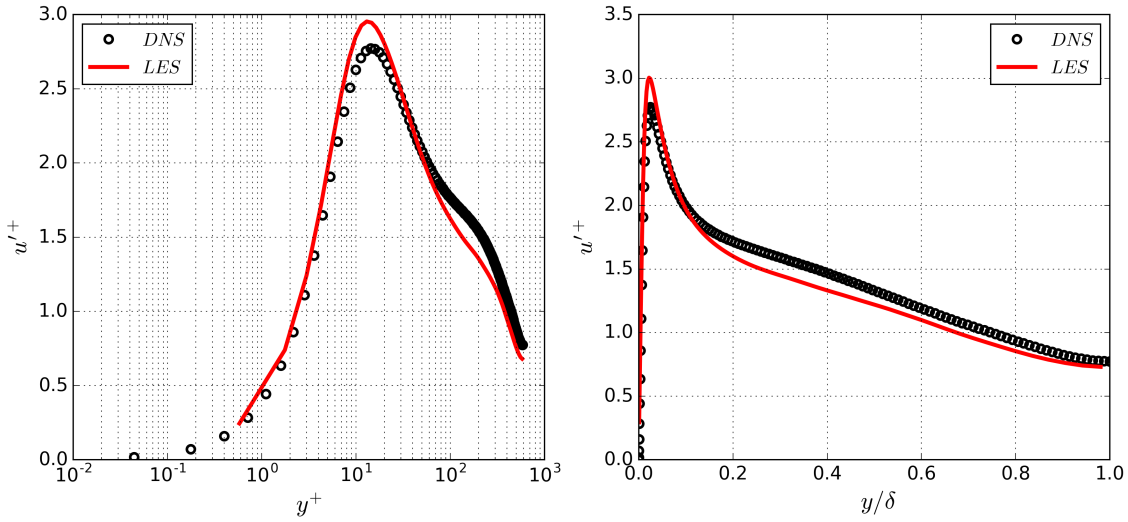

Figure 4.6: *Profiles of the normalized standard deviation of the streamwise component of velocity (u'^+) using LES compared with DNS data by Moser et al. (1999) for fully developed channel flow at $Re_\tau = 590$.*

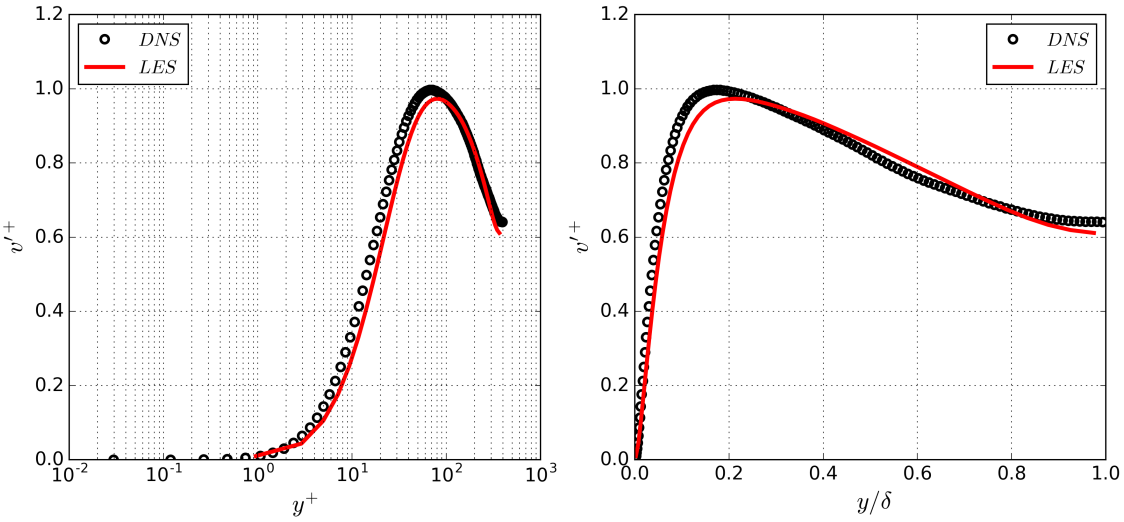

Figure 4.7: *Profiles of the normalized standard deviation of the wall-normal component of velocity (v'^+) using LES compared with DNS data by Moser et al. (1999) for fully developed channel flow at $Re_\tau = 395$.*

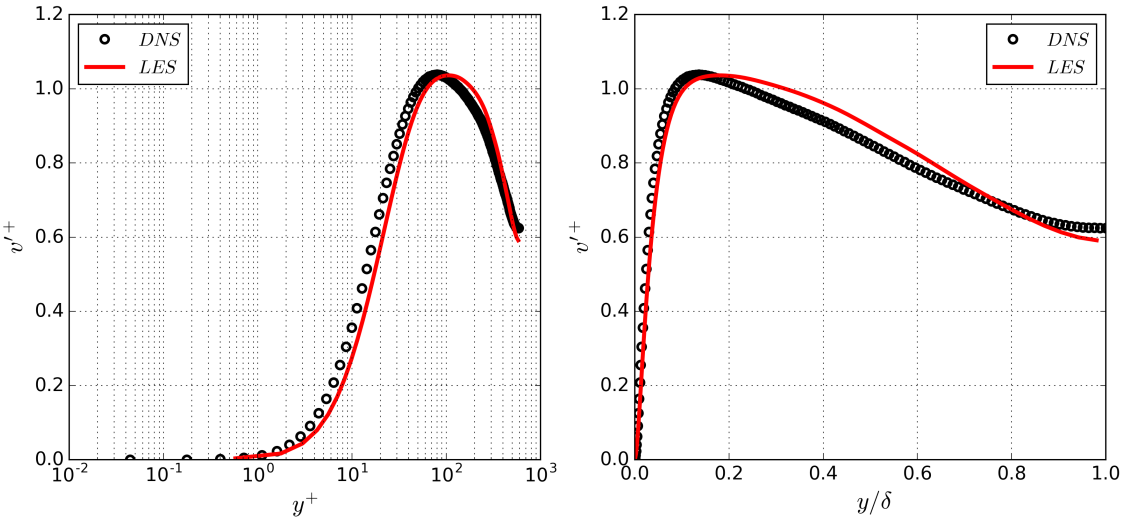

Figure 4.8: *Profiles of the normalized standard deviation of the wall-normal component of velocity (v'^+) using LES compared with DNS data by Moser et al. (1999) for fully developed channel flow at $Re_\tau = 590$.*

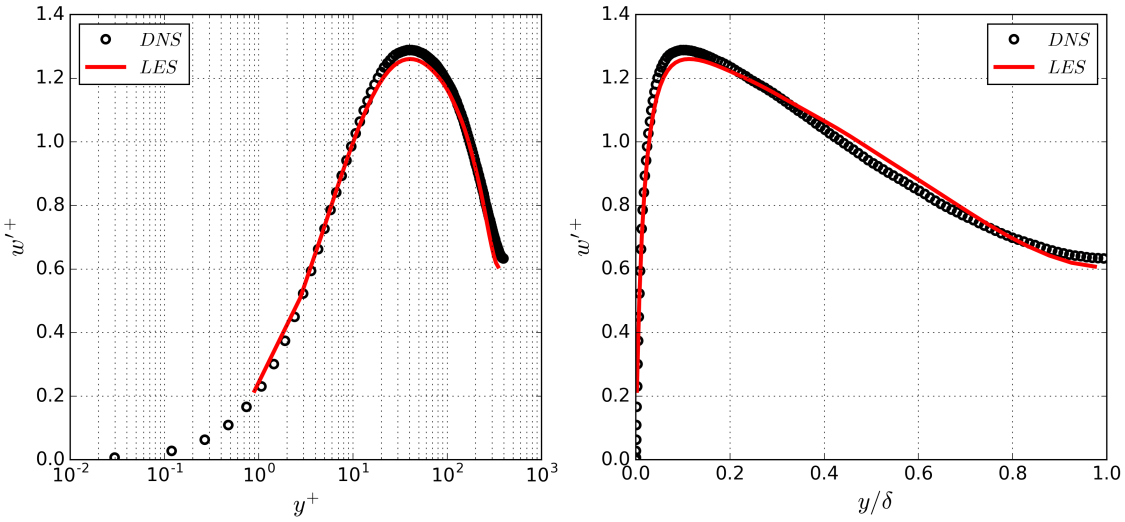

Figure 4.9: *Profiles of the normalized standard deviation of the span-wise component of velocity (w'^+) using LES compared with DNS data by Moser et al. (1999) for fully developed channel flow at $Re_\tau = 395$.*

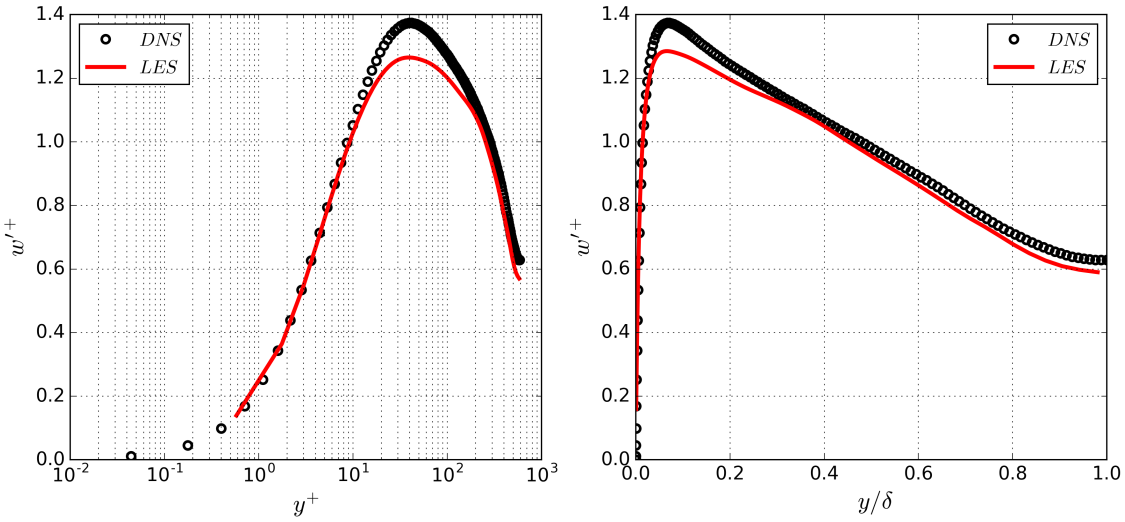

Figure 4.10: *Profiles of the normalized standard deviation of the span-wise component of velocity (w'^+) using LES compared with DNS data by Moser et al. (1999) for fully developed channel flow at $Re_\tau = 590$.*

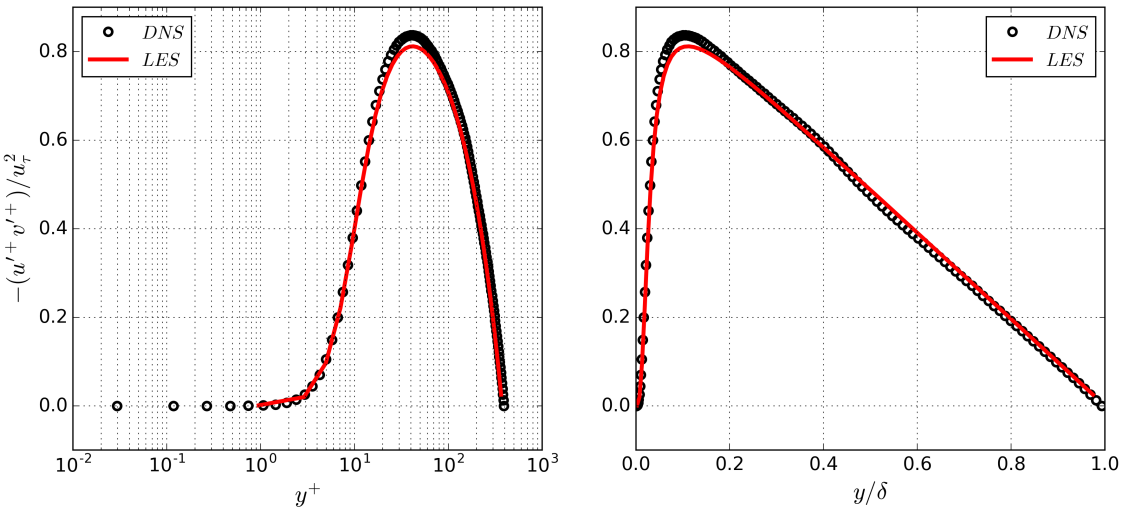

Figure 4.11: *Computed normalized turbulent shear stress profiles using LES compared with DNS data by Moser et al. (1999) for fully developed channel flow at $Re_\tau = 395$.*

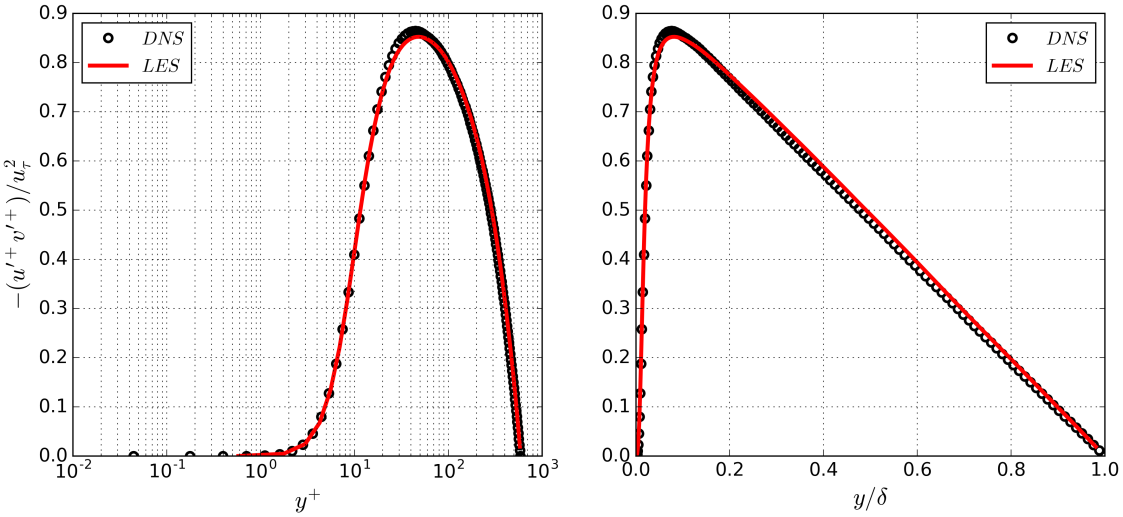

Figure 4.12: *Computed normalized turbulent shear stress profiles using LES compared with DNS data by Moser et al. (1999) for fully developed channel flow at $Re_\tau = 590$.*

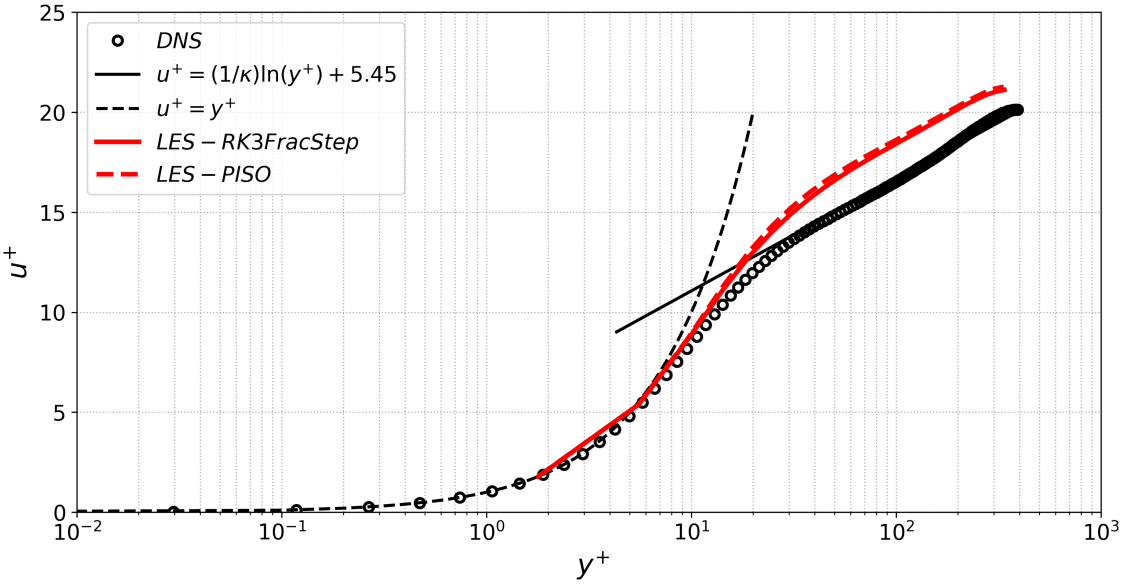

Figure 4.13: *Computed mean streamwise velocity profiles obtained from* `RK3FracStep` *and* `pisoFoam` *solvers for fully developed channel flow at* $Re_\tau = 395$. *DNS data from Moser et al. (1999).*

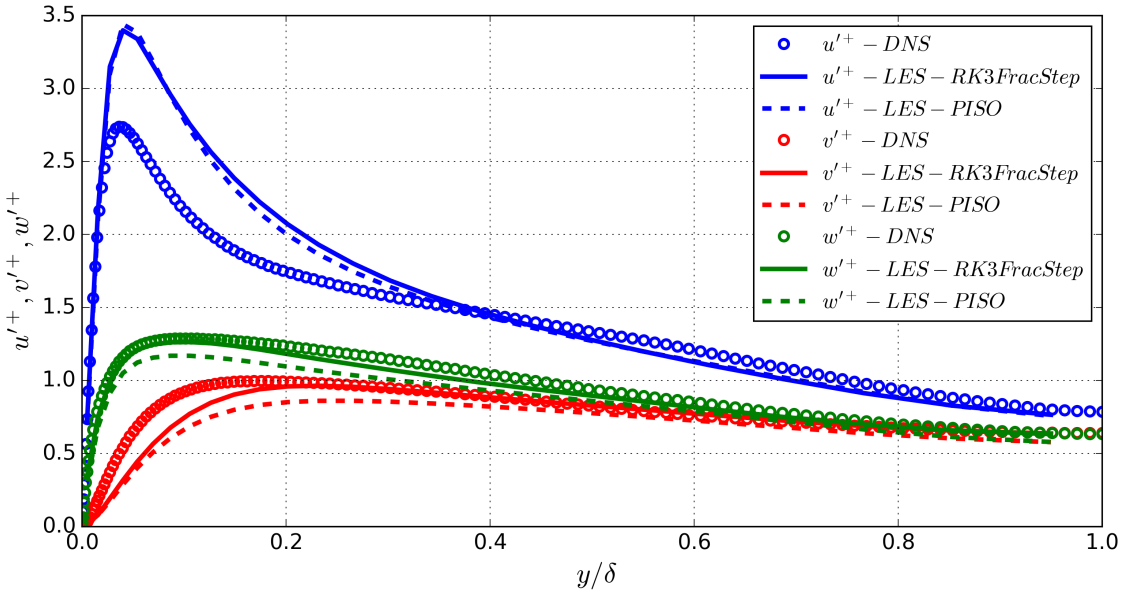

Figure 4.14: *Comparison of normalized turbulent intensities computed by RK3FracStep and PISO solvers for fully developed channel flow at* $Re_\tau = 395$. *DNS data from Moser et al. (1999).*

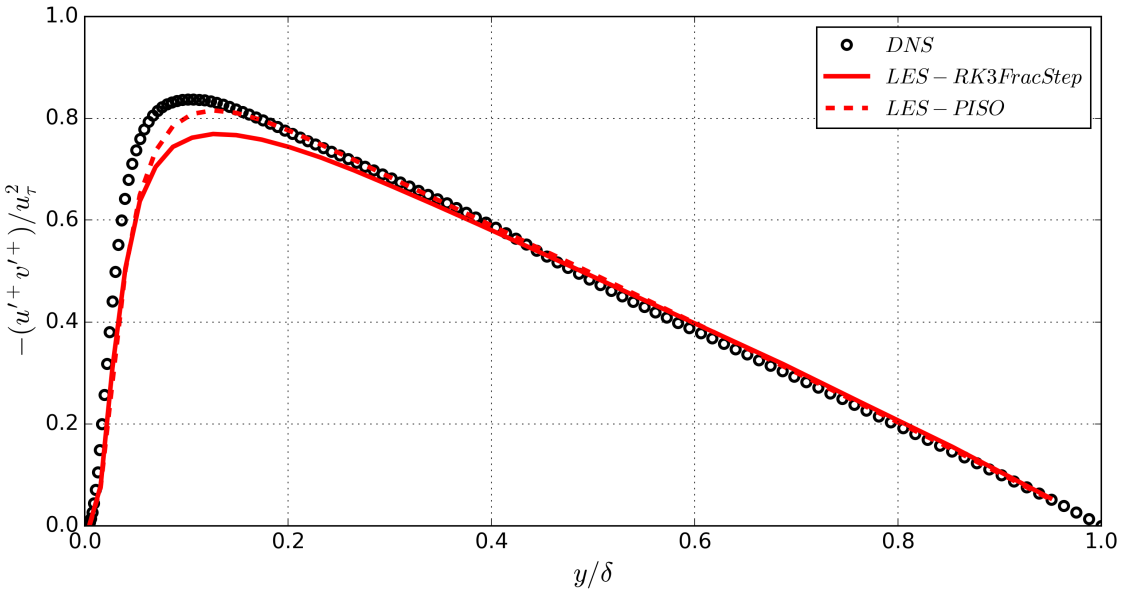

Figure 4.15: *Comparison of normalized turbulent shear stresses computed by RK3FracStep and PISO solvers for fully developed channel flow at $Re_\tau = 395$. DNS data from Moser et al. (1999).*

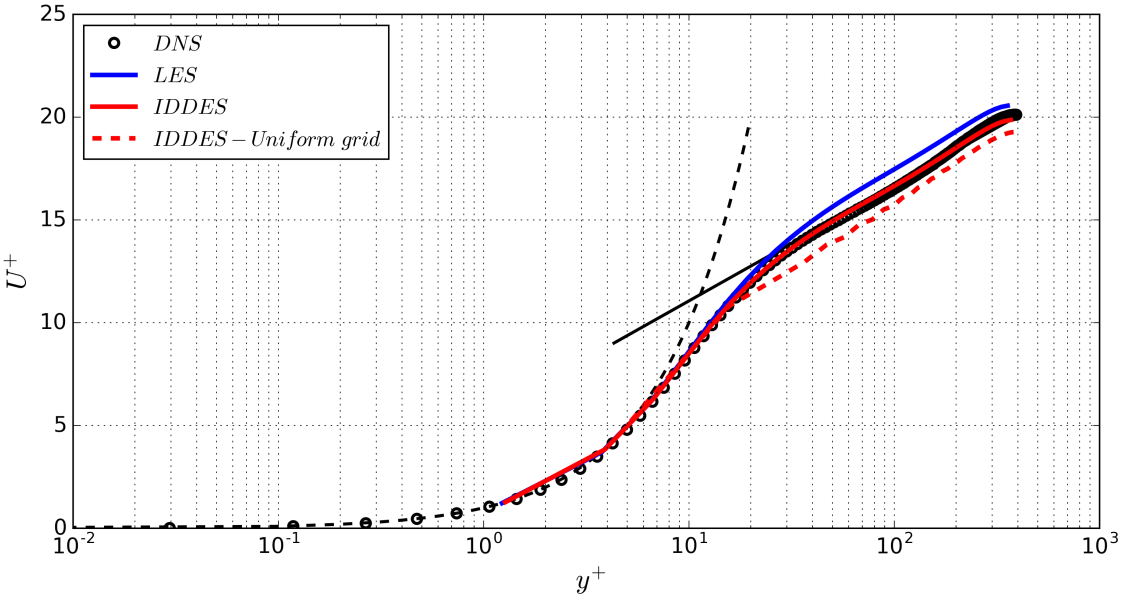

Figure 4.16: *Computed mean streamwise velocity profiles using LES and SA-IDDES turbulence models for fully developed channel flow at $Re_\tau = 395$. DNS data from Moser et al. (1999).*

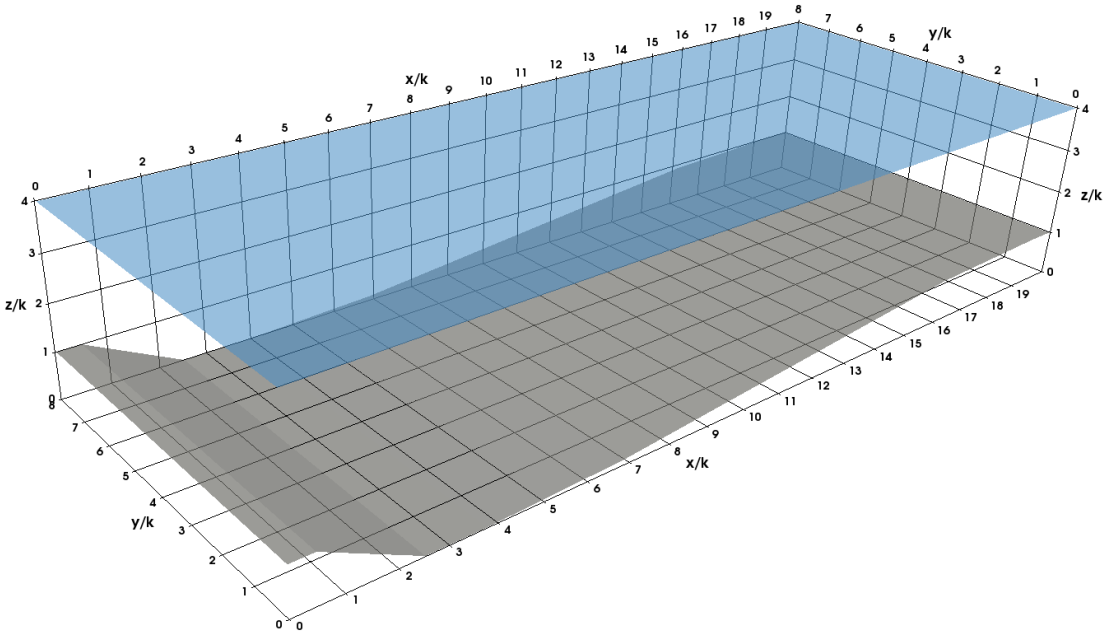

Figure 4.17: *Three-dimensional geometry of the dune.*

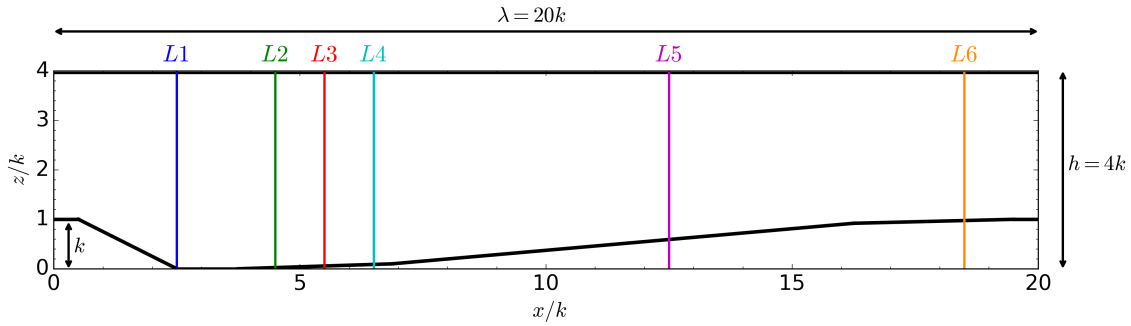

Figure 4.18: *Cross section of the computational domain and location of the LDV measurement verticals.*

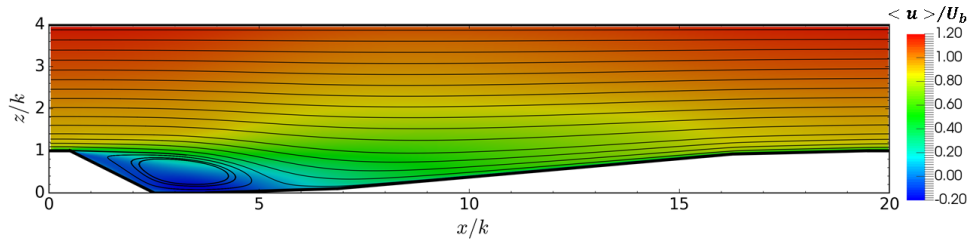

(a)

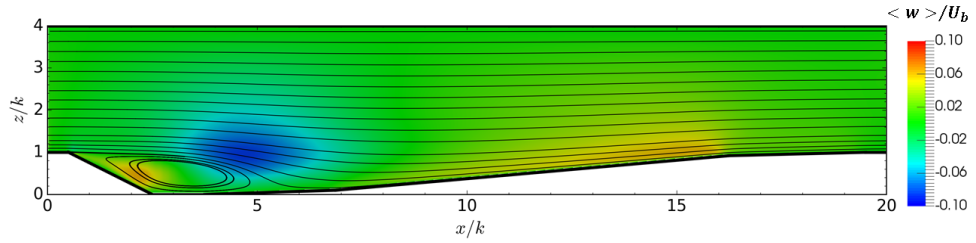

(b)

Figure 4.19: *Streamlines and mean average velocities; (a) streamwise or x-direction and (b) wall-normal or z-direction.*

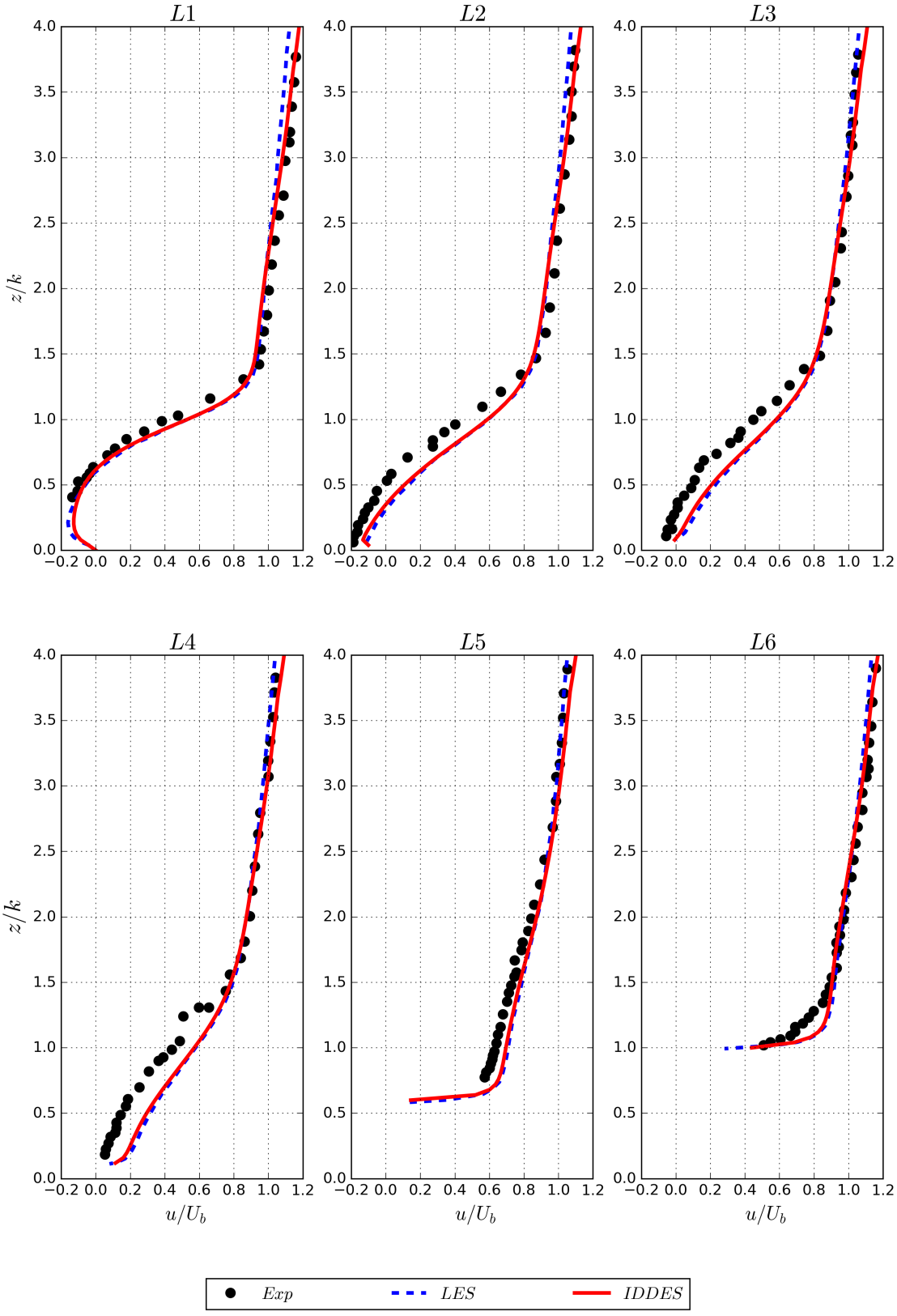

Figure 4.20: *Comparison of mean streamwise velocities along the six measurement verticals. Experimental (Exp) from Polatel (2006) and large eddy simulation (LES) from Stoesser et al. (2008).*

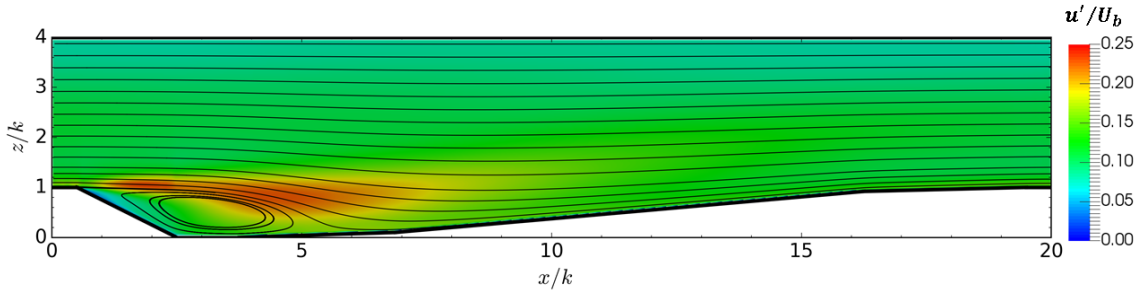

(a)

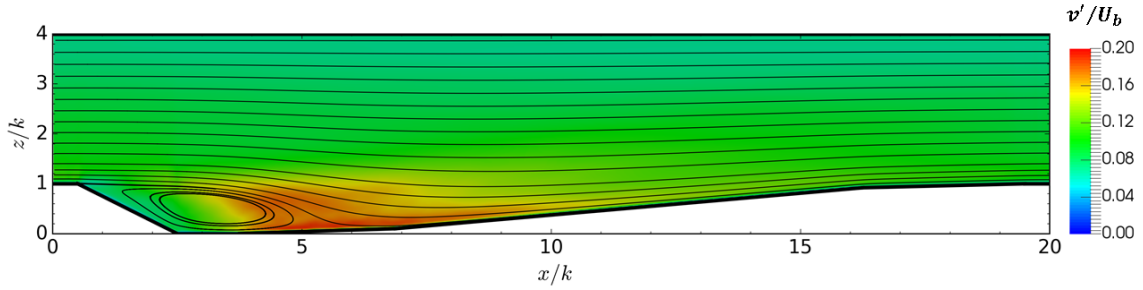

(b)

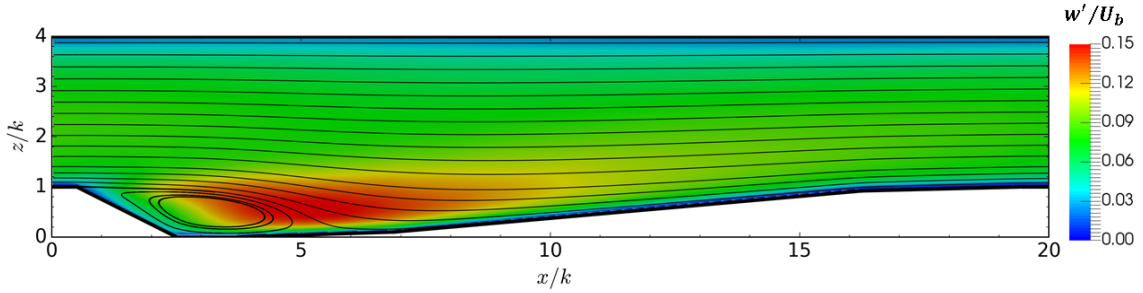

(c)

Figure 4.21: *Streamlines and mean turbulence intensities; (a) streamwise or x-direction, (b) spanwise or y-direction (c) wall-normal or z-direction.*

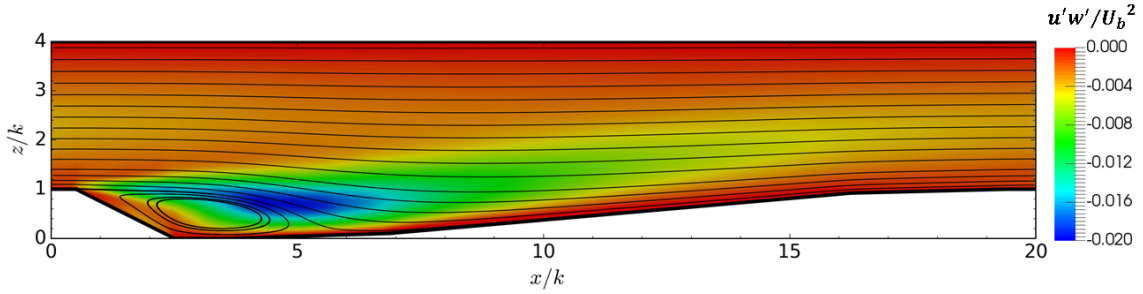

Figure 4.22: *Streamlines and mean turbulence shear stress*

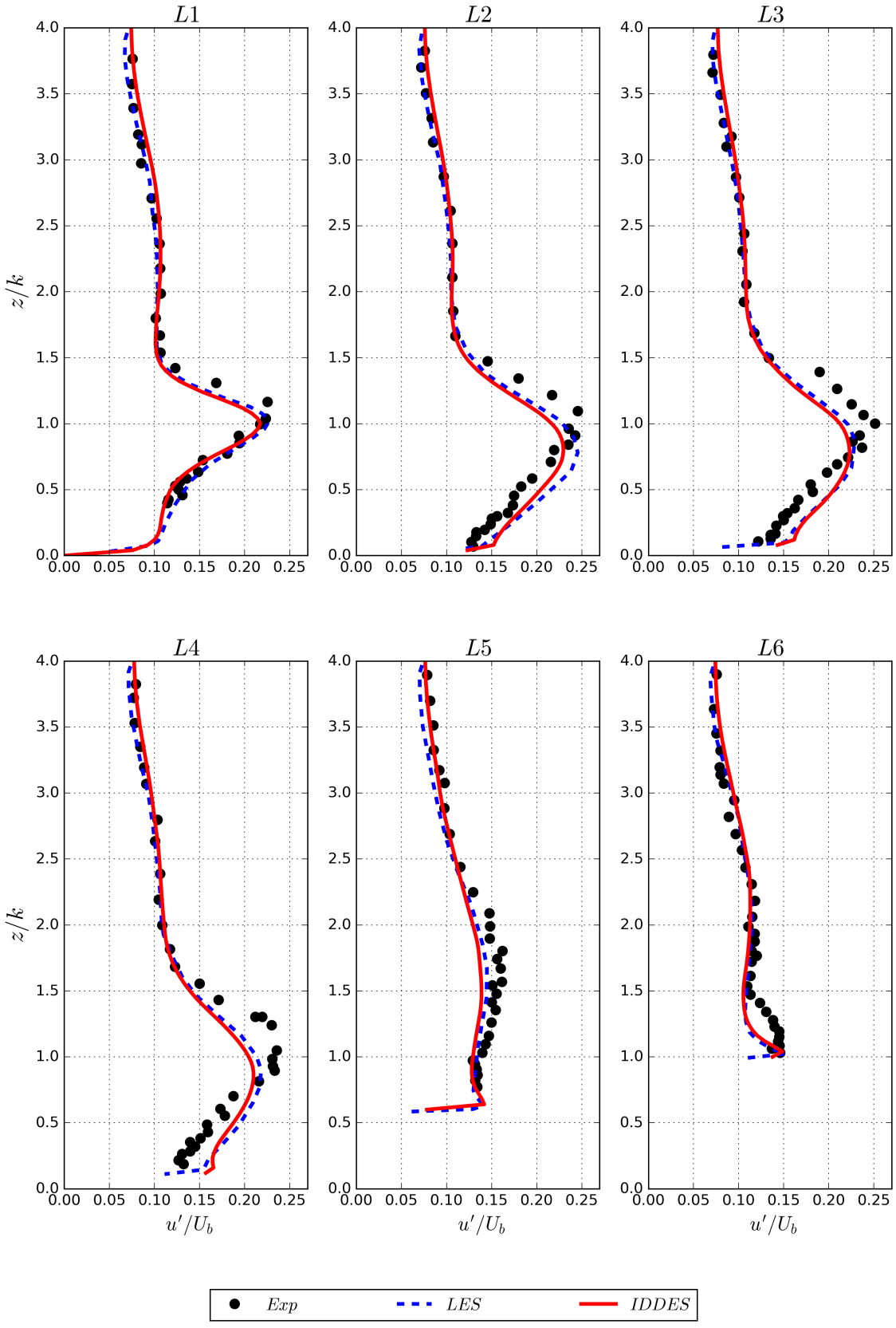

Figure 4.23: *Comparison of streamwise turbulence intensities along the six measurement verticals. Experimental (Exp) from Polatel (2006) and large eddy simulation (LES) from Stoesser et al. (2008).*

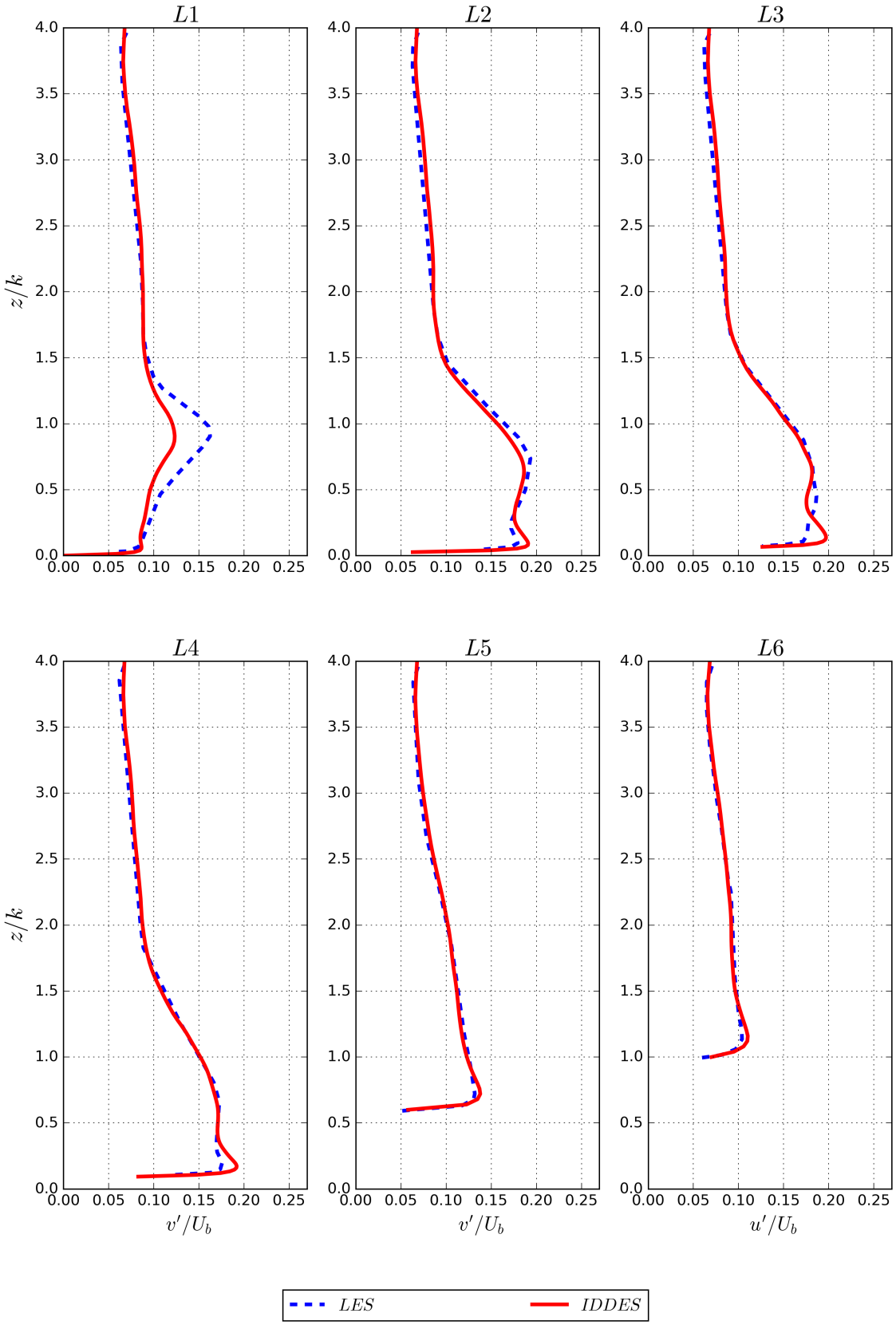

Figure 4.24: *Comparison of spanwise turbulence intensities along the six measurement verticals. Large eddy simulation (LES) from Stoesser et al. (2008).*

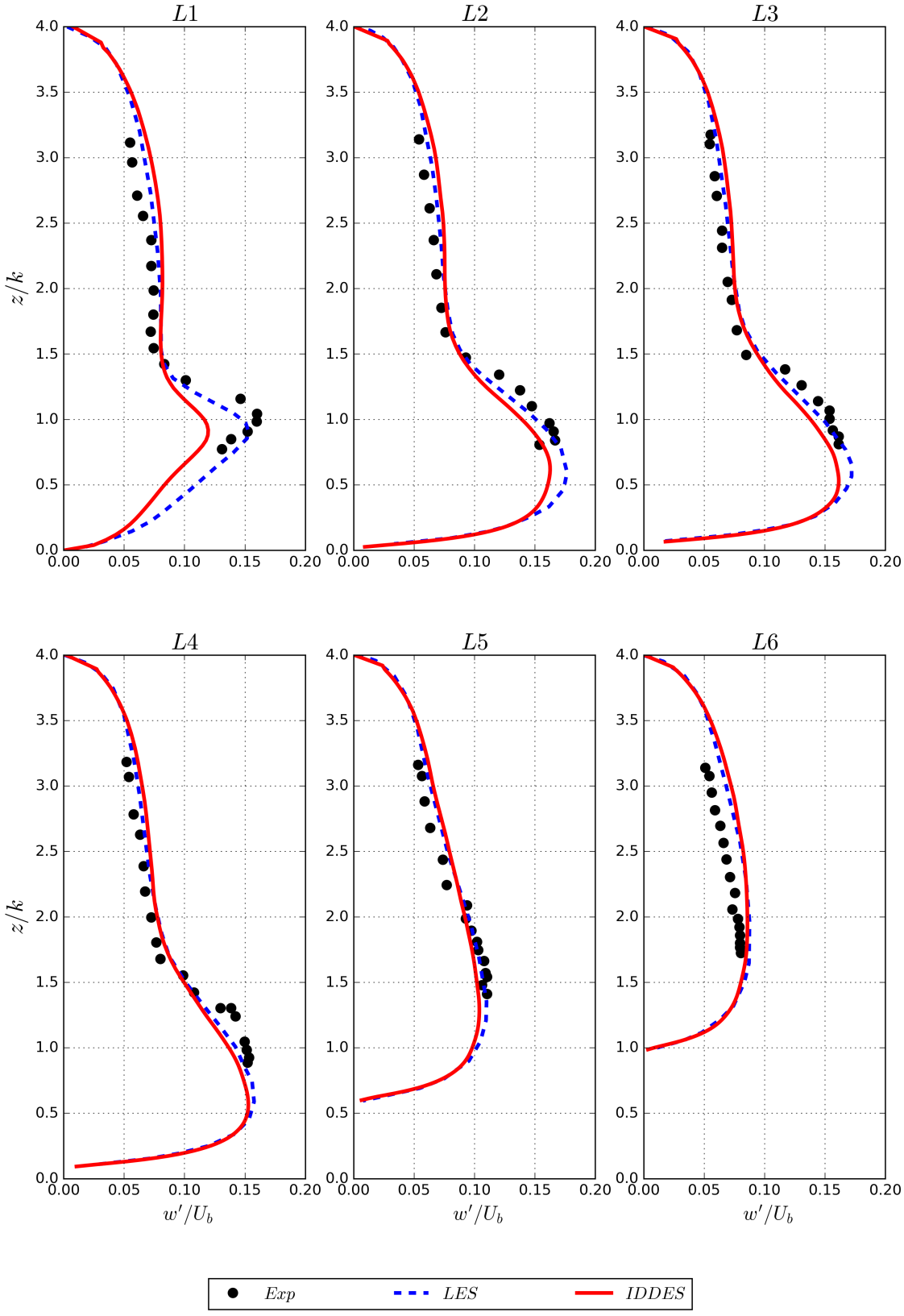

Figure 4.25: *Comparison of wall-normal turbulence intensities along the six measurement verticals. Experimental (Exp) from Polatel (2006) and large eddy simulation (LES) from Stoesser et al. (2008).*

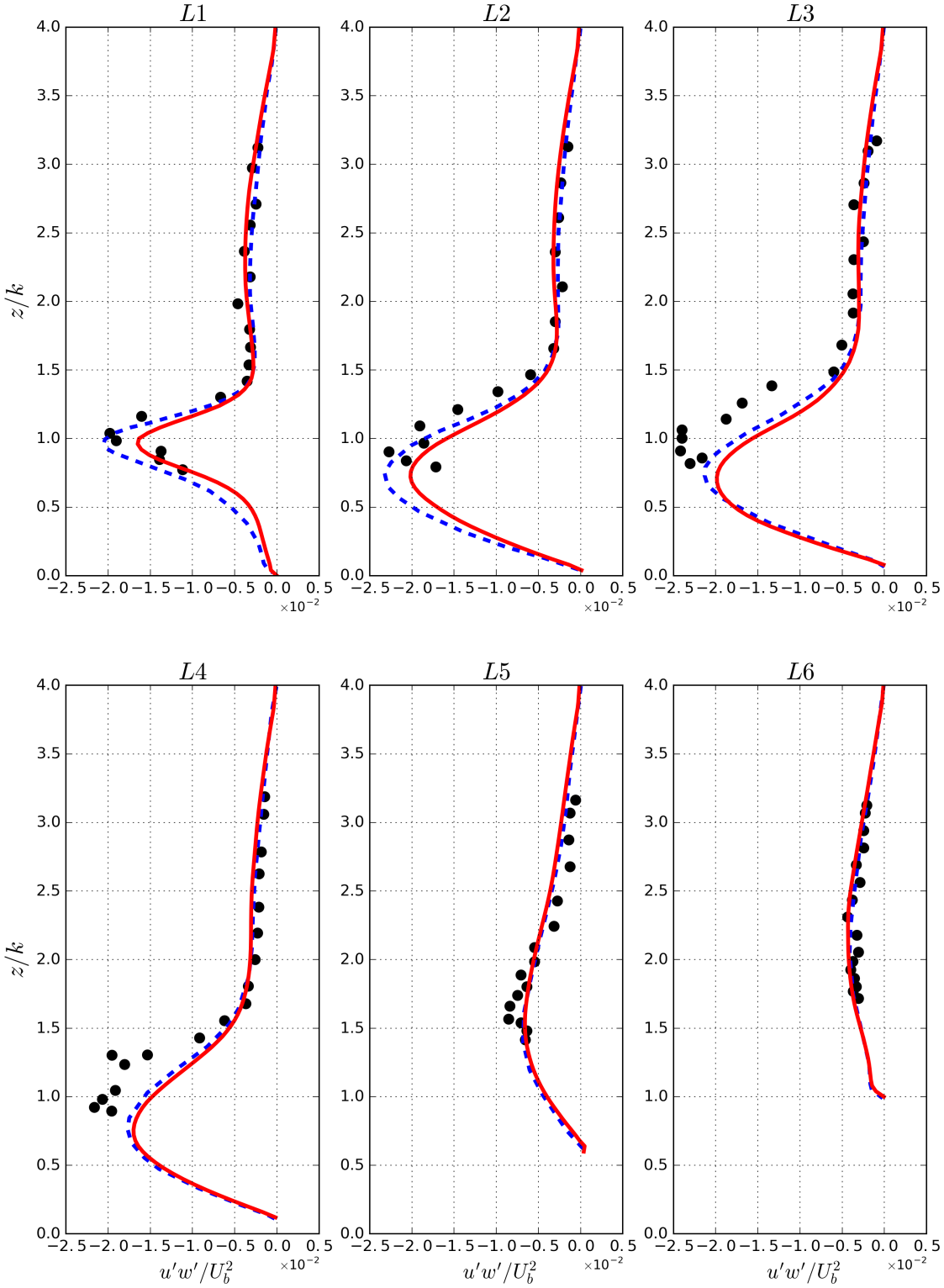

Figure 4.26: *Comparison of Reynolds-shear-stresses along the six measurement verticals. Experimental (Exp) from Polatel (2006) and large eddy simulation (LES) from Stoesser et al. (2008).*

5 PHYSICAL MODEL TEST

In this chapter general description of the case study as well as the physical model test are presented. Moreover the measurement device and its underlying measuring principle are described. In addition, the procedure of obtaining and processing of the velocity values are reported. Finally, the results are illustrated and briefly discussed. In the next chapters, these results are compared to the results obtained using numerical models.

5.1 Introduction

The Mur river is the longest river in Austrian state of Styria. The river springs up from the valleys of the Alps, south of Salzburg province with its source being 1898 meter above the sea level. It is approximately 480 kilometres long; from which 330 kilometres are within Austria, 95 kilometres in and around the Slovenian border with Austria and Croatia (SURS, 2000), and around 55 kilometres which forms the border between Hungary and Croatia. The river joins Drava in Croatia and subsequently Danube. The rivers basin covers an area of 13800 km^2 (DZS, 2015) in total. The largest city on the river is Graz with average discharge of 130 cubic meter per second measured at Graz station from 2009 to 2013 according to the Hydrographical Yearbook of the Austrian Federal Ministry of Agriculture, Forestry, Environment and Water Management (BMLFUW, 2014).

The Mur river has a great potential for ROR plants. In fact, several ROR plants have already been built with the first one, Lebring, put into operation in 1903 (Verbund, 2017). In the past decade, numerous HPPs have been renovated or rebuilt (e.g Gralla and Pernegg). Because of high electricity demand in Austria and the government's plan to increase electricity production via renewable sources, several HPP projects are planned or under construction. Indeed more than 27 ROR plants are exist or planned on Mur river in Styrian province alone. This is shown in Figure 5.1 where the hydropower cascade system on this river is shown. Among these projects, Gratkorn HPP located approximately 15 km north of Graz on the Mur river. The location of the project is shown in Figure 5.2. The plant has a typical ROR block layout with bed enlargement (see Figure 2.1e) where the power house is locate at the right side of the river with two Kaplan turbines and the weirs on the left side (see Figures 5.5 and 5.6). The design capacity is approximately 10.8 MW, the design discharge is 205 m^3/s and the reservoir water level is at 371.0 MASL. The layout and arrangement of the upstream of the ROR are shown in Figures 5.6 and 5.7. This project is chosen for this study because of its similarity to other ROR projects in several aspects. Furthermore, availability of a physical model provides the possibility to study the flow as well as validation of the numerical results. Successful numerical modelling of this case facilitate future investigation for other similar projects and possibly optimization of the designs.

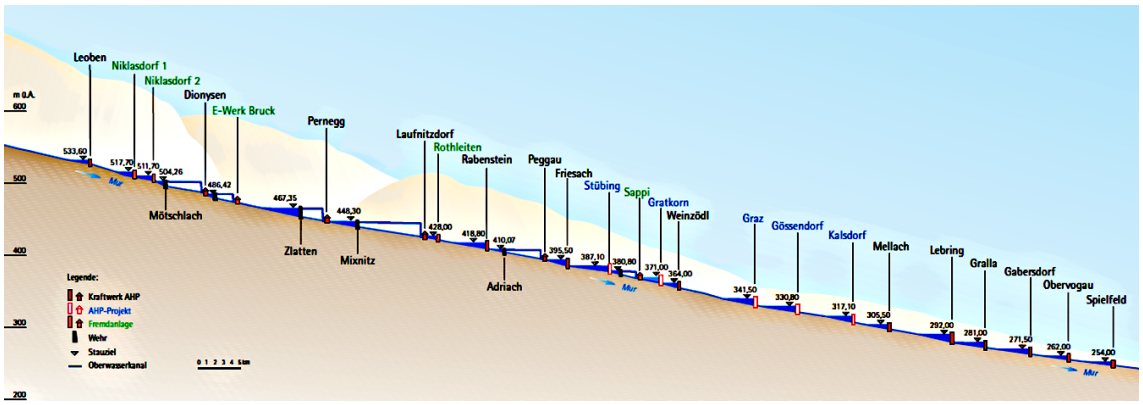

Figure 5.1: *The hydropower cascade system on the Mur river (source: Verbund Hydro Power GmbH).*

The physical model study of Gratkorn HPP is carried out at the Hydraulic Laboratory of the Institute of Hydraulic Engineering and water resources management of the Graz University of Technology. The construction of the model has started at the beginning of 2013. After completion, wide range of studies have been carried out until 2015. These studies were include evaluation of the approach flow to the turbines, performance of the weirs and sedimentations. Figure 5.5 shows an overview of the physical model and the relevant parts.

The physical model is constructed based on Froude similarity law with 1:40 scale. The approximate total length of the model is 18.5 m (740 m in nature) with 2.4 m (96 m in nature) width at the inlet of the model. The power house and the weirs are approximately located 6.5 m (260 m in nature) from the model's inlet. In order to improve inflow condition, flow straightener placed at the inlet. The model is made of bricks and cement mortar, however, the weirs and their moving parts are constructed from opaque plastic. Furthermore, the intake structure is made from transparent acrylic glass (Figure 5.3). Openings are placed at the top of the turbine's intakes to measure the approach flow velocities to the turbines. Finally, the water level in the reservoir adjusted by reducing the cross-section downstream of the intakes. Locations of the regulator is shown in Figure 5.3.

In order to optimise the performance of the HPP, it has been subjected to several modifications. One of the most important change is the geometrical modification of the intake structure. The initial design has shown highly irregular velocity distribution at the left side of the turbine two. The initial design is illustrated in Figure 5.4(a). Series of modifications have been done in order to improve the flow condition. The last modified version is illustrated in Figure 5.4(b). It has been found that this arrangement with thicker divider wall and a submerged pier improved the flow condition.

In this study, the last variation of the intake structure is investigated. In the next section, more detail about the geometry of the case study will be discussed and cross-sections which the measurement have been carried out will be presented.

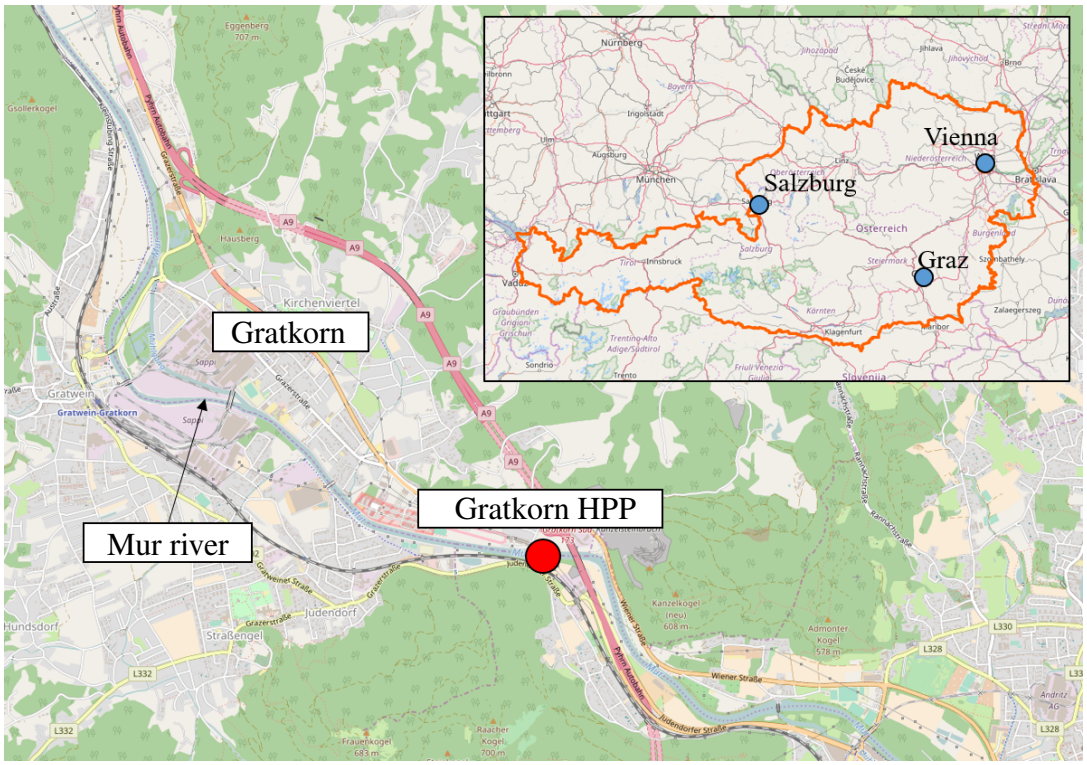

Figure 5.2: *Approximate location of Gratkorn HPP. Map from OpenStreetMap available under a creative commons CC BY-SA licence (see www.openstreetmap.org/copyright), ©OpenStreetMap-contributors*

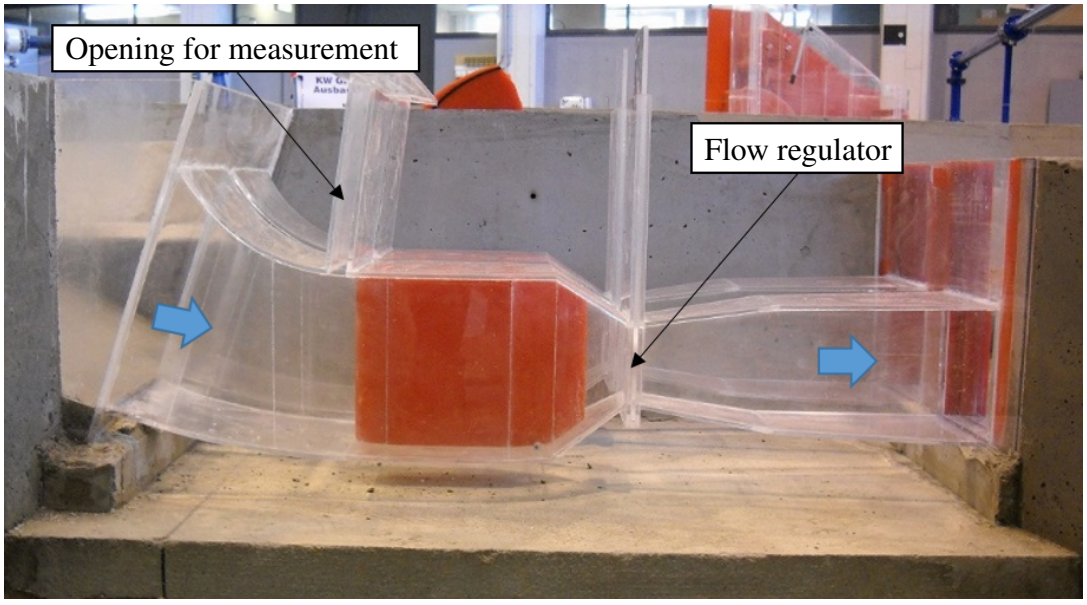

Figure 5.3: *View of the turbines illustrating the flow direction, location of the openings and the flow regulators*

(a) (b)

Figure 5.4: *(a) Initial design of the intake, (b) Final shape of the intake with submerged separation pier and thicker divider wall*

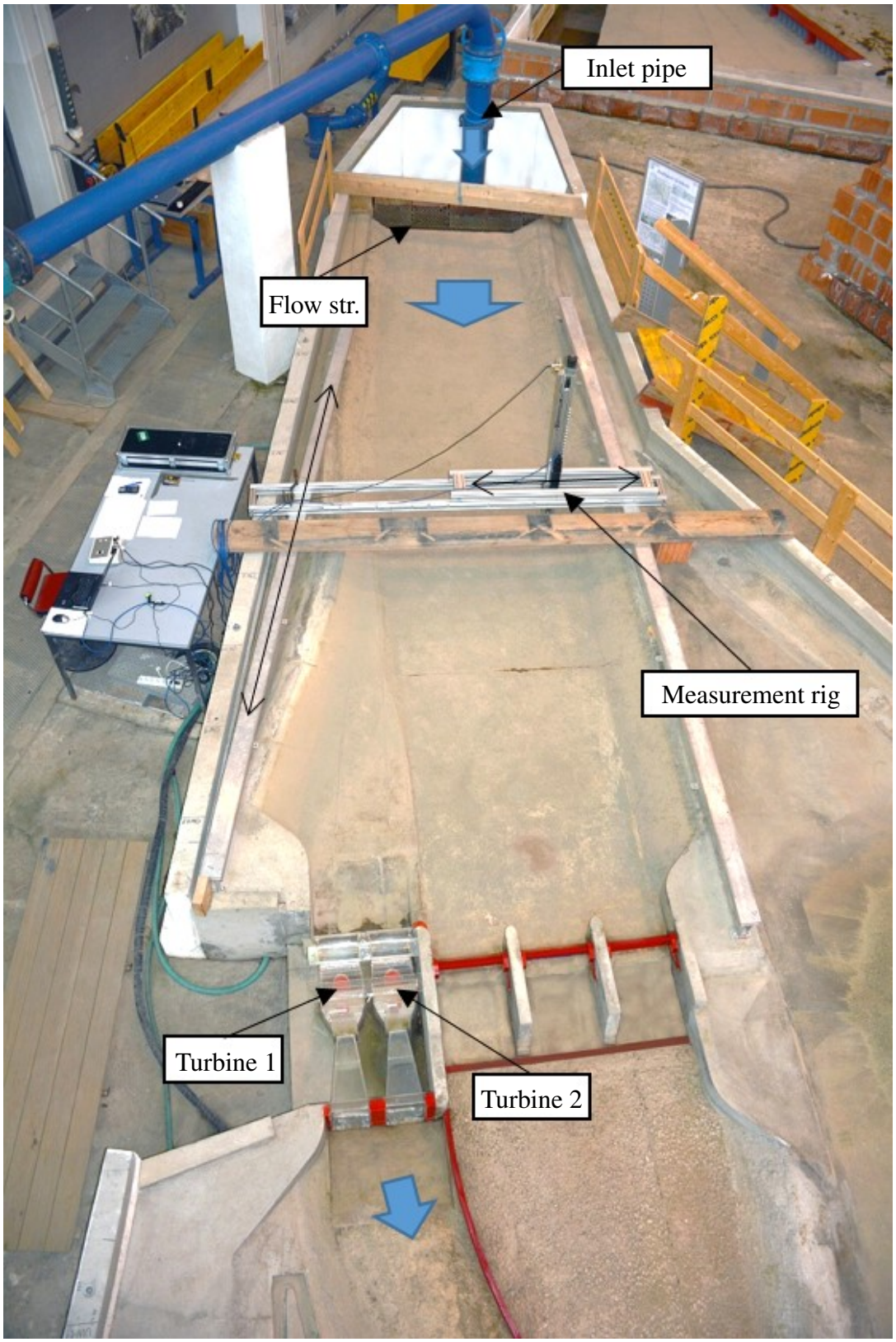

Figure 5.5: *Upstream view of the physical model.*

5.2 Selection of the measurement device

Initially the velocities are measured using pitot or Prandtl probe inside the intakes. This measurement device consists of a tube pointing directly into the flow and it measures the stagnation or total pressure. The probe has additional opening on the sides to measure the static pressure. Then the dynamic pressure and consequently velocity of the fluid can be computed. However, this technique has its drawbacks. The device is only capable of measuring the magnitude of the velocity. Furthermore, it is shown that significant error is expected when the angle of attack is increase. Indeed in this study it was observed that in particular locations when the angle of attack is high, the velocity which was reported by the probe was unreliable. Finally, because of the above issues the flow velocities are measured with Acoustic Doppler Velocimetry (ADV) device. This method is not only does not have the pitot probe's problems, it is capable of providing accurate three dimensional velocity vectors at high frequencies. The principal of the ADV technique and data processing are described in Section 5.4.

5.3 Measurement sections

The flow velocities are measured at several sections and at each sections for several points in the physical model. The physical model layout and the location of the sections are illustrated in Figures 5.6 and 5.7. sections D to I are predefined sections of the project. Additionally, sections A, B and C are defined to investigate the approach flow in details. Only the results measured at Section A is presented here due to its importance in the evaluation of the flow in ROR projects. The results from the other sections can be found in Roth (2018). Section A is the closest section to the turbines in the pressurized zone of the intake structure (Figure 5.7). The velocities are measured at 100 points for each intake, 200 points overall for the entire section. The location of the points are shown in Figure 5.8.

5.4 Acoustic Doppler Velocimetry

Acoustic Doppler Velocimetry (ADV) is a device to measure and record instantaneous velocity components at a single point using Doppler shift effect. Based on the Doppler principle, the sensor transmits ultrasonic signals which are reflected by small particles naturally flowing in the water. The device measures the flow velocities in three spatial directions in the sampling volume. Figure 5.9 shows ADV probe and its measuring principle. The device which is used to measure velocities is Vectrino+ from Nortek AS with fixed stem side-looking probe (see Figure 5.9). It has one transmitter and four receivers. The acoustic frequency is 10 MHz and the sampling rate can be adjusted to values of up to 200 Hz. The high sampling rate allows the resolution of turbulent fluctuations of the flow which can be used for computing Reynolds stresses and analysing turbulent characteristics. For further details about this particular device the reader is referred to the Nortek Vectrino manual (Nortek (2009)).

The Vecterino device measures the velocities in 3-dimensions. Figure 5.10 shows the orientation of the coordinate axes for side-looking probe. The z-axis is aligned with the probe's support, the y-axis is pointing outward from the transmitter and the x-axis is indicated on the device. In order to avoid velocity ambiguities, it is recommended by

Wahl (2000) that large velocity component in the direction of the transmitter, in this case y-axis, must be avoided. Therefore for all measurements the probe orientated in way that the large component of the velocity is approximately perpendicular to the transmitting direction.

Measuring flow velocities with ADV tool has its own set of unique requirements due to the method of operation and the inherent limitations of the measurement technique (Wahl, 2000). As discussed above, the techniques relies on reflected ultrasonic signals from the small particles in the water to measure velocities. Therefore it is necessary to provide adequate particles in the flow for the accuracy of the measured data. In this study, this was done by introducing fine grain seeding material at the model's inlet. The particles were mixed properly with the water by the time the flow reached the measuring point due to the high turbulent flow before the model's inlet. This significantly improved the quality of the measured data. The Vectrino software provides two additional important parameters which helps to evaluate the accuracy of the flow velocities. Signal-to-noise ratio (SNR) determines the relative density of acoustic particles in the flow and the resulting strength of the signal received compared to the device's noise level. Vecterino manual recommends an average value to be above 5 when measuring average flow velocities. However, when instantaneous velocities and turbulence quantities are required, this value must be equal to or higher than 15. As an example, Figure 5.11 shows values of SNR for point A1 of Section A, intake 2. The second important parameter is Correlation (COR). This parameter, on the other hand, indicates the relative consistency of the behaviour of the particles in the sampling volume during the sampling process. The range of the COR value is from 0 corresponding to low quality data to 100 which is indicating a high quality data. Recommended value for COR is 70 and higher (Wahl, 2000). In this study, measurement at all points indicates average COR score of 80 and higher. Figure 5.12 shows an example of COR values for point A1 of Section A, intake 2.

The data has been recorded with high sampling rate of 50 Hz. Because of this, recording for several points for long period of time (e.g. several minutes) is very time consuming. Therefore, a series of tests were carried out to find the approximate recording period which velocity converges to the average value without oscillatory behaviour. Figure 5.13 shows such a convergence study at point A1 of Section A, intake 2. The data for this particular point is shown as an example because during the numerical simulations, velocity at this point shown slight transient behaviour. It can be seen that after 60s, the rolling RMS of velocity is converging to its total RMS value. Similar convergence study are also carried out for other points to obtain confidence that 60s of recording provides enough data for computation of the flow parameters.

Analysing recorded data during and after the measurement by SNR, COR and convergence rate is a good tool to determine possible errors. However, in order to improve the quality of the data it is necessary to apply additional filters during post-processing to reduce errors associated with ADV measurement. In the next section, the post-processing procedures are described.

5.5 Data Post-processing

In ADV measurement, post-processing the data is a crucial step. More specifically, filtering the ADV data is important because not all data obtained from the measurement is

suitable for computing flow parameters (e.g. average velocities, turbulent kinetic energy, etc.). In this study, three filters, two based on SNR and COR along with despiking technique, are used to improve the raw data. The filters applied using WINADV software from the bureau of reclamation in cooperation with Nortek and sontek.

Correlation value and signal-to-noise ratio provide a good indication of the possible problems during an ADV measurement. Filtering based on these values can improve the recorded data. The filtering technique works by removing data which their SNR and COR values are lower than the cut-off level. In this study, the cut-off value for COR value is set to 70, however, Wahl (2000) stated that values much lower than 70 still can be used particularly when the SNR is high and the flow is relatively turbulent. On the other hand, SNR values are relatively more important than the correlation scores for computation of turbulent kinetic energy or Reynolds stresses. Therefore high cut-off value of 15 is used to filter out potentiality erroneous values from the raw data.

Although filtering based on SNR and COR values are a good tool to remove data containing velocity ambiguities, other filters which involves with despiking the velocities have shown success in removing corrupted data. The acoustic noises and errors related to the aliasing of the Doppler signal appear as spikes in the samples. Cea et al. (2007) studied several despiking filters for highly turbulent free surface flow. It is shown that the turbulent energy added by spurious spikes to the total turbulent kinetic energy is significant and filtering out the spikes is necessary to compute the correct turbulence parameters. Furthermore, Cea et al. (2007) concluded that although none of the despiking filtering methods can considered as a superior over the others, all the methods produced clean signals with significantly less spurious turbulent kinetic energy.

The spike detection filter which is used in this study is based on a method developed by Goring and Nikora (2002) and further modified by Wahl (2003). This method, known as phase-space threshold filter, is based on the fact that valid ADV data are tightly clustered within an ellipsoid in a so-called phase-space. The method works by plotting the fluctuating component of the velocity, approximation of its first and second time derivatives in three-dimension. Then, spikes are those points lying outside of elliptical projections of the ellipsoid onto the three principal phase-space planes. A detailed description of the method can be found in Goring and Nikora (2002) and Wahl (2003).

Figure 5.14(a) shows raw data recorded with the ADV tool. It can be seen that the data contaminated with spikes. On the other hand, Figure 5.14(b) shows the same data after the application of the phase-space threshold filter. Clearly, the filtering method is effectively removed the spikes, hence it improved the data quality. This filtering technique is available in WINADV and it applied to all the measured velocities.

Certainly filtering raw data with the methods that described above improve the quality of data. Moreover, a few other tools can be used to visually as well as quantitatively analyse the filtered data, for instance, power spectrum plot and histogram can be plotted and evaluated for any unusual distributions of velocity. Figure 5.15 shows histogram of the filtered velocities for point A1 of Section A, intake 2. It can be seen that the velocity distribution about the mean values is fairly symmetrical. Similar observation is made also for other measurement points.

Other than visual inspection with the histogram plot, two additional values, skewness and

kurtosis (Cea et al., 2007), also can be computed in order to quantitatively evaluate the data. Skewness value is indicating the asymmetry of the data where values close to zero corresponds to fairly symmetric distribution. for example, for the same point (point A1 of Section A, intake 2), the skewness values for x, y and z components of the velocity is approximately 0.10, 0.04 and 0.01 respectively. The positive sign of the skewness values indicates that velocity is more likely to take on positive values than negative values. Finally, the kurtosis or flatness of the data is an indicator of the size of the fluctuations. Data with high intermittent extreme events has high kurtosis. Again, at point A1 of Section A, intake 2, the kurtosis values for x, y and z components of the velocity is approximately 0.20, -0.14 and 0.11 respectively. It is worth mentioning that the despiking filters considerably reduced the skewness and kurtosis values.

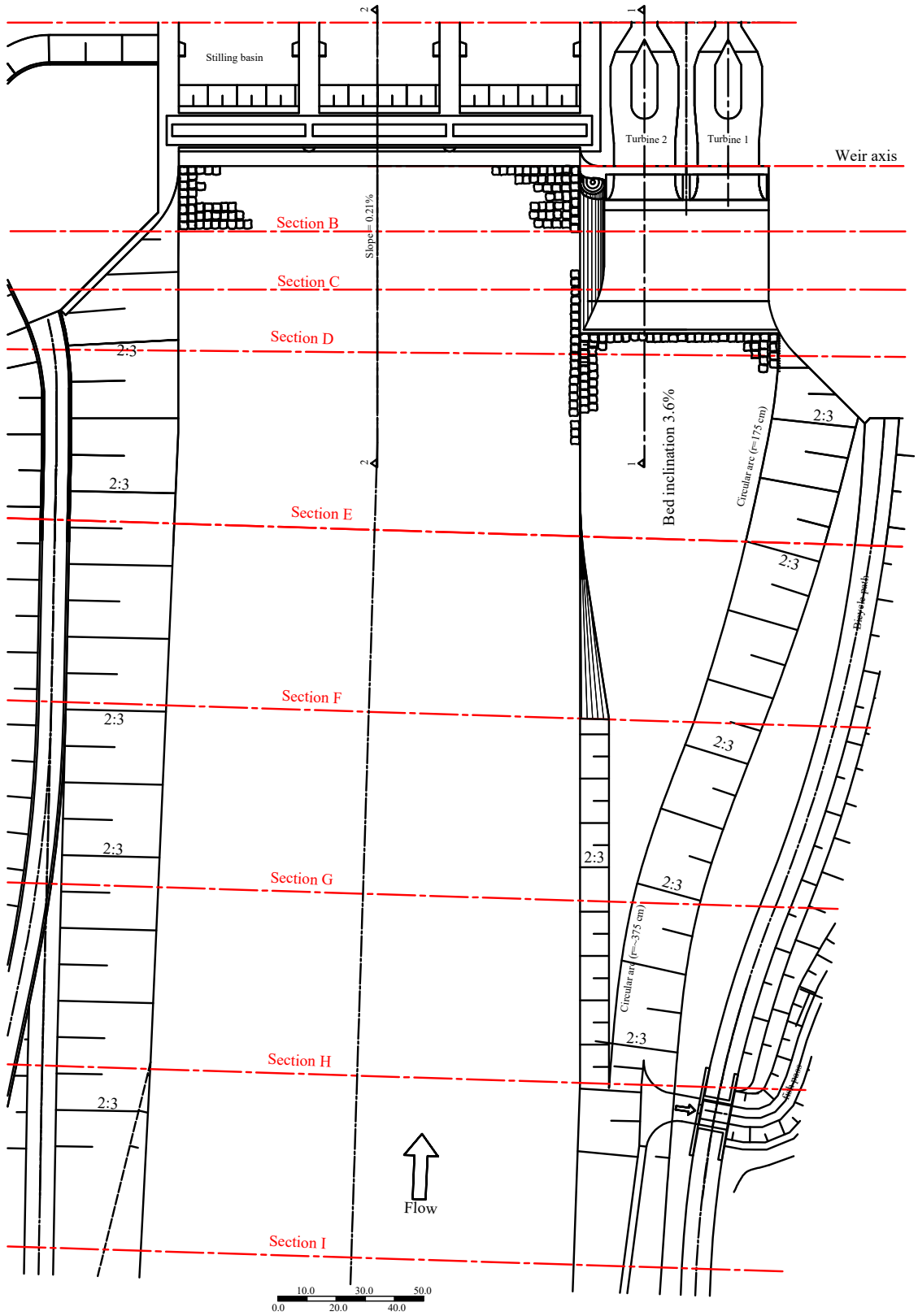

Figure 5.6: *Layout and dimensioning of the physical model test (the ruler is in cm).*

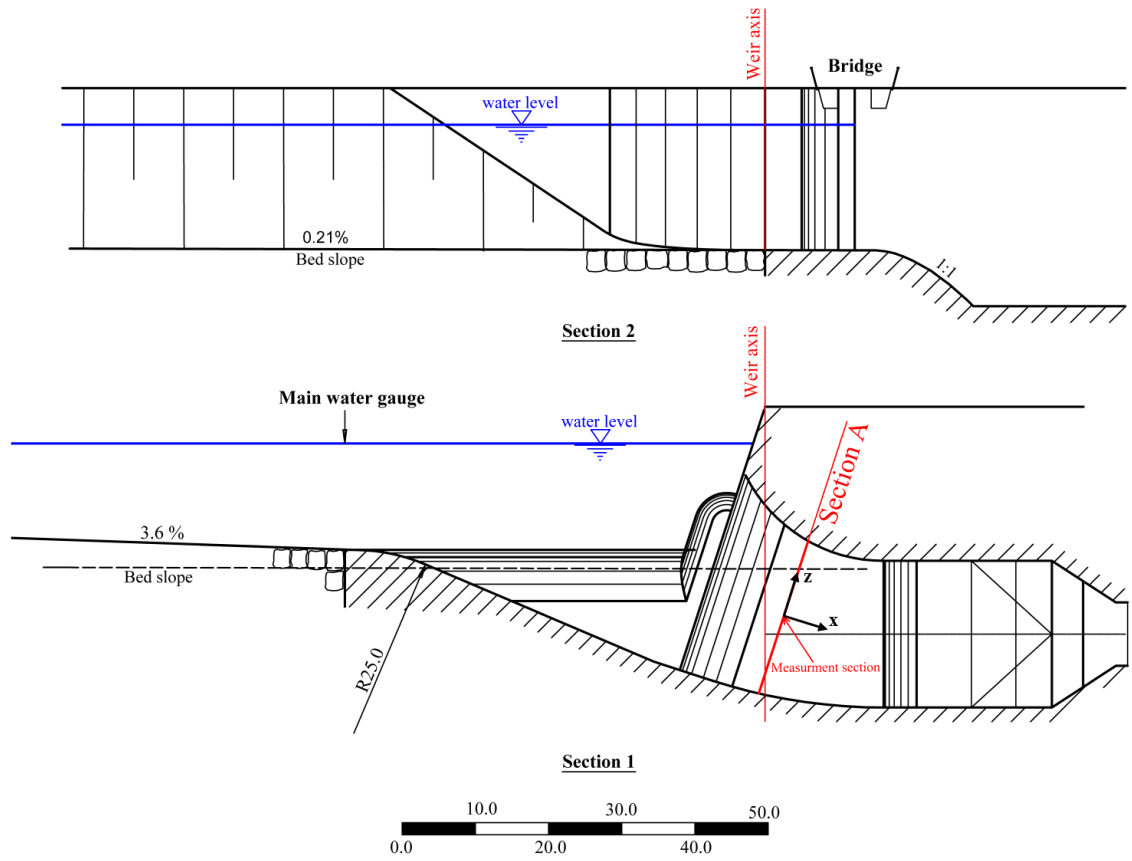

Figure 5.7: *Vertical sections through the models (the ruler is in cm and scale of the model is 1:40). Top: through weirs, Bottom: through the left intake and turbine.*

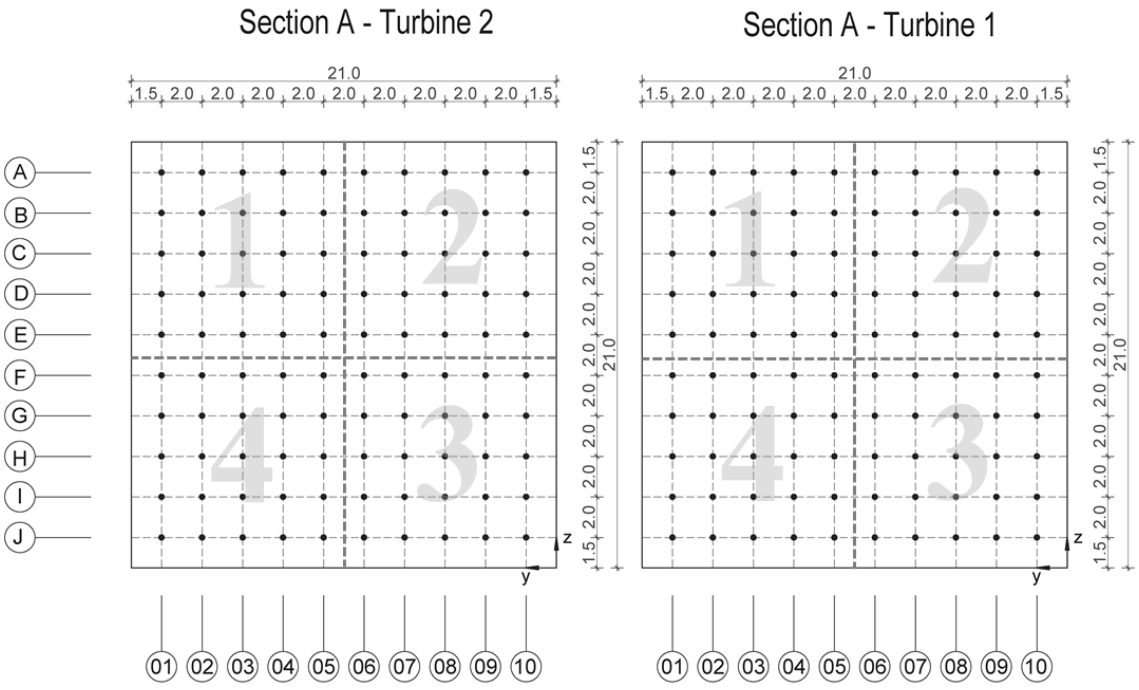

Figure 5.8: *Section A, measurement points in the physical model (the dimensions are in cm and scale of the model is 1:40).*

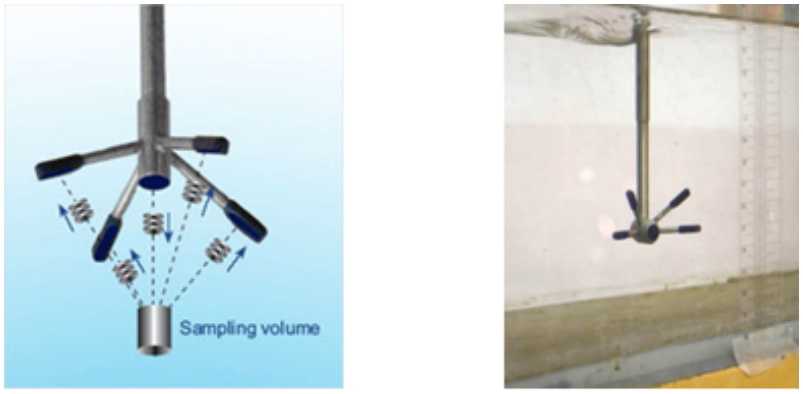

(a) (b)

Figure 5.9: *(a) ADV measuring Principle (Nortek, 2009), (b) Fixed stem side-looking Vectrino.*

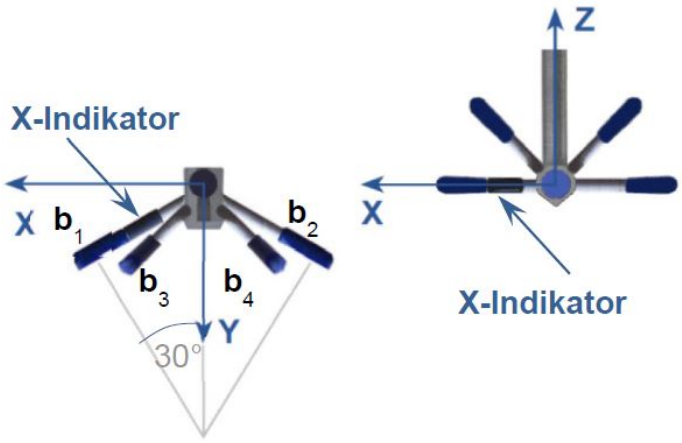

Figure 5.10: *Coordinate system of the Vectrino (Nortek, 2009)*

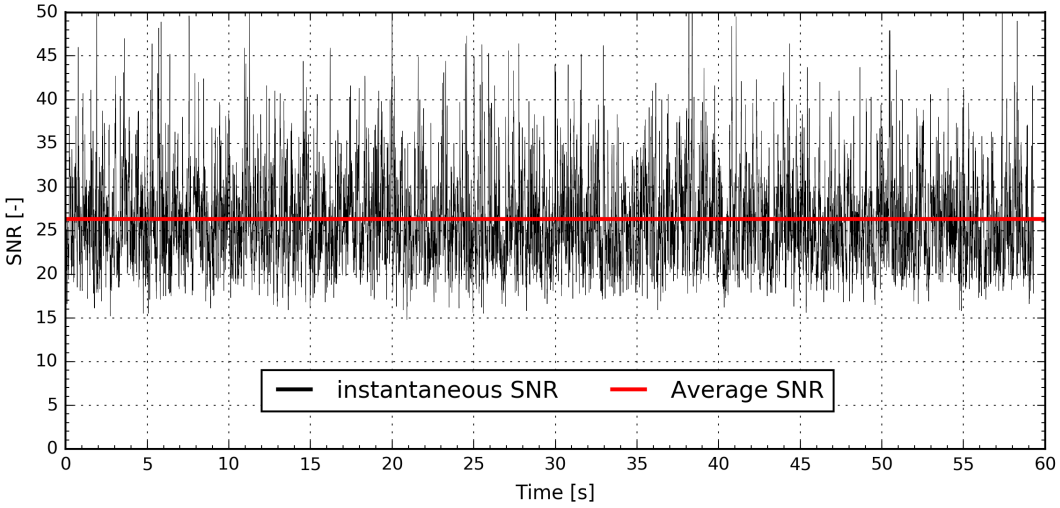

Figure 5.11: *Unfiltered measured SNR values for 60s at point A1 of Intake 2.*

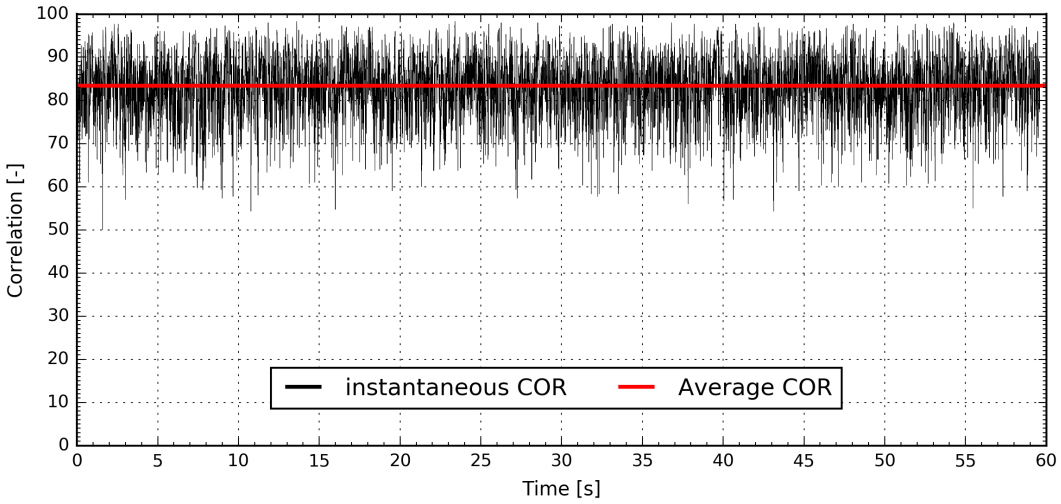

Figure 5.12: *Unfiltered measured COR values for 60s at point A1 of Intake 2.*

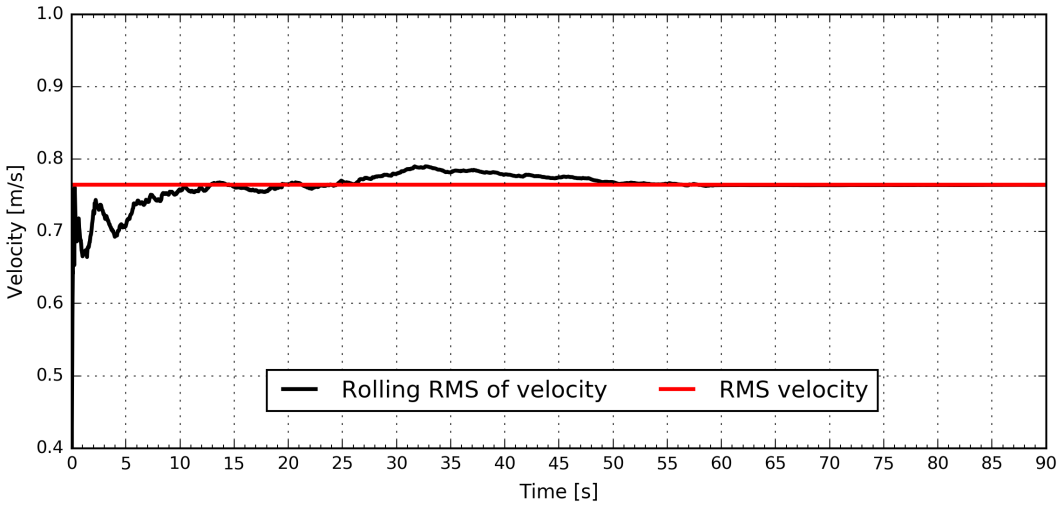

Figure 5.13: *Velocity convergence of unfiltered data at point A1 of Intake 2.*

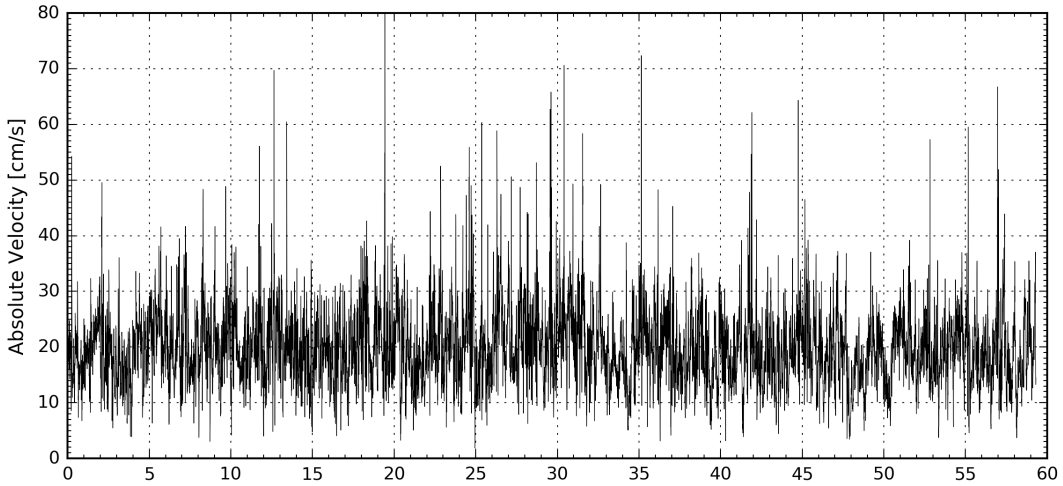

(a)

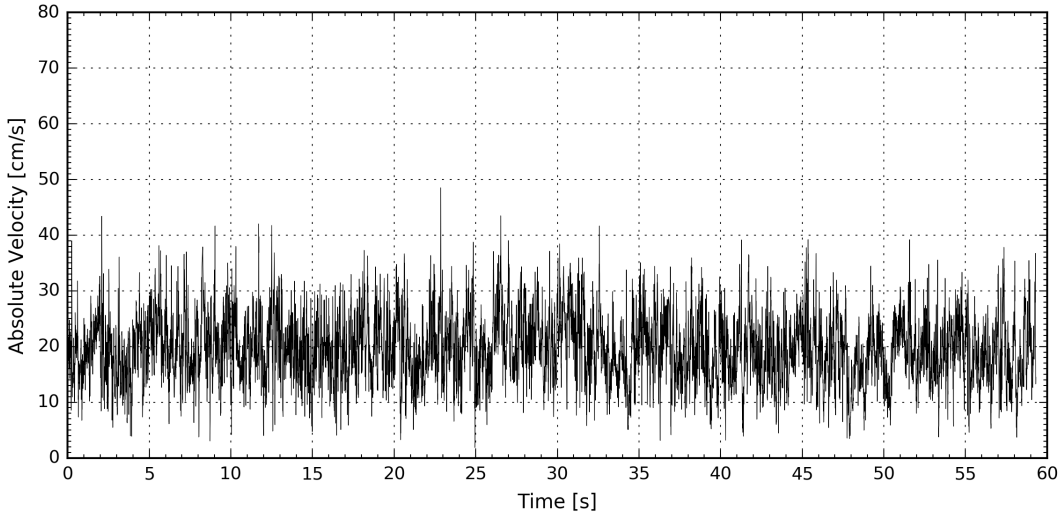

(b)

Figure 5.14: *Unfiltered velocity, (a), in comparison with filtered velocity, (b) at point A1 of Intake 2.*

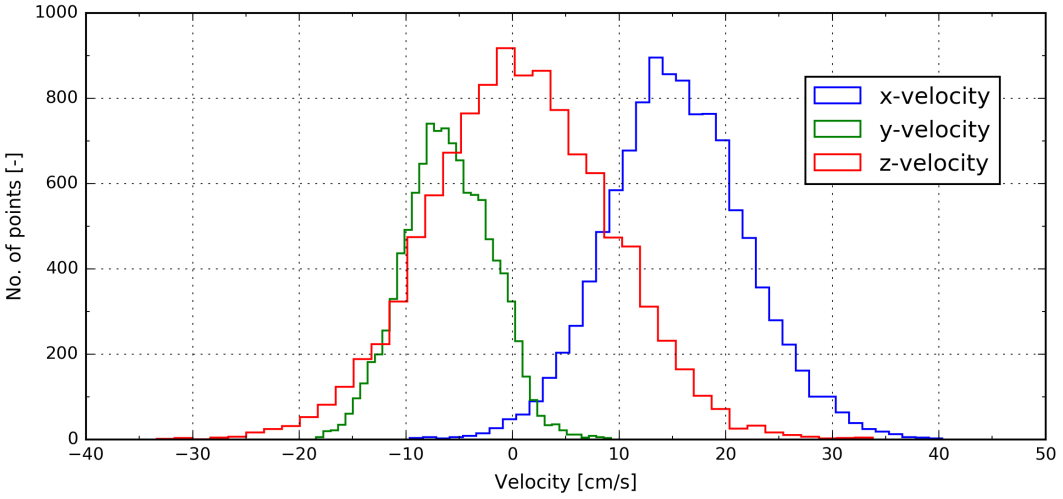

Figure 5.15: *Example of histograms of filtered velocity components.*

5.6 Results

The filtering methods followed by the tools for quality control of the data were described above. These techniques have been applied to the measured values at all the points to reduce velocity ambiguities and evaluate the quality of filtered data. The final results are divided into four categories; average velocities, turbulence intensities, kinetic energy and finally evaluation of the results based on the guidelines (Section 2.9). The time-averaged velocities are computed in x, y, z directions where x represents the normal or out-of-plane direction, y represents horizontal direction and z represents vertical direction. Furthermore, the turbulence kinetic energy and intensities are calculated from the fluctuating velocity components.

5.6.1 Mean velocities

Figures 5.16 and 5.17 are illustrating the time-averaged velocities in x, y and z directions for intake 1 and 2 respectively. The velocities are normalized based on the average velocity of the section, u_{ave}. In both intakes in x direction, high vertical gradient exist where the higher velocities reaching up to 1.3 times the mean velocities located at the top of section. In general, the maximum velocities of intake 2 in y and z directions are twice higher than the ones from intake 1. In y direction, high negative and positive velocity zones in intake 1 is located at the left side of the section. The opposite is true in z direction where the values reaching its maximum at the top and bottom left corners. In intake 2, strong swirling flow can be detected when contour plots of velocities in y and z directions are considered. The location of this swirling flow is at the left side of the section close to the wall with velocity values are reaching up to ± 0.4 times the streamwise mean velocity. It is important to investigate if this swirling flow is local or it is extended downstream. This swirling will be studied further in the numerical sections in details.

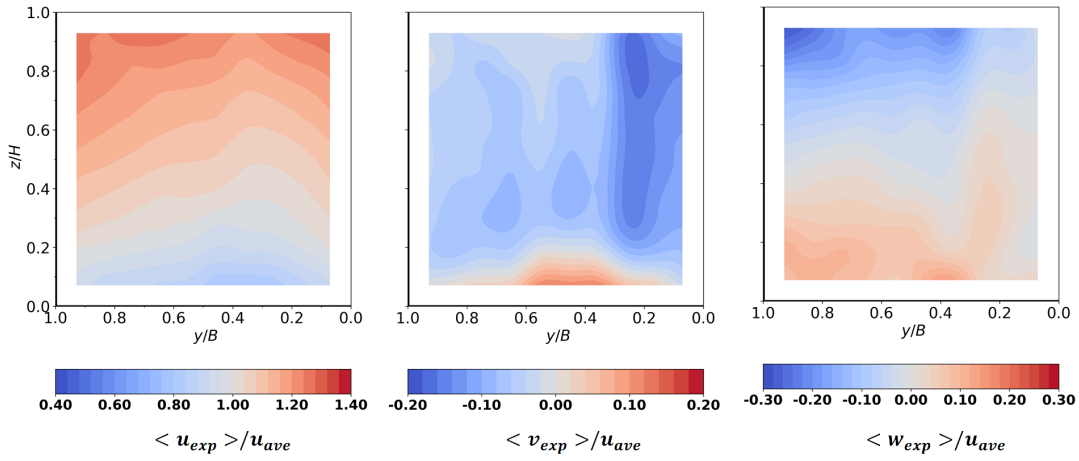

Figure 5.16: *Measured mean velocities in x (left),y (middle) and z (right) directions for Turbine 1.*

5.6.2 Turbulence intensities and kinetic energy

In addition to the mean velocities, second-order statistics are also computed. Figures 5.18 and 5.19 show turbulence intensities in x, y and z directions for intake 1 and 2

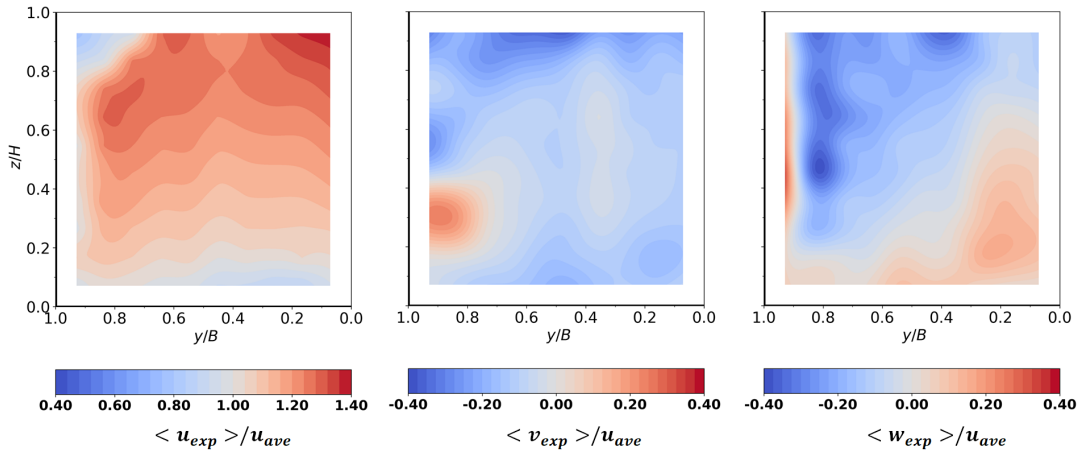

Figure 5.17: *Measured mean velocities in x (left),y (middle) and z (right) directions for Turbine 2.*

respectively. The values are normalized based on the mean streamwise velocity of the section. It is shown that in intake 1, the values in all directions are fairly similar with the turbulence intensities in streamwise direction being higher than the other directions. Moreover, the higher values are located at the top and the bottom of the section. This is more noticeable in the streamwise direction where the values are reaching up to 0.15. The turbulence intensities in intake 2 (Figure 5.19) shows completely different distribution. The noticeable feature is the presence of a zone near the left wall where the turbulence intensities are significantly higher than the rest of the section reaching up to 0.4. This is the same zone where the swirling flow on the left side of the section along with a low velocity zone at the top left corner are detected in Figure 5.17. Finally, Figure 5.20 shows turbulence kinetic energy normalized by the mean streamwise velocity. Similar to turbulence intensities above, in intake 1, the peak of the turbulence kinetic energy is located at the top and bottom of the section near the walls. In intake 2, the high values are located at the left side of the section with the peak values reaching up to 4 times the rest of the section.

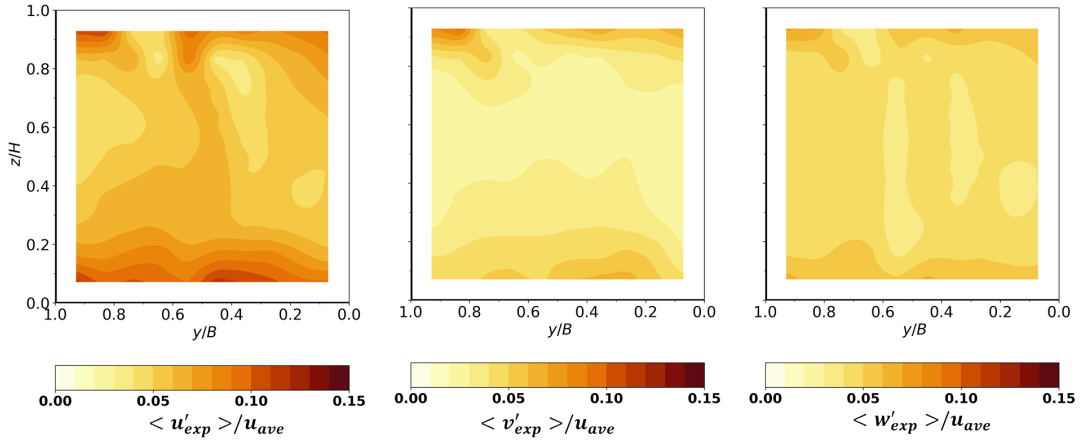

Figure 5.18: *Measured turbulence intensities in x (left),y (middle) and z (right) directions for Turbine 1.*

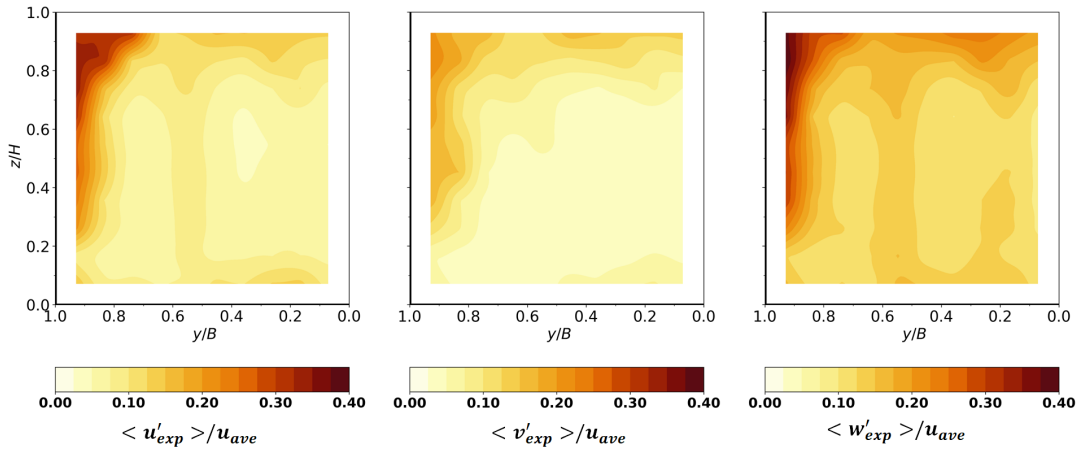

Figure 5.19: *Measured turbulence intensities in x (left),y (middle) and z (right) directions for Turbine 2.*

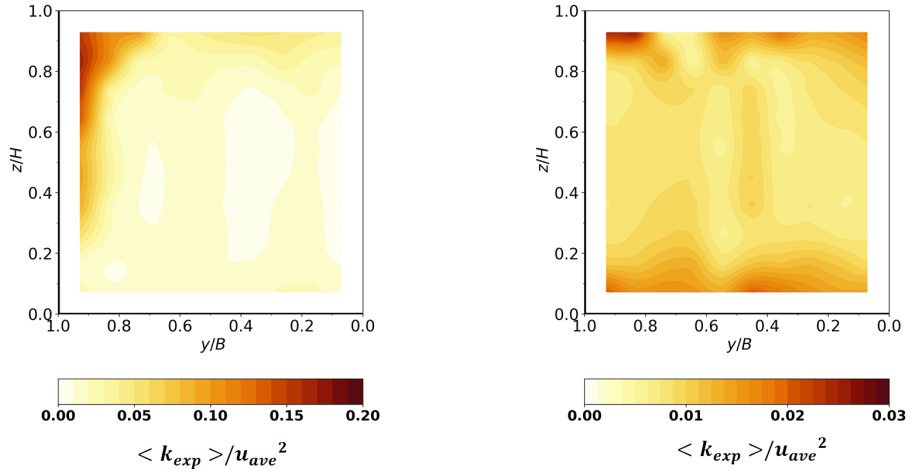

Figure 5.20: *Measured kinetic energy for Turbine 2 (left) and Turbine 1 (right).*

5.6.3 Evaluation of results based on the guidelines

The measured values are also used to evaluate the flow using the conditions from Section 2.9. Figures 5.21 and 5.22 show condition C6, also known as Fisher and Franke criterion. In both intakes the computed values are showing the same trend as Fisher and Franke proposed boundaries. However, in intake 2 in Figure 5.22, the computed values are exceeding the limit significantly in the higher range where $u_n > 1.0$. This is less noticeable when intake 1 is considered in Figure 5.21.

Figures 5.23 and 5.24 show condition C2 where histograms of the local velocity deviations from the axial velocities in y and z directions are computed. It is evident that significant amount of data are higher than 5 or 10% which is the limit of the condition. In general, the local velocity deviations are less noticeable in intake 1. However, in intake 2, the values which are outside of the range is relatively higher with more than 50% of the data points having more than 10% deviations in both directions. The deviations in intake 2 are reaching up to 40% where in intake 1 maximum value is approximately 20%.

Figures 5.25 and 5.26 show condition C4 where histograms of the local velocity deviation angles from the axial velocities are computed. This condition states that the angels must be lower than 5 degrees. Based on this, technically none of the intakes are fulfilling the condition. However, the flow condition in intake 1 is better than intake 2 with more than 70% of the data points are located below 5 degrees. On the other hand, in intake 1, the deviation angles are reaching up to 20 degrees with a small number of points having higher angles (between 20 and 30 degrees).

Finally, Figure 5.27 shows condition C3 where the deviation of discharges for each quadrants are computed for each intakes. The numbering of the quadrants are illustrated in Figure 2.19. In intake 1, quadrants 1 and 2 are showing positive deviations of about 2% from the ideal flow condition. The opposite is true for quadrants 3 and 4. This is aligned with what was observe previously in Figure 5.16. Similar trend can be observed in intake 2 with exception of quadrant 1 which is almost lay on the ideal flow line. In general, the deviations of discharges are all within the limit of the condition.

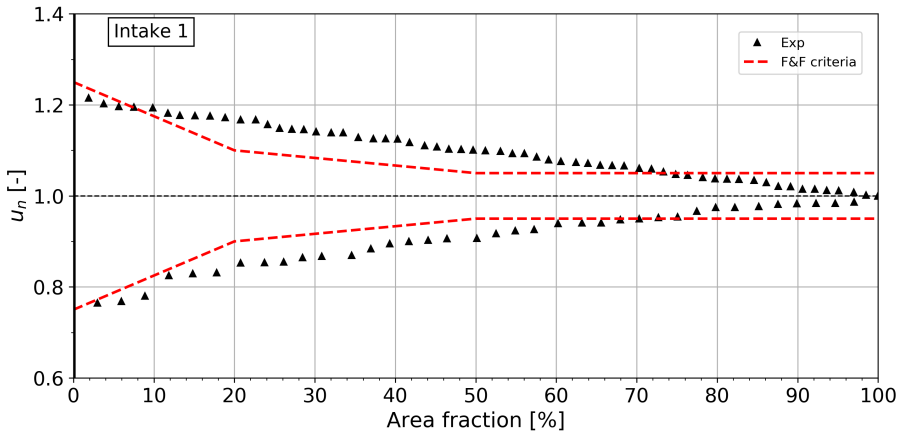

Figure 5.21: *Flow evaluation of Turbine 1 based on Criterion 5 (C5) of the design guideline.*

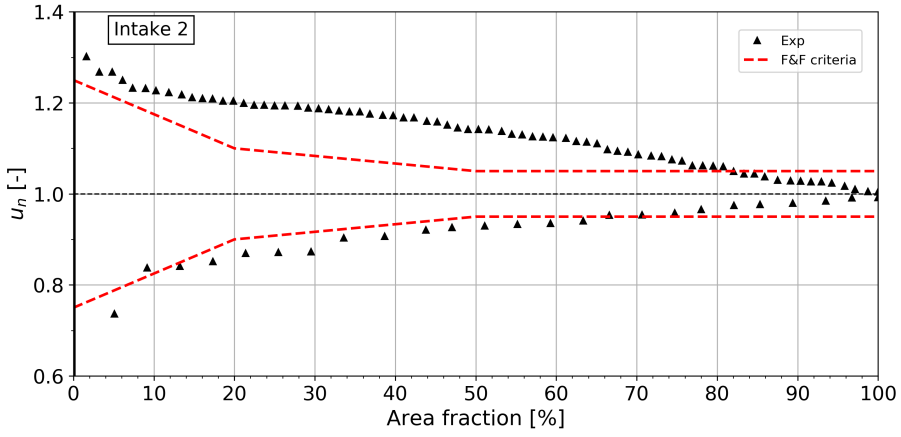

Figure 5.22: *Flow evaluation of Turbine 2 based on Criterion 5 (C5) of the design guideline (Section 2.9).*

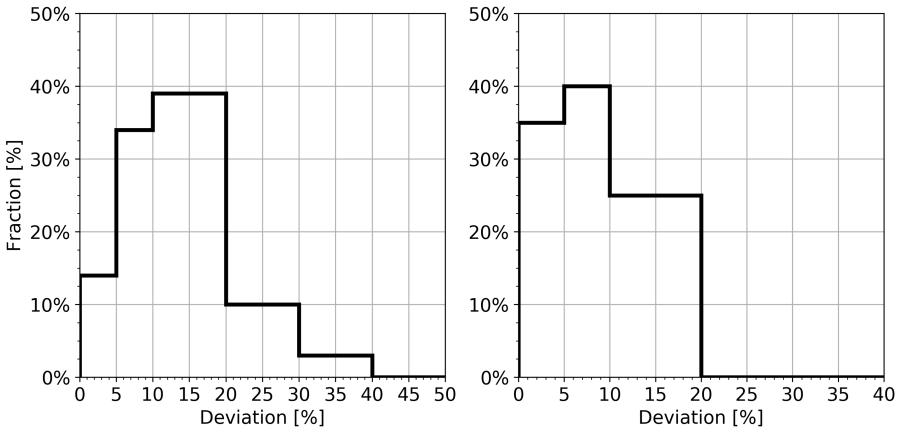

Figure 5.23: *Flow evaluation of Turbines 1 (right) and 2 (left) for y component of the velocity vector based on Criterion 2 (C2) of the design guideline (Section 2.9).*

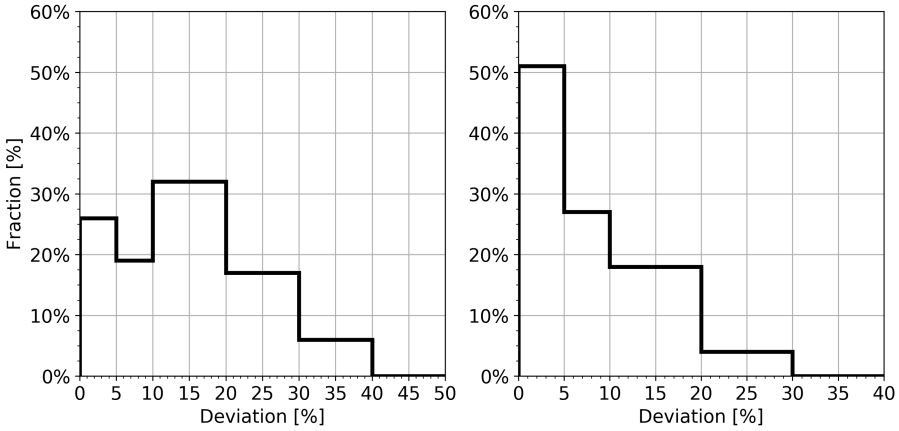

Figure 5.24: *Flow evaluation of Turbines 1 (right) and 2 (left) for z component of the velocity vector based on Criterion 2 (C2) of the design guideline (Section 2.9).*

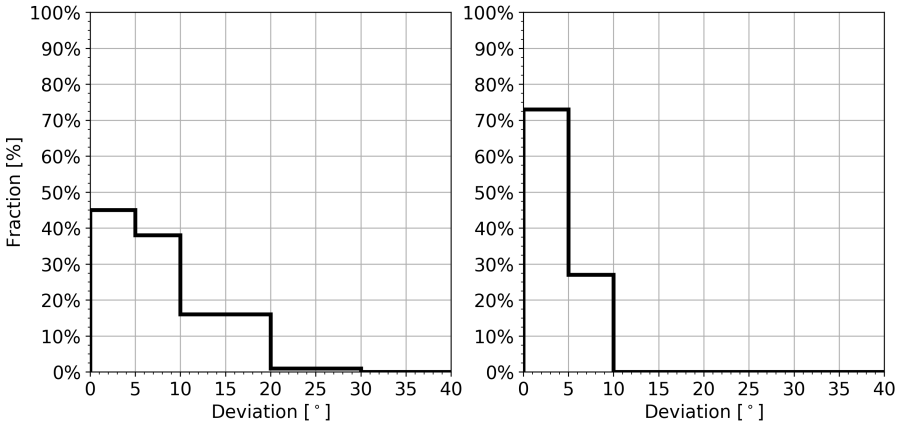

Figure 5.25: *Flow evaluation of Turbines 1 (right) and 2 (left) for y component of the velocity vector based on Criterion 4 (C4) of the design guideline (Section 2.9).*

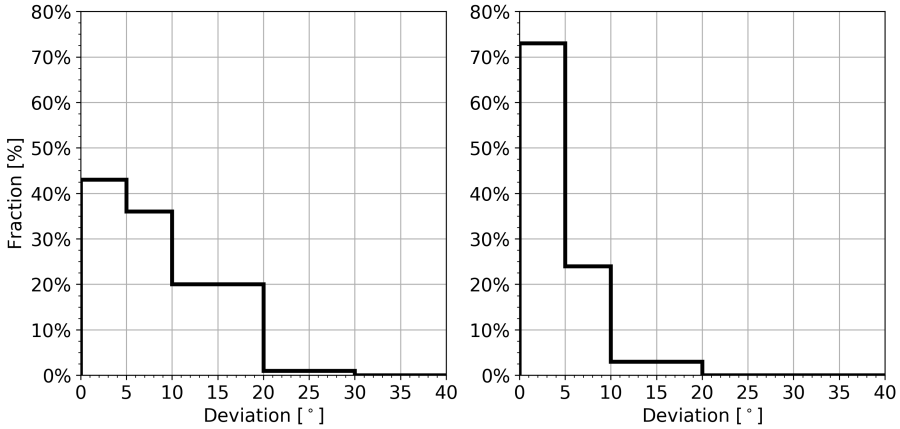

Figure 5.26: *Flow evaluation of Turbines 1 (right) and 2 (left) for z component of the velocity vector based on Criterion 4 (C4) of the design guideline (Section 2.9).*

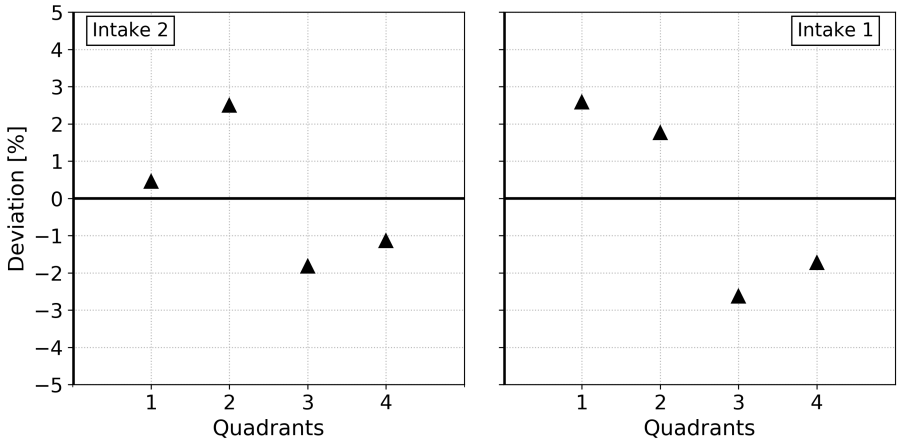

Figure 5.27: *Flow evaluation of Turbines 1 (right) and 2 (left) based on Criterion 3 (C3) of the design guideline (Section 2.9).*

6 RANS PARAMETER STUDY

In this Chapter, a series of parameter studies are carried out using RANS approach. The main objective of this chapter is to identify important parameters in predicting the flow when RANS is employed. The effect of different parameters are evaluated with respect to the flow inside the intakes. The investigation starts off by a grid convergence study. This follows by a series of studies where the scale and roughness effects are determined. Moreover, the effect of the inlet location is investigated. In addition, three RANS turbulence models are employed to study the role of turbulence modelling in predicting the flow. The results are also compared to the experimental results. This chapter is concluded by a study on the simplified model followed by a proposal for a suitable evaluation section.

6.1 Geometry

In numerical modelling, the first step is the spatial discretization of the domain. Prior to this step, the bounding surfaces of the domain must be defined. In this process, it is important to simplify the model. This must be done for two reasons; first to omit unnecessary details that does not have significant effect on the flow, hence save time. Furthermore, the second reason and most importantly is to generate high quality computational grids. A geometry with spikes and sharp angels can in worst case leads to very low quality elements which subsequently leads to inaccuracy and convergence difficulties.

The geometry of the upstream portion of the HPP is generated from the runner of the turbines to the trapezoidal approach channel. The geometry is created in a way that it represents, as much as possible, the physical model dimensions with high precisions. The process consists of: first generating all necessary 3D lines in AutoCAD. Then, in the second step, these lines are imported to ANSYS DesignModeler for generating 3D surfaces from the imported lines to obtain a watertight 3D geometry. These surfaces are grouped into four patches, `inlet`, `outlet`, `walls` and `rigidLid`, which later can be used to assign boundary conditions. The three-dimensional geometry of the upstream part of the Gratkorn HPP and numerical patch names are illustrated in Figure 6.1. In the final step, these surfaces are imported to ANSYS ICEM for grid generation.

6.2 Grid generation

After creating the geometry of the models, the domain must be subdivided into finite number of non-overlapping control volumes. As described in Section 3.3, integration over each cell is necessary to discretize and transform the partial differential equations into algebraic equations. Grid generation for numerical models is a challenging and time consuming step in analysis process. Last few decades, considerable amount of efforts have been devoted to facilitate mesh generation process along with significant numbers of

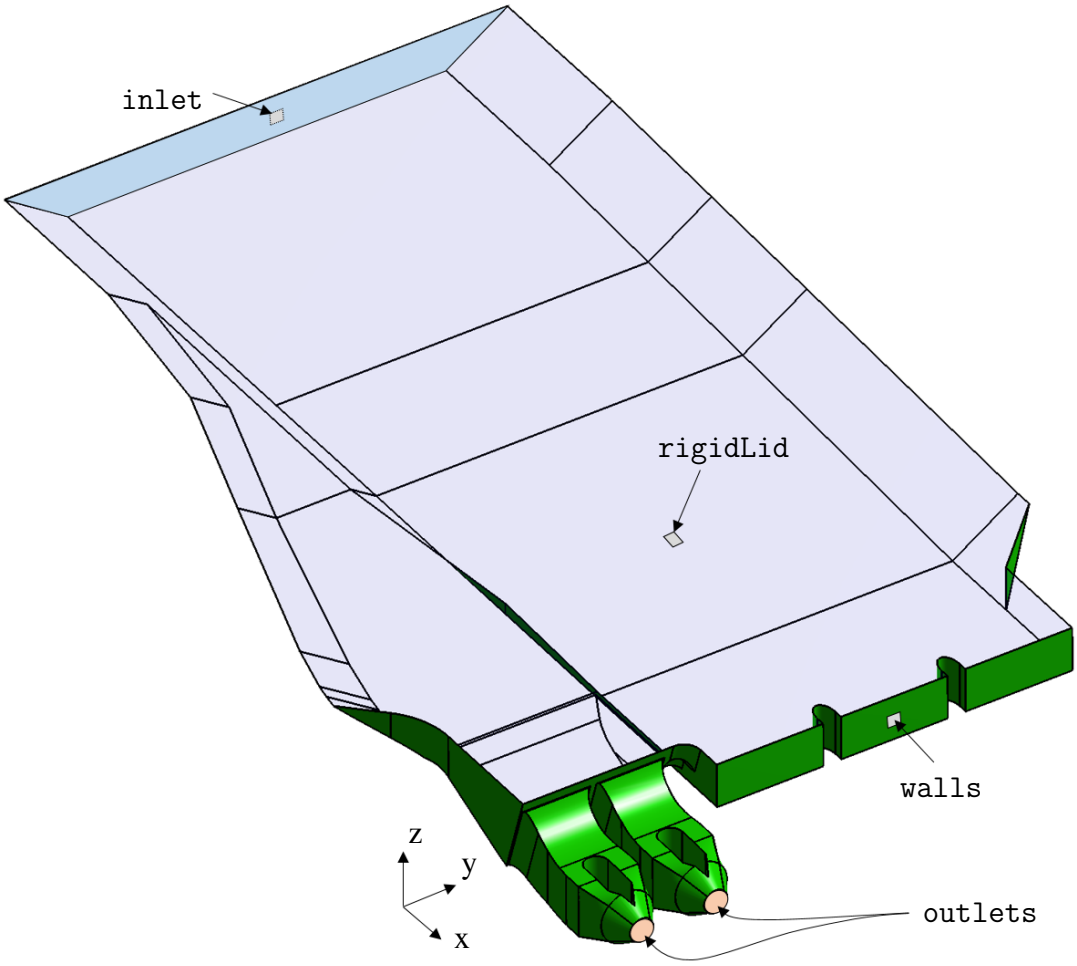

Figure 6.1: *Three-dimensional geometry of the computational domain and names of the boundary surfaces.*

studies on this topic. A "good" quality mesh is not only crucial for convergence of CFD simulations but also it is very important for obtaining accurate results.

There are several open-source and commercial codes available to generate mesh for CFD calculations depends on the solver being used. Among available open-source codes, `OpenFOAM` provides two mesh generation utilities, `blockMesh` and `snappyHexMesh`. Generating mesh with `blockMesh` for simple geometries is a straightforward procedure. However, for complex geometries, mesh generation with this utility can be a cumbersome procedure, instead, `OpenFOAM` provides another mesh generation utility `snappyHexMesh` for complex geometries. The `snappyHexMesh` utility generates three-dimensional grids from a geometry in Stereolithography (STL) file format using hexahedral and split-hexahedral. The mesh approximately represents the geometrical surfaces by iteratively refining a base mesh and snapping the resulting split-hexahedral mesh to the surfaces. One of the advantages of `snappyHexMesh` is that the mesh created with this tool complies with the mesh requirements of `OpenFOAM`. However, in this case, `snappyHexMesh` performed poorly, especially for generating inflation layers near the walls. Near the walls and at the corners, the generated layers tends to collapse. Furthermore, in several places the grid quality found out to be poor and did not follow the complex surfaces of the domain.

Finally, it is decided to generate the grid using ANSYS ICEM software. The grid generation adopted the blocking strategy where the domain divides into blocks similar to `blockMesh` utility of `OpenFOAM` with a powerful graphical user interface (GUI). Although this technique is time consuming for a complex geometry, it provides full control over the entire grid generation procedure. This technique is not only found to produce high quality elements, it also reduces the number of elements in comparison with other grid generation strategies. The coarse computational grid is shown in Figure 6.2 with global element size of 1 m in prototype scale or 2.5 cm in physical model scale using all high quality hexahedra elements. This base mesh is then used in the studies in this chapter and for Eddy-resolving simulation in Chapter 7. In each corresponding sections, the number of elements and the grid sizes are described separately.

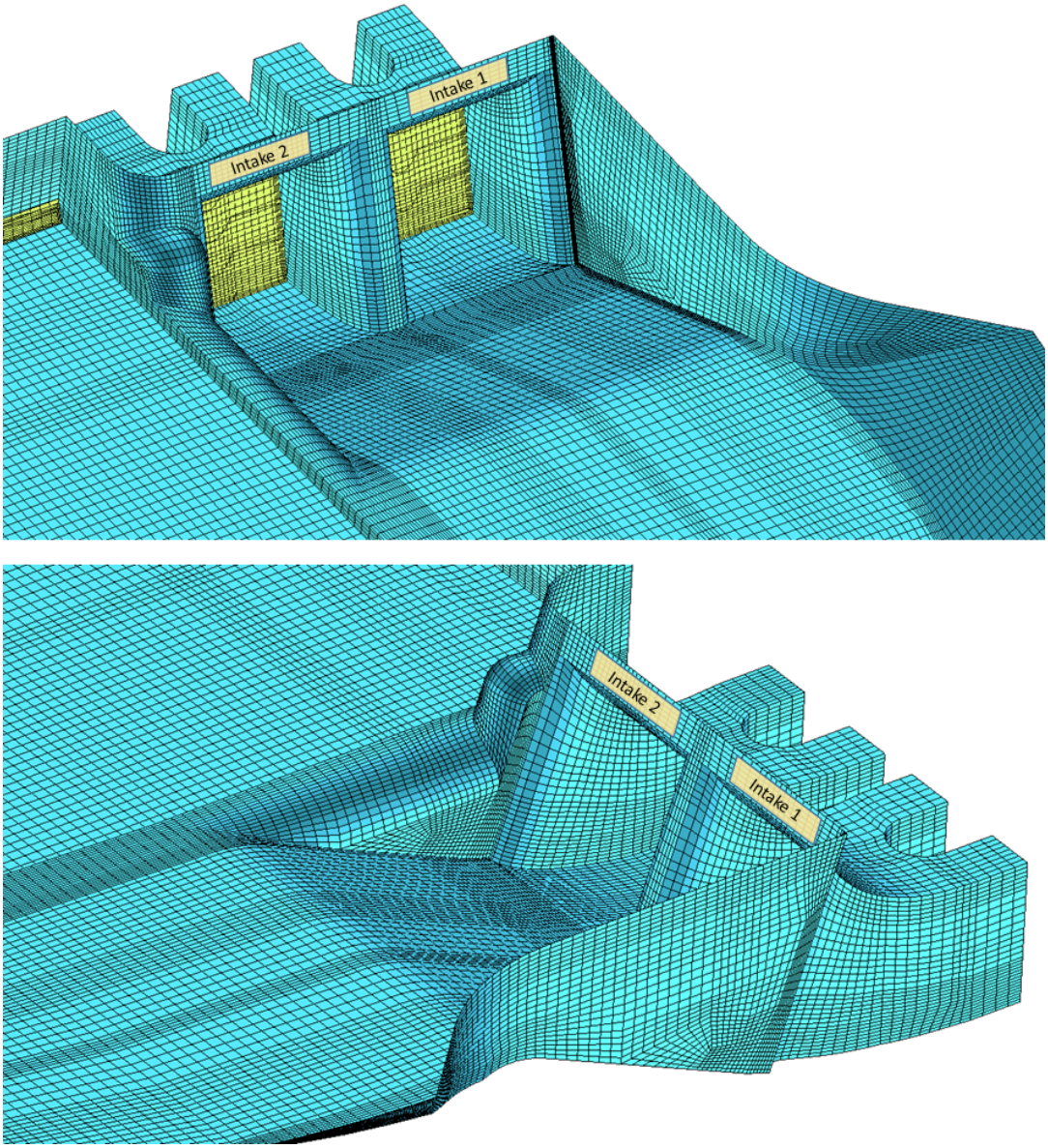

Figure 6.2: *Three-Dimensional view of the coarse computational grid.*

6.3 Boundary conditions

In order to solve the discretized equations defining boundary conditions is necessary. In `OpenFOAM` the boundary conditions are defined at the patches (named surfaces) of the domain. Depends on the solver and turbulence models being used, they are defined in `0` folder in separate files for each parameter such as `U` for velocity, `p` for pressure and depends on turbulence model being used, turbulence parameters . Additionally, the initial values (initial conditions) are prescribed in this folder.

The names of the patches are defined for the geometry surfaces and subsequently for the descritised domain. The locations of each patch are shown in Figure 6.1. In general, the most robust boundary conditions for such cases, where there is one inlet and one outlet, are fixed velocity and turbulence values at the inlet and fixed pressure at the outlets. Adopting this approach, following boundary conditions are defined in each correspondent files for each patches:

- `outlets`: The pressure is set to zero for these patches. Additionally, the boundary condition for velocity, `U`, is set to `inletOutlet`. This BC type is applying a `zeroGradient` condition in case of an outflow, however, when inflow (reverse flow) occurs, the value of the inflow can be set to a certain value. In this study, the inflow value for the outlet is set to zero, hence no inflow is permitted. Finally, the BC for all other parameters are set to `zeroGradient` for the outlet of the model.
- `Walls`: The velocity at the wall is set to zero by prescribing `noslip` condition. Furthermore, the BC type for pressure, `p`, is set to `zeroGradient`. Finally, depends on the turbulence model, appropriate wall functions are assigned for the turbulence parameters.
- `rigidLid`: Assuming that the variation of the water level in the domain is negligible, rigid-lid condition (`Symmetry`) is used for this patch. This condition introduces a small error in the continuity equation, however, this error considered negligible if the water surface deviations are smaller than 10% of the local water depth (Rodi et al., 2013).
- `inlet`: In this patch, as mentioned earlier, the values for velocity and turbulence parameters (e.g. turbulent kinetic energy, dissipation rate) must be prescribed. For accuracy, these values are calculated using precursor simulations using periodic channel. Then these values are mapped to the inlet of the model.

The boundary conditions for SKE turbulence model are summarised in Table 6.1. Similar boundary conditions are also used for other turbulence models (e.g. Spalart-Allmaras and Shear Stress Transport models).

6.4 Grid convergence study

The aim of the grid convergence study is to determine the optimum grid size and, perhaps more importantly, to estimate the descritisation error for the simulation. Alongside incomplete iterative convergence and the computer round-off error, the spatial and temporal

	U	p	k	epsilon	nut
inlet	Mapped	zeroGradient	Mapped	Mapped	calculated
outlets	inletOutlet	fixedValue	zeroGradient	zeroGradient	calculated
walls	noSlip	zeroGradient	kqRWallFunction	epsilonWallFunction	nutkRoughWallFunction
rigidLid	slip	slip	slip	slip	slip

Table 6.1: *Boundary conditions of the numerical model for k-epsilon turbulence model*

discretisation are the main source of the numerical errors in CFD computations. Several methods available for evaluating the spatial and temporal convergence of CFD simulations. These methods are presented in the book by Roache (1998) and they are based on Richardson's Extrapolation (RE). Since its first application by Richardson (1911), this method has been studied by several authors. Although this method has well known limitations, it is currently the most reliable method available for the prediction of the numerical uncertainties (Celik et al., 2008).

Richardson extrapolation is a technique for obtaining a higher-order approximation of the continuum value (at zero grid spacing) from a series of lower-order discrete values. Based on the theory of generalized Richardson extrapolation, Roache (1998) proposed a methodology for the uniform reporting of grid refinement studies. In order to achieve this and perhaps provide an error band on the grid convergence of the solution, the method uses a Grid Convergence Index or GCI in short. In order to accurately approximate the order of convergence and to check that the solutions are within the asymptotic range of convergence, the GCI must be computed using three levels of grid.

Model	Turbulence model	Roughness (k_s)	Scale	Element size [m]	No. of elements
PT01	SKE	0	1/1	0.8	4K
PT02				0.4	1.8M
PT03				0.2	14M

Table 6.2: *Boundary conditions of the numerical model for k-epsilon turbulence model*

Several authors including Roache (1998), Celik et al. (2008) and Slater (2006) presented a step by step procedures to compute and report GCI. These procedures are very similar in principal and they consist of five main steps as follows:

Step 1. The first step in evaluation of the grid convergence is the determination of a representative grid size h. This can be done for three-dimensional models using:

$$h = \left[\frac{1}{N}\sum_{i=1}^{N}(\Delta V_i)\right]^{1/3} \tag{6.1}$$

where ΔV_i is the volume and N is the total number of cells. Celik et al. (2008) recommends using Equation 6.1 for integral quantities and using the local cell size for field variables, e.g., velocity and pressure.

Step 2. The next step is to select three significantly different sets of grids and performing the simulations to determine the values of key variables at the desired locations. It is recommended by Celik et al. (2008) that the grid refinement ratio $r = h_{coarse}/h_{fine}$ must be higher than 1.3 and Slater (2006) advises using minimum value of 1.1 to allow the discreization error to be differentiated from other error sources like iterative convergence or computer round-off errors. In this study, following Celik et al. (2008) recommendation, the local grid size at the intakes was used to determine the value of h for the evaluation of velocities. Three different sets of grids have been created with grid size of $h_1 = 20cm$, corresponds to the fine grid (F), $h_2 = 40cm$ represents the intermediate grid (M) and finally grid with $h_3 = 80cm$ was set to be the coarse grid (C). The model parameters are summarized in Table 6.2. Based on the chosen grid sizes, the grid refinement ratios, $r_{21} = h_2/h_1$ and $r_{32} = h_3/h_2$, are approximately 2.0 for three sets of grids.

Step 3. Let ϕ be a variable (velocity, pressure, etc...) for which the grid convergence study is being performed on, the apparent order p of the method can be calculated from the grid refinement ratios r_{21} and r_{32} using the expression

$$p = \frac{1}{ln(r_{21})}|ln|\varepsilon_{32}/\varepsilon_{21}| + q(p)| \tag{6.2a}$$

$$q(p) = ln\left(\frac{r_{21}^p - s}{r_{32}^p - s}\right) \tag{6.2b}$$

$$s = 1 \cdot sgn(\varepsilon_{32}/\varepsilon_{21}) \tag{6.2c}$$

where $\varepsilon_{32} = \phi_3 - \phi_2$ and $\varepsilon_{21} = \phi_2 - \phi_1$. Equation 6.2a can be easily solved using fixed-point iteration since Equation 6.2b returns zero. According to Karatekin (1997), the absolute value in Equation 6.2a is necessary to ensure extrapolation toward $h = 0$.

Step 4. Now the extrapolated value of ϕ can be calculated to estimate the continuum value. This can be done using expression

$$\phi_{ext}^{21} = (r_{21}^p\phi_1 - \phi_2)/(r_{21}^p - 1) \tag{6.3}$$

Similarly Equation 6.3 can be used to compute the extrapolated value of ϕ_{ext}^{32}.

Step 5. Finally, the approximate relative error will be calculated from

$$e_a^{21} = |(\phi_1 - \phi_2)/\phi_1| \tag{6.4}$$

and fine grid convergence index can be computed using expression

$$GCI_{fine}^{21} = \frac{F_s e_a^{21}}{r_{21}^p - 1} \tag{6.5}$$

where F_s is a factor of safety. Slater (2006) recommends using $F_s = 3.0$ for comparisons of two grids and $F_s = 1.25$ for comparison over three or more grids. Since three sets of grids have been defined and compared in this study, $F_s = 1.25$ has been adopted.

In principal, the method which was described above are valid only in a monotonic convergence case. In case of oscillatory convergence or noisy grid convergence it has been

shown by Celik et al. (2005) that the Approximate Error Spline method (AES) method performs overwhelmingly well compared to other techniques and it provides a better estimation of the grid convergence error than Richardson extrapolation technique. Therefore, here, both methods are utilized to compute GCIs, estimate the errors and true values for the three models (Table 6.2) to evaluate their application for this particular case.

The grid convergence study is carried out on five points for each intake, one for each corner (points B2, B9, I2 and I9 in Figure 5.8) and one approximately in the middle of the section (point F6 in Figure 5.8). the results are summurized in Table 6.3 and Table 6.4 for intake 1 and 2 respectively. In general, almost all computed GCIs are below 5% especially for intake 1. The highest GCI values are located at points B2 and I2 in both intakes. However, grid refinements tend to reduce these values significantly especially in intake 1. On the other hand, some points in intake 2 shows irregular convergence, for example, GCI values at point B2 and B9 in intake 2 are increased after refinement.

It is evident from Table 6.3 and 6.4 that AES method performs better in two aspects; first, in computing true values and second, in estimating the GCI values with exception of point B2 in intake 2. Regarding the estimated true values, at point B9 in intake 1 for example, it seems reasonable to assume that the true value would fall under the computed velocity by the fine grid since the trend is descending. However, estimated value by RE method is the opposite. Similarly, in two points in each intake, the computed GCI for fine grid is higher than the one from the coarse grid when RE method is used. A closer look at the values revealed that, particularly in these points, the convergence is oscillatory and the assumption that the solution is within the asymptotic range of convergence is not valid. On the other hand, AES in almost all points performed well except for point B2 in intake 2.

In order to have a general picture of the effect of the grid refinements, the discharge distributions are computed for each quadrants. These values are summarized in Figure 6.3 for both intakes. It is shown that the discharge distribution is not affected significantly by the grid refinements. The maximum differences can be found in intake 1, quadrant 2 with the difference between the coarse and fine grid is well below 1%.

In conclusion, the GCI values are low even for the case with coarse grid. among two utilized methods to compute GCI values, AES performed better than the other method. Moreover, it is found that the grid refinements does not affect the overall discharge distribution. This indicates that for initial analysis, a coarse grid with element size of 80 cm in prototype scale can be used. In the following sections, the model with intermediate grid size is used for other investigations.

Points	Grid	Velocity $[m/s]$	Estimated true value $[m/s]$		Grid Convergence Index $[\%]$		
			AES	RE	AES	RE	
B2	C	1.78	1.74	1.71	3.01	3.68	—
	M	1.76			2.17		4.61
	F	1.75			1.06	—	
I2	C	1.29	1.32	1.32	2.77	0.58	—
	M	1.32			0.49		0.12
	F	1.32			0.02	—	
B9	C	1.71	1.69	1.72	1.42	0.64	—
	M	1.71			1.90		1.12
	F	1.70			1.07	—	
I9	C	1.25	1.26	1.26	1.01	0.19	—
	M	1.26			0.79		0.019
	F	1.26			0.61	—	
F6	C	1.38	1.39	1.39	0.88	0.36	—
	M	1.39			0.34		0.14
	F	1.39			0.12	—	

Table 6.3: *Turbine 1 Grid convergence Indices*

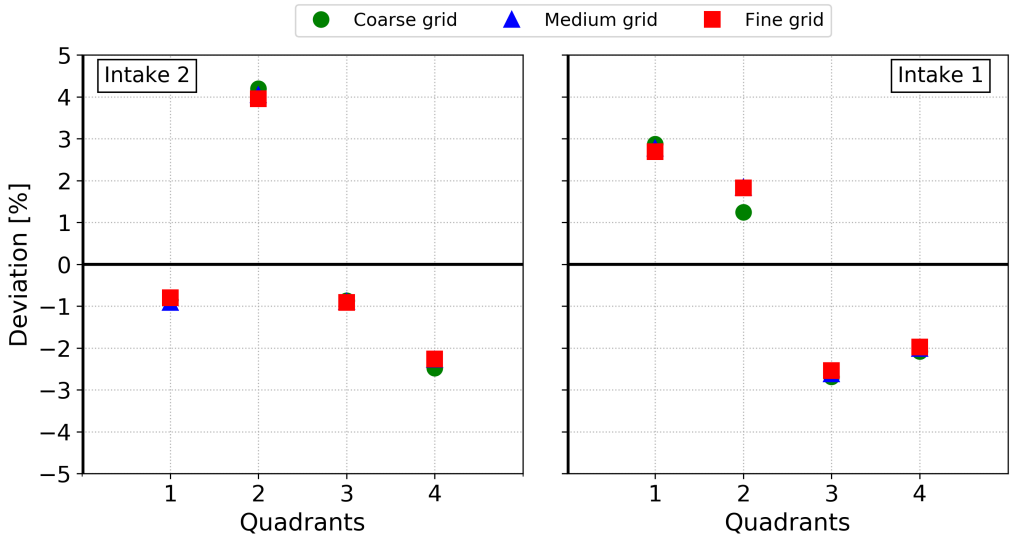

Figure 6.3: *Flow evaluation of Turbine 1 (right) and turbine 2 (left) based on Criterion 3 (C3) of the design guideline (Section 2.9).*

Points	Grid	Velocity $[m/s]$	Estimated true value $[m/s]$		Grid Convergence Index $[\%]$		
			AES	RE	AES	RE	
B2	C	1.26	1.26	1.29	0.03	3.20	—
	M	1.32			5.88		1.21
	F	1.30			3.79	—	
I2	C	1.26	1.30	1.32	4.00	2.48	—
	M	1.27			2.89		3.48
	F	1.29			1.43	—	
B9	C	1.74	1.74	1.74	0.18	0.88	—
	M	1.76			1.39		0.37
	F	1.75			0.88	—	
I9	C	1.24	1.27	1.26	2.30	0.28	—
	M	1.25			2.05		0.06
	F	1.26			1.07	—	
F6	C	1.46	1.42	1.41	2.97	2.08	
	M	1.45			2.21		2.90
	F	1.43			1.09		

Table 6.4: *Turbine 2 Grid convergence Indices*

6.5 Scale and roughness effects

In hydraulic engineering, the physical model tests play an important role in studying hydrodynamics and sediment transport processes. Often, a physical model in the laboratory is a scaled down representation of a large prototype using similarity laws. Considerable differences can be observe between the up-scaled results from the model test and the measured values from the prototype due to scale effects, hence, choosing an appropriate value for the scaling value is highly important. Recently, Heller (2011) published a paper, extending and updating Heller (2007), reviewing extensively scale effects concerning physical hydraulic models.

The estimation of how scale effects, qualitatively and quantitatively, affect the model's results and whether or not they can be neglected is challenging. Numerical simulations on the other hand may be able to consider these effects. Furthermore, it is important to know the effect of the roughness on the models in both physical and prototype scale. In this section, scale as well as roughness effects are investigated via numerical models. In these models, all numerical parameters kept constant except the scale of the geometry, discharge and wall roughness. It is assumed that the walls are from concrete and according to Huebsch et al. (2009), the equivalent sand grain roughness,k_s, for this material is between 0.3 to 3.0 mm. In the physical model where roughness is considered, Model S02, k_s value assumed to be 1 mm. In the prototype scale, however, higher values, 3.0 and 10.0 mm, are adopted for the wall roughness. The relevant numerical and geometrical parameters of the models are summarized in Table 6.5. Furthermore, the presentation and discussion of the results are limited to the velocity distribution in the intake structure.

In general, the difference between the results are negligible. In order to investigate the effect of the scaling on the results, Model S01 and PT01 are compared. Flow velocities in x, y and z direction is plotted in Figures 6.5, 6.6 and 6.7. It is shown that the velocity distribution inside the intakes are almost identical between the scaled model and the prototype scale model with smooth walls. Similar conclusion is made when the roughness of the walls are considered in the scaled models S01 and S02. This is partly due to low velocity and Reynolds numbers of the models. On the other hand, in the prototype scale, the roughness has slightly more effects on the distribution of the velocity at the investigated section. The highest difference is near the walls due to the effect of the roughness and the boundary layer. The roughness, reduce near wall velocity and subsequently the velocity in the other areas are increased. In general, the highest difference between the two cases (PT01 and PT03) is approximately 2.0%. Also, the roughness increased wall shear stress values significantly in the areas where the velocity is relatively high. It is worth noting that the roughness value which is used in case PT03, is relatively high for concrete material and it is likely that this value is smaller in reality (between 0.5 to 3.0 mm). Figure 6.4 illustrates the computed discharge distribution for both intakes. It is shown that the roughness does not affect the discharge distributions in the prototype model and, in general, the changes are all below 0.5% and negligible.

Model	Turbulence model	Roughness (k_s)	Scale
S01	SKE	0	1/40
S02		1.0 mm	
PT02		0	1/1
PT04		3.0 mm	
PT05		10.0 mm	

Table 6.5: *Boundary conditions of the numerical model for k-epsilon turbulence model*

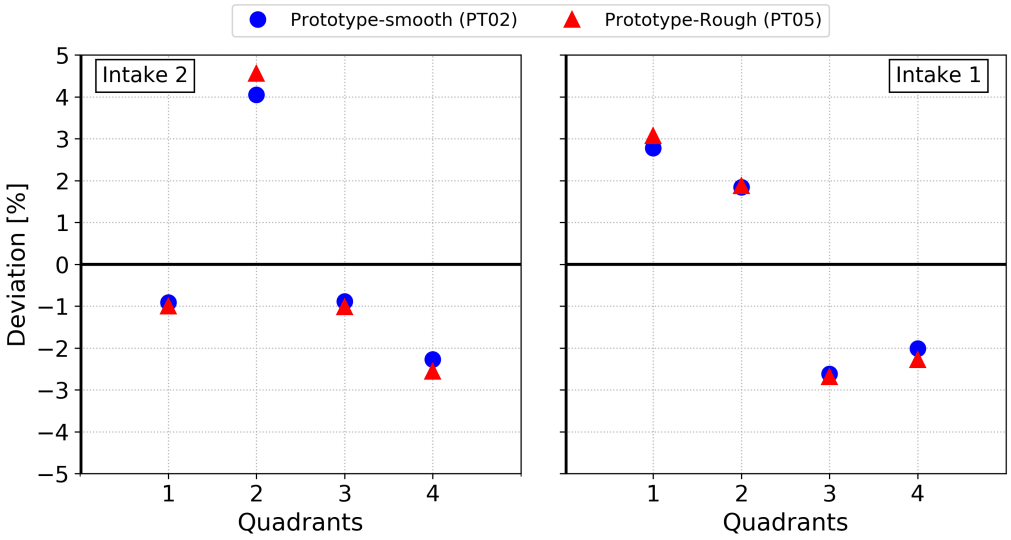

Figure 6.4: *Flow evaluation of Turbine 1 (right) and turbine 2 (left) based on Criterion 3 (C3) of the design guideline (Section 2.9).*

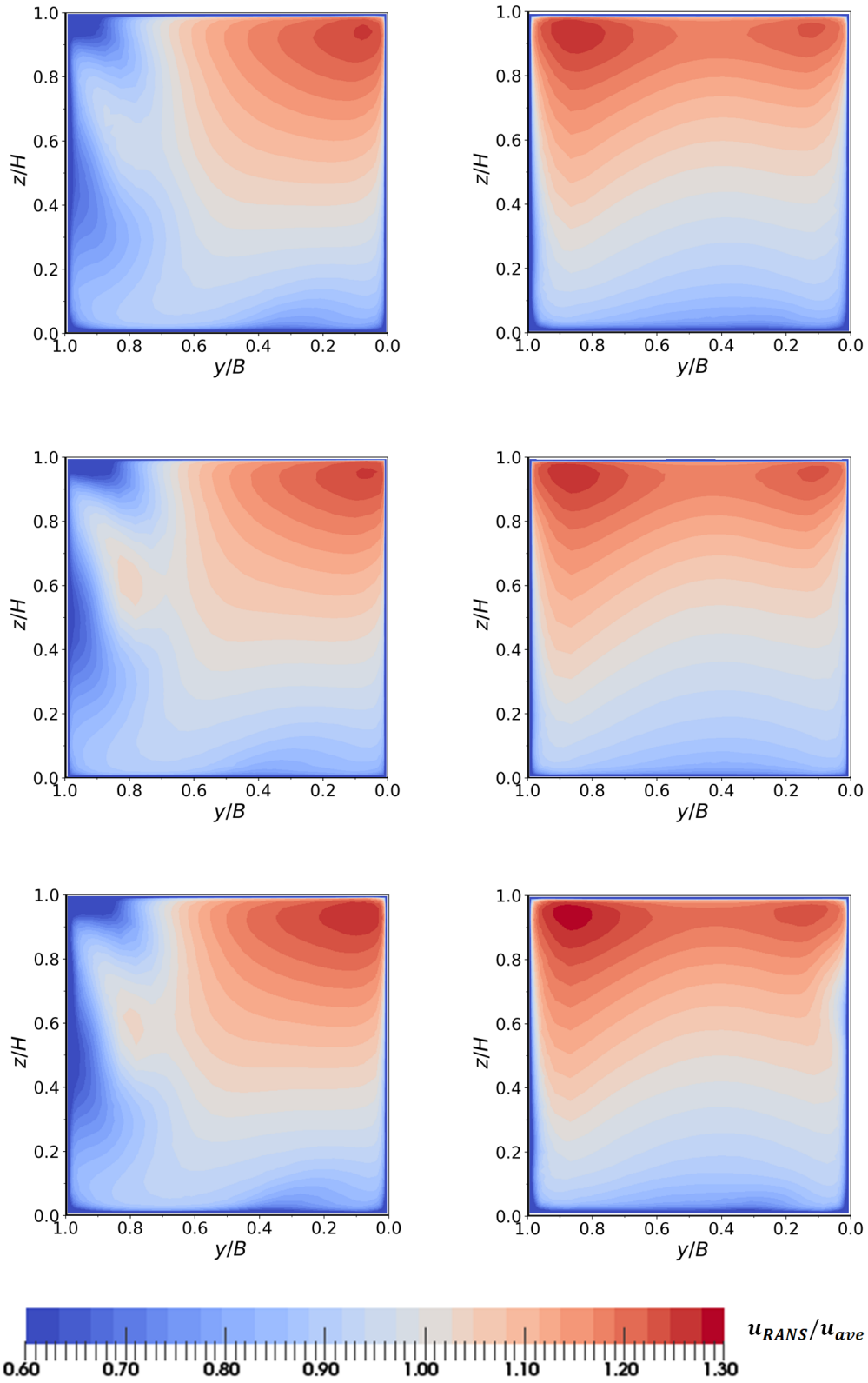

Figure 6.5: *Contour plots of velocity in out-of-plane or x-direction illustrating scale and roughness effects (Top: Model S01, middle: Model PT02 and bottom: Model PT05).*

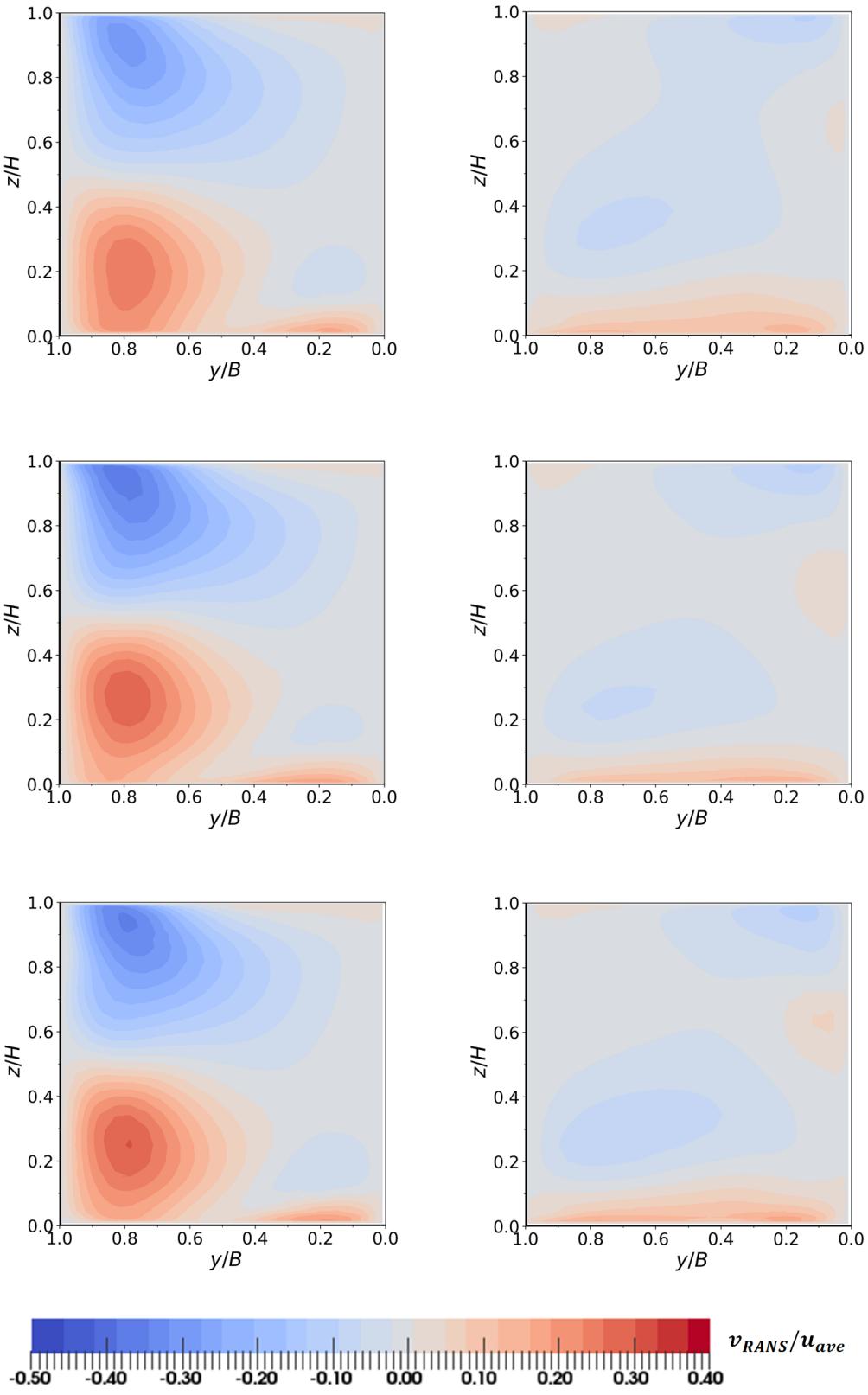

Figure 6.6: *Contour plots of velocity in y-direction illustrating scale and roughness effects (Top: Model S01, middle: Model PT02 and bottom: Model PT05).*

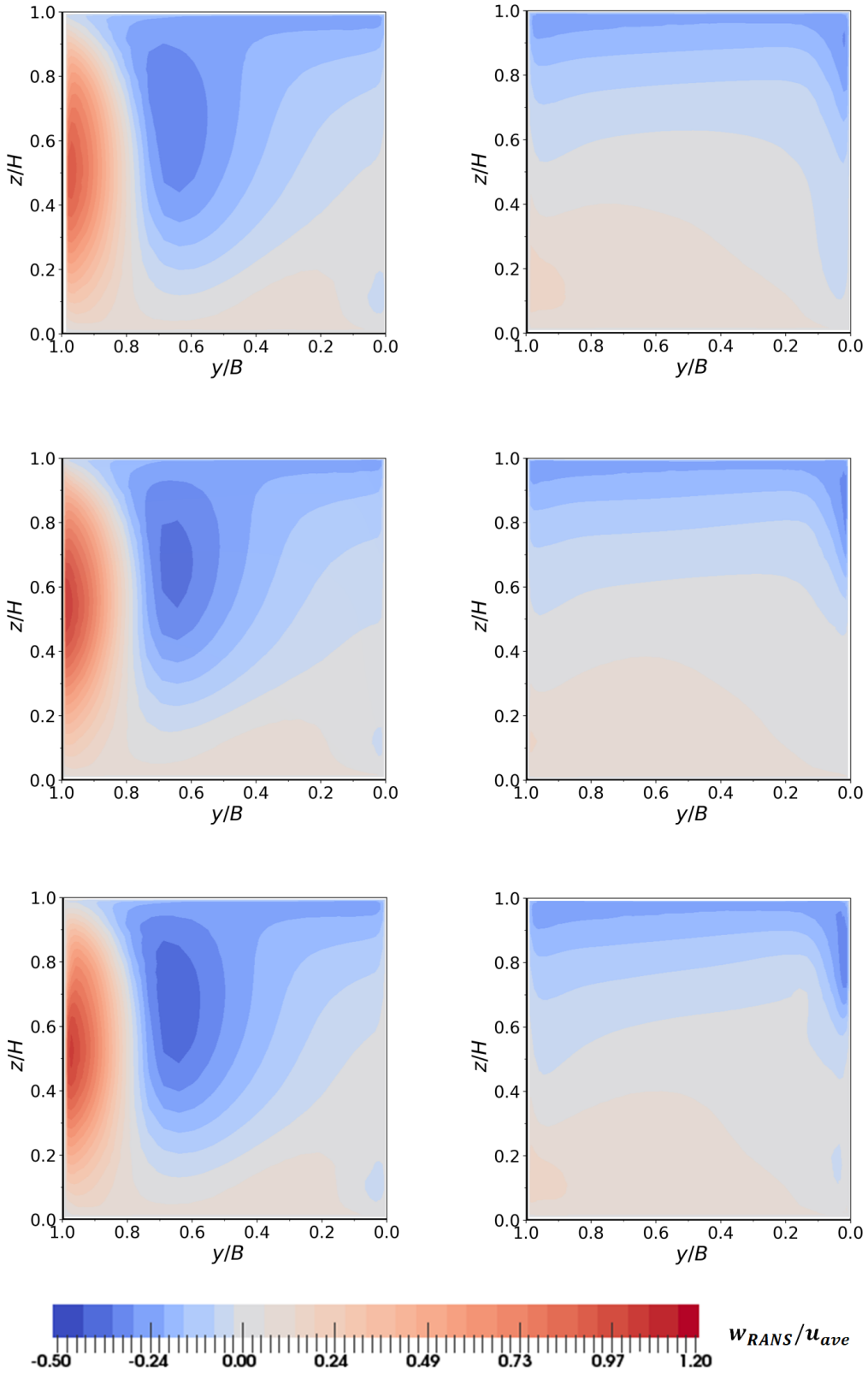

Figure 6.7: *Contour plots of velocity in z-direction illustrating scale and roughness effects (Top: Model S01, middle: Model PT02 and bottom: Model PT05).*

6.6 Inflow condition

In a single phase internal flows, it is common that the boundary conditions are velocity inlet and pressure outlet. In this set up, the pressure at the outlet is defined (usually 0 in case of one outlet) and velocity along with turbulence parameters are defined for the inlet. Usually the values are defined as constant using empirical formulas or they are obtained via precursor analysis. The velocities can be computed for the entire section with assumption that it is constant over entire section. For turbulence values e.g. kinetic energy, (k), and dissipation rate, (ε), these values can be computed using expressions:

$$k = \frac{3}{2}(u_{ave}I)^2 \tag{6.6}$$

$$\varepsilon = C_{\mu}^{3/4}\frac{k^{3/2}}{l} \tag{6.7}$$

where u_{ave} is the average velocity at the inlet section, l is the length scale (e.g. hydraulic diameter), C_{μ} is an empirical constant and I is the turbulence intensities and it can be approximated by:

$$I = 0.16(Re)^{-1/8} \tag{6.8}$$

Using expression 6.8, the turbulence intensities are 5% and 2.5% for scaled (physical model) and prototype respectively. Similar formulas are also available to compute turbulence parameters such as Modified Turbulent Viscosity for Spalart-Allmaras model or Specific Dissipation Rate, ω, for SST model (Fluent, 2018).

It is deemed sufficient to impose constant values according to the expressions above at the inlet. This is due to the fact that prominent geometrical features are presents in the model and these features are creating instabilities and hence the results becomes less sensitive to the inlet boundary conditions. However, in order to increase accuracy of the simulations, the inlet values are computed using precursor simulations using periodic channels and the values are imposed on the inlet of the domain.

In order to investigate how the location of the inlet in the numerical models impact the results inside the intakes, three numerical models are compared. These models and their relevant parameters are summarized in Table 6.6. In Model PT07, the inlet placed immediately before the bay and in Model PT06 and PT02 the approach channel is extended upstream of the bay by eight and sixteen times the channel's water depth respectively. In all the simulations SKE turbulence model is used. Figure 6.8 shows the locations of the inlets for these three models.

The discussion of the results starts off by comparing normalized velocities in x, y and z-directions for the control section. These are illustrated in Figures 6.9 to 6.11. It is shown that the velocity distribution in all directions are very similar with only small differences

are noticeable in the zones where maximum and minimum velocities are located. The same conclusion can be made when the discharge distributions are computed and plotted in Figure 6.12. Finally, Figure 6.13 shows the streamwise distribution of the velocity normalized by the bulk velocity at the beginning of the bay. The velocity distribution corresponds to the shortest model, Model PT07, is showing a developed channel flow since this was the inflow condition provided at that location (inlet). On the other hand, the velocities immediately before the bay for the other models show that the high velocity zone which is located at the center of the channel in Model PT07 is dragged to the right banks. This indicates that the bay and the intake structure affecting the velocity distribution as far as the forebay zone.

In conclusion, as far as the velocity distribution inside the intakes is of concern, the inlet of the model can be placed at the beginning of the bay. This can reduce the size of the computational domain and consequently decrease the computational resources required to model this type of hydro power plant. Also it indicated that the geometrical features which are presents upstream of the intakes have strong influence on the flow. Furthermore, if the results beyond the intake is required, the approach channel must be included and extended at least to eight times the water depth in the channel. Finally, in all the simulations in this Chapter, the longest model with approach channel length equal to 16 times the water level is adopted for higher accuracy.

Model	Turbulence model	Roughness (k_s)	Scale	Inlet's location
PT02	SKE	0	1/1	16H
PT06				8H
PT07				0

Table 6.6: *Models used to determine sensitivity of the results to the inlet location.*

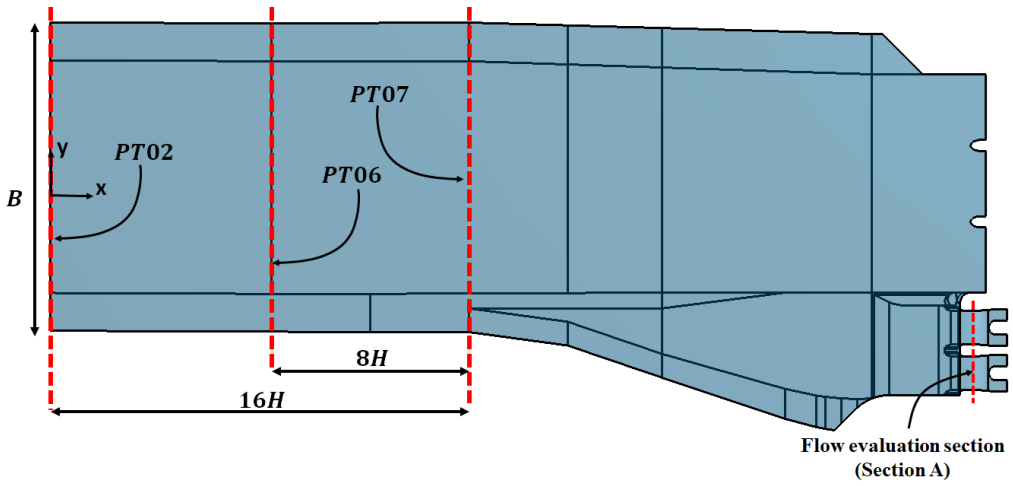

Figure 6.8: *Inlet Locations and their distances from the forebay based on the water depth (H) of the approach channel.*

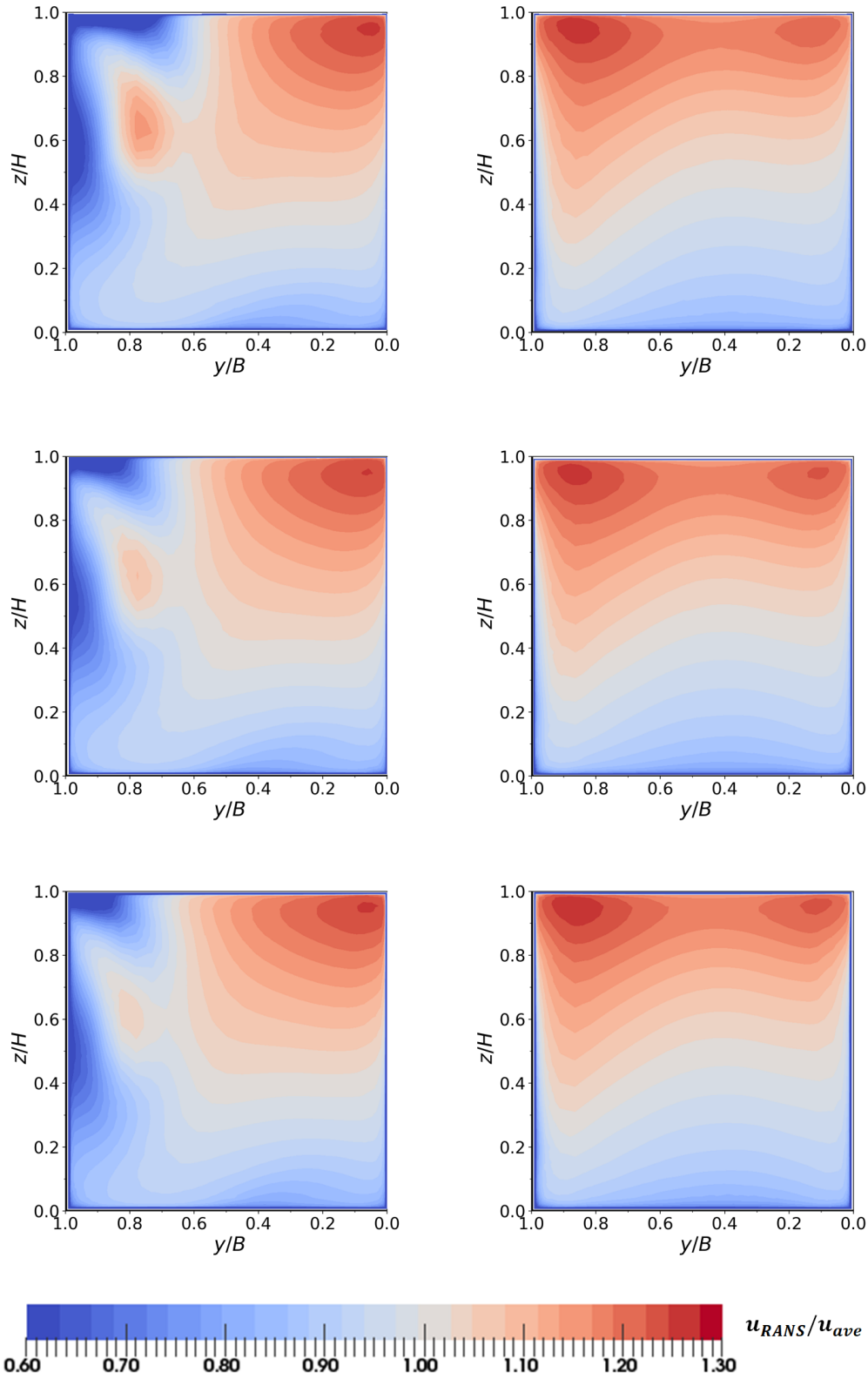

Figure 6.9: *Contour plots of velocity in out-of-plane or x-direction for different inlet locations (Top: Model PT07, middle: Model PT06 and bottom: Model PT02).*

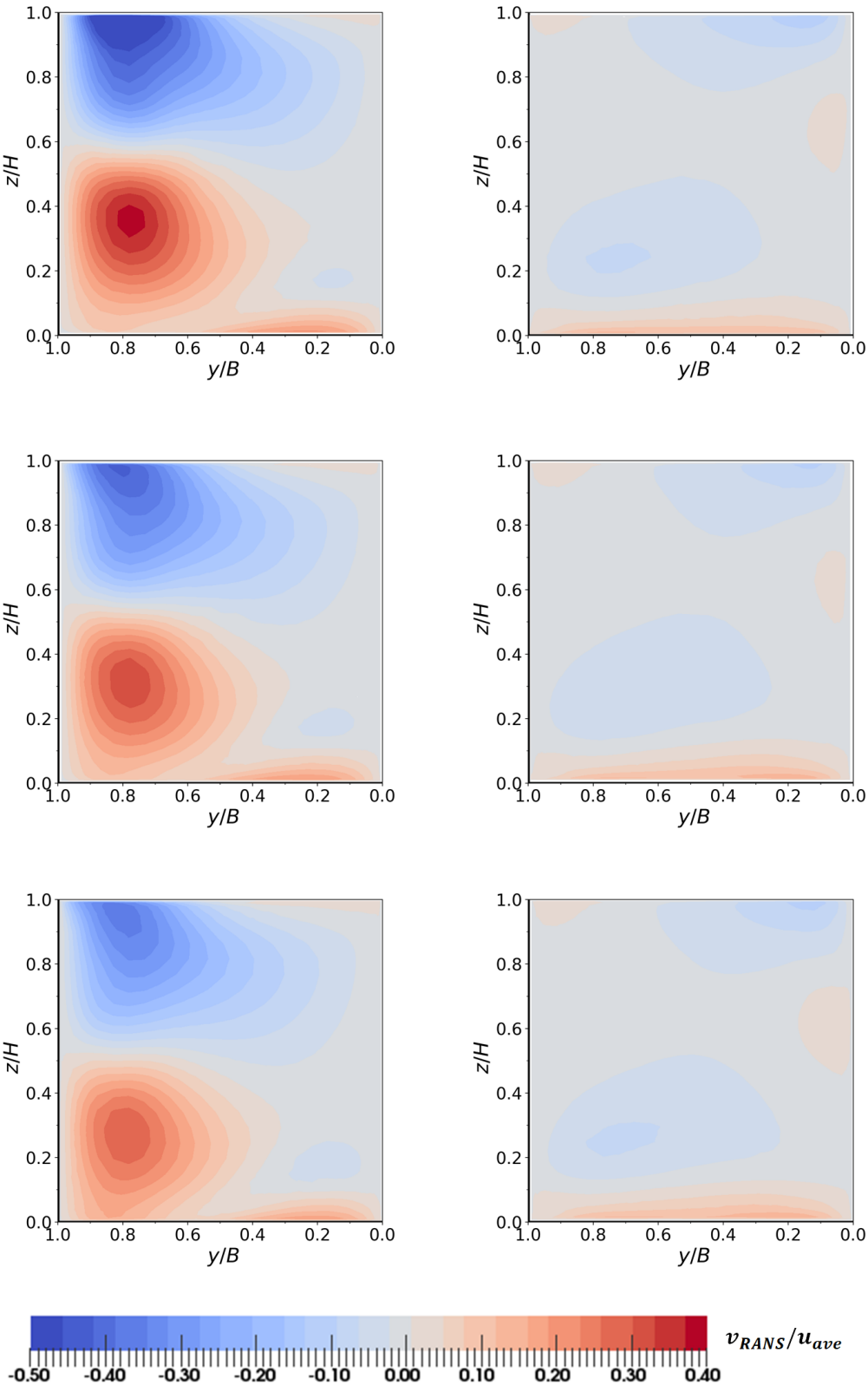

Figure 6.10: *Contour plots of velocity in y-direction for different inlet locations (Top: Model PT07, middle: Model PT06 and bottom: Model PT02).*

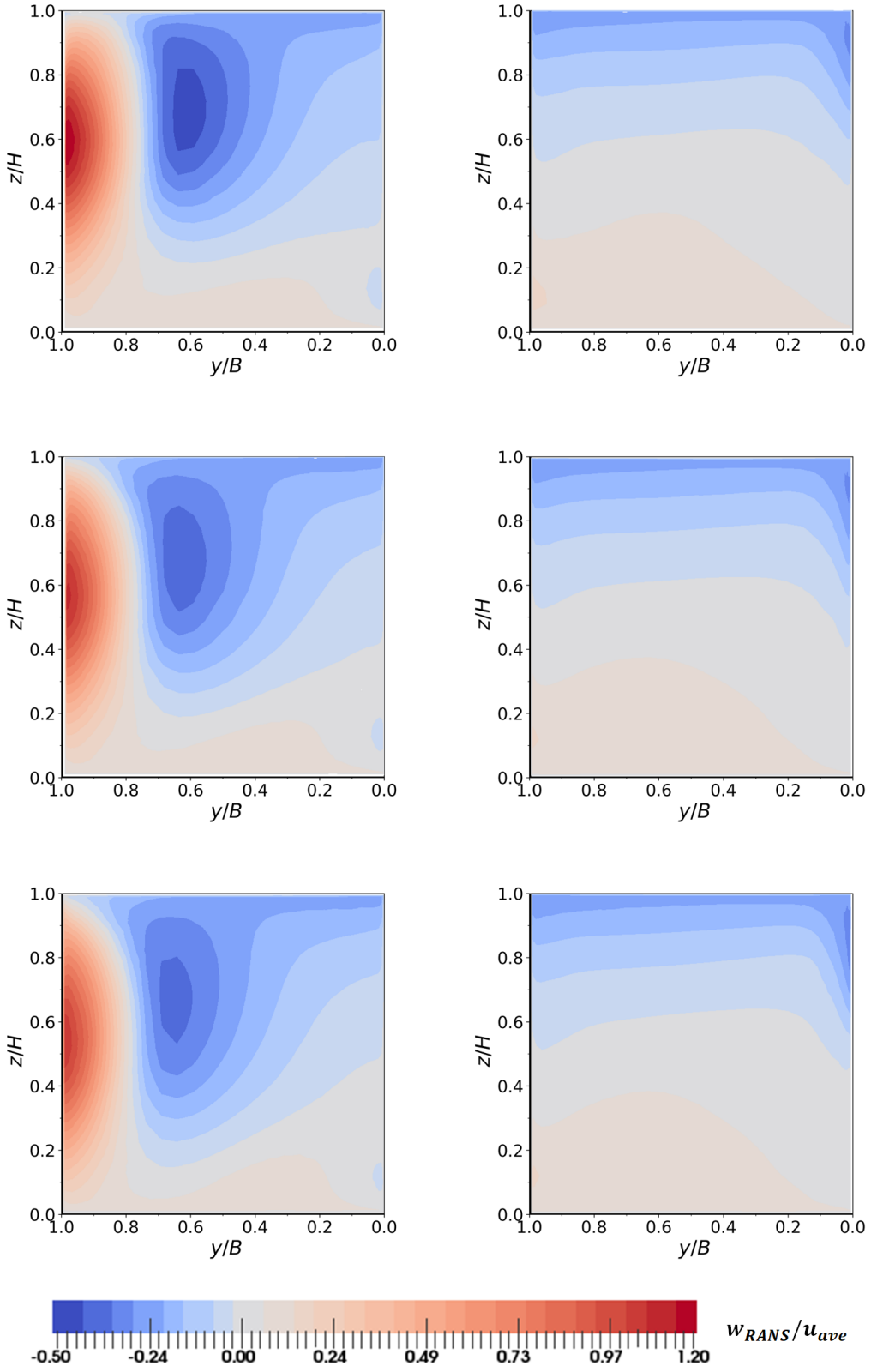

Figure 6.11: *Contour plots of velocity in z-direction for different inlet locations (Top: Model PT07, middle: Model PT06 and bottom: Model PT02).*

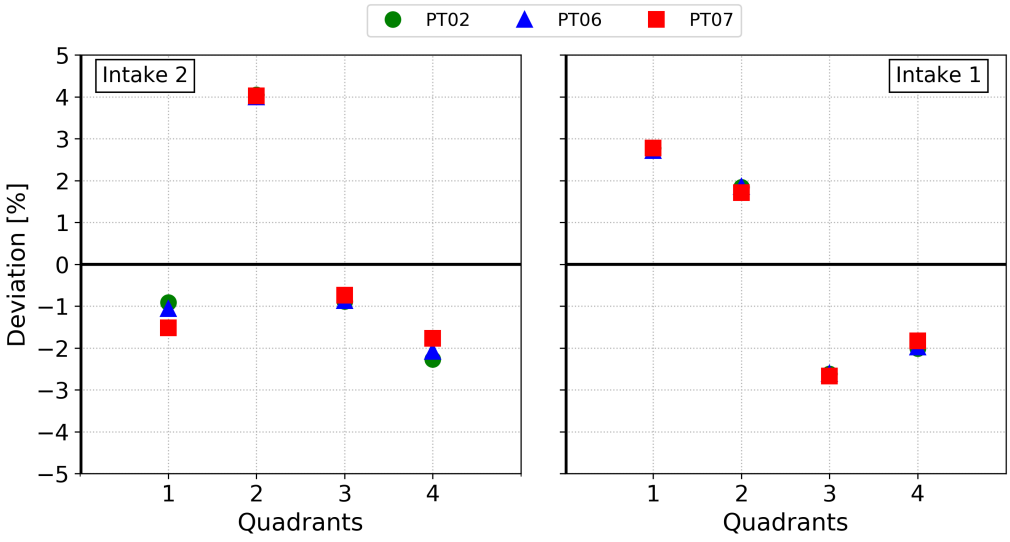

Figure 6.12: *Flow evaluation of Turbine 1 (right) and turbine 2 (left) based on Criterion 3 (C3) of the design guideline (Section 2.9).*

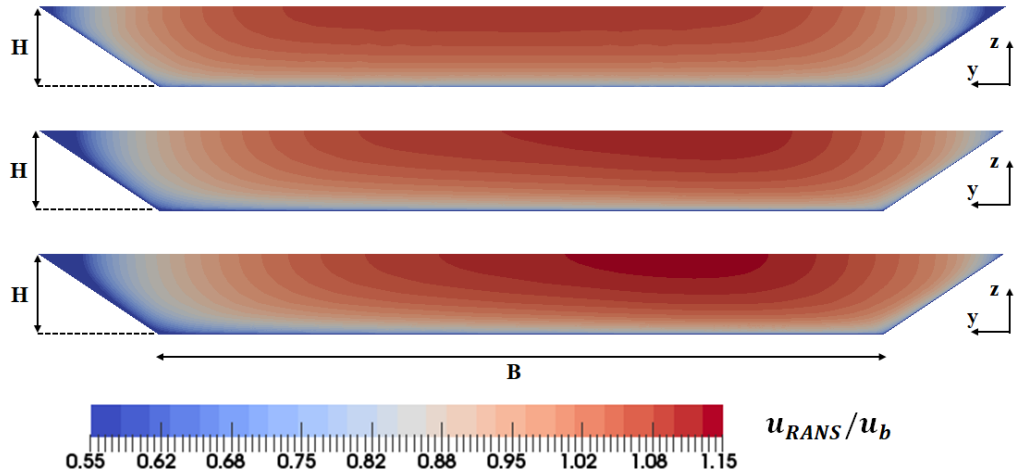

Figure 6.13: *Contour plots of the velocity in streamwise direction immediately before the bay (Top: Model PT07, middle: Model PT06 and bottom: Model PT02).*

6.7 RANS turbulence models

In previous sections, it is shown that as long as the distribution of the velocity in the intakes are concern, the results are not significantly affected by grid refinement, scale and roughness effects and the location of the inlet. In this section, the effects of RANS turbulence models are investigated. This is done using three commonly used RANS models; SKE, SA and SST models. The mathematical descriptions of these models are presented in Chapter 3. Table 6.7 summarized the model parameters of this study. The study is performed on scaled models for three reasons:

1. Later these results can be directly compared to the results from Eddy-resolving simulation (Chapter 7).
2. It is found that the convergence is relatively easier using the scaled model compared to the prototype scale especially in the model where SST is used.
3. it is shown previously that the scaling does not affect the results significantly, hence, following results are also valid for the prototype.

Model	Turbulence model	Scale	Wall roughness (k_s)	Inlet location
S01	SKE	1/40	0 (Smooth)	16H
S03	SA			
S04	SST			

Table 6.7: *RANS models*

The velocities in x, y and z directions are shown in Figures 6.14 to 6.16. In intake 1, similar velocity distributions are estimated by all the models in all directions. In this section, higher streamwise velocities are located at the upper regions and lower streamwise velocities are in the lower part of the section. This results are in agreement with the experimental results in Figure 5.16 for intake 1. A closer look at the results reveals that a small vortical structure is predicted by the SST model on the right side of intake 1. This vortical structure is visualized using isosurface of the Q-criterion (second invariant of the velocity gradient tensor) in Figure 6.20. It starts from the water surface and stops approximately at the investigated section. Also this vortical structure with clockwise rotation can be detected in Figure 6.17 and Figure 6.18 where the streamwise vorticity and surface streamlines are plotted. This structure was not predicted by the other models and it was not observed in the experimental results.

In intake 2, the difference between the computed values are significant. More specifically between SST and the other models. This was expected as previously in Section 5.6, in the experimental test, it was revealed that at this section, the flow is complex, highly turbulent with strong swirling and separation due to upstream features. Indeed by comparing the velocities in x,y and z directions in Figures 6.14 to 6.16, significant differences can be observed between the models, especially between SST and other models. In the streamwise direction in Figure 6.14, on the right hand side, the distribution of velocities

are fairly similar between the models. This is also true when velocities in other directions are considered. However, on the left side of the section in the streamwise direction, the velocity distribution which is computed by SST model is in a better agreement with the results from the physical model test (Figure 5.17). In y direction (Figure 6.15), the results from SKE and SA are similar and they both indicating high values at the left top and bottom corners. On the other hand, in the SST model, there are various zones with high velocities in y direction with the bottom zone at the bottom corner having the largest values. This zone was not observed in the physical model test (Figure 5.17). However, the other two zones with their centres located at $z/H = 0.4$ and 0.6 are in a good agreement with the experimental results in term of locations and their values. Finally, the velocities in z direction are shown in Figure 6.16. It is evident that there is an agreement between all the numericals as well as between the numerical and the experimental results. The results indicate that there are two zones with high vertical velocities on the left side of the section with opposite directions. however, the width of these zones are larger than those measured experimentally.

In order to better understand the swirling flow which is detected in the velocity contour plots in intake 2, streamwise vorticity and surface streamlines are plotted in Figure 6.17 and 6.18. It can be seen that a large distinct clockwise swirling flow on the left side followed by a smaller zone at the right bottom corner are predicted by all the models. In order to detect the source of this strong swirl, isosurface of the Q-criterion are plotted in Figure 6.19. The geometrical features on the left side along with flow from the left side of the intakes leading to a strong swirling flow which is extended through the left intake. This will be discussed in details later in Chapter 7. Furthermore, isosurface of Q-criterion for the SST case shows a free-surface vortex at the left side of the intake structure. This was not observed with other turbulence models.

Finally, in this section, similar to the physical model test in section 5.6.3, the results are presented according to Fisher-Franke guidelines (Section 2.9) in Figures 6.21 to 6.27. In these figures, only the results from the SST model is shown because of its better agreement with the physical model test results. Figure 6.21 and 6.22 show the criterion C6 or Fisher-Franke criterion for intake 1 and 2 respectively. Physical model results are also added to the graphs for comparison and completeness. Furthermore, two different strategy is employed in computing and presenting the numerical results. One based on all data points (all cell-centres) for the entire section which is indicated by SST-ES and one computed based on the cloud of points according to measured points in the physical model test. In the upper portion of the both intakes where the streamwise velocities are higher than the average velocity, the differences between the point cloud approach and using all data points are negligible. However, in intake 1, in the lower side of the graph the velocity deviation from the average velocity is significantly reduced when point clouds are considered. This is due to, partially, exclusion of the low velocities near the walls. In intake 2, the lower values ($u_n < u_{ave}$) are reduced even further when point clouds are considered. In terms of comparison between the numerical and the experimental results, in general, in the upper part of the graphs the agreements netween the numerical and experimental values are good. This is also true for the lower part of intake 1 specially when point cloud is used. The most significant difference between the two is located at the lower part of intake 2 where the values predicted by SST model is significantly lower than the ones from the experiment. Furthermore, in the lower part of both intakes (below 5% area fraction)

where the values from all data points of the numerical model is considered significant gradient toward zero values are observed. These can be interpreted as the flow in the boundary layer where the velocities are approaching zero toward the walls.

Figures 6.23 and 6.24 show criterion C2 for velocity deviations in y and z directions respectively. In intake 1, significant number of points (more than 80%) are showing deviation less than 10% when numerical results are considered. In terms of agreement between the numerical and experimental results, excellent agreement is found in z direction, however, in y direction more data points are found to be between 0% to 5% deviations by the numerical model and less data points in the range of 10% to 20% deviations. On like intake 1, in intake 2 significant number of data points are shown to have deviation higher than 10% in both y and z directions. This is in agreement with the experimental results. In y direction, numerical model predicted more data points within 0% to 5% range compared to the experiment. This is followed by less number of points within 5% to 20% deviation. In z direction, the agreement is better although it can be seen that more data points are predicted with higher deviation than 40%. These values are also can be confirmed visually via the normalized velocity contour plots in Figure 6.15 and 6.16.

Figure 6.25 and 6.26 illustrate histograms of local deviation angles (criterion C4) for both intakes. The deviation angle between y and z components of velocity from the local axial velocities in intake 1 are shown to be under 10° with more than 80% of the data below 5°. On the other hand, in intake 2, the deviation angles in y direction are shown to have significant number of data points located higher than 10°. These numbers are increased significantly when the deviation angles in z direction are considered in Figure 6.26. It can be seen that 10% of data having angles higher than 50°. These points are correspond to flow near the left wall of intake 2. In terms of agreement between the numerical and experimental results, similar trends are predicted by the numerical model.

The kinetic energy flux coefficient α (criterion C6) for both intakes are computed. As mentioned earlier, a value of 1 indicates a completely uniform flow and for turbulent flow conditions it is usually equal to 1.2. In intake 1, α estimated to be approximately 1.15 which is in good agreement with α from the experiment. On the other hand, in intake 2 this value is estimated to be 1.45, slightly higher than the experimental value of 1.3, indicating a non-uniform flow condition.

Finally, Figure 6.27 shows the deviation of discharges for each quadrants corresponding to criterion C3. In both intakes, the deviation is below 5% for all quadrants. In intakes 1, the computed values are in an excellent agreements with the physical model test. In quadrants 1 and 2, the discharges are higher than the ideal discharge and in quadrants 3 and 4 the discharges are lower than the ideal discharge. This is aligned with the contour plots of the velocities in Figure 6.14. In intake 2, the maximum deviations are approximately 5 and 4% for quadrant 2 and 4 respectively. Additionally, in these two quadrants significant differences can be observed between the physical model and the numerical models results. According to the guidelines, this value must be below 5% which in all the quadrants this is fulfilled.

In this section, effects of turbulence models on the results are investigated. Furthermore, the flow condition is evaluated using the flow criteria (Section 2.9) for SST turbulence model. Following conclusions are made through this study: (1) The estimated velocities using All RANS turbulence models are similar in intake 1. Furthermore, they are in a good

agreement with the physical model. However, there is significant differences between the models when the results in intake 2 are compared specially between SST and the two other models. In general, the values computed using SST are closer to the measured values. However, this model predicted extra high velocity zone in y direction at the bottom left corner which it was not observed in the model test. (2) The isosurfacees of Q-criterion are shown that a strong swirling flow is present at the left side of the intake 2 due to flow from the left over the seperation wall. Additionally, SST model shown that more swirling flow presents in intake 1 and 2. (3) The inflow condition criteria are evaluated for the SST model. It is shown that only criterion C6 at the intake 1 and criterion C3 at both intakes are fulfilled. Although criterion C5 is not fulfilled, however, the results are very close to the Fisher-Franke's boundaries specially when point cloud is used. (4) Good convergence achieved by the three models, however, obtaining convergence with SST model is found to be difficult with SKE model being the most robust among the models.

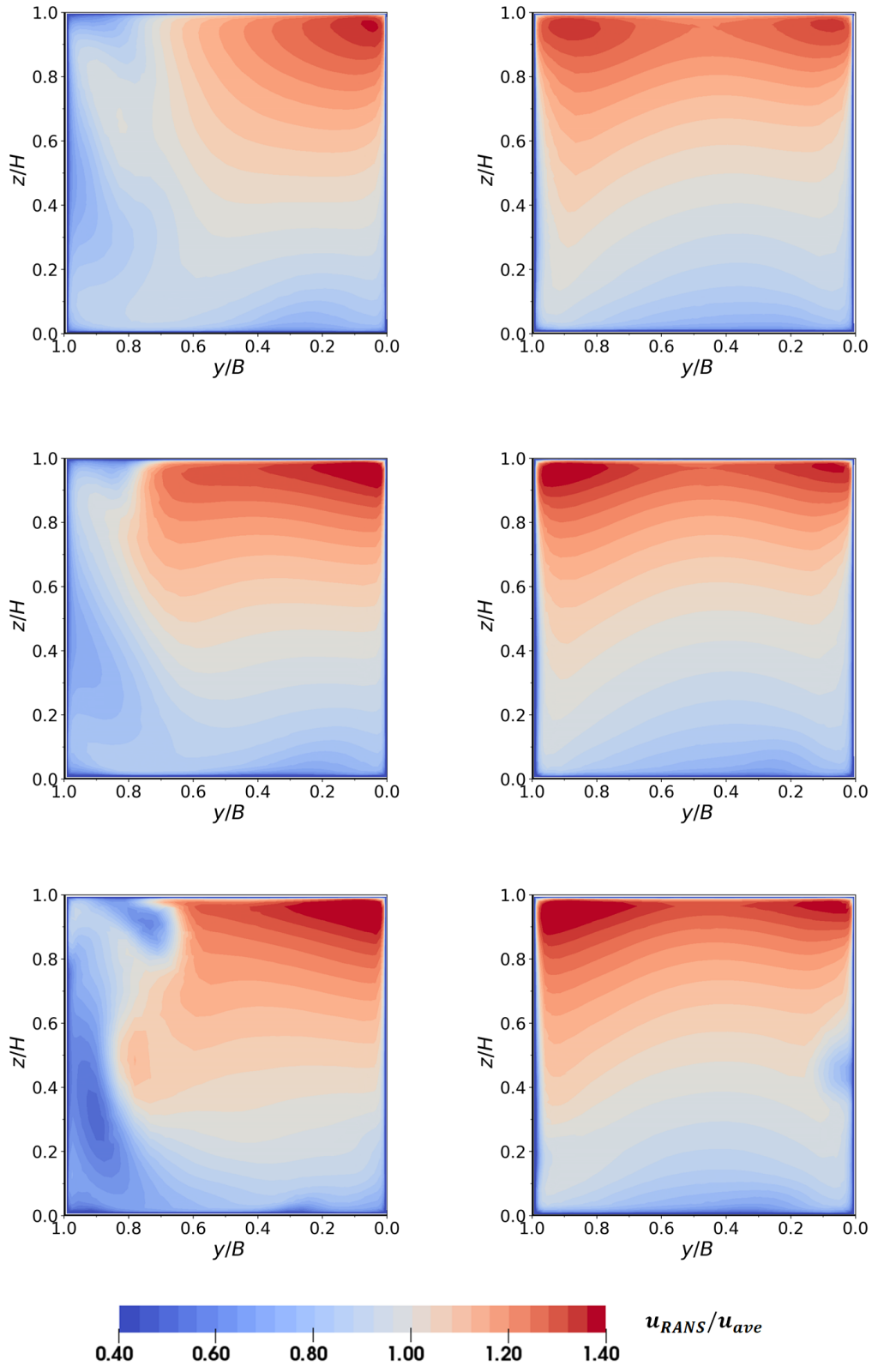

Figure 6.14: *Contour plots of velocity in out-of-plane or x-direction computed by different RANS turbulence models (Top: Model S01, middle: Model S03 and bottom: Model S04).*

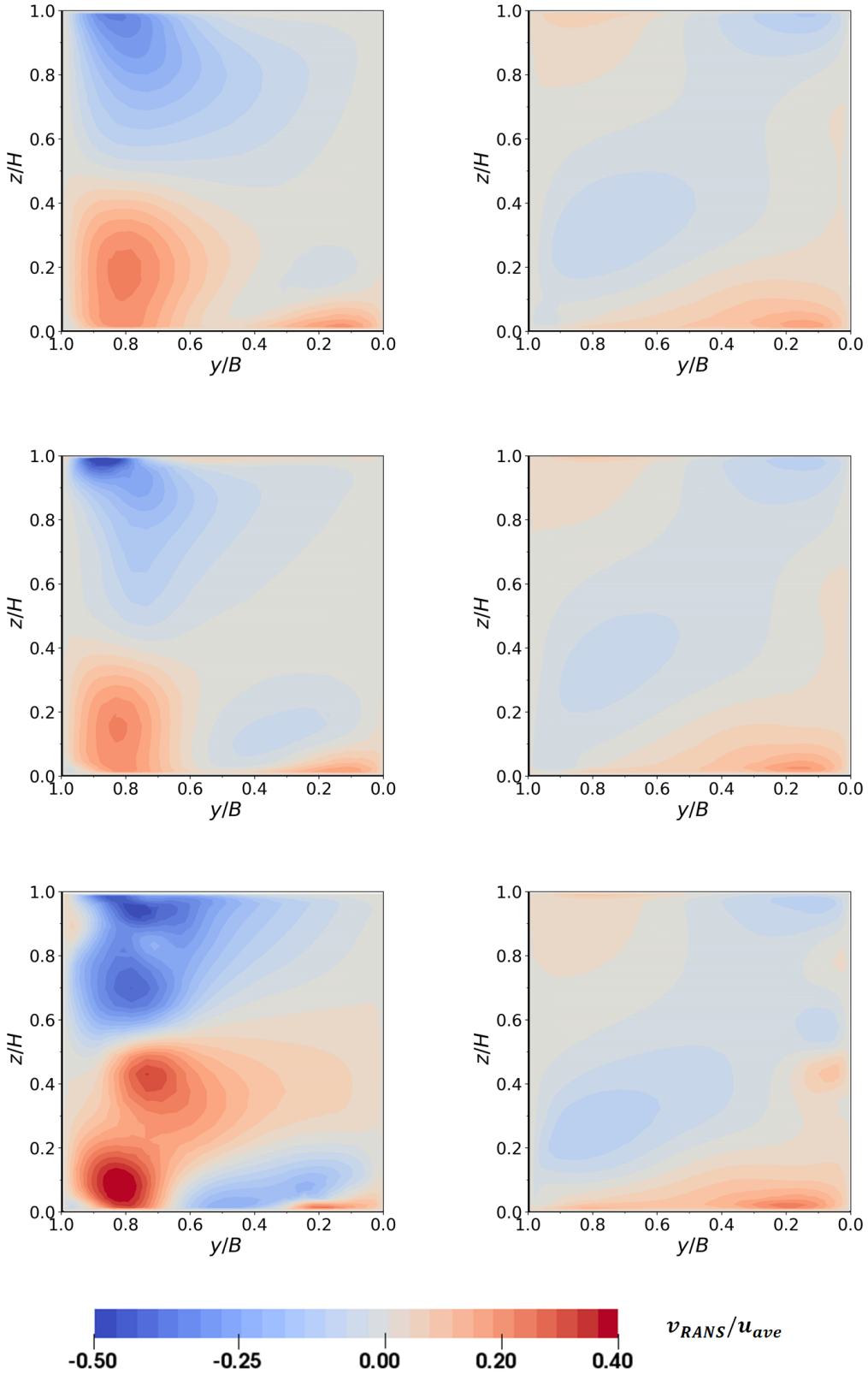

Figure 6.15: *Contour plots of velocity in y-direction computed by different RANS turbulence models (Top: Model S01, middle: Model S03 and bottom: Model S04)*

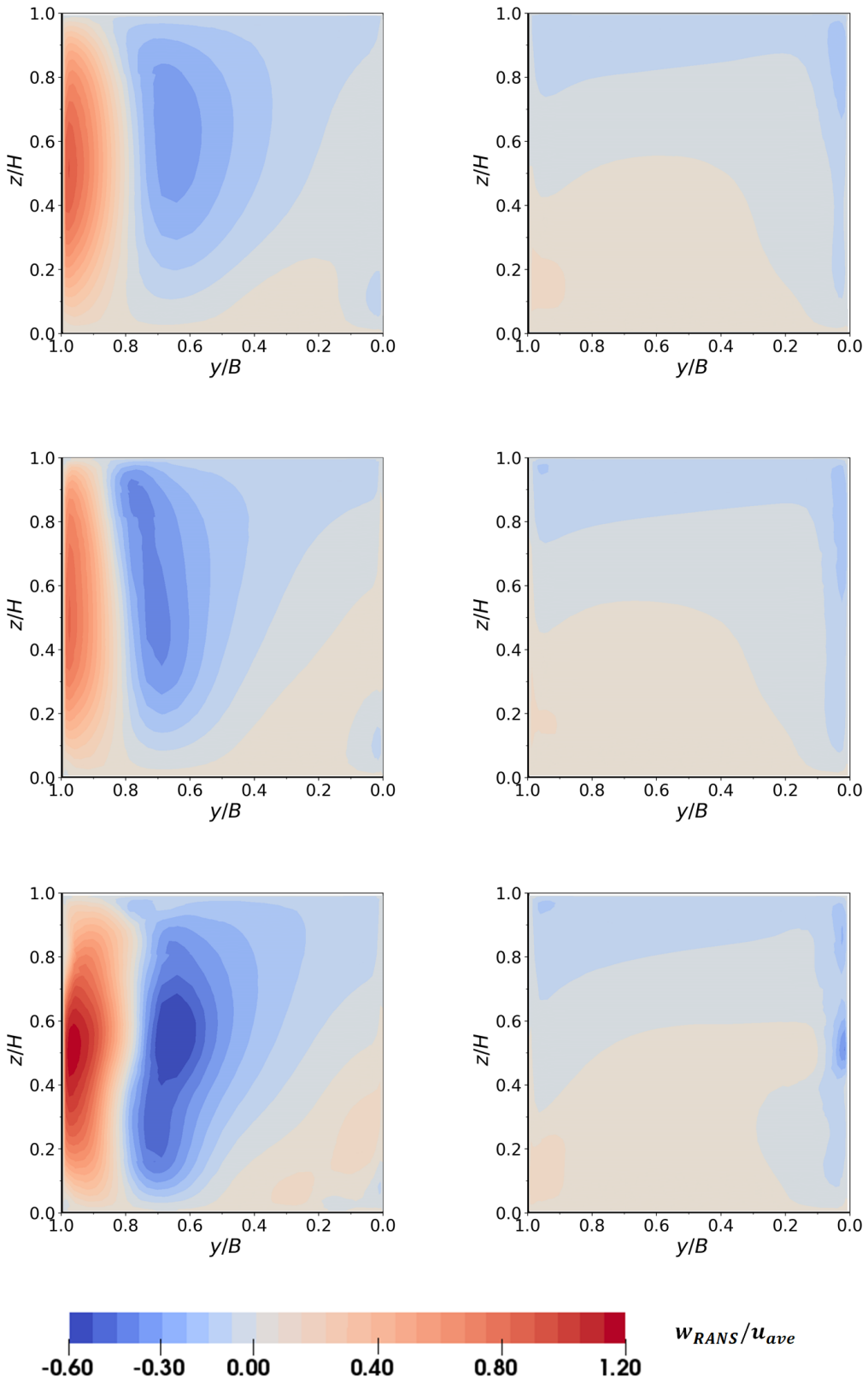

Figure 6.16: *Contour plots of velocity in z-direction computed by different RANS turbulence models (Top: Model S01, middle: Model S03 and bottom: Model S04)*

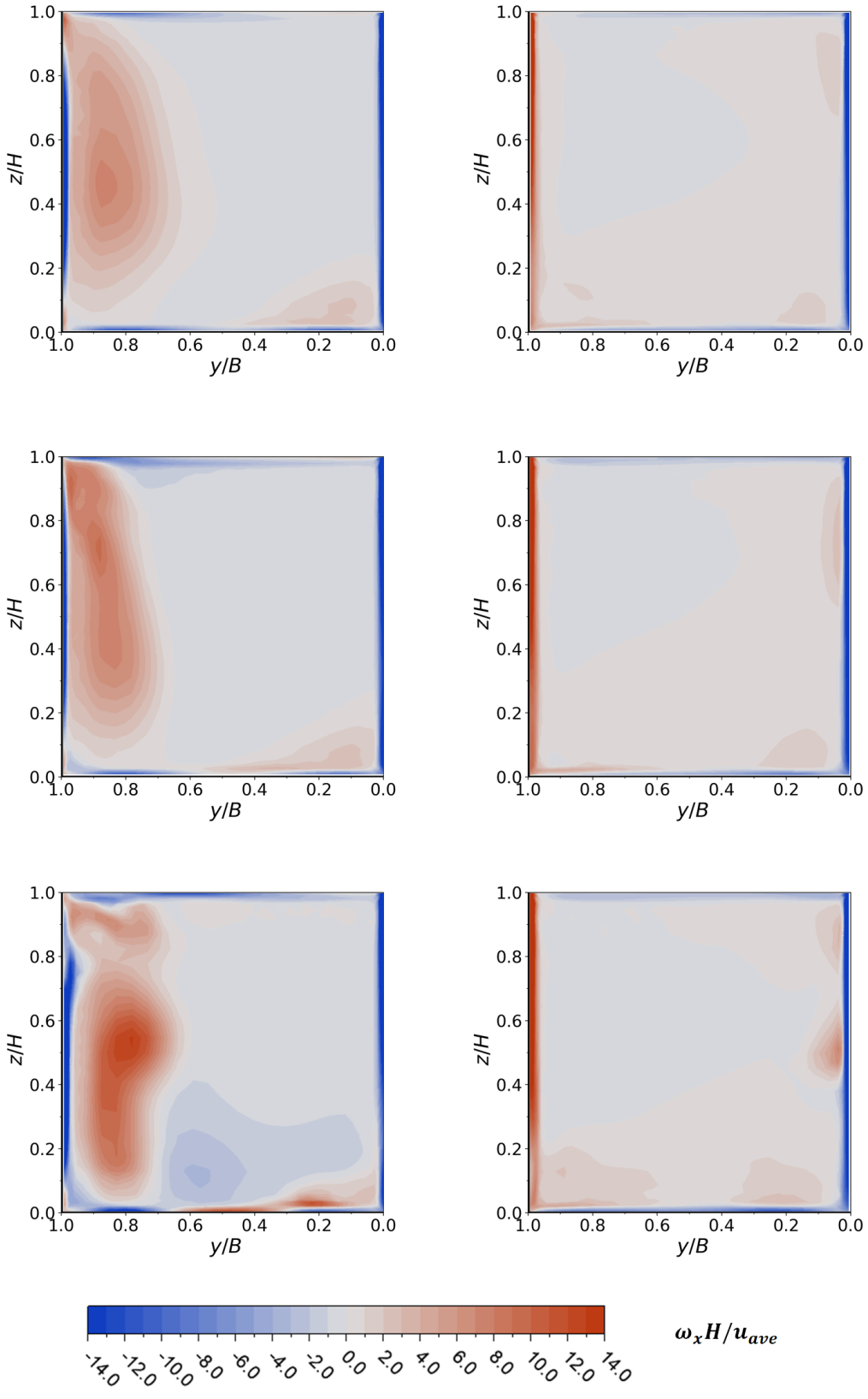

Figure 6.17: *Contour plots of out-of-plane vorticity computed by different RANS turbulence models (Top: Model S01, middle: Model S03 and bottom: Model S04)*

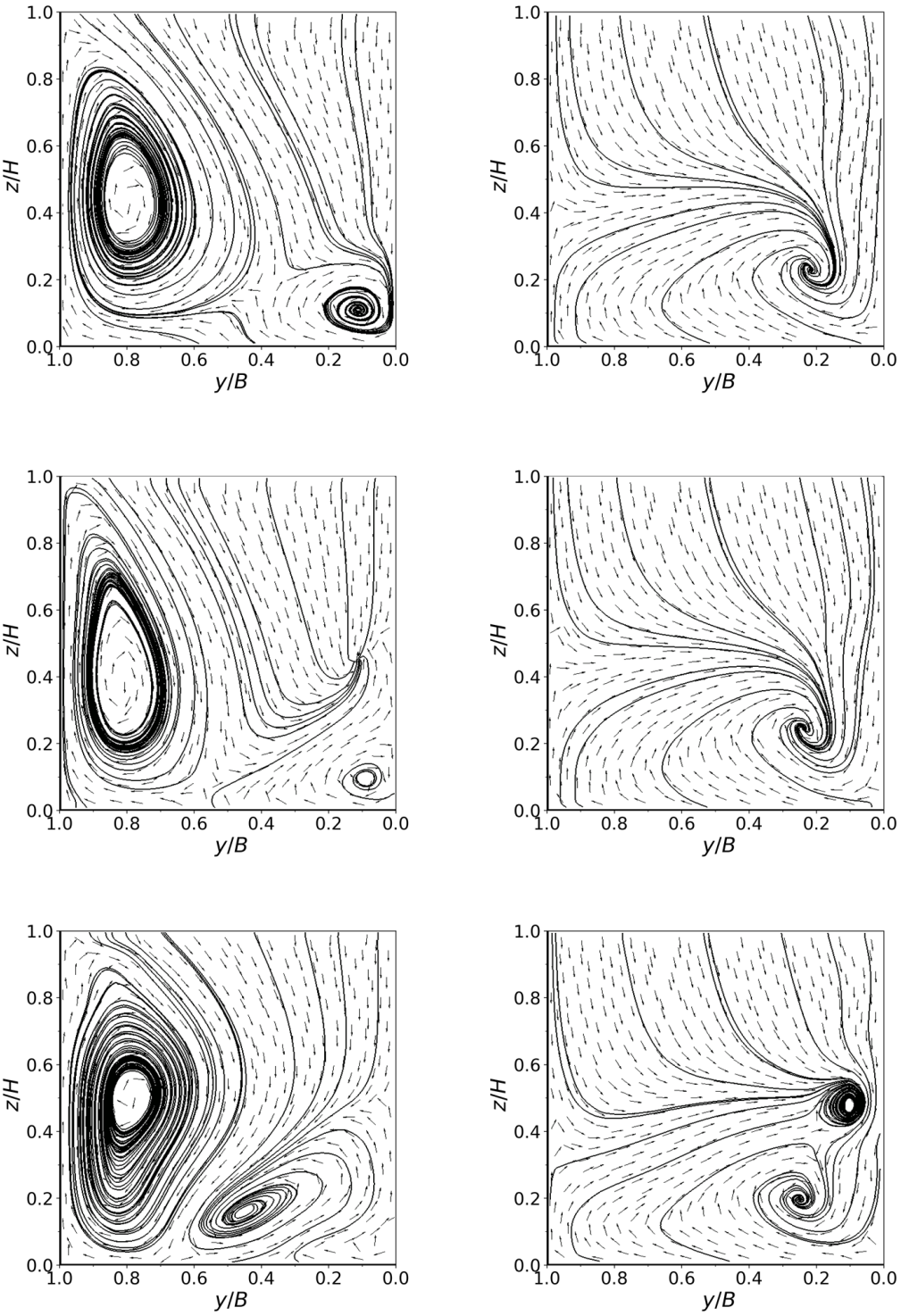

Figure 6.18: *Streamlines and surface vectors computed by different RANS turbulence models (Top: Model S01, middle: Model S03 and bottom: Model S04)*

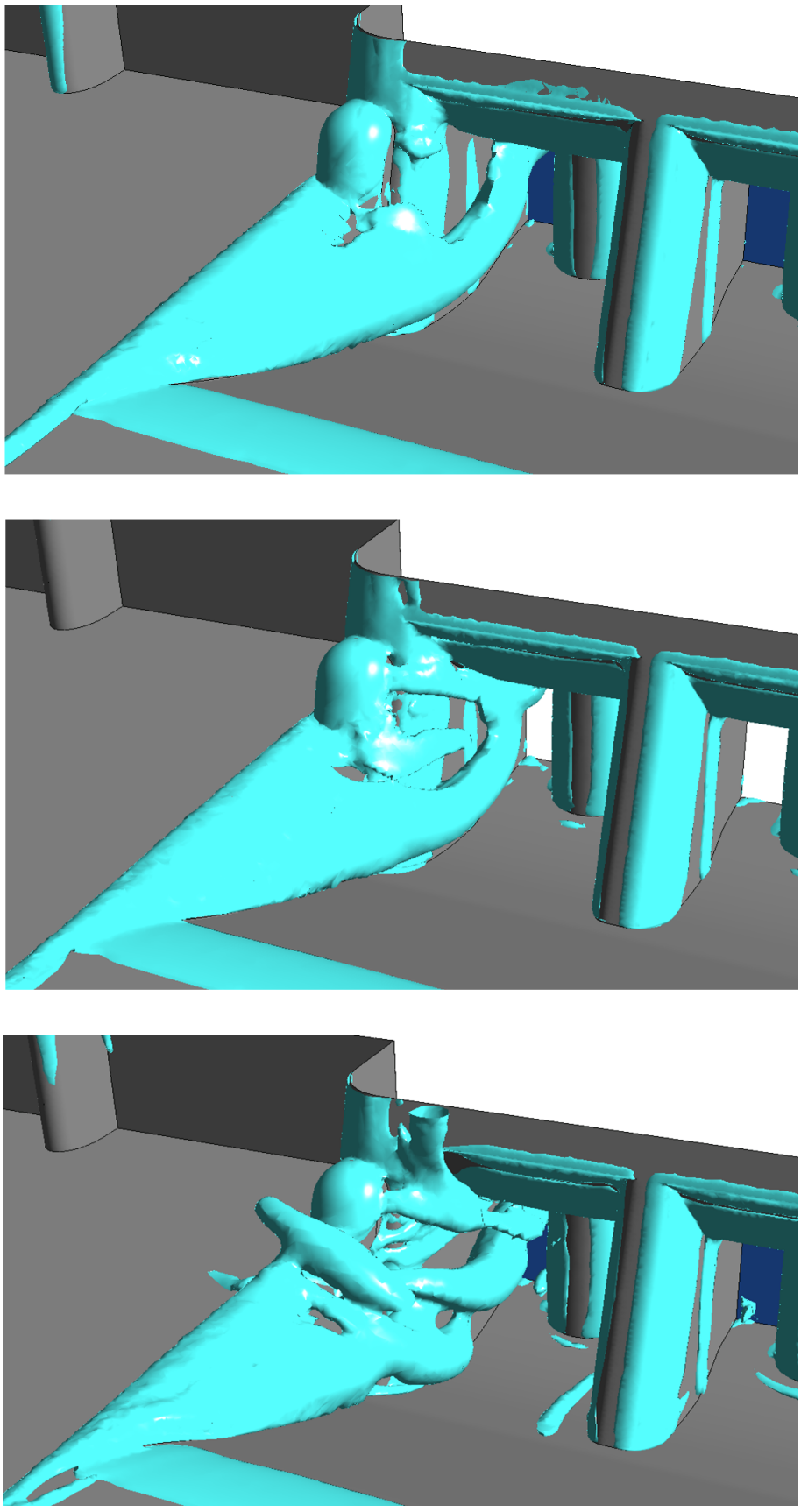

Figure 6.19: *Isosurfaces of Q-criterion computed by different RANS turbulence models (Top: Model S01, middle: Model S03 and bottom: Model S04)*

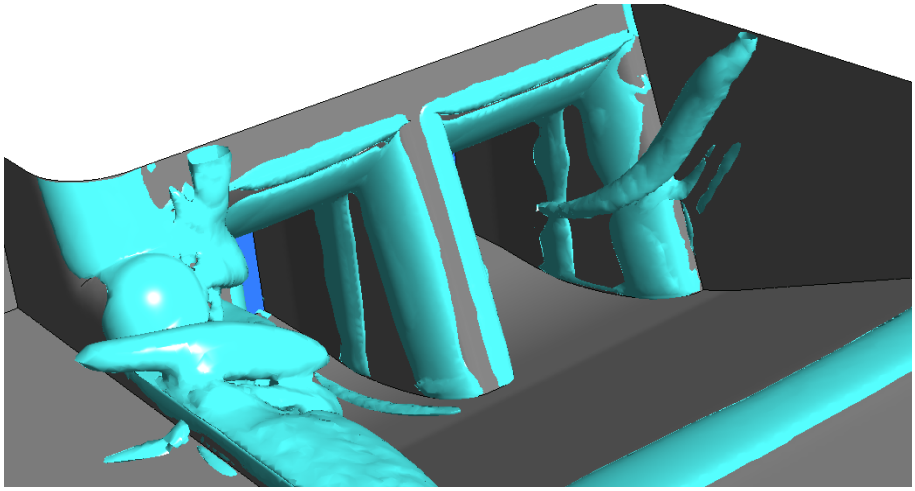

Figure 6.20: *Isosurfaces of Q-criterion computed by SST model.*

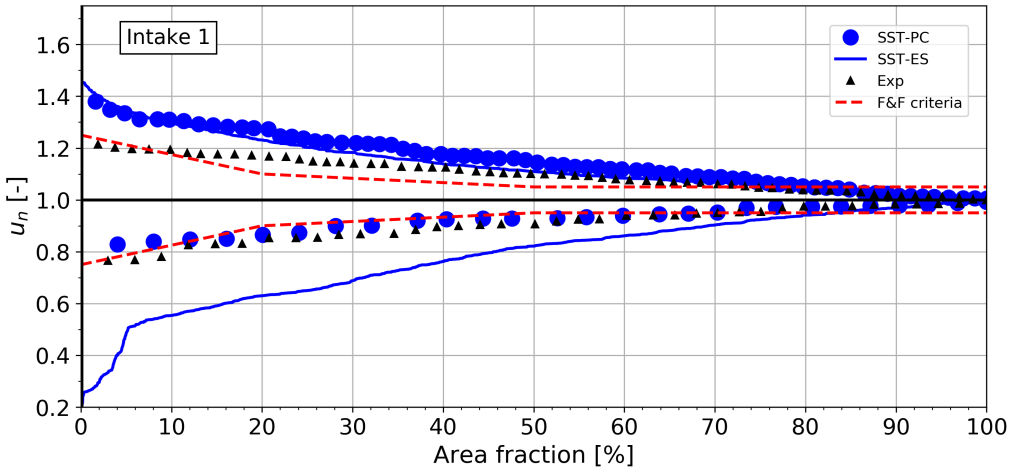

Figure 6.21: *Flow evaluation of Turbine 1 based on Criterion 5 (C5) of the design guideline (Section 2.9). SST-PC: results from point cloud, SST-ES: results from the entire section and Exp: experiment.*

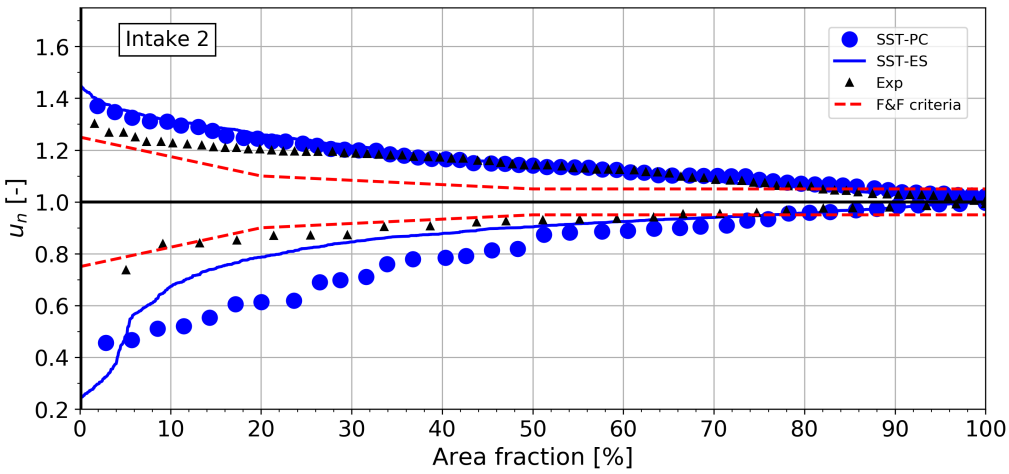

Figure 6.22: *Flow evaluation of Turbine 2 based on Criterion 5 (C5) of the design guideline (Section 2.9). SST-PC: results from point cloud, SST-ES: results from the entire section and Exp: experiment.*

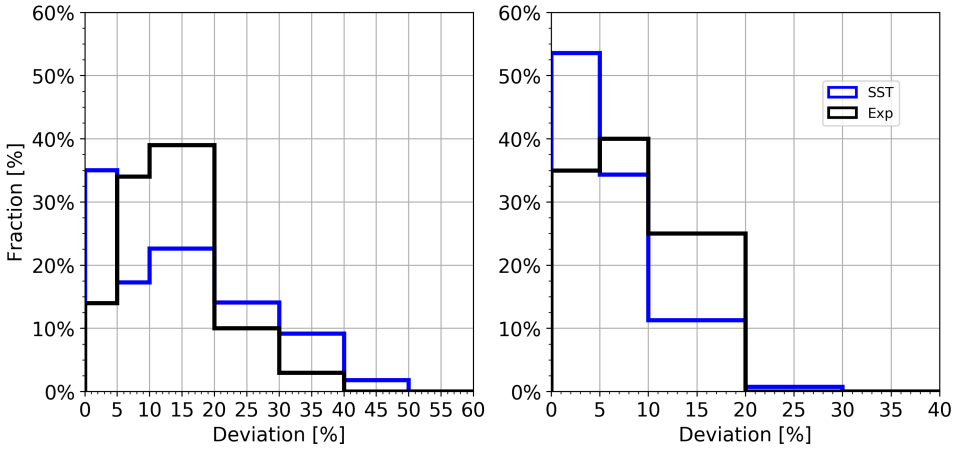

Figure 6.23: *Flow evaluation of Turbine 1 (right) and 2 (left) for y component of the velocity vector based on Criterion 2 (C2) of the design guideline (Section 2.9).*

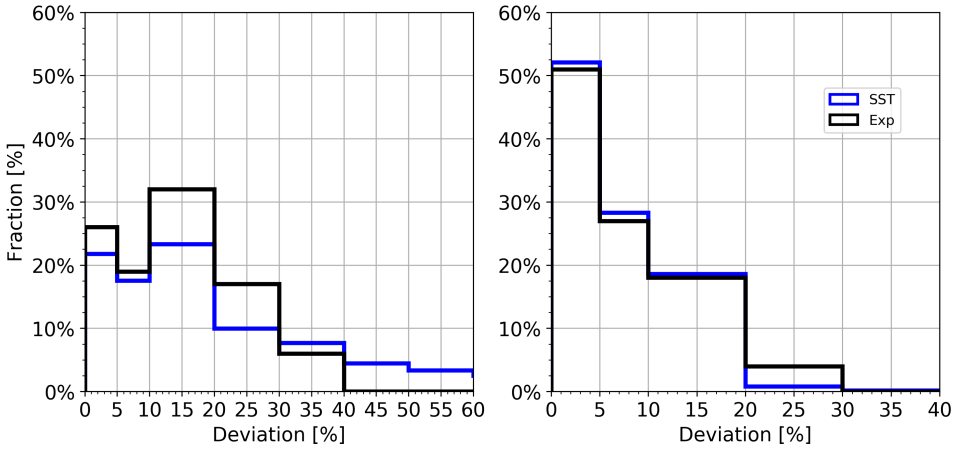

Figure 6.24: *Flow evaluation of Turbine 1 (right) and 2 (left) for z component of the velocity vector based on Criterion 2 (C2) of the design guideline (Section 2.9).*

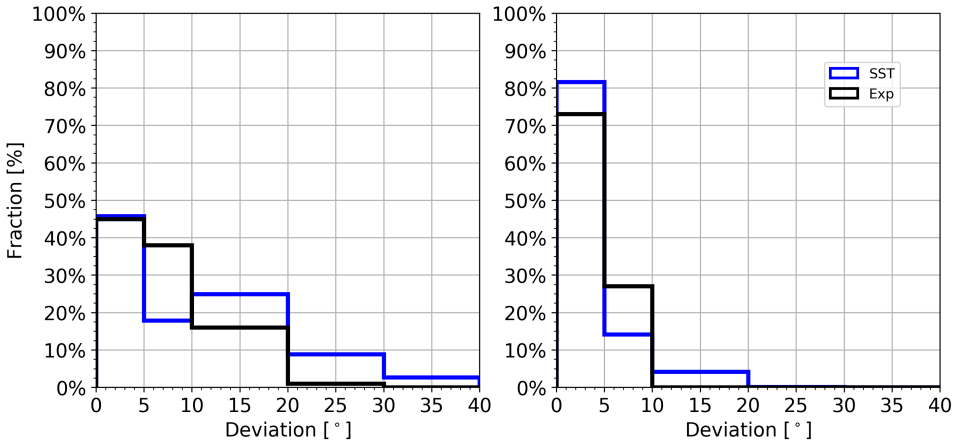

Figure 6.25: *Flow evaluation of Turbine 1 (right) and 2 (left) for y component of the velocity vector based on Criterion 4 (C4) of the design guideline (Section 2.9).*

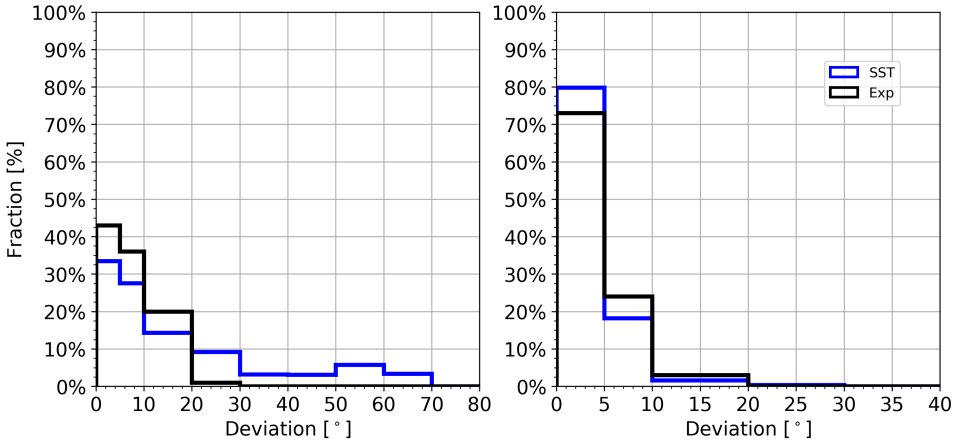

Figure 6.26: *Flow evaluation of Turbine 1 (right) and 2 (left) for z component of the velocity vector based on Criterion 4 (C4) of the design guideline (Section 2.9).*

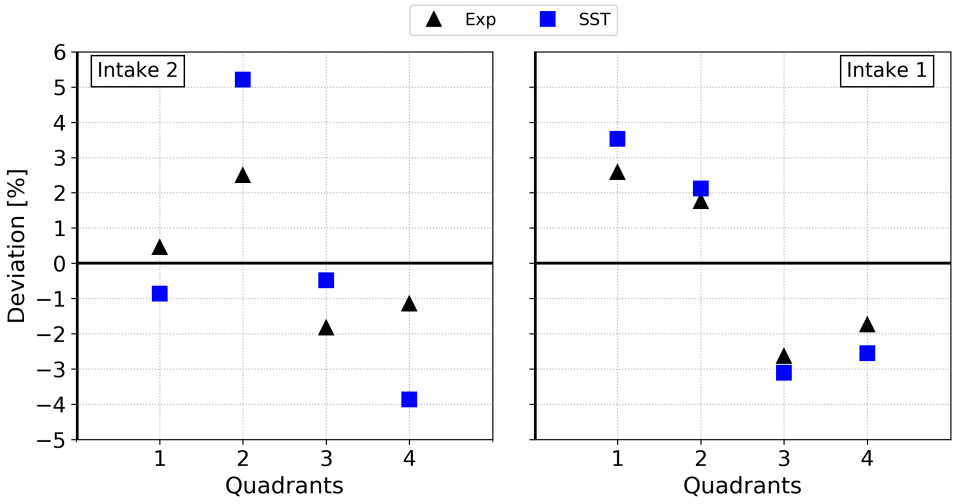

Figure 6.27: *Flow evaluation of Turbine 1 (right) and 2 (left) based on Criterion 3 (C3) of the design guideline (Section 2.9).*

6.8 Study on the simplified models

In the previous sections, the complex system of the approach flow is modelled and investigated. It is also compelling to know the flow characteristic in a simple geometry free from the complex geometrical features. In order to achieve this, two simplified models, SM01 and SM02, are created. These models are illustrated in Figure 6.28 and 6.29. Model SM01 consist of three identical intakes side by side. Periodic boundary condition is applied to the sides along with symmetry boundary condition (rigid lid) at the water surface. Model SM02 is identical to SM01 except that the slope to the intakes are significantly reduced to investigate the effect of the approach slope on the flow characteristics in the intake. The relevant numerical parameters are summarized in Table 6.8. Both models are scaled to the physical model test's scale (1/40) with the assumption of that the walls are smooth. Furthermore, SST turbulence model is used and the computational grid is based on the grid which is generated previously. The inlet boundary condition is generated using a precursor simulation of a periodic channel with streamwise and spanwise periodicity. Finally, the results are only evaluated for the central intake at the same location where the previous studies carried out and they are normalized based on the average velocity of the section 1 in Figure 5.7.

Figure 6.30 shows normalized velocities in x, y and z directions for models SM01 and SM02. In the streamwise or axial direction, the velocity distribution are similar to the results of the full model in intake 1 where the high velocities are located at the top of the section and the lower velocities at the bottom. A closer look reveals that the difference between the high and low velocities in model SM01 is significantly higher in comparison to model SM02. This is also true for other directions. For example, in y direction at the bottom of the sections, the normalized velocities are reaching -0.4 and 0.4 in model SM01. On the other hand, these values, although at the same location, are -0.2 and 0.2 for model SM02. In the z direction, maximum velocity is localized at the bottom center of the section with normalized value of 0.3 in model SM01. On the other hand, in model SM02, the positive z velocities are spread across the entire lower part of the section.

Figure 6.31 shows the surface velocity vectors and the streamlines for the study section. In model SM01, two distinct swirling flow structures can be identified. In model SM02 these are much weaker and further apart from each other. In order to visualized these structures, isosurface of Q-criterion is plotted in Figure 6.34. Clearly in model SM01 with higher approach slope, these two streamwise flow structures are present and distinguishable. Additionally, two swirling flow structures are present at each side of the entrance. These structures are generated due to the large separated zone on the approach slope. Figure 6.32 shows the streamwise velocities at a vertical section at the center of the intakes. A large separated zone is shown in model SM01 due to the steep slope. This zone is also clearly shown via the surface streamlines in Figure 6.33.

Figure 6.35 shows the velocities in local coordinate system at a vertical spanwise section at the center of the slope for model SM01. The velocities are normalized based on the average streamwise velocity at the section 1 in Figure 5.7. It is shown that near the bottom in axial direction, a negative axial velocity is present confirming the separated zone which is shown in Figure 6.32. Moreover, velocities in y direction are showing distinct symmetrical zones where the center of the intakes are the symmetry planes. This is similar to the contour plot of nomalized velocity in y direction in Figure 6.30 with two

additional zones. The values however are fairly small. In vertical direction (z direction in Figure 6.35), the velocities are all positive with a low velocity layer at the bottom of the section.

Model	Turbulence model	Roughness (k_s)	Scale	Intake's slope [%]	Element size [mm]
SM01	Shear Stress Transport (SST)	0	1/40	42.5	5.0
SM02				8.75	

Table 6.8: *Simplified models and their relevant parameters.*

The results from the both models are assessed based on the guidelines and conditions in Section 2.9. Figures 6.36 to 6.39 summarized these conditions. Figure 6.36 shows the condition C5. none of the models fulfilled Fisher-Franke criterion with model SM01 being the worst. Reducing the approach slope seems to improve the condition drastically. Figure 6.37 shows the histograms of local velocity deviation (condition C2). In y direction, the deviation of velocity from the axial velocity is reaching up to 40% in model SM01 with steep approach slope, however, reducing the approach slope (in model SM02) reduced this significantly. In z direction, both models perform the same way with many data points located higher than 10% degrees. The reason behind this, perhaps, is the entrance shape on the top of the intakes. Figure 6.38 shows the local deviation angles. Similar to condition C2 in y direction, The local deviation angle is reduced significantly when the approach slope is reduced. On the other hand, in z direction, the deviation angle remains high for both intakes with significant number of points located between 5 and 20 degrees. Additionally, the inflow is evaluated using condition C3 where discharges are computed for the quadrants. This condition is illustrated in Figure 6.39. It can be seen from the distribution of the axial velocities in Figure 6.30 that the velocities are more uniform in model SM02. Indeed, this is also reflected on the quadrant's discharges with the reduction of the discharge deviations from 4% to 2% from model SM01 to SM02. Finally, the kinetic energy flux coefficients, α, are computed for both models. It is found that this value is 1.4 for model SM01 and 1.15 for model SM02 showing significant improvement.

In conclusion, the computed velocities in the intakes are very similar to the intake 1 of the actual domain (Figure 6.14), specially when simplified model SM02 is compared. Reducing the approach slope is significantly improving the overall flow at the investigated section. Finally, it is shown that even in the most simplest form, the flow is not satisfying all the conditions. This means that perhaps this section is not suitable for evaluation according to the Fisher-Franke conditions. In the next section, these conditions are applied to a new section further downstream inside the intakes.

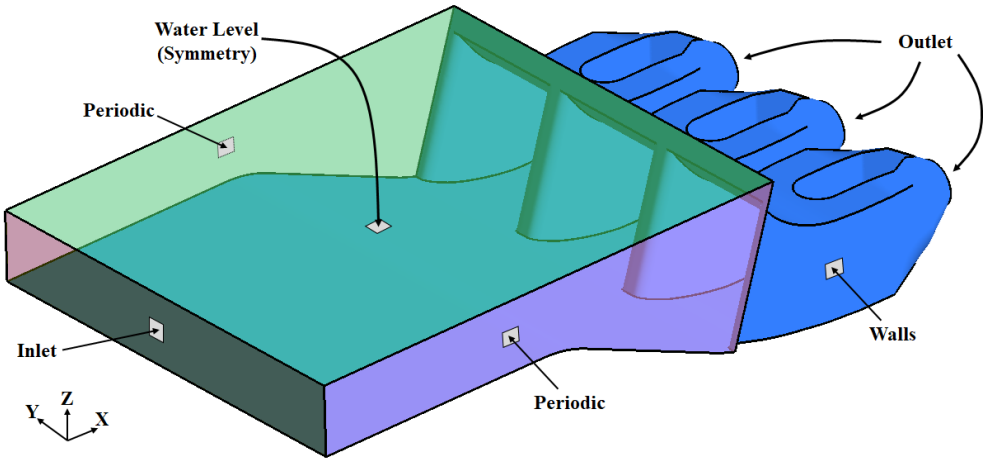

Figure 6.28: *Computational domain of the simplified model SM01.*

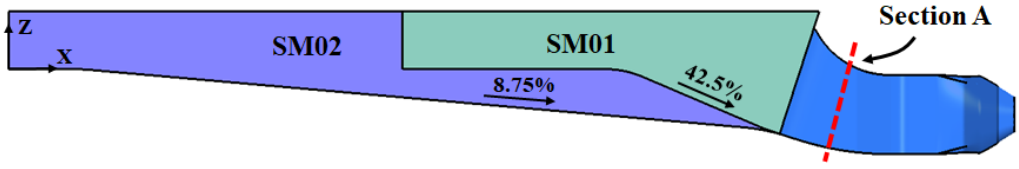

Figure 6.29: *Illustration of the difference between the simplified models SM01 and SM02. The 8.75% slope of SM02 corresponds to approximately* 5 *degrees angle.*

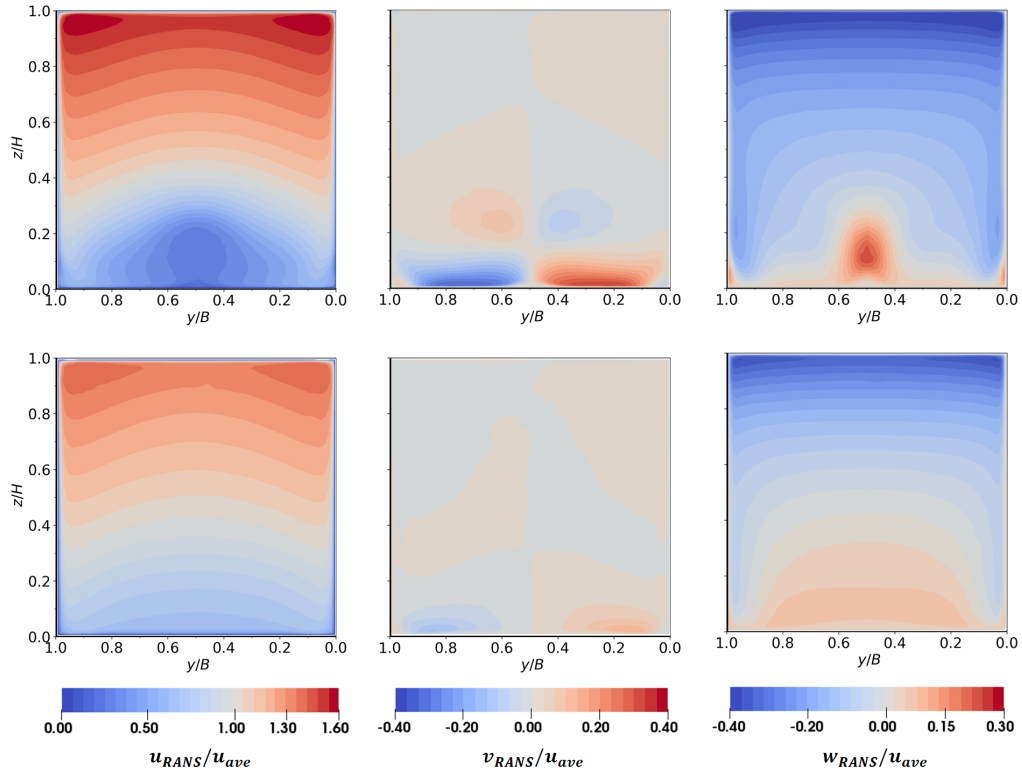

Figure 6.30: *Contour plots of velocity components of SM01 (top row) and SM02 (bottom row).*

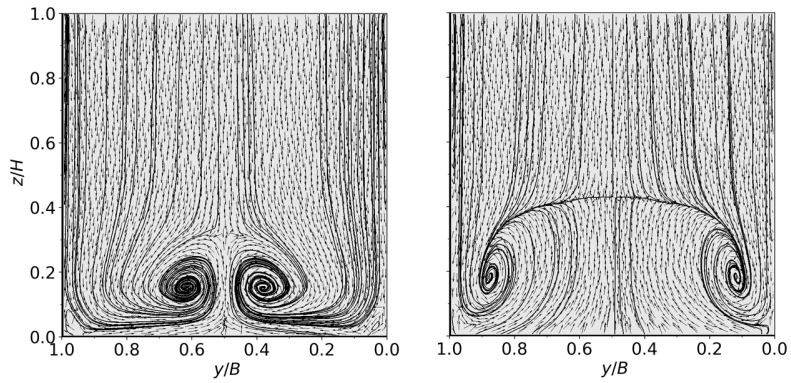

Figure 6.31: *Surface streamlines and velocity vectors of SM01 (right) and SM02 (left).*

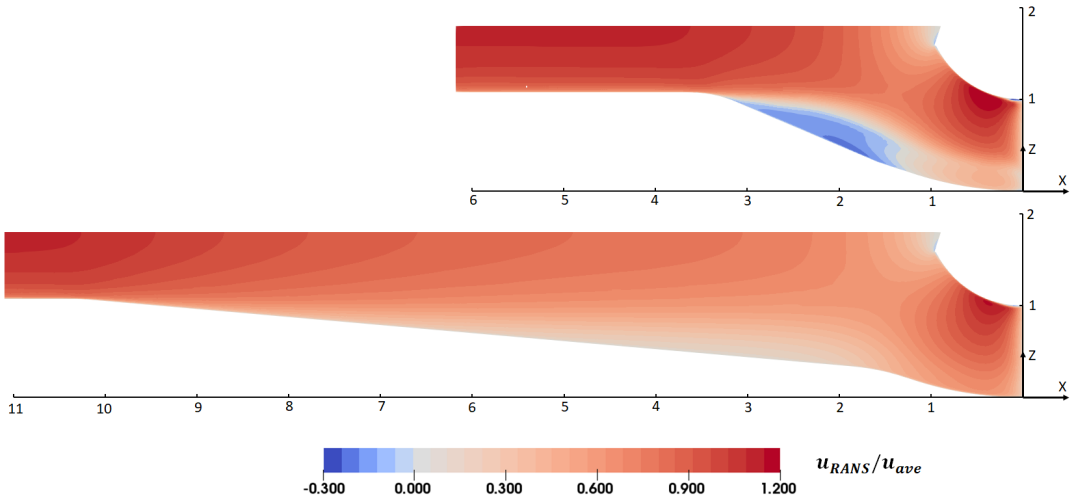

Figure 6.32: *contour plots of x component of velocity on a vertical section through the center of the intakes (top: SM01 and bottom: SM02).*

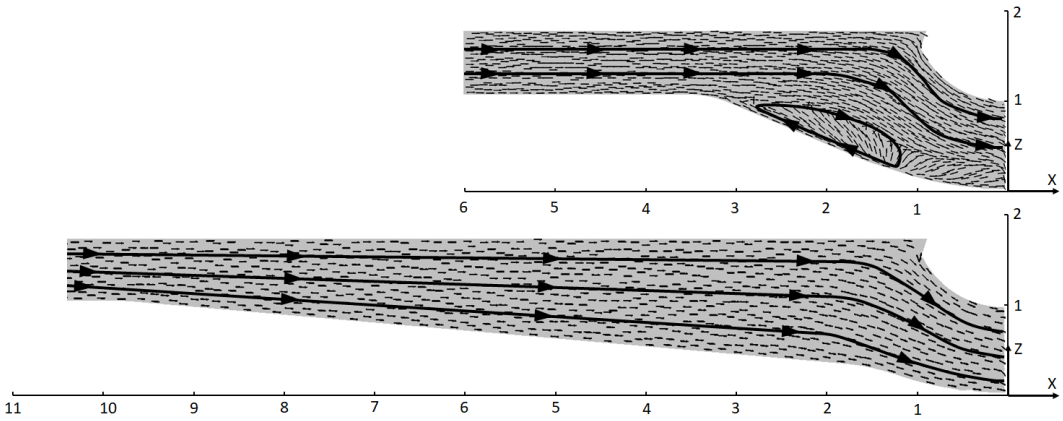

Figure 6.33: *Surface streamlines and vectors on a vertical section through the center of the intakes (top: SM01 and bottom: SM02).*

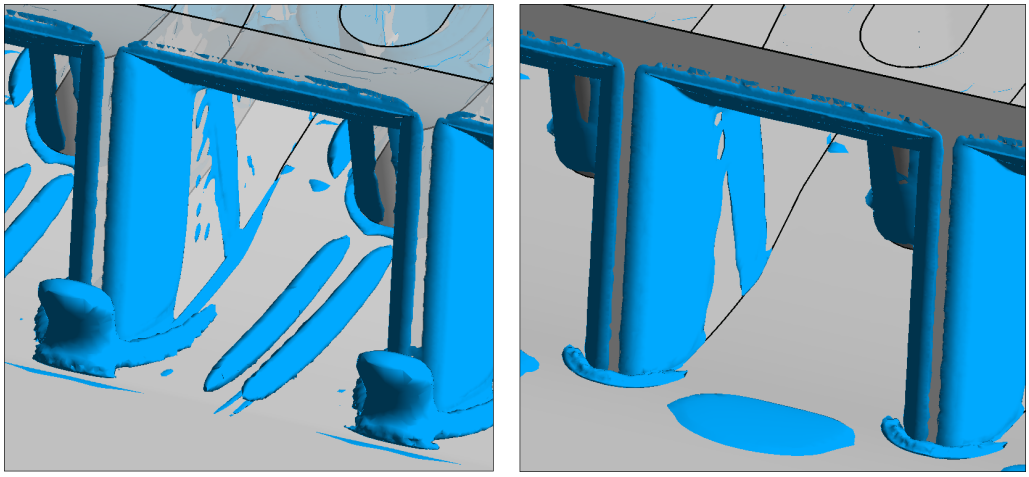

Figure 6.34: *Isosurfaces of Q-criterion (left: SM01 and right: SM02).*

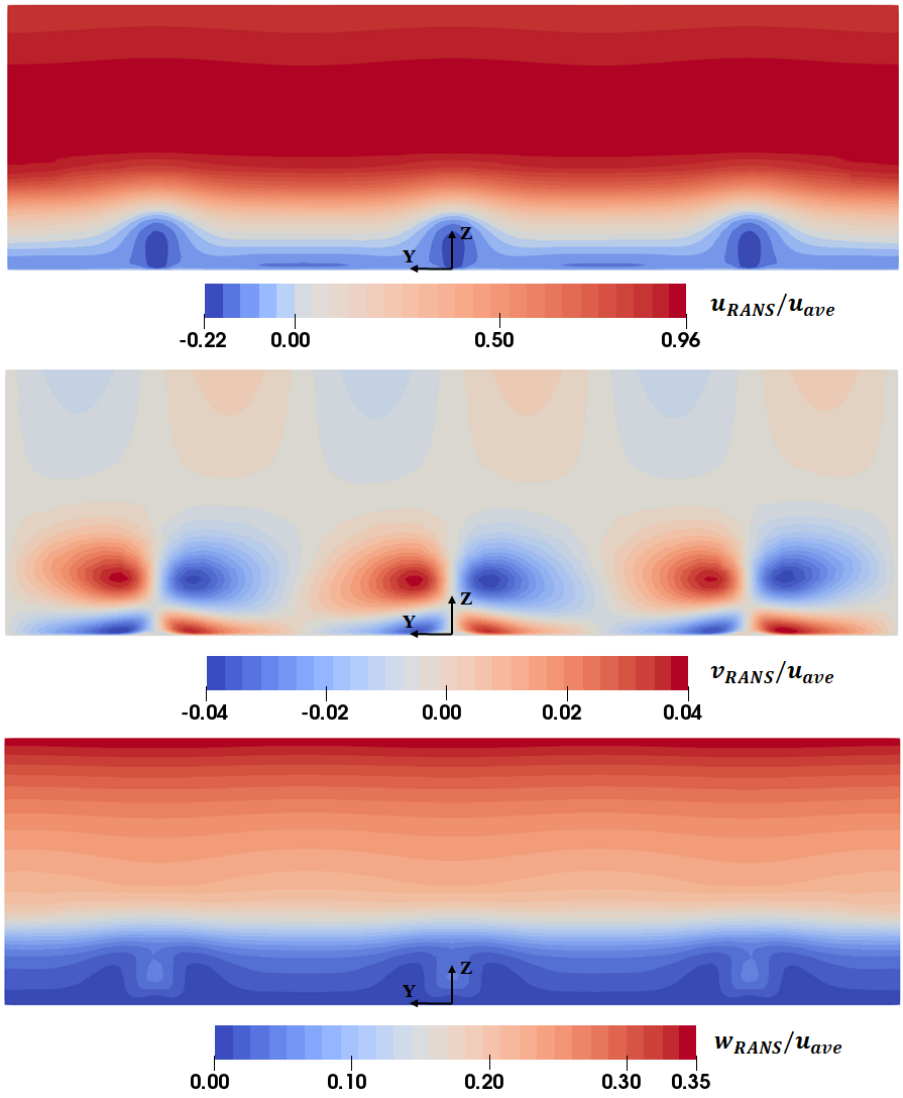

Figure 6.35: *Contour plots of velocity components on the vertical section perpendicular to the flow at the center of the SM01 model's slope to the intakes.*

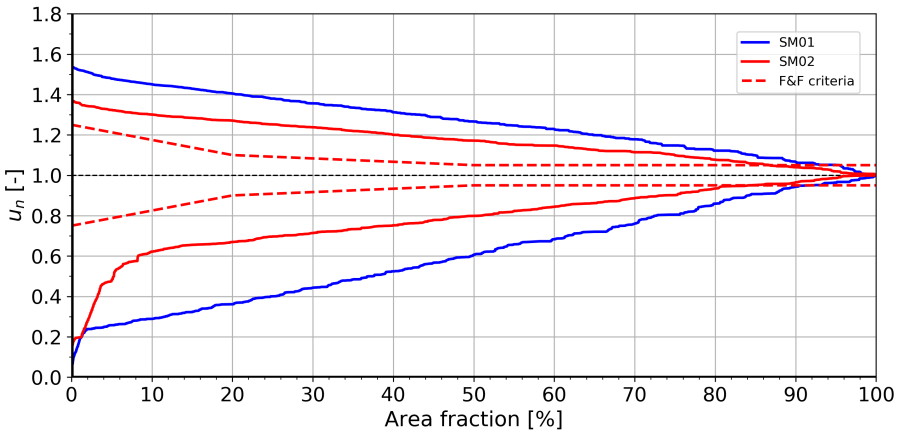

Figure 6.36: *Flow evaluation of the models SM01 and SM02 based on Criterion 5 (C5) of the design guideline (Section 2.9).*

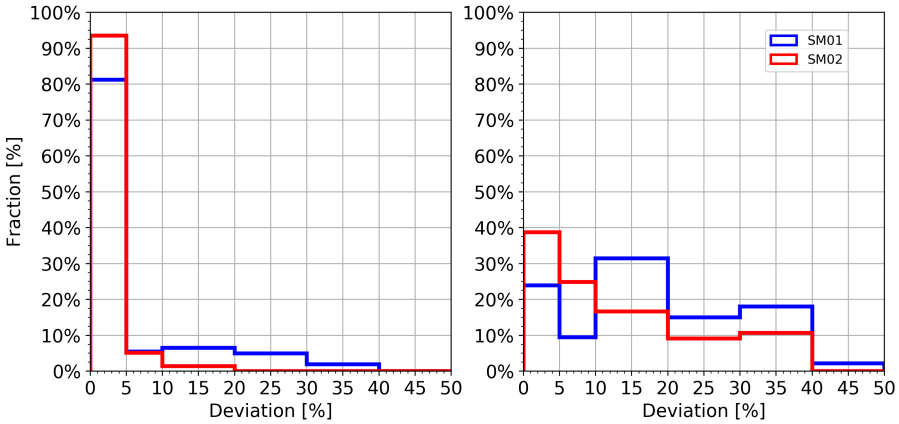

Figure 6.37: *Flow evaluation of the models SM01 and SM02 for y (left) and z (right) components of the velocity vector based on Criterion 2 (C2) of the design guideline (Section 2.9).*

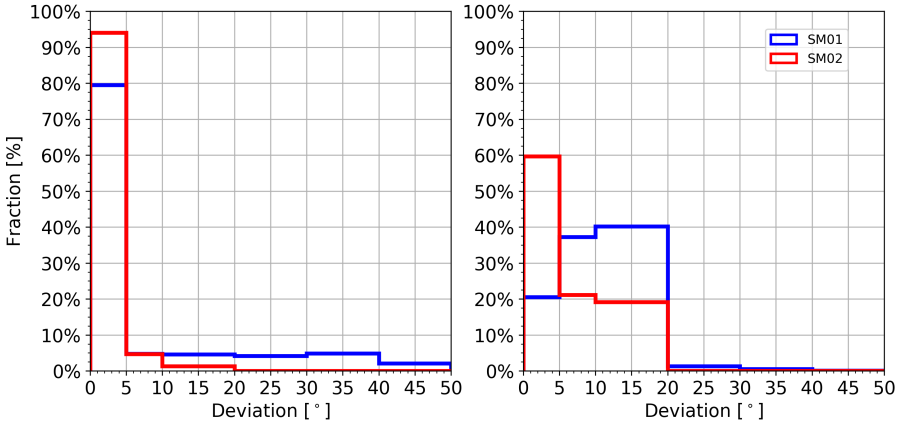

Figure 6.38: *Flow evaluation of the models SM01 and SM02 for y (left) and z (right) components of the velocity vector based on Criterion 4 (C4) of the design guideline (Section 2.9).*

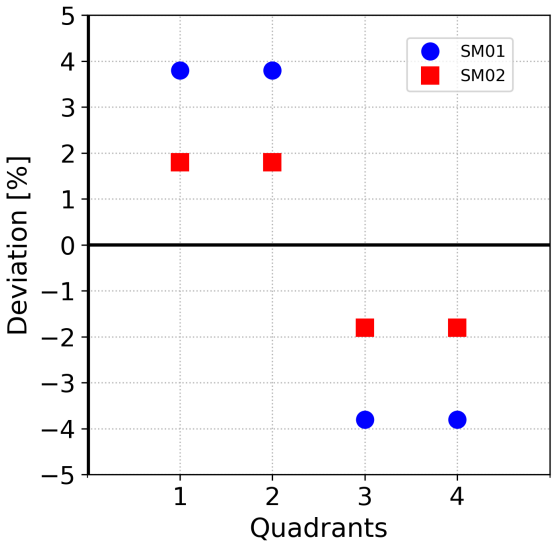

Figure 6.39: *Flow evaluation of the models SM01 and SM02 based on Criterion 3 (C3) of the design guideline (Section 2.9).*

6.9 Proposed section for flow evaluation

In the previous sections, the flow is evaluated at Section 1 (Figure 5.7) based on the guidelines described in Section 2.9. According to Fisher and Franke (1987), the location of this section is downstream of the trash rack and upstream of the turbine. Also, it is common in the physical model studies that the velocities are measured at this location due to its accessibility. However, it is shown that even for the simplest case, not all the criteria can be fulfilled. This indicates that the chosen section is too close to the entrance and the flow is still under influence of the entrance shape and not fully developed. Gabl et al. (2018) proposed using a section as close as possible to the turbines where the cross section is circular. However, in the physical model, it is difficult to measure the values at this location using ADV and in reality, at these locations, the velocities are affected by the guide vanes and the runner. Here, instead, a cross section is chosen between the runner of the turbine and the previously investigated section. This cross section is deemed to be far enough from the entrance, hence flow is more developed, at the same time, it is far from the turbine's runner and guide vanes that their effects are negligible on the cross section. The location of this new section is illustrated in Figure 6.40.

In this section, three models, S04, SM01 and SM02, are re-evaluated and compared for the new cross section. The velocities are shown in Figures 6.41 and 6.42. They are normalized based on the streamwise velocities. Figure 6.41 illustrates the normalized velocities in x, y and z directions for the simplified models. It is shown that the velocities are symmetric in both parts of the sections due to the symmetry of the model itself. In x direction, the velocities are almost identical between the two models with a small low velocity region at the corners and a high velocity zone adjacent to the inner walls. In both y and z directions the normalized velocity values and its gradients are significantly higher for a model with steep approach slope.

The normalized velocities at the new section is also illustrated in Figure 6.42 for the full mode (S04). In intake 1, the streamwise (x direction) velocities are uniform similar to the

results of the model SM02. In other directions, no significant deviation can be observed. This is also true for the right part of the intake 2. On the other hand, in intake 2, the velocities in x direction on the left part of the section showing low velocity in the upper zone followed by high velocities in the lower zone. Inspection of the velocities in y and z directions show a large rotating flow located at the upper zone of the left section with the values reaching up to approximately 0.4 times the axial velocities. This swirling flow is the swirling flow observed at Section A extended downstream.

The flow conditions are also evaluated using the criteria from Section 2.9. Figure 6.43 shows condition C5, deviation of the axial velocities from the average velocity of the section. In the upper zone where the values are higher than the average velocity, all the models fulfill the criterion specially at the higher values with intake 1 of the model S04 being the best. On the other hand, similar to the other section, almost all lower values are not within the range of the criterion. In fact, in this section, the values are much worst than the section after the trash rack. The reason behind this is that the area which has the low velocity values is small. It is mainly located near the walls and corresponds to the boundary layer with very low velocities.

Figure 6.44 shows condition C2, local deviation of the velocities, in both y and z directions. It is shown that in both directions the deviations are significantly reduced compared to Figure 6.23, 6.24 and 6.37, specially in z direction. The only exception however is intake 2 of the full model which shows small areas containing high deviation values. Similar conclusion can be made by comparing the computed values for condition C4 in Figure 6.45 for the new section with Figures 6.25, 6.26 and 6.38. The local deviation angles are significantly reduced. Finally, Figure 6.46 shows condition C3 where deviation of discharges are computed for each quadrants. The numbering of the quadrants follows the same rule as the other section where the numbering starts from the top left corner and follows clockwise direction. computed deviation values for all the quadrants for model SM01, SM02 and intake 1 of model S04 are significantly improved with all located below 1%. However, as it was seen before, intake 2 of model S04 shows high deviation values specially in quadrant 1.

It is shown that in the lower range of the criterion C5, the condition is not satisfied. This is due to the low velocities especially near the boundaries. This is misleading since in simplified models and the intake 1 of the full model, the velocity distribution is satisfying every other conditions. Furthermore, a visual inspection of the axial (streamwise) velocities shows that the flow at this section is fairly uniform. The reason behind this is that this condition is developed and proposed for experimental investigations where a limited number of points, usually further away from the walls, are selected. In order to put this into the test, a relatively coarse rectangular grid of points (14 and 10 points in vertical and horizontal directions for each intake) are selected at the new section, A_{DS}, and values are computed and plotted for condition C5. This is shown in Figure 6.47. It can be seen that In the higher range ($u_n > 1.0$), the values showing the same trends as Figure 6.43 where the numerical grid is used for the calculation. On the other hand, in the lower range where $u_n < 1.0$, there is a significant improvement where the values from intake 1 of model S04 is completely fulfill the condition. Therefore, in order to evaluate condition C5 for a section from a numerical model, it is recommended to use a cloud of points, preferably equally spaced for evaluation of the flow based on condition C5.

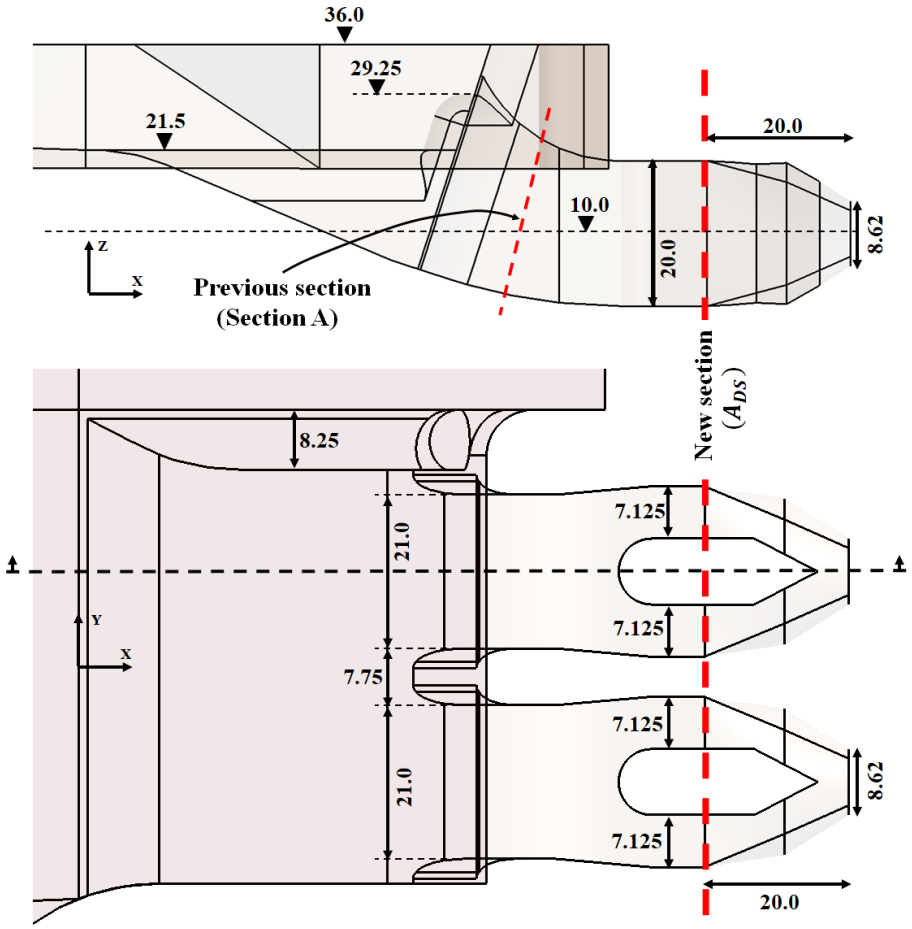

Figure 6.40: *Location of the new section for flow evaluation (top: plan view and bottom: vertical cross section thought the left intake.)*

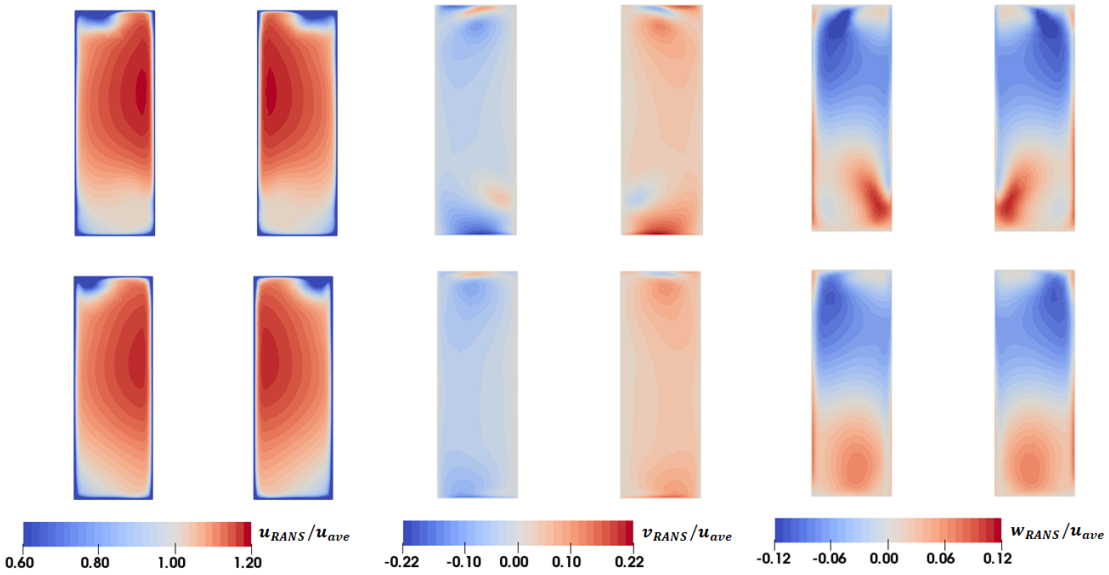

Figure 6.41: *Contour plots of the velocity components at the new section, A_{DS} (top: model SM01 and bottom: model SM02).*

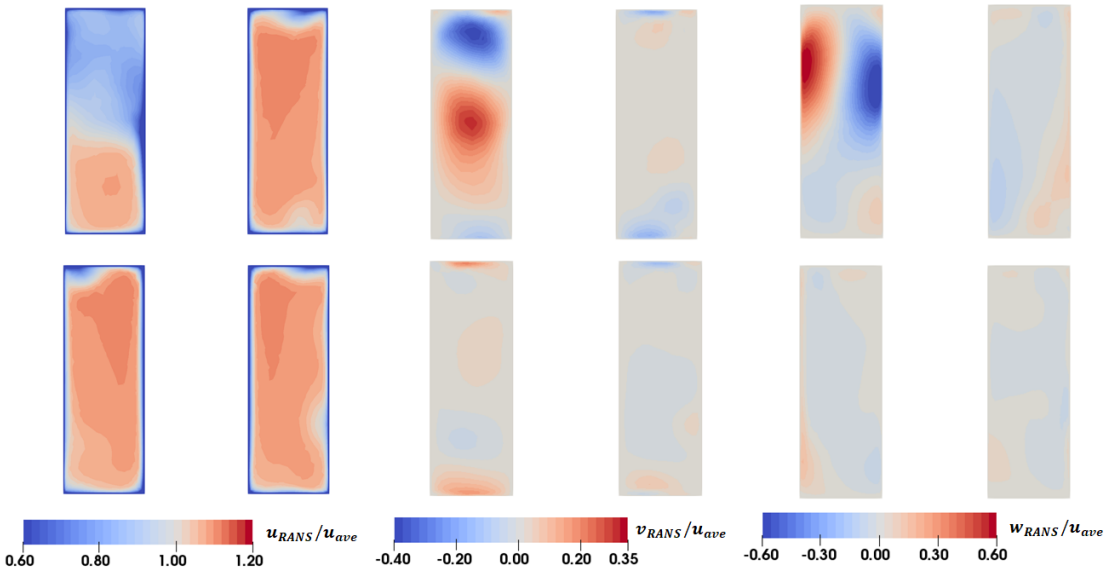

Figure 6.42: *Contour plots of the velocity components at the new section, A_{DS}, of model S04 (top: Turbine 2 and bottom: model Turbine 1).*

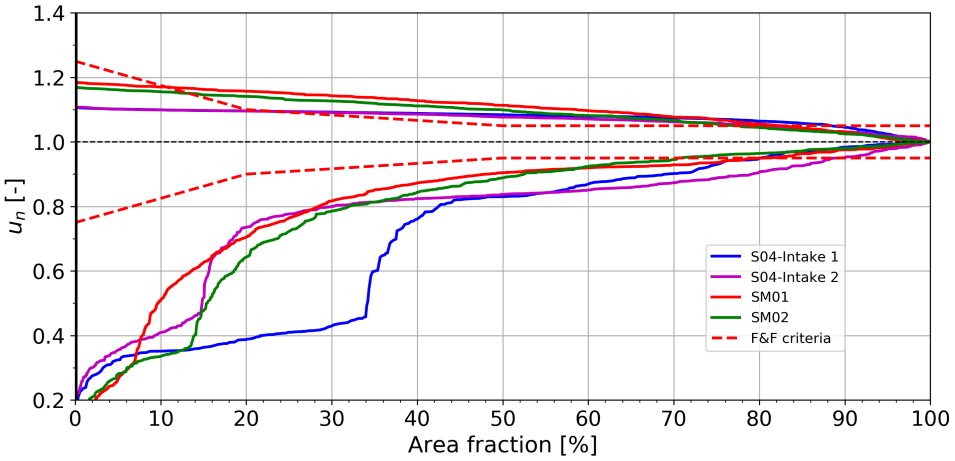

Figure 6.43: *Flow evaluation of the models S04, SM01 and SM02 at the new section, A_{DS}, based on Criterion 5 (C5) of the design guideline (Section 2.9).*

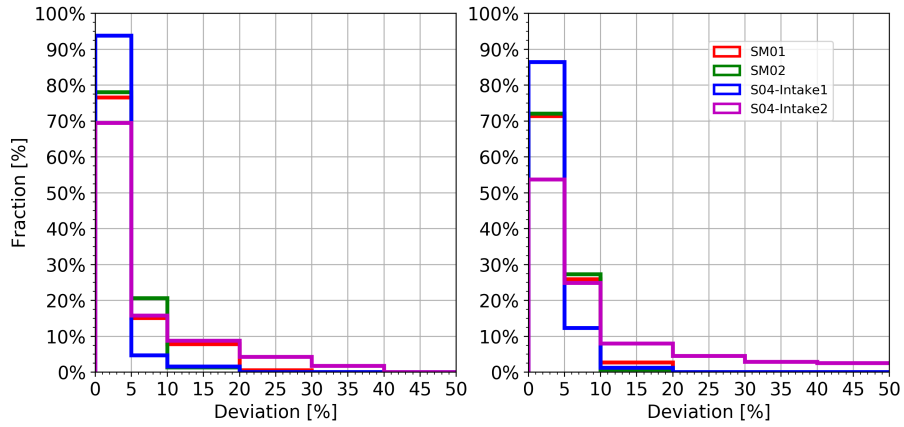

Figure 6.44: *Flow evaluation of the models S04, SM01 and SM02 for y (left) and z (right) components of the velocity vector at the new section, A_{DS}, based on Criterion 2 (C2) of the design guideline (Section 2.9).*

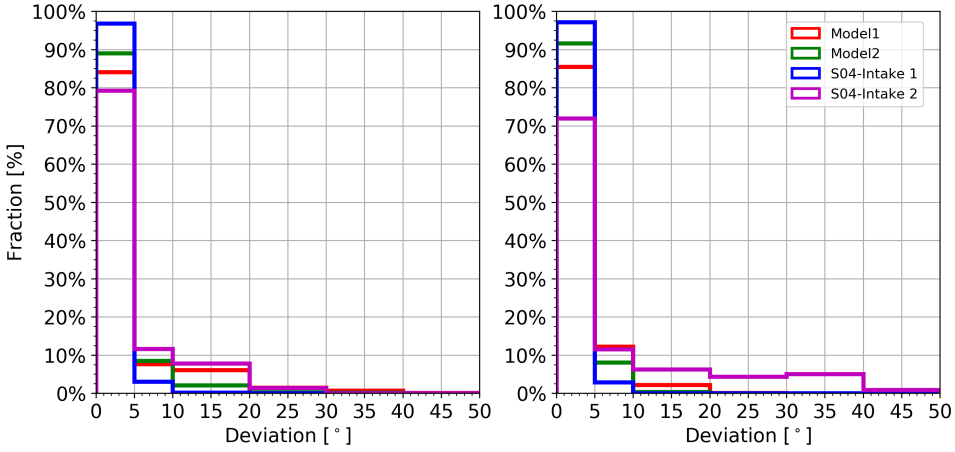

Figure 6.45: *Flow evaluation of the models S04, SM01 and SM02 for y (left) and z (right) components of the velocity vector at the new section, A_{DS}, based on Criterion 4 (C4) of the design guideline (Section 2.9).*

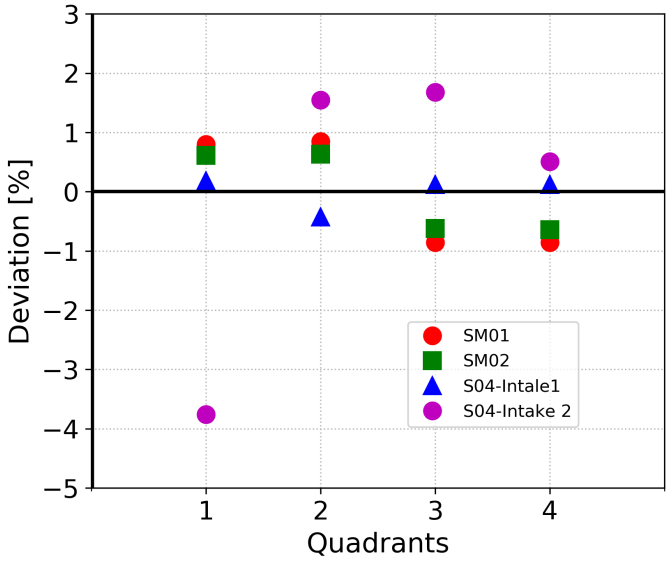

Figure 6.46: *Flow evaluation of the models S04, SM01 and SM02 at the new section, A_{DS}, based on Criterion 3 (C3) of the design guideline (Section 2.9).*

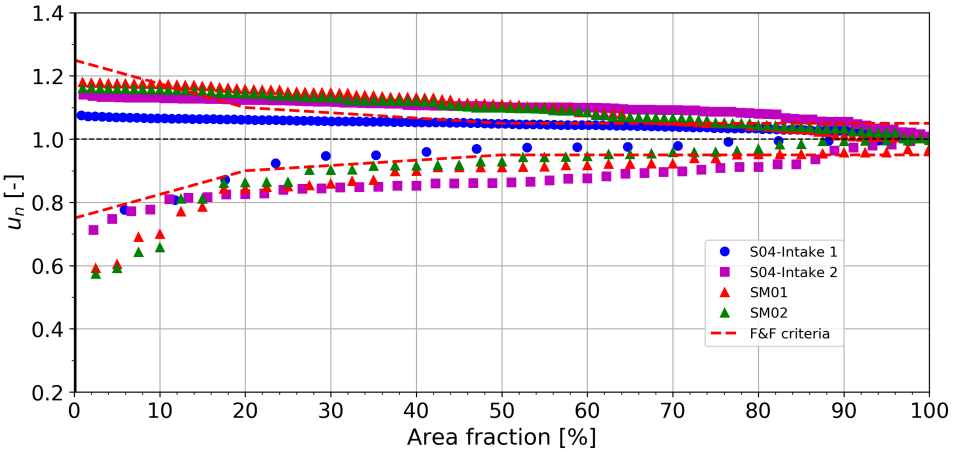

Figure 6.47: *Flow evaluation of the models S04, SM01 and SM02 at the new section, A_{DS}, based on Criterion 5 (C5) of the design guideline (Section 2.9). The values are computed from a grid of points instead of the whole section.*

7 EDDY-RESOLVING NUMERICAL SIMULATION

In Section 3.2.3, it is discussed that Hybrid RANS-LES approaches are relatively new techniques with promising capabilities to model complex flow problems. In comparison to LES, the computational costs of these models are relatively low. Among these methods, DES family of methods have been applied to relatively large hydraulic problems (see Section 3.2.3 for examples). In this section, improved version of DES, known as IDDES, is utilized to model the approach flow to the run-of-river. The mathematical formulation of the model is discussed in Section 3.2.3. The aim of this study is to use DES to gain better insight into the complex flow of this type of hydropower plant. Furthermore, it is important to identify the advantages and the drawbacks of this technique for modelling the approach flow including computational costs, boundary conditions, grid requirements and several more. In this Chapter, first the computational grid is described followed by the boundary conditions, more specifically the inflow condition. Then the results are presented for the periodic trapezoidal channel which is used for generating the inflow values. The results of this simulation is validated based on theoretical and empirical expressions. Finally, the results of the main domain is presented for various sections and parameters. The results are presented and discussed in two groups: time-averaged values and the instantaneous flow fields.

7.1 General computational aspects

In this study, third-order Runge-Kutta solver which is described and validated in Chapter 4 is used. Central differencing scheme is used for convective and diffusive terms. Furthermore, the maximum Courant number is set to 0.5 and the residual threshold is set to 1.0E-6 for all the equations. The simulations are carried out on Vienna Science Cluster (VSC3). The cluster consists of 2020 computational nodes with each node equipped with 2 intel Xeon E5-2650V2, 2.6 GHz, 8 cores. The nodes are internally connected with inlet QDR-80 dual-link high-speed infiniBand fabric. More specifically, the simulation of the periodic trapezoidal channel is carried out using 4 nodes (64 cores). However, the simulation of the main domain is carried out using 16 nodes (256 cores).

7.2 Computational grid

The procedure to generate the grid is presented in Section 6.2. The model operates in two mode, RANS near the walls and LES further away from the walls. It is important to resolve the boundary layer and provide adequate grid refinement near the walls. In this study, the first layer is generated in a way to achieve $y^+ = 1$ just about everywhere,

although it is shown (see for example Section 4.4.1.5) that much higher values are also possible. In the LES zone, the grid is refined in a way that the large eddies can be resolved. The required grid for the main domain is estimated using the precursor simulation of the periodic trapezoidal channel. Extra refinements are applied to the intake zones where the Reynolds number is higher due to the geometrical features and the higher velocities. The final grid consists of approximately 10 million hexahedra elements.

7.3 Boundary conditions

The boundary conditions are very similar to the RANS simulations (see Section 6.3) except the inlet which requires a special treatment. One of the difficulties in LES is to impose a realistic inflow boundary condition. In RANS, the inflow can be prescribed by constants values. These values can be obtained from analytical or empirical formulas for an open channel (Nezu and Nakagawa, 1993; Nikora and Goring, 2000). However, in LES, the inflow must contain realistic turbulent fluctuations as function of time and space. Moreover, the turbulent structures must contain realistic energy distribution and wave-number range. Extensive research have been carried out to develop techniques which provide the realistic turbulent contents as well as reduce the computational costs. A brief description of the techniques can be found in Georgiadis et al. (2010) and Rodi et al. (2013). In `OpenFOAM`, three methods, or combination of them, can be utilized to generate the inflow values:

- Precursor simulation: One of the common techniques in LES of open channels is to use a precursor simulation. In this case, a simple channel is modelled with periodic boundary condition in the streamwise direction (Figure 7.1). The simulation is carried out until a fully turbulent flow is obtained. Then the flow variables are stored for a particular cross section (e.g. outlet of the model) for a particular period of time. Then these values will be used as the inflow for the main simulation.
- Recycling/Rescaling: This technique first introduced by Spalart (1988) and later simplified for incompressible flows by Lund et al. (1998). The principal idea behind this technique is to extract flow variables at some location downstream and introducing these as the inflow in a dynamic way.
- Divergence Free Synthetic Eddy Method (DFSEM): This method is proposed by Poletto et al. (2013) and it is based on Synthetic Eddy Method (SEM) of Jarrin et al. (2009). The general idea behind the method is to continuously generate and inject synthetic eddies at the inlet to generate coherent flow structures that persist into the domain.

In this study, a precursor simulation in combination with DFSEM is used to generate realistic turbulent inflow for the main simulation using a periodic channel. The computational domain of the periodic channel is illustrated in Figure 7.1. The water depth, $H = 0.16$ meter and width of the channel, B, is approximately $4.6H$ with the bank angle of $33\,\mathrm{deg}$. In the streamwise direction The domain is extended to $D = 8H$. The average streamwise velocity is $0.075m/s$ leading to the Reynolds number, $R_e = 12000$, based on the water depth. The computational grid is generated using `blockMesh` utility consisting of approximately 2 million hexahedra elements. A coarsened computational grid is shown

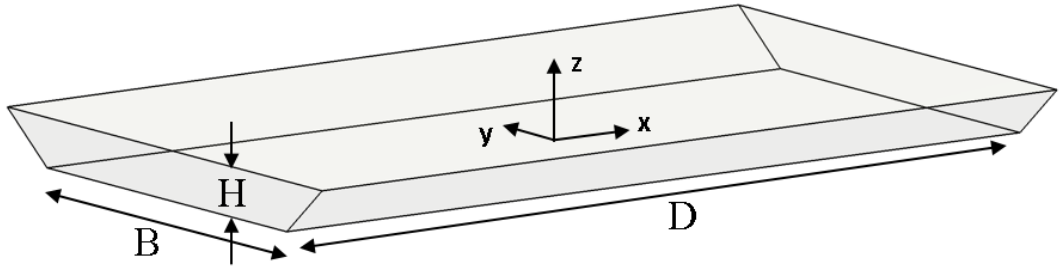

Figure 7.1: *Numerical domain of a straight channel with periodicity in streamwise direction.*

in Figure 7.2. The dimensionless grid spacing based on the wall shear stress at the center of the channel, here referred to as the global shear stress, in streamwise and spanwise directions are $\Delta X^+ = 40$ and $\Delta Y^+ = 20$ respectively. In the wall normal direction, computational grid consists of 50 layers where grid size is coarsen toward the water surface with the ratio of the largest element to the smallest is equal to 8. This ensures that $z^+ < 2$ everywhere based on the time-averaged values.

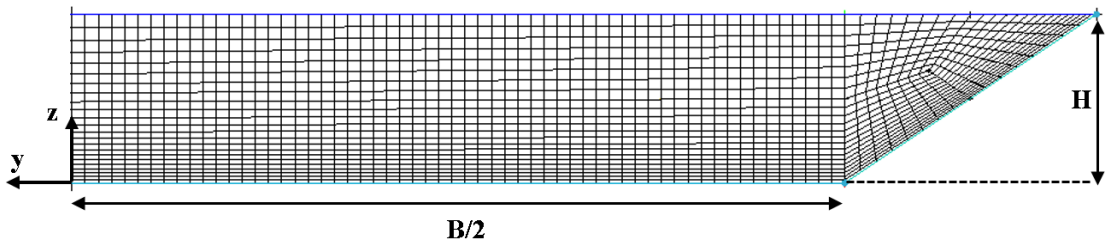

Figure 7.2: *Coarse computational grid of the trapezoidal channel.*

First the simulation is initialized using the DFSEM method to create a fully turbulent flow for 100 flow passes, then, the boundary conditions are changed to cyclic in streamwise direction and the simulation performed for another 100 flow passes. In the final step, the simulation continued for 1000 seconds and flow variables are stored at the outlet of the model. All the simulations are carried out using `RK3FracStepFoam` solver along with Second-order central differences for the convective and the diffusive terms. Finally, the results are analyzed to ensure accuracy and suitability of the computed values.

7.4 Results and Discussion

In this section, the results obtained from the DES are presented. It is organized in two main categories. First, the results from the simulation where the periodic trapezoidal channel is modelled are presented. The main focus is to validate the results using theoretical and experimental values and expressions related to open channels specially trapezoidal channel. In the second part, the results correspond to the main domain is presented. The mean values are computed and presented in a way to be comparable with the physical model tests and numerical results in Chapters 5 and 6. Additionally, the mean characteristics of the flow is investigated via mean values (velocities, streamlines, vorticity and turbulence parameters) for different sections along with visualization of the flow structures using the Q-criterion. This chapter is then concluded by study of the flow using instantaneous flow parameters. It is expected that these chapter gives an insight into the flow characteristics and hydrodynamic processes of the approach flow of such hydro power plants.

7.4.1 Flow in a trapezoidal periodic channel

In principle the streamwise velocity at the center of the channel must follow the log-law up to the water surface. Figure 7.3 shows the streamwise velocity profile at the center of the trapezoidal channel. It is shown that the computed values are in an excellent agreement with the theoretical values with mean y^+ values around 2 for the first point away from the wall. Figure 7.4 shows a contour plot of the velocity in streamwise direction. Only half of the channel is shown for clarity due to symmetry of the domain. Moreover, the results from the SKE model is also shown for comparison in Figure 7.4. It is evident that the results are different especially near the bank between DES and RANS. In the results obtained from DES, the bulging of the velocity is observed at the side wall. This bulging is also observed in experimental study of Tominaga et al. (1989) for trapezoidal channel. Additionally, similar to a study by Wright et al. (2004) where trapezoidal channel has been modelled using RANS and LES models, only results from LES are showed this bulging. Moreover, Wright et al. (2004) observed an additional bulging near the channel's bed similar to the results of DES in Figure 7.4. It is well-known that RANS models which are based on the eddy-viscosity hypothesis have shortcoming in predicting the secondary flow accurately and Reynolds stress equation models perform significantly better (Pope, 2001).

Previously, it is stated that DES works by operating in RANS mode near the walls and it switches to LES further away from the walls. This is illustrated in Figure 7.5 by plotting the DES regions. The RANS region located near the walls consists of 4 layers of elements. The transition from RANS to LES is occurring through two layers of elements and the model is operating in LES mode in the rest of the domain. The thickness of the RANS layer is relatively constant during the simulation.

One of the advantages of DES is that it predicts the secondary flows accurately in comparison with RANS. Figure 7.6 shows the secondary flow as well as vertical and spanwise velocity components close to the right bank of the channel. These secondary flows in trapezoidal channels are well known and they have been observed in numerical (Wright et al., 2004; Ansari, 2011) as well as experimental (Tominaga et al., 1989) studies. Also it can be seen from Figure 7.6 that three distinct secondary flow cells are presents from

the right wall to approximately $B/4$ distance from the wall. These secondary cells are illustrated in Figure 7.7 along with the results from the physical model tests results of Tominaga et al. (1989).

In order to evaluate further the accuracy of the computed values, in Figure 7.8, the turbulence intensities are plotted along a vertical line in the middle of the channel. The computed values are then compared with semi-theoretical expressions of Nezu and Nakagawa (1993):

$$u^{'}/u_{\tau} = 2.30exp(-z/H) \tag{7.1}$$

$$v^{'}/u_{\tau} = 1.63exp(-z/H) \tag{7.2}$$

$$w^{'}/u_{\tau} = 1.27exp(-z/H) \tag{7.3}$$

In general there is good agreement between the computed values and the semi-theoretical values,especially in $z/H > 0.2$ range. In vertical direction, the turbulence intensity is reduced to zero due to the boundary condition. In $z/H < 0.2$ however, the results are slightly differs. This differences are due to the characteristic of the Equations 7.1 to 7.3. A closer look at the measured values from Nezu and Nakagawa (1993) in Figure 7.10 shows that the computed values are in fact accurately computed. This is not only true for the magnitudes of the values but also the location of the peaks relative to the wall are accurately estimated. Analysis of the results in vertical direction is finalized by plotting turbulent kinetic energy in Figure 7.9. The computed values along the depth at the center of the channel is then compared to the expression for turbulent kinetic energy of Nezu and Nakagawa (1993):

$$k/u_{\tau}^2 = 4.78exp(-2z/H) \tag{7.4}$$

and Nikora and Goring (2000):

$$k/u_{\tau}^2 = 1.84 - 1.02ln(-z/H) \tag{7.5}$$

Figure 7.9 shows a good agreement between the computed values and the expression from Nezu and Nakagawa (1993). However, the values from Nikora and Goring (2000) are overpredicting the kinetic energy especially in $z/H > 0.2$.

We continue the analysis of the results by considering the spatial two-point autocorrelations of the velocity components in streamwise direction for several points. These results can be used to determine if the periodic length in streamwise direction is large enough. The locations of these points are illustrated in Figure 7.11. They are selected in a way that they cover most important zones of the computational domain. Figure 7.12 shows

the computed values in streamwise direction. At every point, the normalized two-points velocity correlations in all directions are reduced significantly at approximately $x/H = 1$. Furthermore, at $x/H = 3$, the values are well below 0.1. This perhaps indicates that the recycling distance can be reduced to $6H$. However, this is only true with a detailed study of the length scales and turbulent structures. Finally, it can be concluded that recycling distance of $8H$ is sufficient for the main analysis since all the values are sufficiently small.

The analysis of the results for the periodic trapezoidal channel is concluded by considering the instantaneous velocities. Figure 7.13 shows instantaneous streamwise velocities in three different depths. On the water surface, The mean streamwise velocities reaching up to approximately 1.18 times the bulk velocity. On the other hand, the instantaneous velocities on the water surface reaching up to 1.3 to 1.4 times the bulk velocity. The magnitude of the velocities decreasing when the other sections closer to the walls are compared. Visualization of the velocities near the wall reveals streaky like patterns in streamwise direction which is in agreement with the flow pattern near the walls.

To conclude this section, the computed values are in a good agreement with the experimental observation and expressions. This indicate that the model is accurately predicting the flow and it is suitable for generating the inflow values for the main simulations. The values are recorded for 1000 seconds at the outlet of the model and fed into the inlet of the main model.

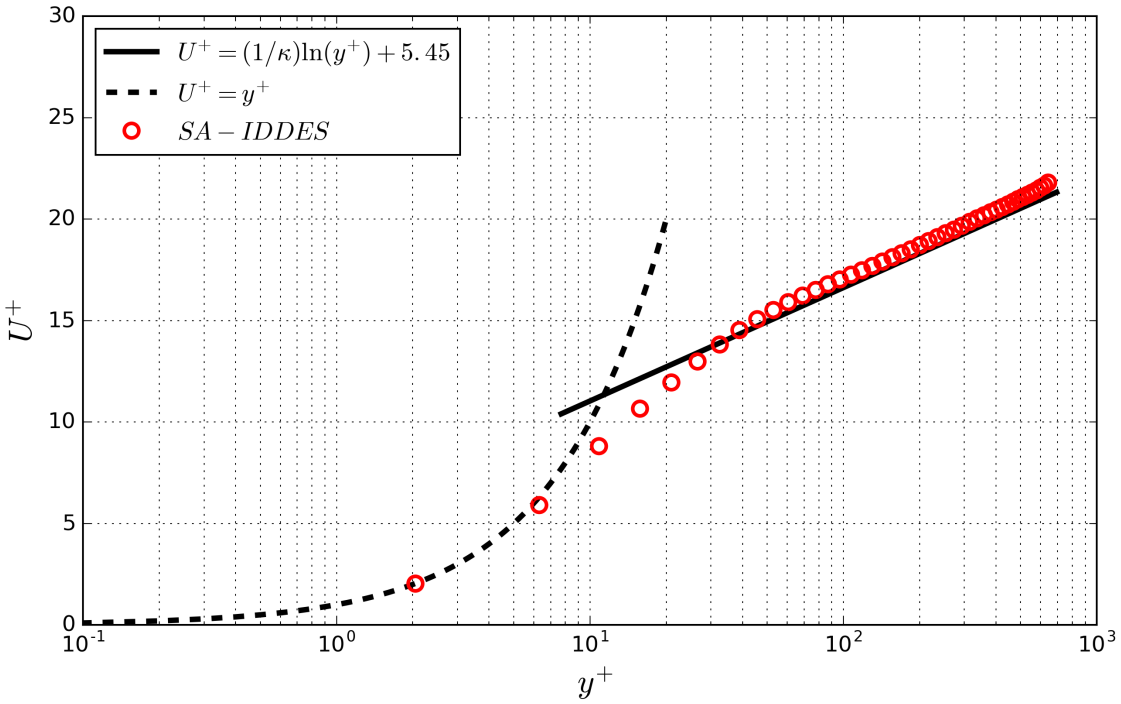

Figure 7.3: *Profile of mean streamwise velocity at the center of the channel.*

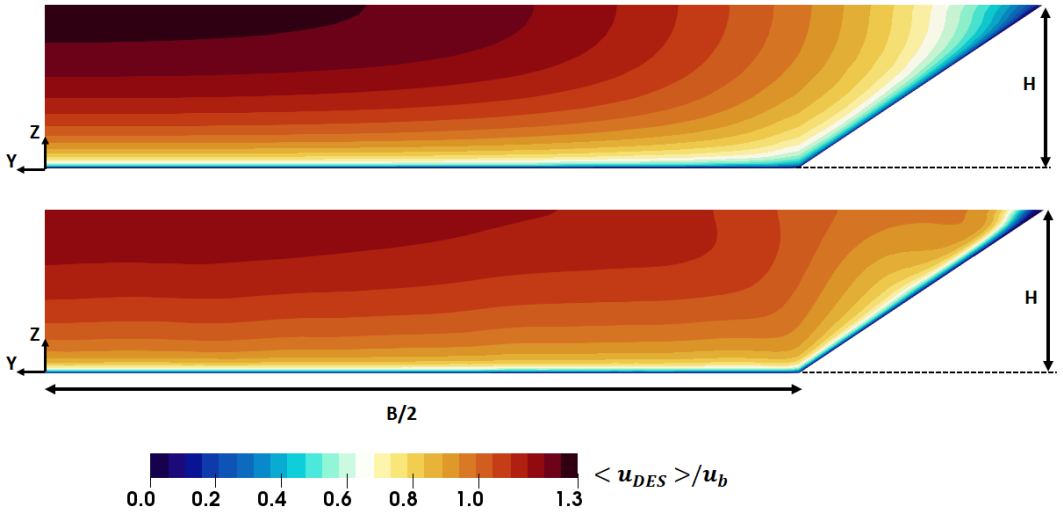

Figure 7.4: *Normalized streamwise velocity contour plot(top: from SSKE, bottom: SA-IDDES).*

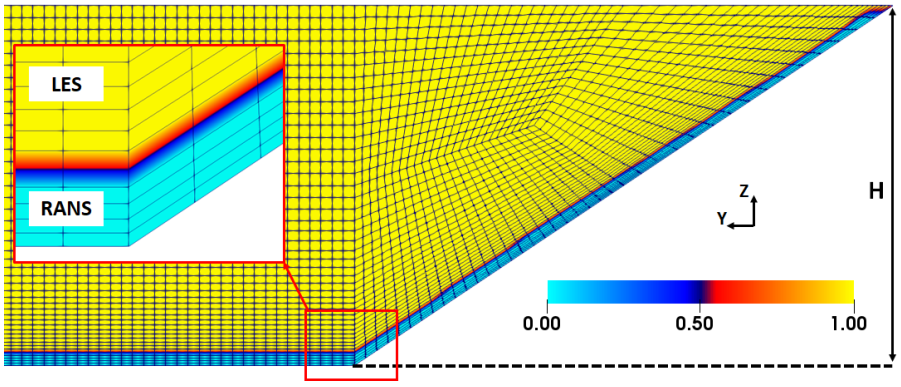

Figure 7.5: *Illustration of DES zones in the domain of the periodic trapezoidal channel.*

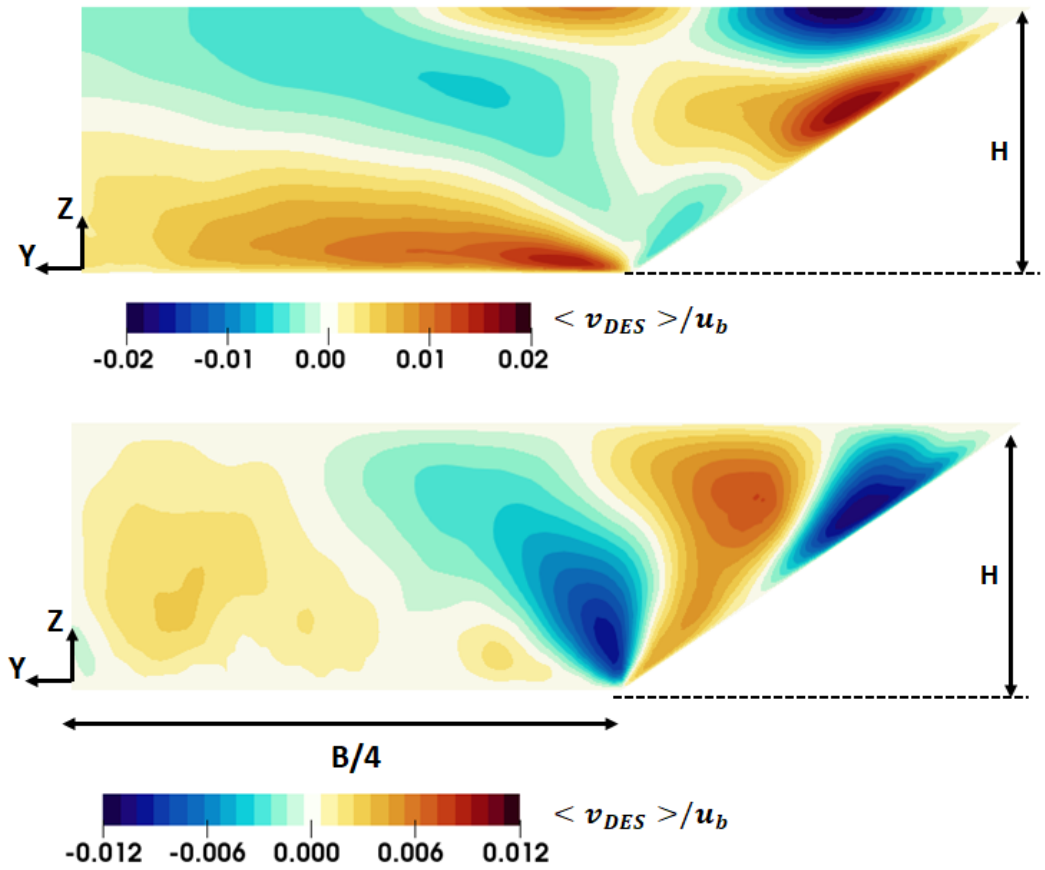

Figure 7.6: *The spanwise and vertical components of the velocity.*

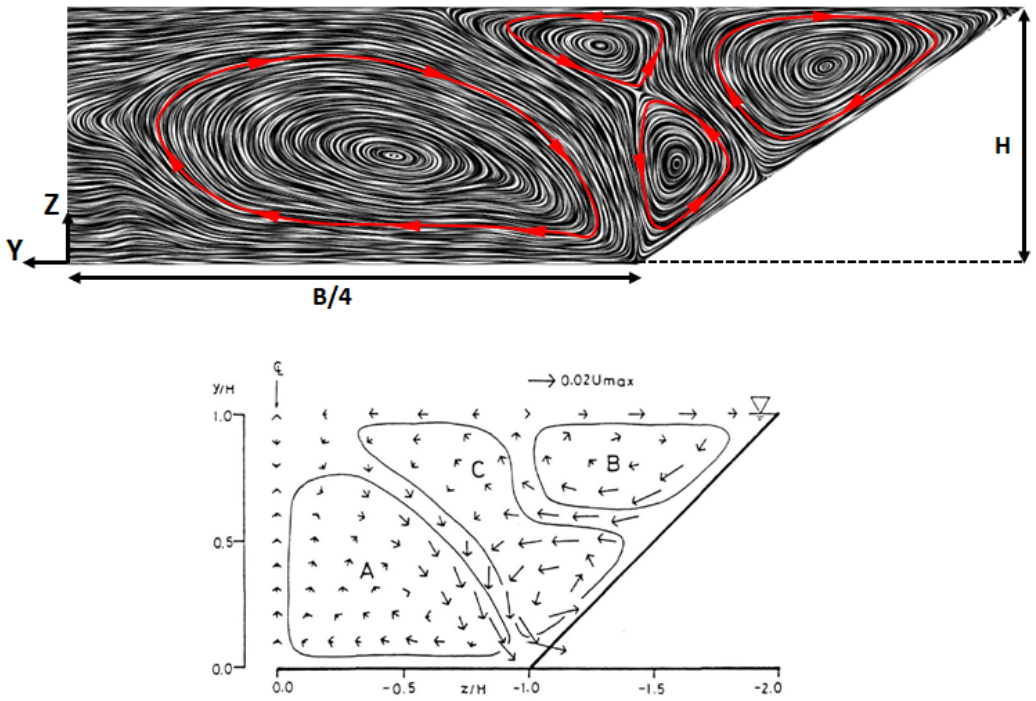

Figure 7.7: *Secondary flow cells pattern in smooth trapezoidal channel (Top: current study and bottom: experiment by Tominaga et al. (1989)).*

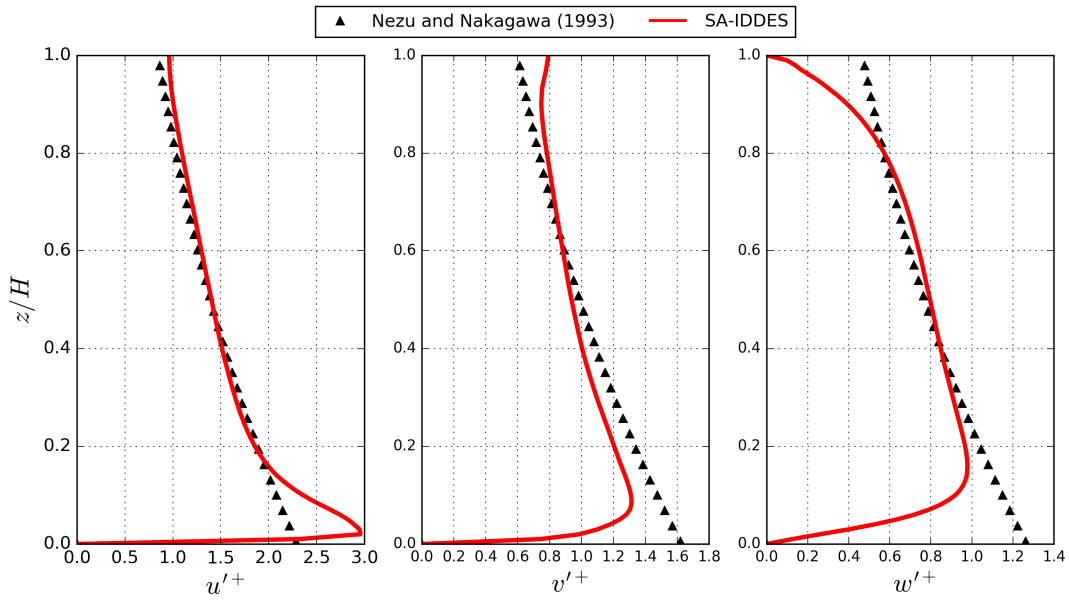

Figure 7.8: *Turbulence intensity profiles at the center of the channel in streamwise, spanwise and vertical directions. The semi-theoretical values are from Nezu and Nakagawa (1993).*

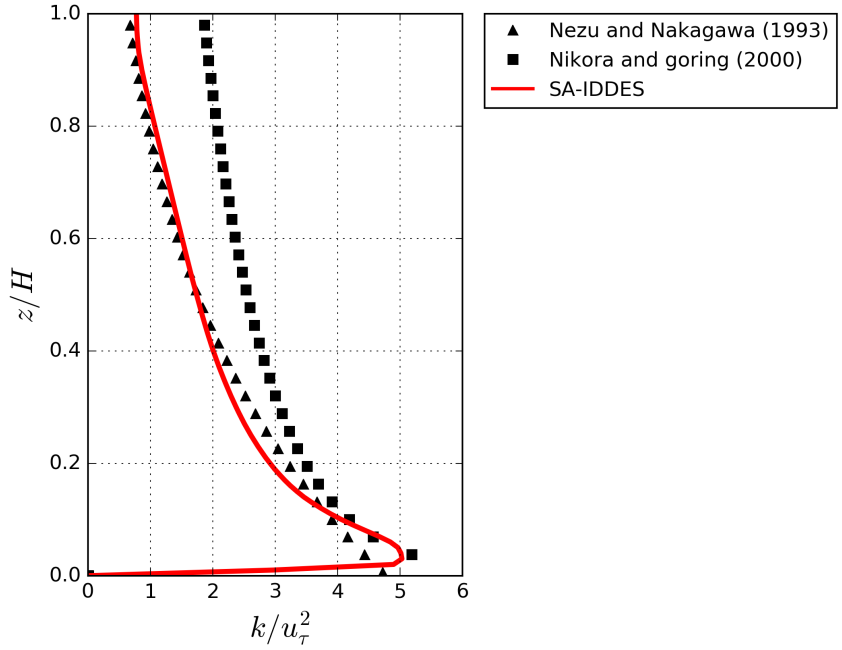

Figure 7.9: *Turbulence kinetic energy at the center of the channel in comparison with the semi-theoretical values from Nezu and Nakagawa (1993) and Nikora and Goring (2000).*

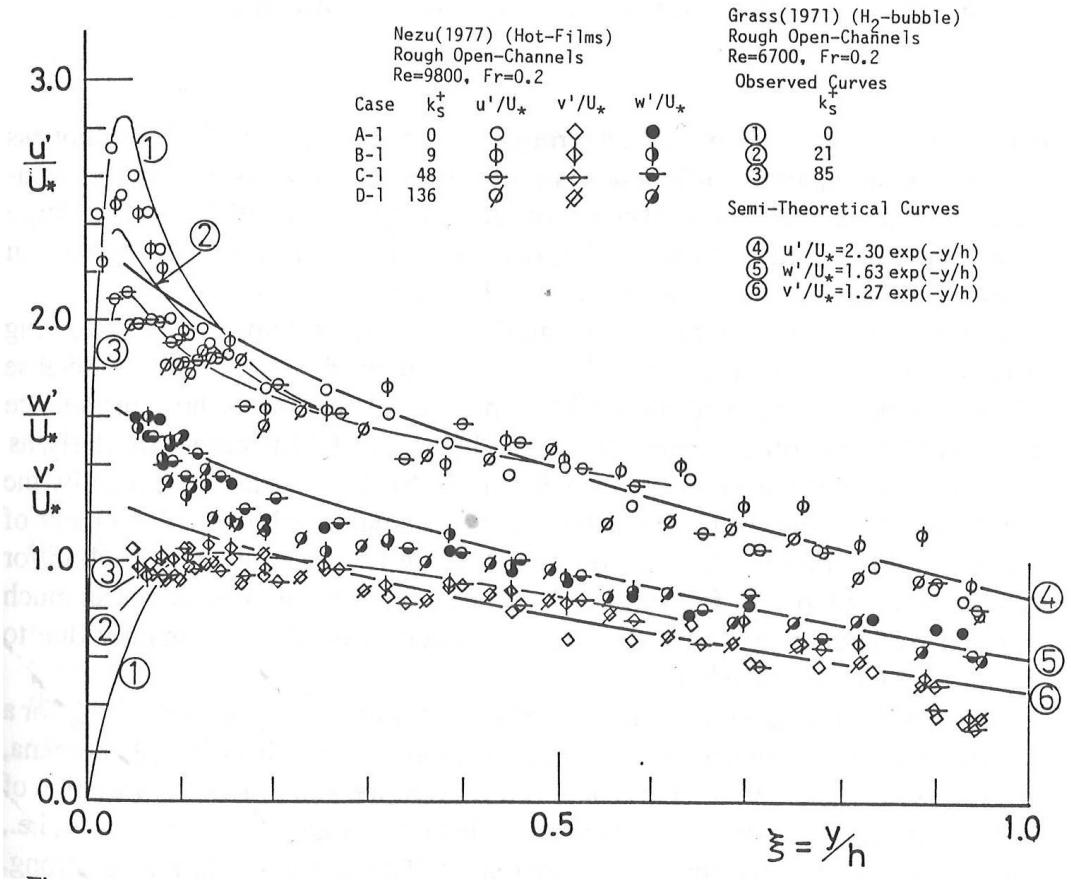

Figure 7.10: *Variation of turbulence intensities over smooth and rough beds as a function of y/h (Figure from Nezu and Nakagawa (1993)). Note that in order to this Figure be relevant to the periodic trapezoidal case, data corresponds to w' must be substitute with v' and vis-versa.*

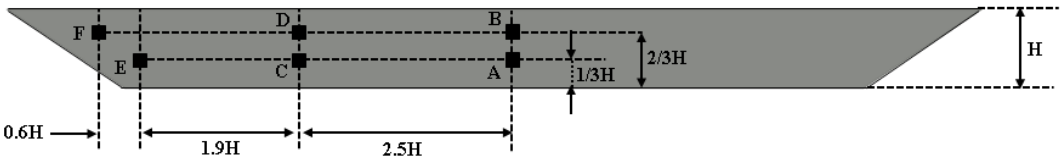

Figure 7.11: *Locations of the points where the two-points velocity correlation computed.*

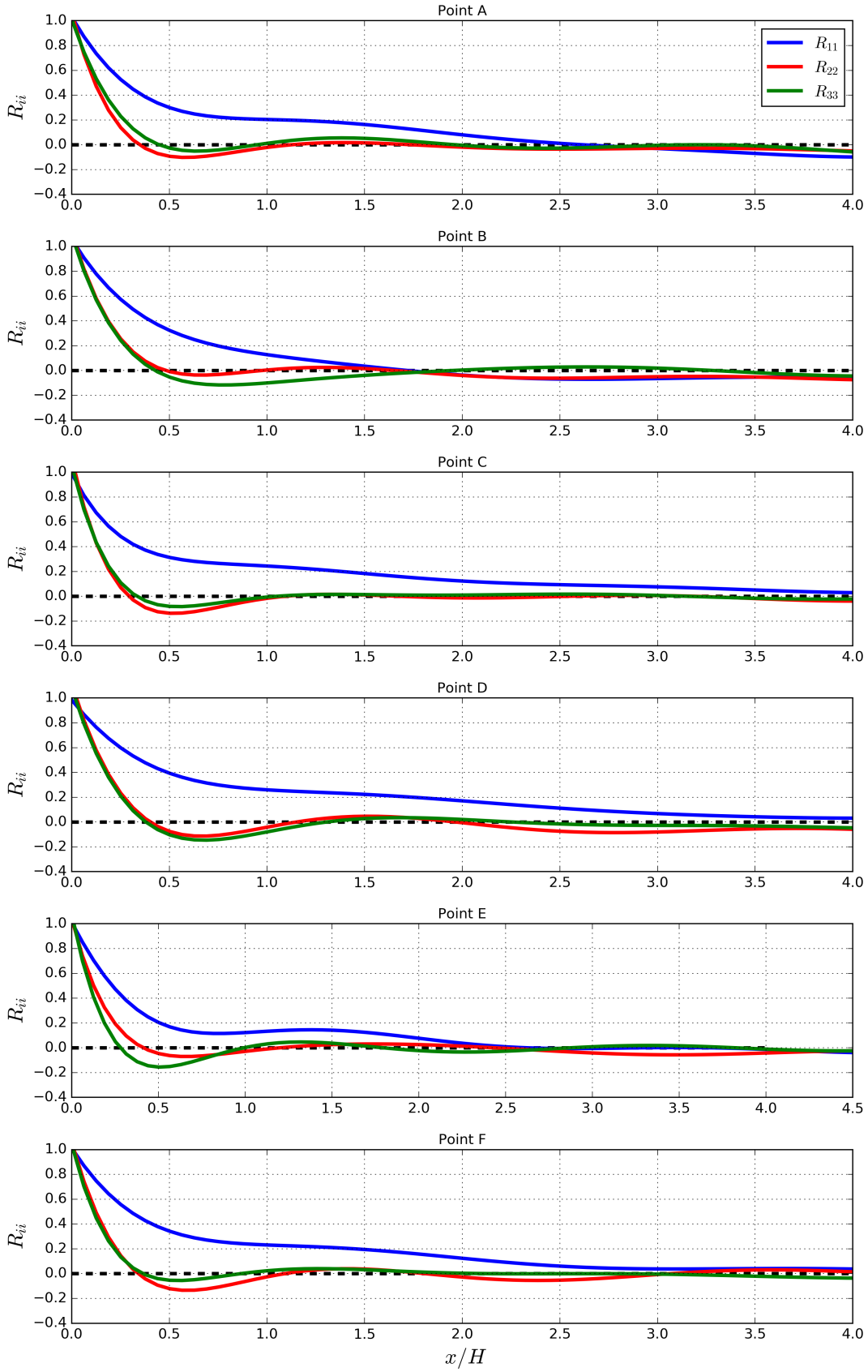

Figure 7.12: *Profiles of the spatial autocorrelations of the velocity components in streamwise direction.*

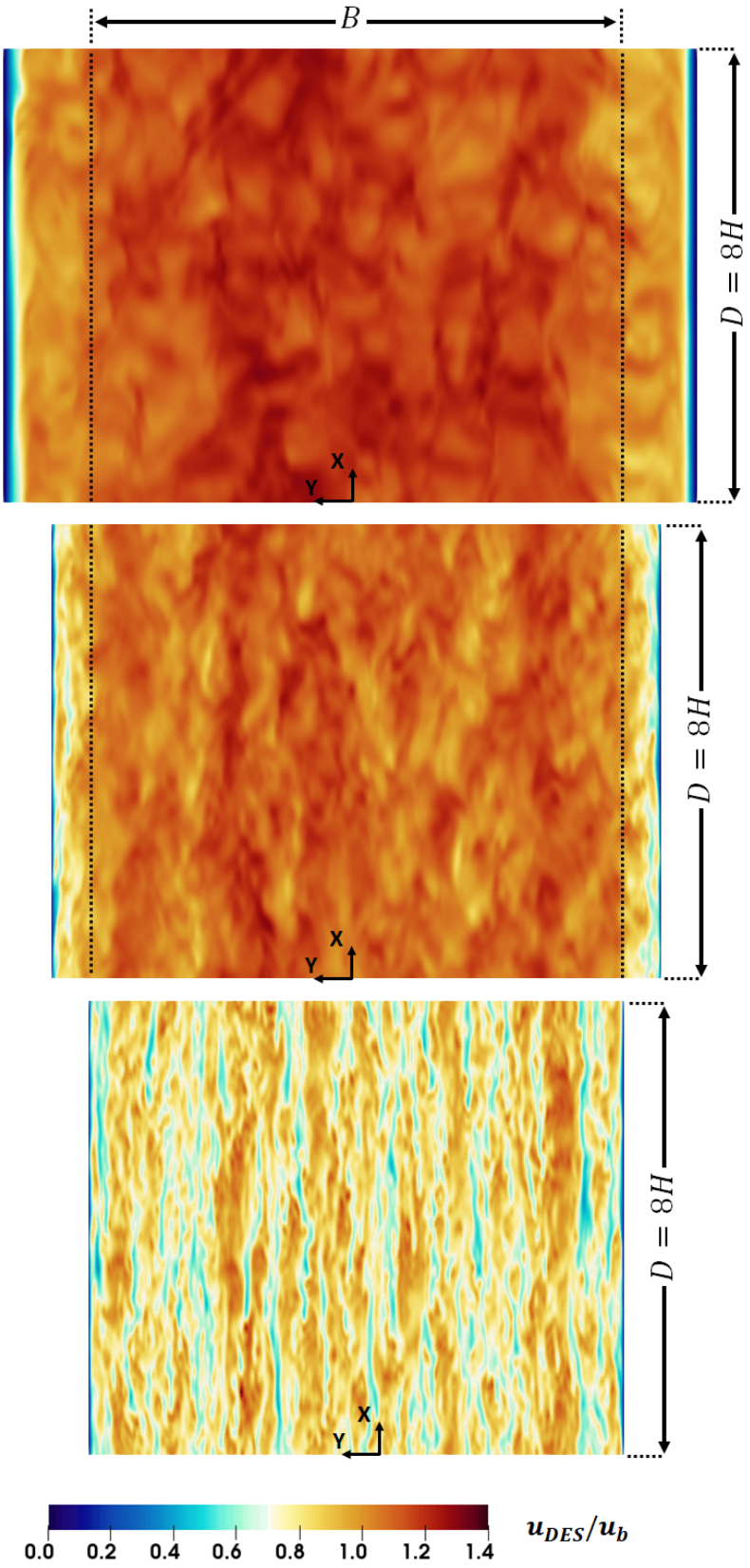

Figure 7.13: *Horizontal contour plots of instantanious streamwise velocities (top: water surface, middle: $H/2$ and bottom: close to the channel's bed).*

7.4.2 First- and Second-Order Statistics

The inflow boundary condition is generated using the procedure above. The values are saved for every second time step for 1000 seconds and applied to the inlet of the main domain. First a preliminary computation carried out for 1000 seconds (approximately 16 flow throw based on the bulk velocity ($u_b = 0.075\ m/s$) to establish a initial filed. Then, in the second part, the simulation performed for 20 flow through and mean values computed. The mean values consist of the velocity, Reynolds stress tensor and mean pressure. Convergence of the mean values are monitored via several probes mostly located in and upstream of the intakes.

7.4.2.1 Water surface

Figure 7.14 shows the magnitude of the mean velocities. Approximately 2/3 of the approach flow immediately takes a path toward the forebay and the intakes directly. On the other hand, the remaining third is taking a longer path through the left side of the reservoir and with a 90 degrees turn joins the approach flow to the intakes. As a consequence, the flow speeds up when it passes above and around the pier on the left side of the intakes. Furthermore, as the flow enters the expanded area and the forebay, a low velocity regions is created near the right bank. This is investigated later in this study using instantaneous velocities at vertical and horizontal sections. In general, the velocities which are computed for the water surface can represent the velocity distribution at the lower heights in the model.

7.4.2.2 Mean velocity at Section A

One of the most important section in this study is Section A (Figure 5.7) located inside the intake where the measurement has been performed. In Chapter 6, Section 6.7 , it is shown that different turbulence models computed slightly different velocity distribution in intake 2 due its complexity. Figures 7.15 and 7.16 show the mean velocities in x, y and z directions (local coordinate system where x direction represents out-of-plane direction). The results are dimensionless based on the average velocity of the section, u_{ave}. In general, there is a significant difference between the two intakes when the velocities in y and z directions are compared similar to what it is observed in the measurement as well as the RANS simulation. In intake 2, the maximum velocities in y direction are almost three times higher than intake 1. On the other hand, in z directions, the velocities in intake 2 are more than four times higher than the ones computed for intake 1 reaching up to 1.2 times the out-of-plane average velocity, u_{ave}, of the section.

The flow in intake 1 is almost identical to what it was measured (Figures 5.16 and 5.17) and simulated via RANS approach (Figures 6.14 to 6.16). The velocities in x direction shows high values at the top with a relatively sharp gradient toward the bottom of the section. These values are also plotted for each line of measurements and compared to the experimental results in Figure 7.17. It is shown that there is an excellent agreement between DES and the physical model test results at this section. In y direction, again similar to the RANS simulation results, the positive velocities are located at the bottom and the rest of the section is showing negative values. Although the results are closer to the measurement, there is a zone at the right hand side of the intake 1 where in measurements it is shown negative values, however, in both DES and RANS results a positive values are

computed. This is shown in Figure 7.19 where the computed values from line 1 to 7 are in excellent agreement with the measured values, however, near the right walls (lines 8 to 10) the differences are noticeable. Similarly, in z direction (Figure 7.21), the computed values are in good agreement with the physical model tests with exception of the measurements line 8 to 10 close to the right wall.

The contour plots of the computed mean velocities in intake 2 is shown in Figure 7.16. In x direction, the velocities are reaching up to 1.3 times the average velocity of the section at the top right corner. Also two low velocity zones are shown; one at the left side of the intake 2 and one at the top left corner. The overall agreement with the experiment is good. The computed values in x direction are slightly different compared to RANS simulations. However, a good agreement is achieved when the velocities are plotted for ten measurement lines and compared with the experiment in Figure 7.18 in x direction. In y direction, the results from DES is much closer to the measured values compared to RANS models. Three distinct zones are shown with all located at the left side of the intake 2 similar to the physical model test. The velocities in this directions are reaching up to 0.4 times the average velocity, slightly overestimated when they are compared with the physical model study. This is clearly shown in Figure 7.20 where the DES results are compared with the measured values. Also, the size of the zone is estimated to be larger than the one measured in the physical model study. It is worth noting that only SST turbulence model predicted these zones relatively accurately, however, this model shown additional zones at the left bottom corner of the intake (see Figure 6.15). This zone was not observed in the experiment (Figure 5.17) and not predicted by DES model in Figure 7.16.

Finally, in z direction, similar to RANS study, two zones with high positive and negative values are predicted at the left side of the intake. In the negative range the values are reaching up to 0.4 times the average velocity, however, in the positive zone, the value reaches up to 1.1 times the average velocity. Due to the size of this region, in the model test, only a small portion of it is shown. This high velocity is also predicted by the RANS models with the results from SST showed the high value similar to DES compared to the model test's results. Figure 7.22 shows the computed values in z direction versus the measured values for 10 measurement lines. It is evident that the predicted values are much higher at L1. On the other hand, comparison of the results at L2 suggests that at this point, the measured velocities are changing the sign which it suggests that at this line the flow is in the negative zone. However, predicted values are showing that the positive zone is extended to L2 and the transition is occurring further away from the wall (L3 for example). Moreover, agreement between DES and experiment is relatively good for the rest of the section.

7.4.2.3 Turbulence quantities at Section A

One of the advantages of DES over RANS models (based on eddy viscosity) is the possibility to compute turbulence intensities in all directions. Hence here these values are computed and presented in Figures 7.23 and 7.24 respectively. In intake 1 the turbulence intensities are relatively uniform in comparison with intake 2. High values are located at the bottom and corners, however, the most distinguishable feature is a small zone with high turbulence intensity at the upper left side of the intake 1. This zone is more pronounced in z and especially in y direction. A closer look reveals that this zone is the

location of the vortex rope 1 which is visualized in Figure 7.38. In Figure 7.25, the kinetic energy for intake 1 is shown where this particular zone is clearly distinguished from the rest with high values. Moreover, this zone is not captured by the physical model study, perhaps, due to its small size and its proximity to the wall. In the RANS study, only SST model predicted this vortical structure. Contour plots of the out-of-plane vorticity in Figure 7.27 shows additional rotating flow at the bottom of the section. This is also confirmed by the plot of the tangantial vector plots and the streamlines in Figure 7.26. This rotating flow is illustrated by vortex rope 4 in Figure 7.38. This type of flow is also observed when a simplified model of the intake is investigated in Section 6.8. A vertical section through the intake 1 is shown in Figure 7.36. The Figure is also shown the effect of the slope in generating such rotating flow. In y direction, there are two distinguishable zones present with the first on near the bottom of the slopes with high positive velocities and one further upstream with high negative values over the first zone. Contour plot of the kinetic energy is also shows this highly turbulent layer in Figure 7.36.

In Figure 7.24, the turbulence intensities in x, y and z directions are shown. Compared to intake 1, the values are much higher especially at the left side of the section. This was also observed in physical model test in Figure 5.19. At least two zones with high turbulence intensity values are present, however, the locations of these zones are further away from the wall in comparison with the physical model test. On the other hand, the values are in a good agreement with the physical model results. Figure 7.25 shows the computed kinetic energy. It is shown that these values are almost one order of magnitude higher than the intake 1 due to the strong rotating flow which is generated from the geometrical features upstream of the intake. This rotating flows are also detected from the contour plots of the mean velocities. The surface streamlines at intake 2 in Figure 7.26 clearly indicates these flows. Further investigation via the out-of-plane vorticity in Figure 7.27 reveals two rotating flow in clockwise directions; one from $z/H = 0.3$ to 0.7 in vertical direction and one from $y/B = 0.9$ to 0.7. These flow structures are visualized by isosurface of the Q-criterion in Figure 7.39 where vortex ropes 2 and 3 are correspond to lower and upper zones. Furthermore, the effects of these rotating bodies are extended to $y/B = 0.5$ (the center line) of the section. This is also shown in Figure 7.37 where a contour plot of the velocity components are illustrated. The hydrodynamic processes which give rise to these flow structures are discussed later.

7.4.2.4 Flow at Section A_{DS}

It is also important to investigate the flow condition further downstream and well inside the intake where the flow is approaching the turbines. Therefore, the flow condition is also studied and evaluated at a section which previously defined in Section 6.9. The location of the section is illustrated in Figure 6.40. Figure 7.28 shows the mean velocities in x, y and z directions for both intakes. In intake 1, the velocities are fairly uniform with small zone on the outer top corners showing low velocities in x direction. The computed mean velocities are almost identical to the RANS model in Figure 6.42. On the other hand, in intake 2 on the left side, the same swirling flow is present. This is identifiable by low velocity in x direction on the top followed by two zones with opposite signs at the same location in y and z directions. This clockwise rotating flow is illustrated by the contour plot of the out-of-plane vorticity in Figure 7.32. This energetic flow has high turbulence intensities and consequently high kinetic energy as it is shown in Figures 7.29 and 7.30

with intensity values reaching up to four times the average intensities. Similarly, the Turbulence shear stresses are also significantly high in this zone as it is shown in Figure 7.31.

7.4.2.5 Upstream flow condition and vortical structures

It is profoundly important to identify the cause of this rotating flow. Clearly, this is due to the upstream geometrical features, therefore, the flow is investigated upstream of the intakes for three vertical sections, B to D, in Figures 7.33 to 7.35. The locations of these sections are shown in Figure 5.6. Additionally, the vortical structures are visualized by isosurface of Q-criterion in Figure 7.39. We start the discussion from upstream of the intakes at Section D immediately before the slope. Figure 7.35 shows the velocities at this Section. In x direction, the high velocity flow is deviated to the right bank. In the contour plots of velocity in y direction a distinct separation can be seen immediately after the step. This separation, very much like a forward step, occurs due to the approach velocity from the left. Due to the angle of the approach flow and the main flow direction at the right side, the generated separation and consequently vortical structures are inclined toward the direction of the main flow. This is shown in Figure 7.39 with vortex rope 1. This separated zone also led to high values of kinetic energy in Figure 7.35. Furthermore, the length of this zone is approximately 3.6 times the step height approximated by the plot of the vectors and the streamlines in Figure 7.35. Later in Section 7.4.3, this topic will be discussed further by visualization and studying the instantaneous velocities.

In order to understand the hydrodynamic processes which give rise to the swirling flow at the left side of the intake 2, two additional sections are considered. These sections are intermediate sections between the intakes and the beginning of the slope (Section B and C in Figure 5.6). It is shown that as we approach closer to the intakes, the intensity of the swirling flow increases. Similar to the flow in Section D, the angle of the approaching flow from the left side is perpendicular to the divider wall. This and the high velocity flow in the streamwise direction interacts with each other at these points and generate the swirling flow. The intensity of this flow increases as it move downstream due to the increase in step's height and attachment of the upstream to the downstream vortices. Moreover, it is shown in Figure 7.33 that the high velocity flow from the left pushes the streamwise flow to the right. Unlike flow at Section D where the separated zone extend horizontally due to the bed of the forebay, in these sections, the separated flow is vertical, located immediately on the right side of the divider wall. This vortical flow structure is indicated in Figure 7.39 as vortex rope 2 by isosurface of Q-criterion.

Finally, there are other vortical structures present near the intakes. At the right hand side of the intake structure two vortices are detected (see Figure 7.38). Vortex rope 2 is located near the water surface and it generated by the relatively sudden bend of the wall. Similarly, due to the bend as well as the transition of the inclined to the vertical bank, vortex rope 3 is generated and extended downstream. Vortex number 5 is a common type which happens at the front of a bridge piers or any cylindrical structures. These vortices, also known as necklace vortices, is well known (see for example Kirkil et al. (2008)). These are also observed inside the intakes before the turbine structures due to their round shapes. Moving to the left side of the intake structure in Figure 7.39, vortex 1 is generated by the step and it is discussed before. Similarly, vortex 2 is the product of the two perpendicular flow in combination with gradually deepening divider wall. Vortex

3 is generated by the pillar when the high velocity flow from the left side of the intakes making their way through the entrance. Finally, additional vortex is observed (Vortex 4) in front of the pillar where the deeper flow on the left side is joining the main flow. This is also shown in Figure 7.45d where dye added to the flow behind the pillar. It is worth mentioning that only SST model was able to predict most of these vortical structure. However, this model predicted an additional vertical vortex from the water surface to the entrance which was not observe in the DES results.

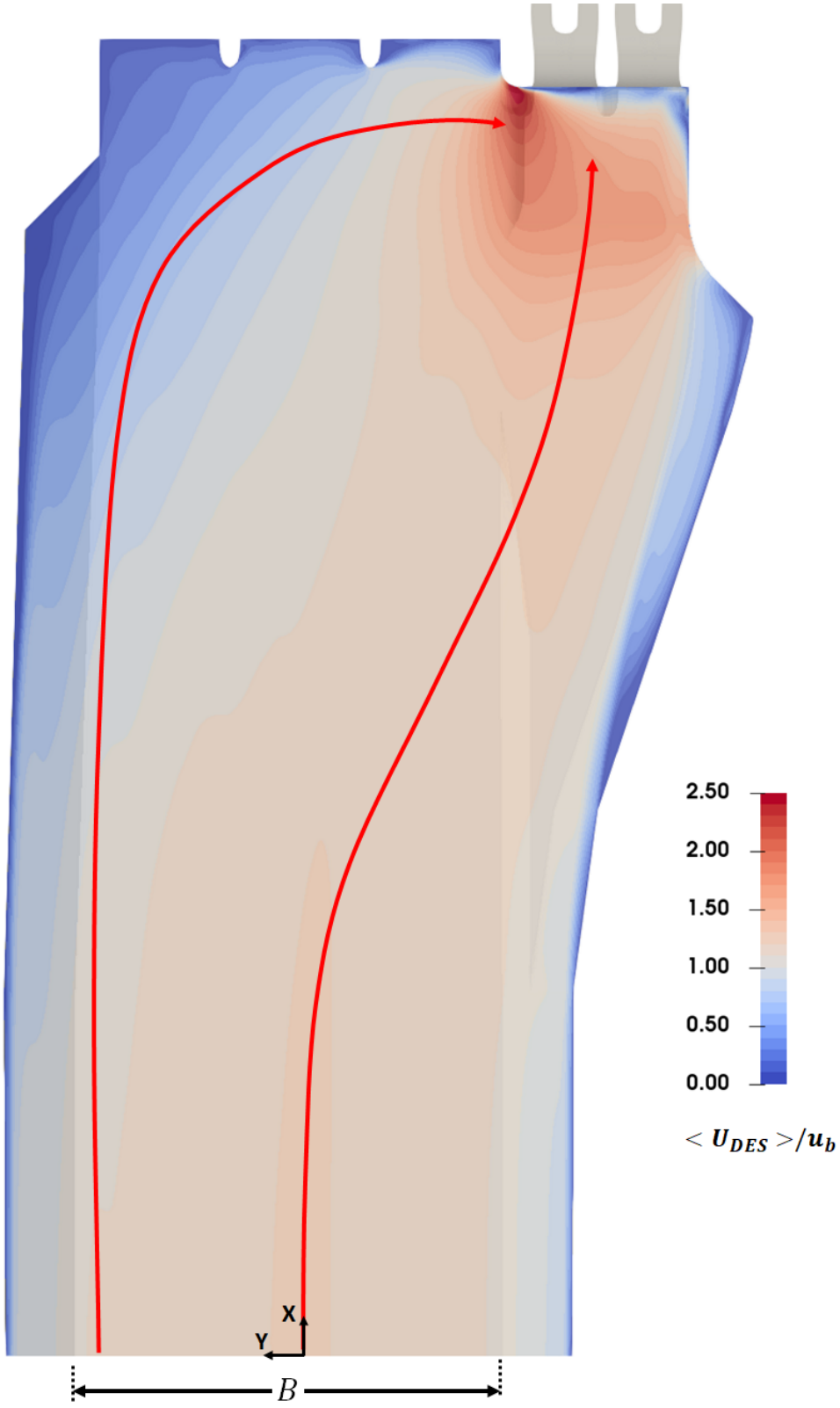

Figure 7.14: *Contour plots of the velocity magnitude at the water surface normalized based on the average velocity at the inlet.*

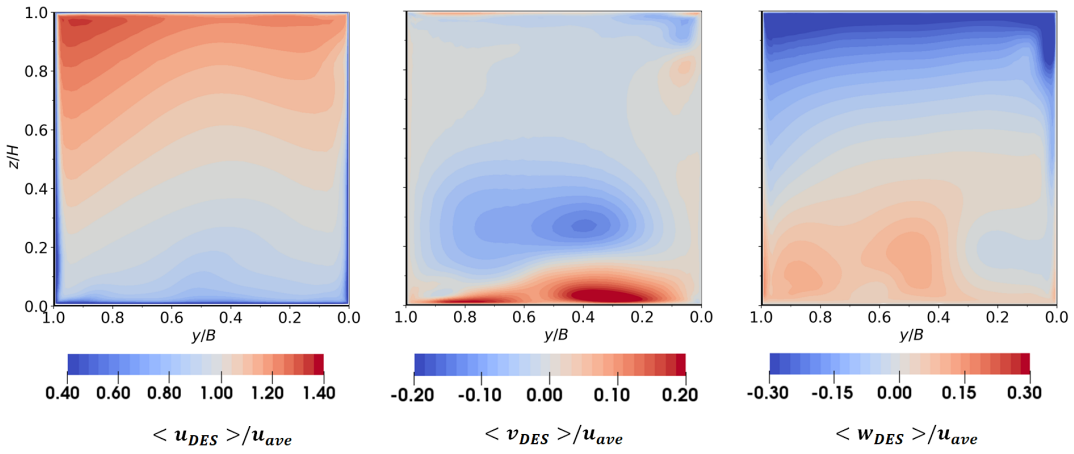

Figure 7.15: *Contour plots of velocity components at Section A, Turbine 1.*

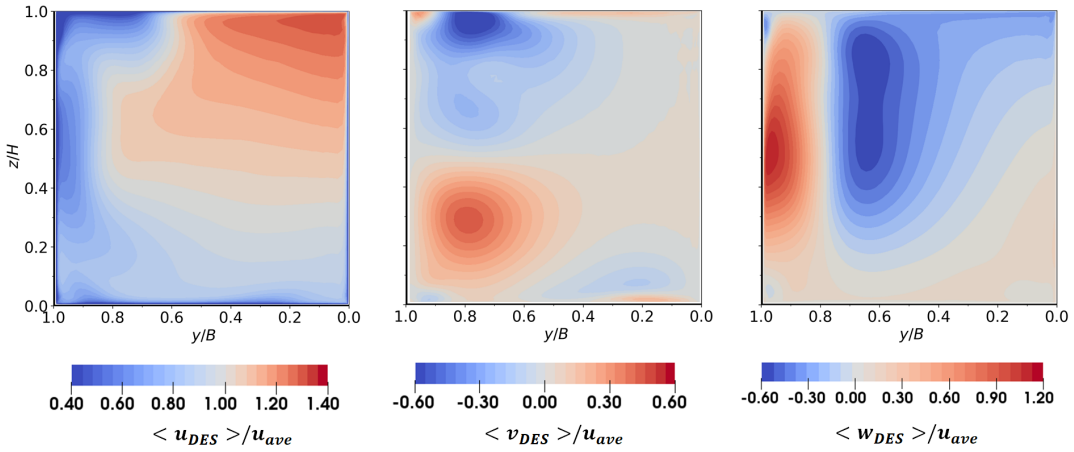

Figure 7.16: *Contour plots of velocity components at Section A, Turbine 2.*

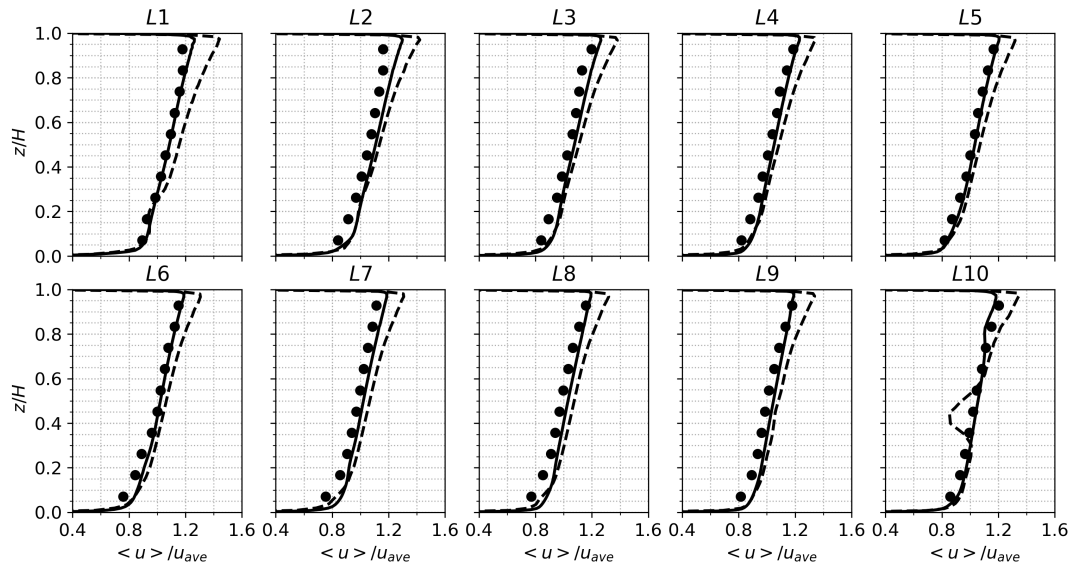

Figure 7.17: *Time averaged Streamwise or out-of-plane velocities at the measurement lines in intake 1 (solid lines: DES, dashed-lines: RANS-SST and markers: Experiment).*

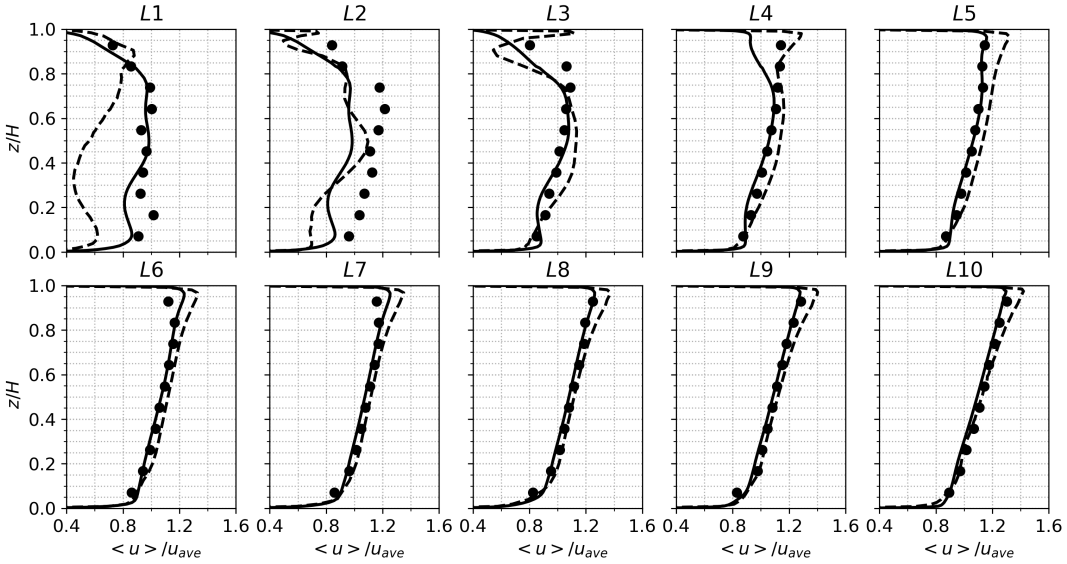

Figure 7.18: *Time averaged Streamwise or out-of-plane velocities at the measurement lines in intake 2 (solid lines: DES, dashed-lines: RANS-SST and markers: Experiment).*

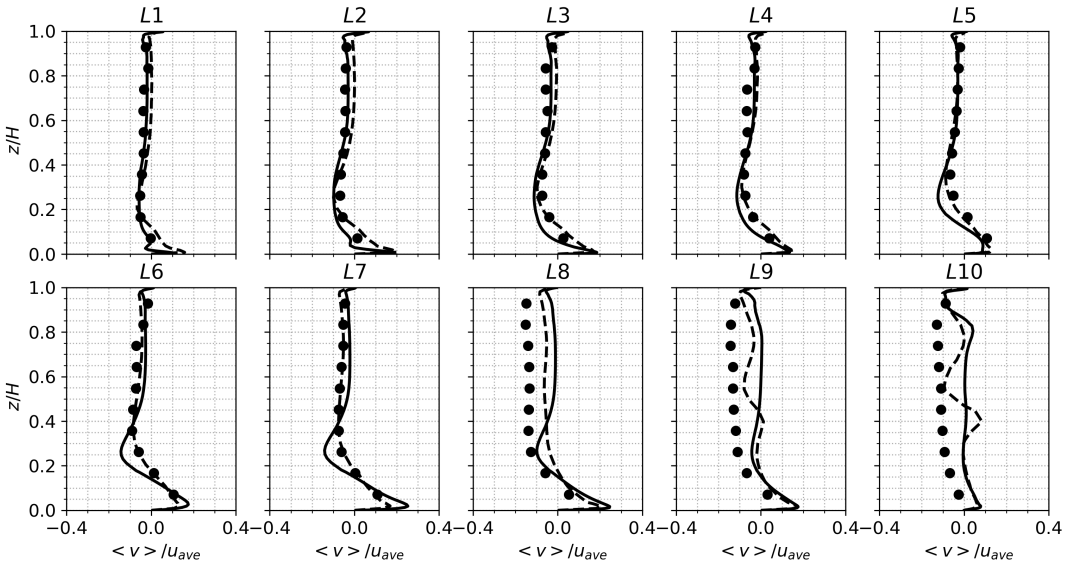

Figure 7.19: *Time averaged y component of velocities at the measurement lines in intake 1 (solid lines: DES, dashed-lines: RANS-SST and markers: Experiment).*

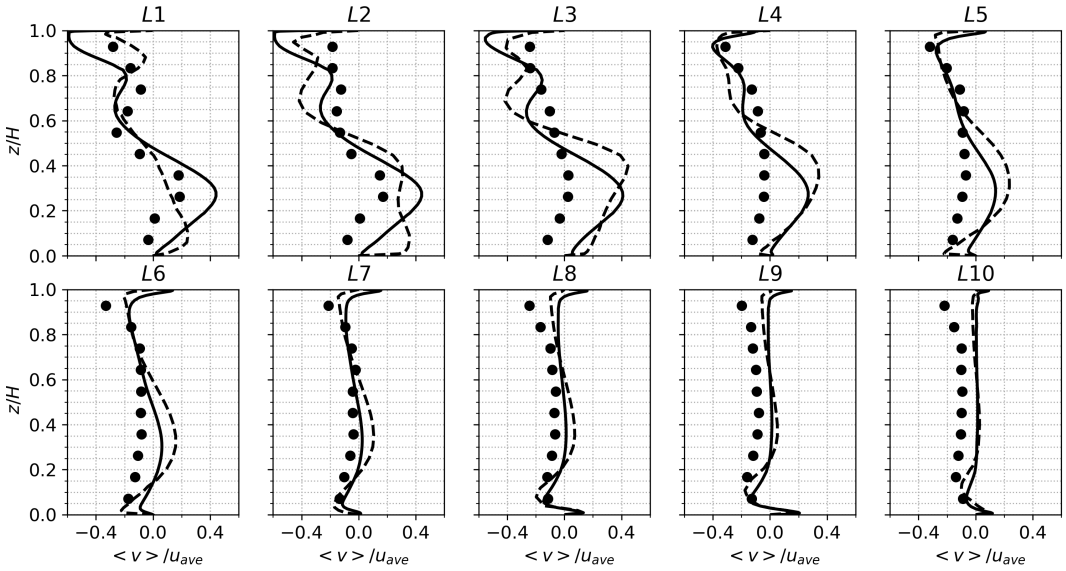

Figure 7.20: *Time averaged y component of velocities at the measurement lines in intake 2 (solid lines: DES, dashed-lines: RANS-SST and markers: Experiment).*

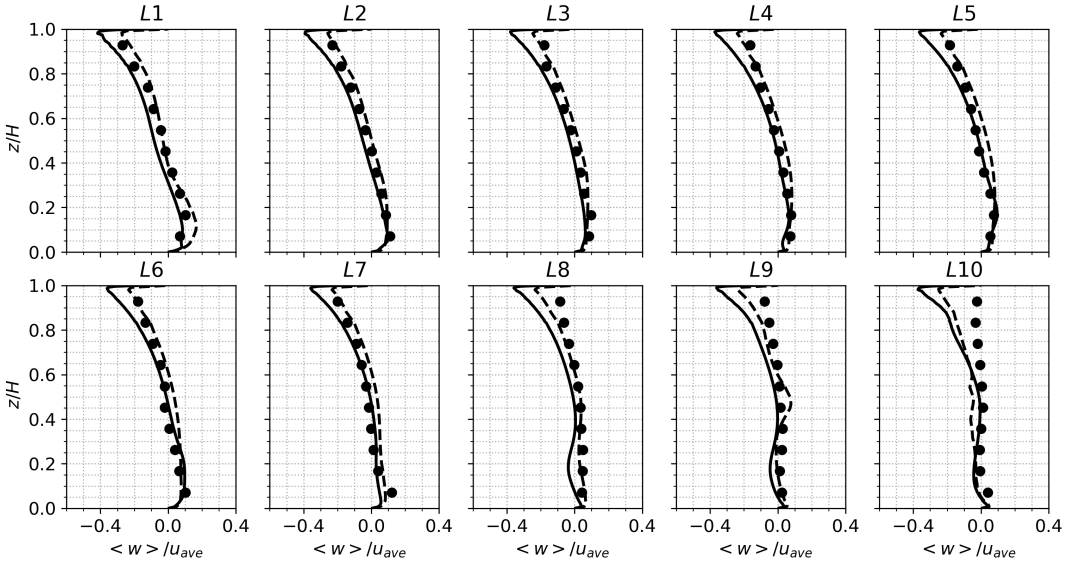

Figure 7.21: *Time averaged z component of velocities at the measurement lines in intake 1 (solid lines: DES, dashed-lines: RANS-SST and markers: Experiment).*

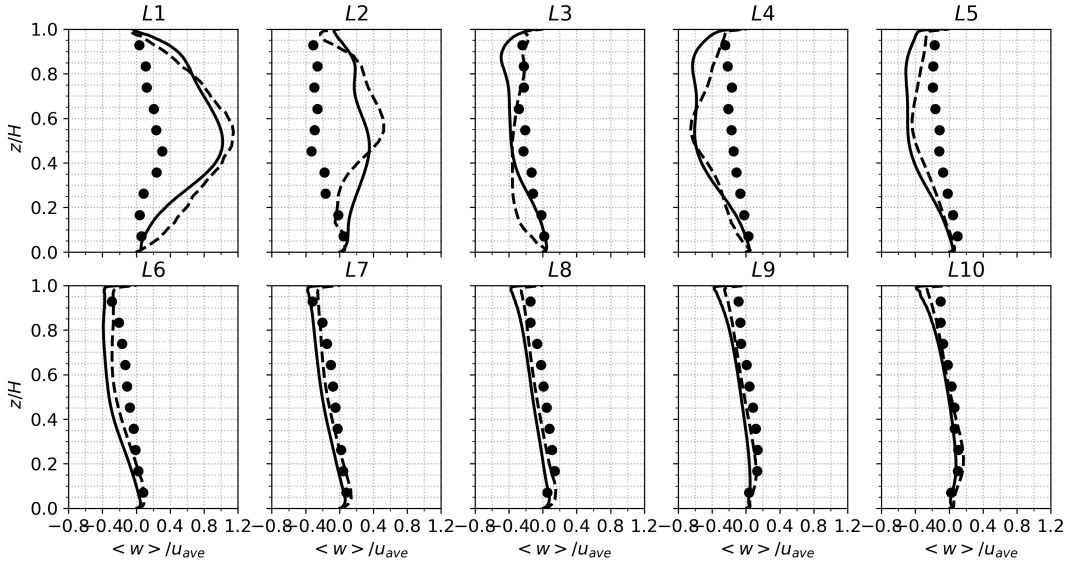

Figure 7.22: *Time averaged z component of velocities at the measurement lines in intake 2 (solid lines: DES, dashed-lines: RANS-SST and markers: Experiment).*

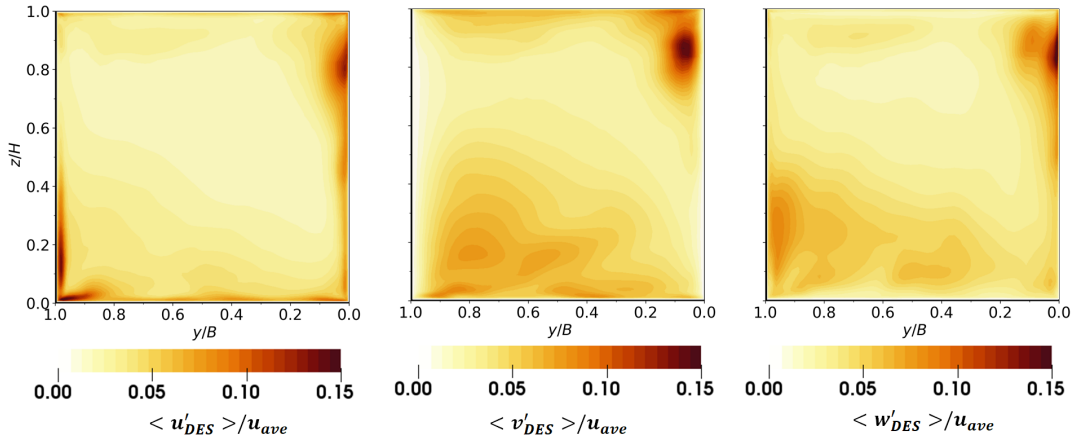

Figure 7.23: *Turbulence intensities at Section A, Turbine 1.*

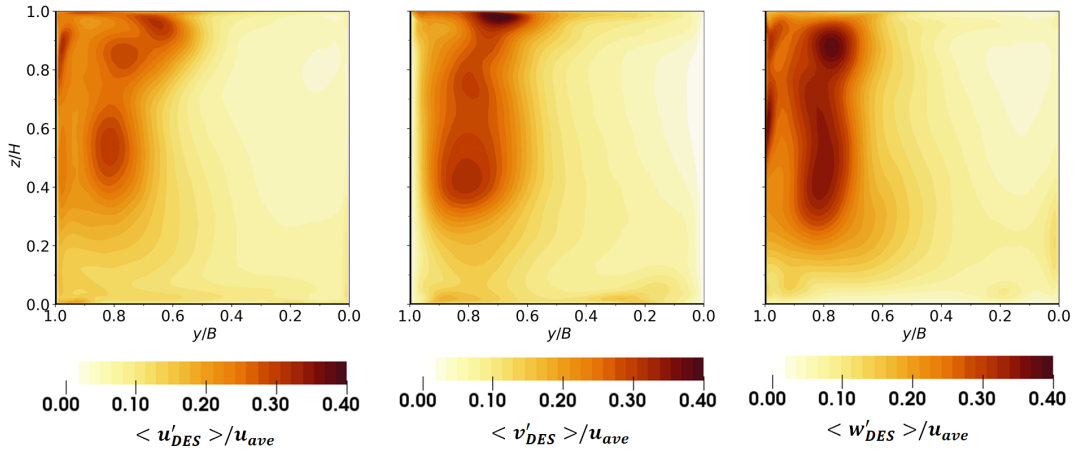

Figure 7.24: *Turbulence intensities at Section A, Turbine 2.*

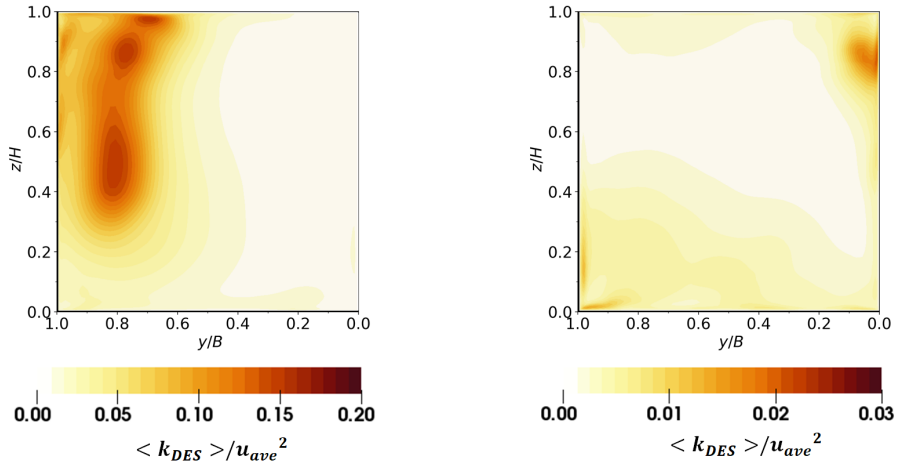

Figure 7.25: *Turbulence kinetic energy at Section A (right: Turbine 1 and left: Turbine 2).*

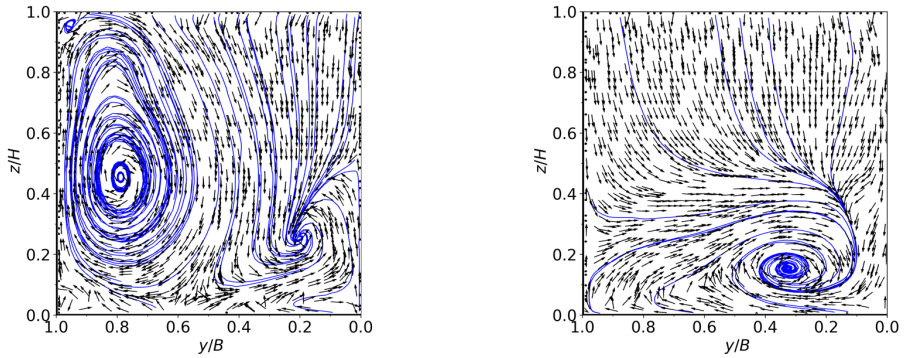

Figure 7.26: *Surface streamlines and vectors at Section A (right: Turbine 1 and left: Turbine 2).*

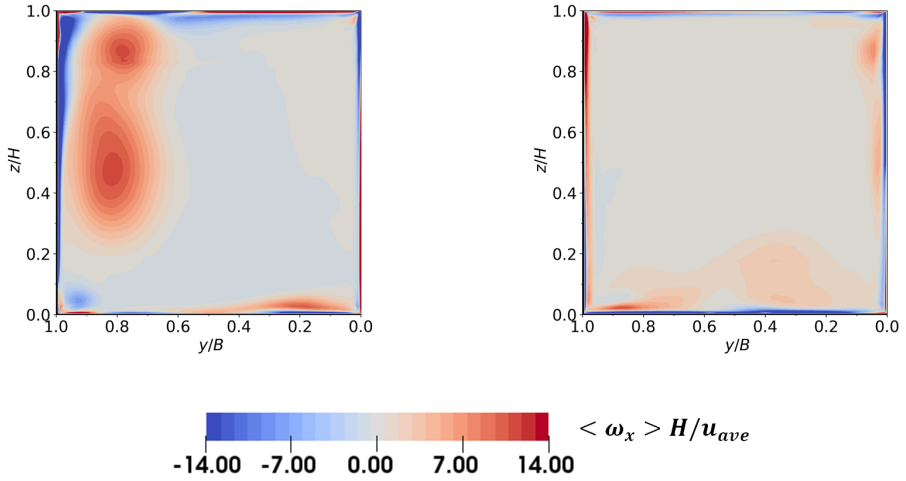

Figure 7.27: *Streamwise or out-of-plane vorticity at Section A (right: Turbine 1 and left: Turbine 2).*

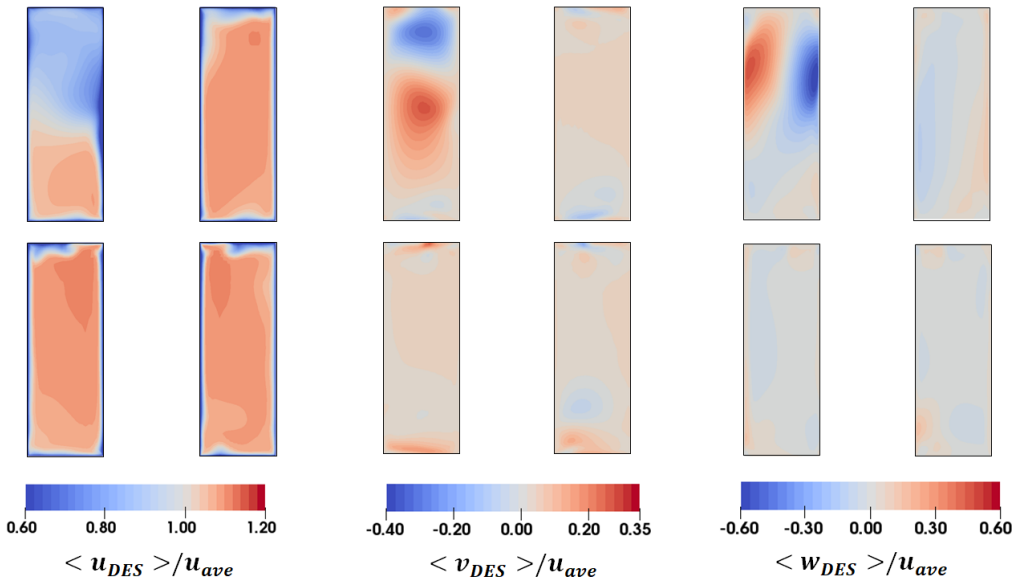

Figure 7.28: *Contour plots of time averaged velocity components at Section A_{DS} (top row: Turbine 2 and bottom row: Turbine 1).*

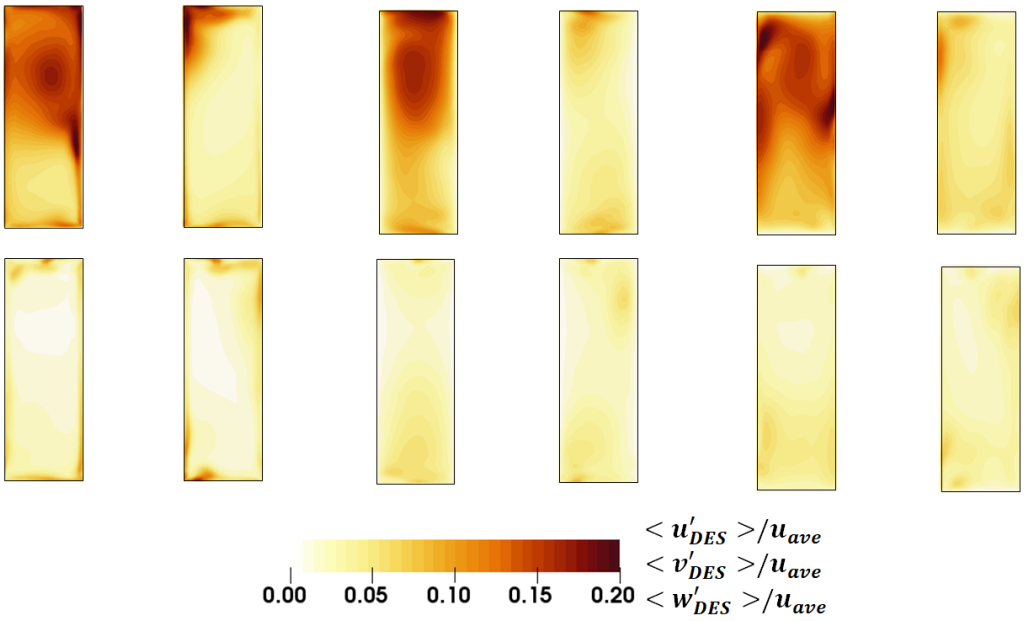

Figure 7.29: *Turbulence intensities at Section A_{DS} (top row: Turbine 2 and bottom row: Turbine 1).*

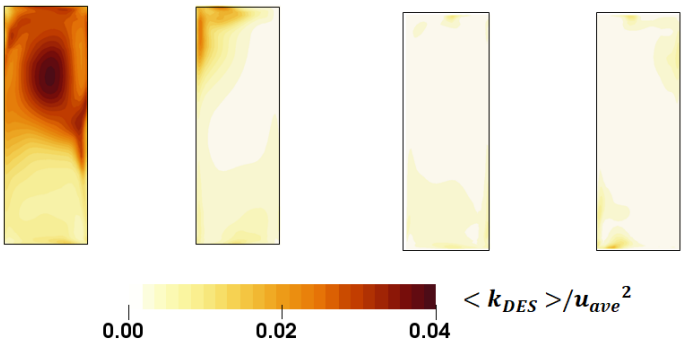

Figure 7.30: *Turbulence kinetic energy at Section A_{DS} (left: Turbine 2 and right: Turbine 1).*

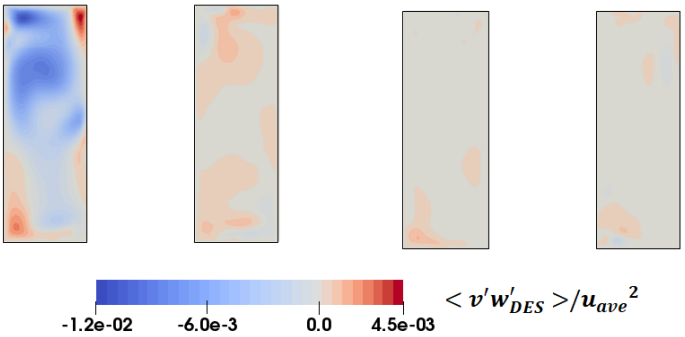

Figure 7.31: *Turbulence shear stress at Section A_{DS} (left: Turbine 2 and right: Turbine 1).*

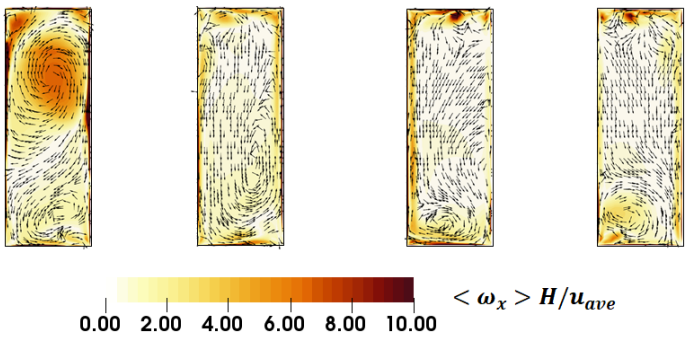

Figure 7.32: *Out-of-plane vorticity and surface velocity vectors at Section A_{DS} (left: Turbine 2 and right: Turbine 1).*

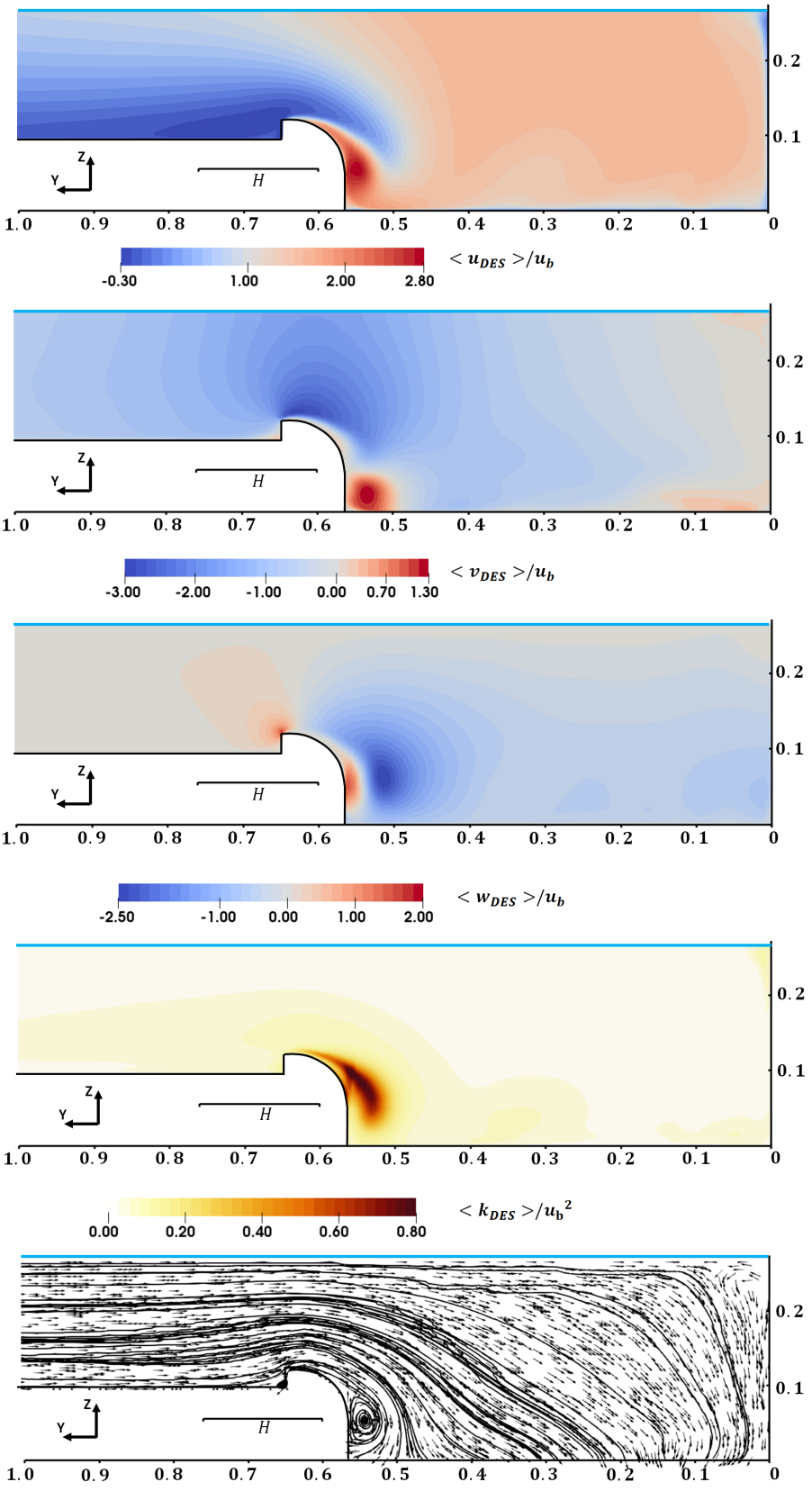

Figure 7.33: *Section B, from top to bottom: contour plots of velocity components, turbulence kinetic energy and surface streamlines.*

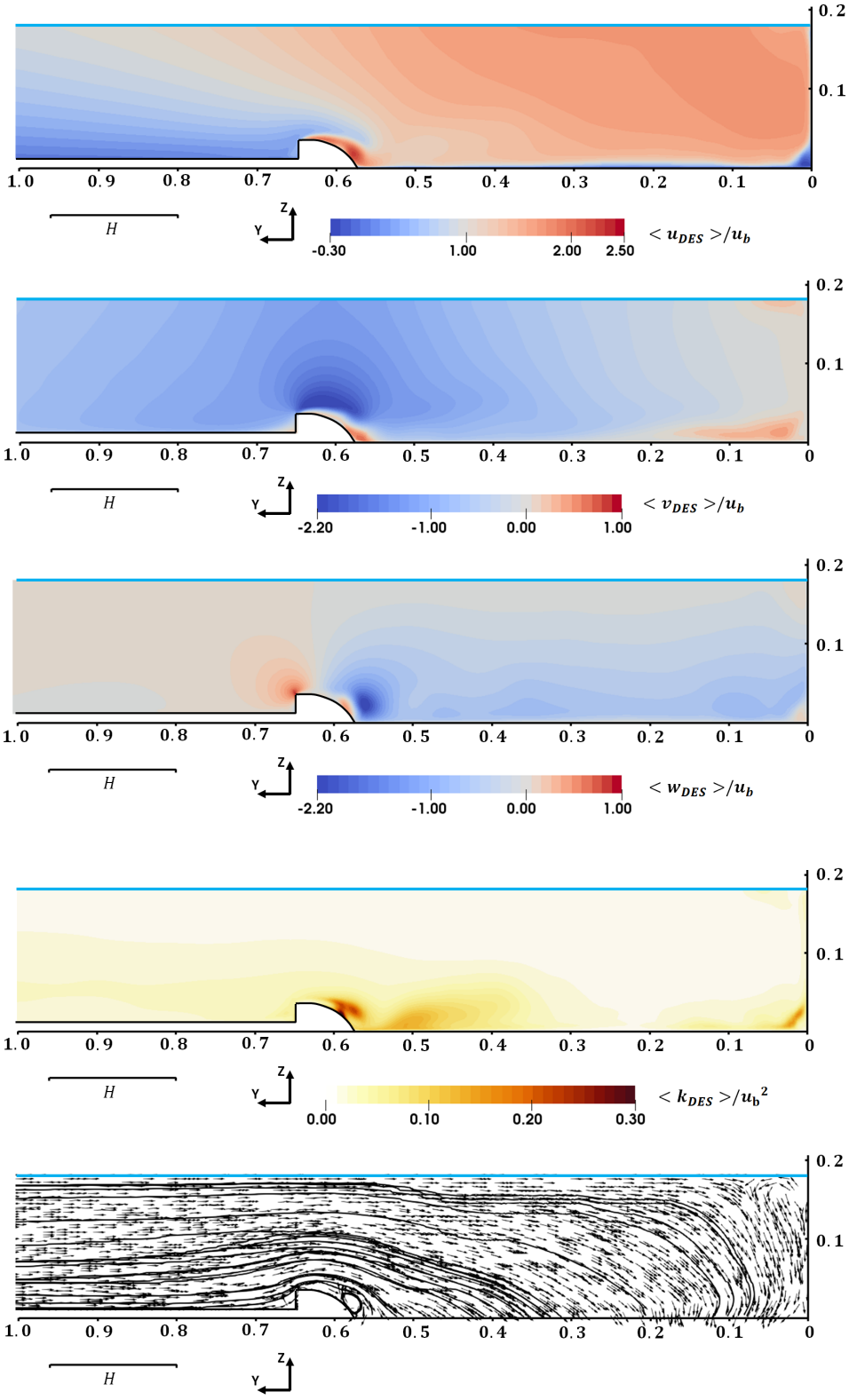

Figure 7.34: *Section C,from top to bottom: contour plots of velocity components, turbulence kinetic energy and surface streamlines.*

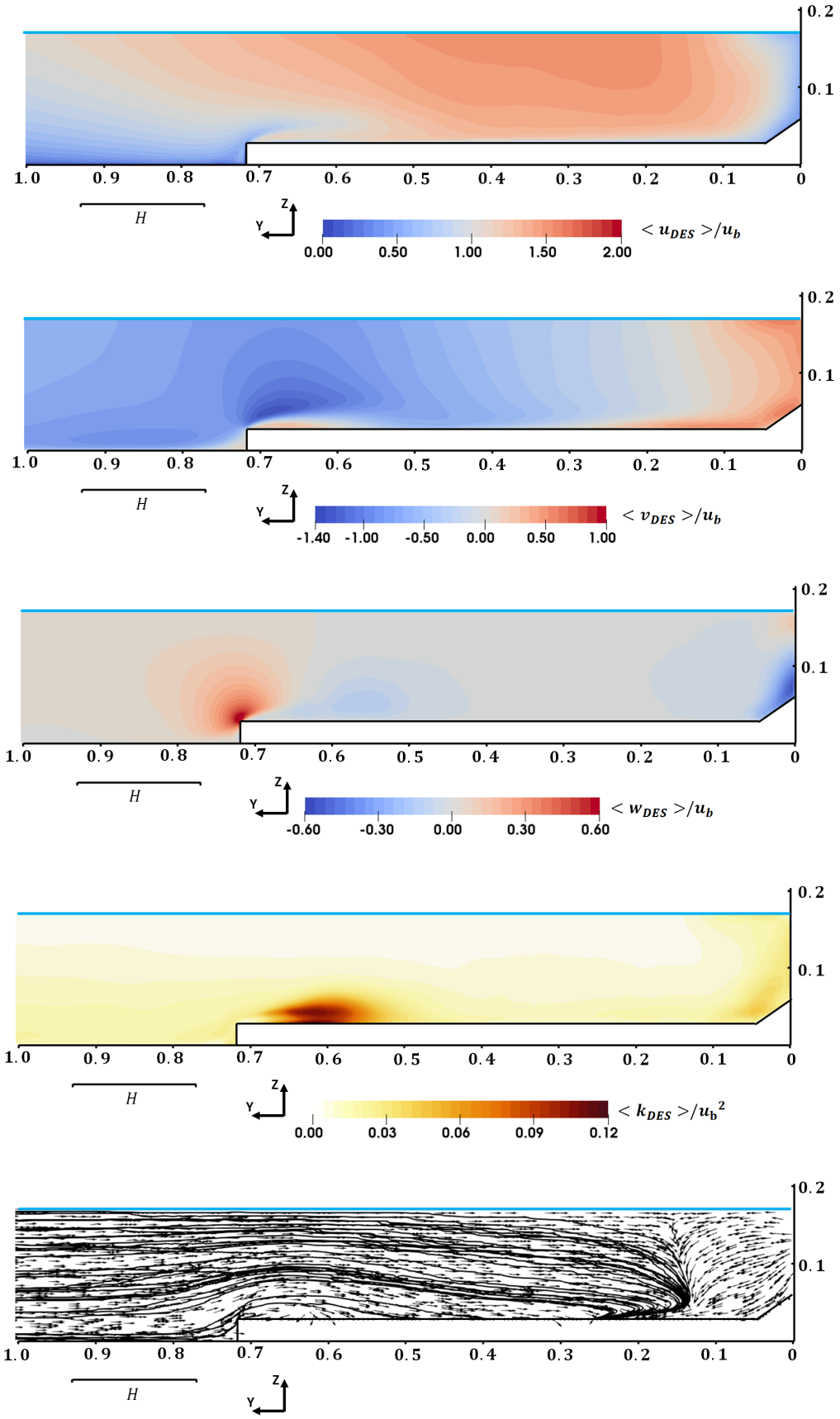

Figure 7.35: *Section D, from top to bottom: contour plots of velocity components, turbulence kinetic energy and surface streamlines.*

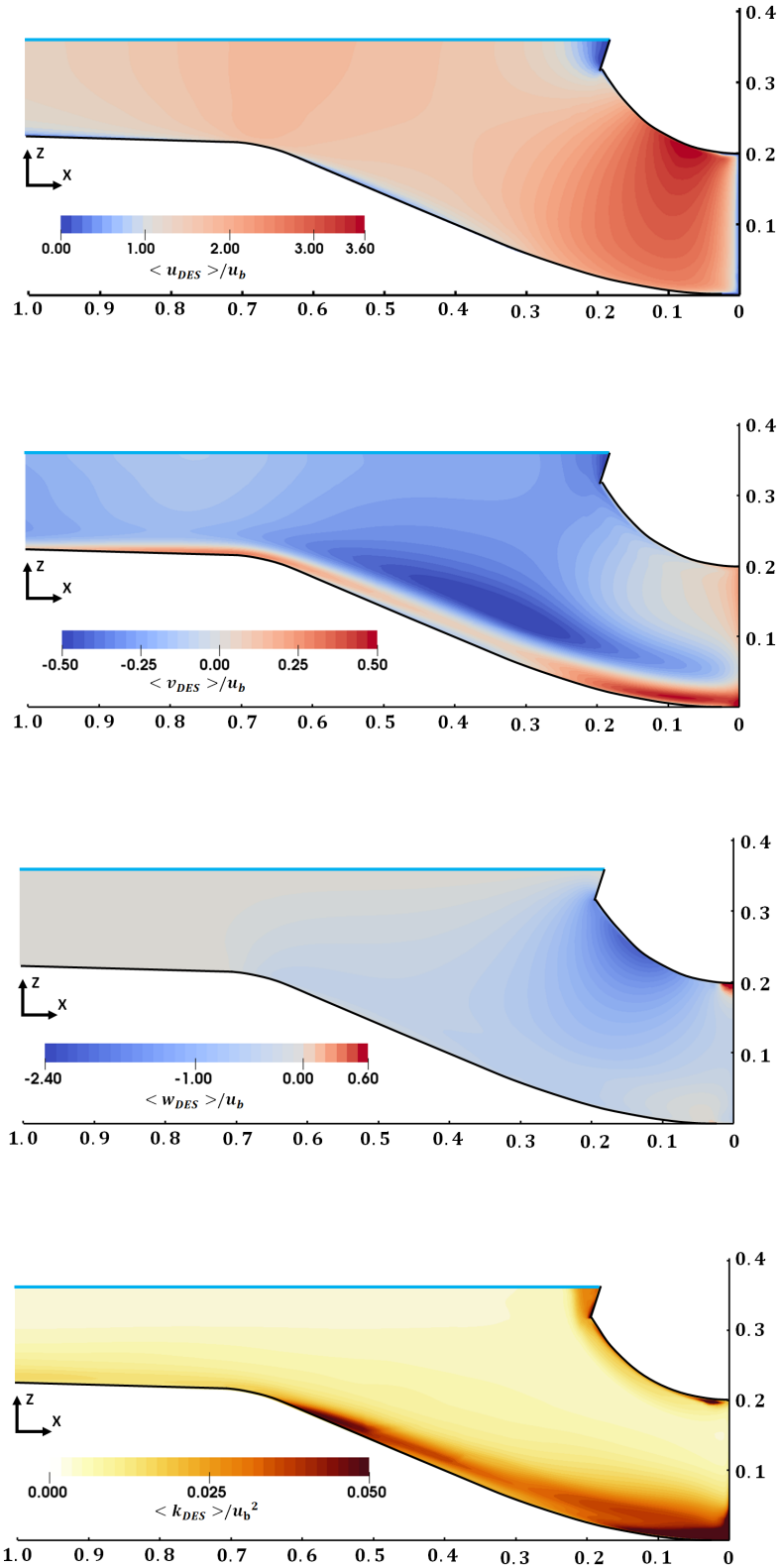

Figure 7.36: *A vertical section through the center of intake 1, from top to bottom: contour plots of velocity components and turbulence kinetic energy.*

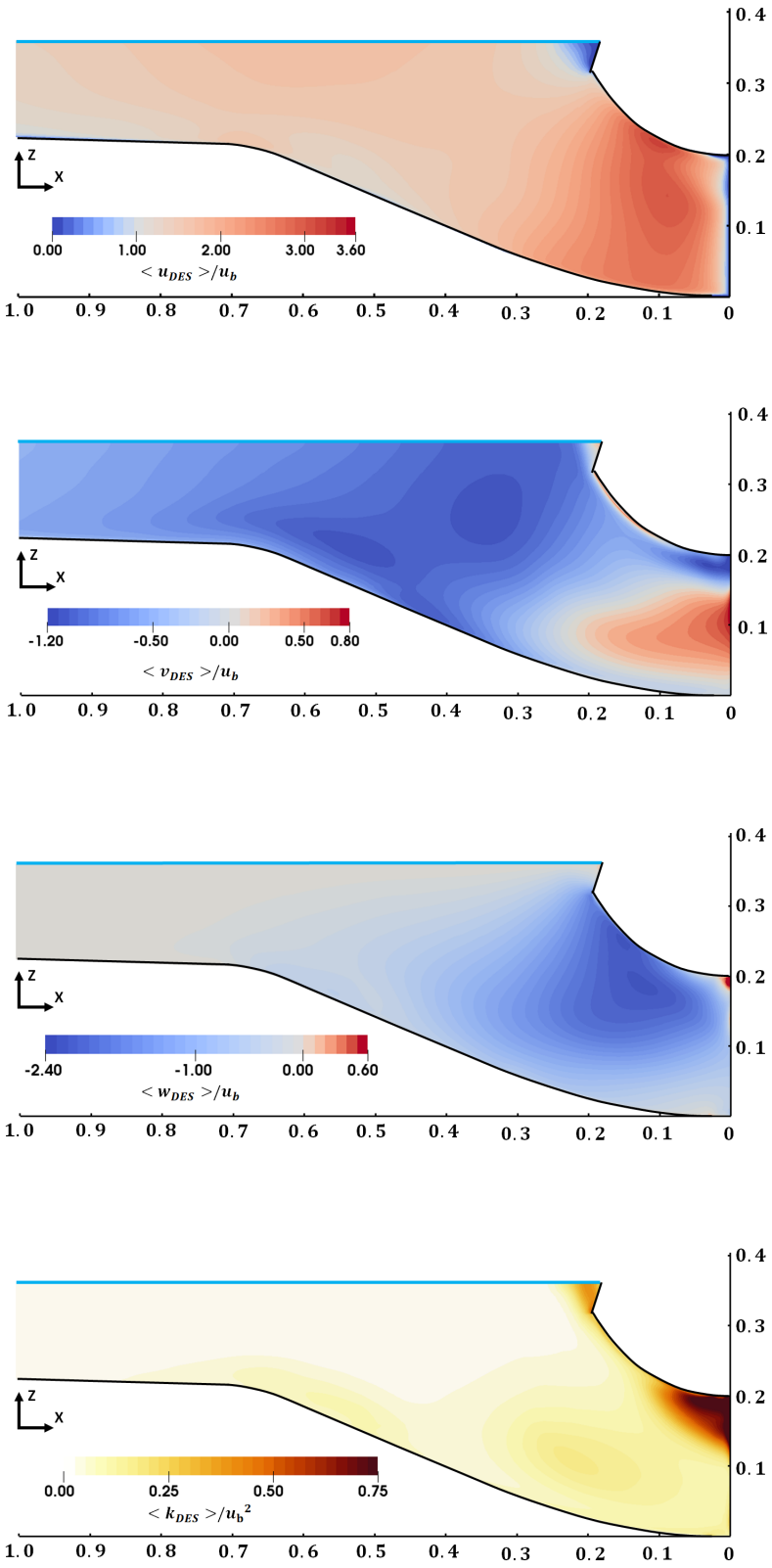

Figure 7.37: *A vertical section through the center of intake 2, from top to bottom: contour plots of velocity components and turbulence kinetic energy.*

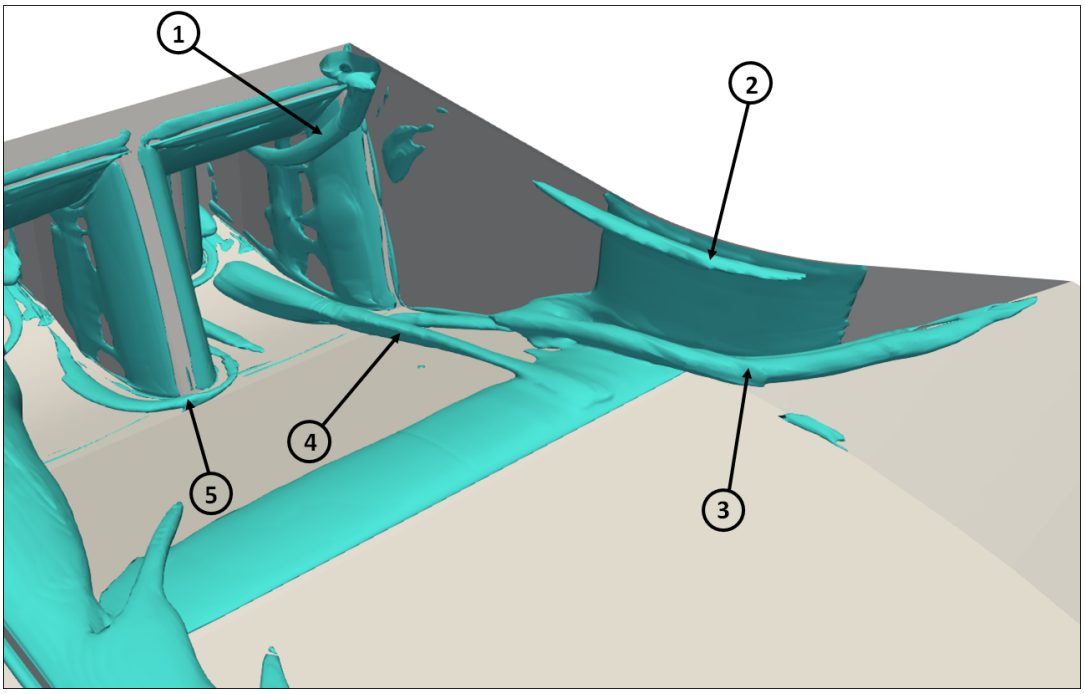

Figure 7.38: *Isosurfaces of Q-criterion visualising the vortical structures at the right side of the intakes.*

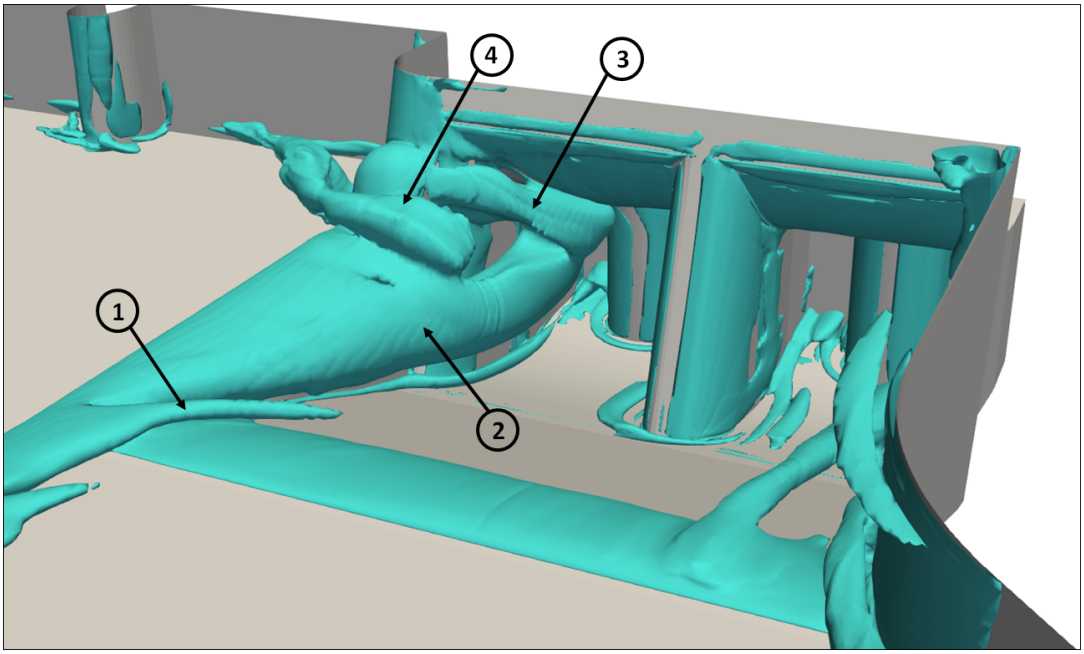

Figure 7.39: *Isosurfaces of Q-criterion visualising the vortical structures at the left side of the intakes.*

7.4.3 Instantaneous Flow Field and Coherent Flow Structures

One of the advantages of DES over RANS, beside accuracy, is the possibility of visualization of the instantaneous flow field. This, in return, provide a better insight into the flow structures and hydrodynamic processes. In this section, the instantaneous flow fields are presented and discussed. They are illustrated for selected instances in time. The results are presented via surface streamlines, vorticities and isosurfaces of Q-criterion. The data is extracted from 120 s data sets in a way to represent major flow characteristics. The discussion starts off from the upstream of the intakes and it continue downstream up to the flow inside the intakes at the measurement (reference) section.

Figures 7.40a-c shows the instantaneous as well as time-averaged surface streamlines at section D. The important aspect of this section is the separation which occurs due to the step and the flow direction. As it discussed earlier, the flow is very similar to the flow in forward facing step cases where the approach flow generated two distinct separation zones, one at the base of the step and one when the flow passes the sharp edge of the step and attaches to the bottom of the forebay (Figures 7.40a). Instantaneous flow visualizations in Figures 7.40b and 7.40c show several additional vortical structures.

In general, the vortices behind the step are mostly in three states:

1. only one large vortical structure is present
2. additionally, several smaller vortices can be observed in some particular time instances
3. in some instances, no vortical structure was detected at the base of the step

On the other side of the step, the only persistent structure is the one which is present immediately after the step. On the other hand, in Figures 7.40b and 7.40c where instantaneous surface streamlines are shown, several others can be observed. These structures are generated from the upstream and extended downstream. In the spanwise direction these structures are observed to stretched out (Figure 7.40c) or clustered together (Figure 7.40b). When these vortices are closer together, they give rise to an additional vortical structure in between with opposite rotation. These vortical structures are visualized using isosurfaces of Q-criterion in Figure 7.40d. These near bed longitudinal flow structures can be grouped into two categories based on the observed vortical structures and their directions by illustration of the instantaneous out-of-plane vorticity in Figure 7.41. The first group is generated by the upstream inclined step. They show higher angle with respect to the streamwise or x direction. The second group is located between the first group and the beginning of the slope to the intakes. The angle of these vortices are lower in respect to the streamwise direction. The second group is also discussed above where the instantaneous flow field is analysed via a vertical section. To understand the trajectory of these vortices, instantaneous isosurface of Q-criterion is shown in Figure 7.42. It can be seen that these vortices are in direction of the pier which divide the intakes. This is also observed in the physical model study. Figure 7.43 shows the flow direction visualized using dye in the experimental study. Beside the flow direction which is in a good agreement with the numerical model, it appears that very large portion of the approach flow is

directed toward the right intake. This, in return, indicates that almost entire flow of the left intake is approaching from the left side of the intakes.

It is discussed above that almost the entire flow for intake 2 is approaching from the left side of the divider wall. This means that a significant amount of water has to flow over the divider wall and around the submerged pier into the left intake. Figures 7.44a-d illustrates the surface streamlines on Section B for time averaged and instantaneous velocities for selected time instances. In the time averaged plot, two longitudinal vortical structures are present and these are discussed in the previous sections. First and smaller one corresponds to the separated flow due to the sharp angle of the divider wall and one because of the propagation of the larger upstream vortices downstream. However, study of the instantaneous flow field reveals that the number of vortices are vary in time. These can be divided into two groups. In the first group, an additional vortical structure is present. This is shown in Figure 7.44b. This is due to the relatively younger vortices which are generated further downstream closer to the section (Figure 7.44e and 7.49). Additionally, due to the proximity of these vortices, they give rise to the another vortical structure between the two with counter-rotating direction. In the second group, the flow is close to the time averaged plot. It is shown that the larger vortex is almost always present. Furthermore, the center of this vortex is at the same location during the investigated period. This vortical structure is shown in Figure 7.44e for one snapshot of the flow and it indicated by number 2 in Figure 7.39. Finally, the instantaneous streamwise (x-direction) vorticity is slightly higher than the values which are computed from the mean velocity.

In the previous section, where time averaged flow characteristic is presented, it is shown that another flow's feature is the presence of a vortical structure indicated by number 4 in Figure 7.39 and it is shown in Figure 7.45a. This is found to be the consequence of a large amount of flow from the reservoir side, passing around the submerged pier and entering into the left intake. Similar flow pattern is also observed in the experiment (see Figure 7.45d). Study of instantaneous flow filed revealed the following flow characteristics:

1. the location of this vortical structure is variable with respect to the submerged pier. In some instances this vortical structure is close to the submerged pier (Figure 7.45c) or further away (Figure 7.45a).

2. the magnitude of the out-of-plane vorticity is twice higher than the time averaged values. This is shown in Figures 7.45a to 7.45c via contour plots of out-of-plane vorticies at a vertical section above and parallel to the divider wall.

3. at no instance of time it is observed that this vortical structure is reaching beyond the separation pier and into the left intake.

In the experiment, a free surface vortex at the left side of the intakes was observed, however, this vortex was not present at all time. This is illustrated in Figure 7.50. In the chapter where the flow is modelled using RANS, only SST model predicted such vortical structure (see Figure 6.19). On the other hand, this is not predicted in the study where IDDES is employed and the vortical structures are visulized using iso surface of Q-criterion based on time averaged values (Figure 7.39). A closer look at this zone via surface streamlines and out-of-plane vorticity at the water surface in Figure 7.46a showed

a mild separation. Nevertheless, several free surface vortices can be observed when the instantaneous flow field is considered. Figures 7.46b and 7.46c show two snapshot of the vertical vorticity as well as the surface streamlines. The plots indicate a flow separation due to the high flow velocity at the water surface on top of the submerged pier. This gives rise to free surface vortices where they propagate and sweep toward the right intake. The magnitude of the instantaneous vertical vorticity are found to be much higher than the time-averaged counterpart. These vortices are also found to reach inside the intake as far as Section A. These vortices can also be observed in Figure 7.48 where instantaneous isosurfaces of Q-criterion are shown. Finally, a larger free surface vortex is predicted by IDDES as well as RANS-SST on the right side of the intakes. This is discussed in previous chapter and sections.

Section A is considered one of the most important section in this study. This is due to the fact that this flow in this section is evaluated for the operation of the ROR plant. Previously it is shown that the most important feature at this section is the large longitudinal vortical structures which is generated by the flow over the divider wall. Additionally, flow past the submerged pier is generating vortices which they extend inside the left intake. This is shown in Figure 7.48 where instantaneous isosurfaces of Q-criterion is shown. Figure 7.47 shows the time averaged and instantaneous out-of-plane vorticity and surface streamlines at section A. The two region in the time averaged plot corresponds to the two processes which are discussed above. On the other hand, the instantaneous flow field reveals four important points:

1. The magnitude of the instantaneous out-of-plane vorticity are more than three times higher than the time averaged values.
2. The center of the lower vortical structure is changing in vertical direction.
3. The two vortical structures on the left are occasionally merging into one.
4. The free surface vortices which are previously discussed can be seen on the upper edge of the section. This is shown by negative values of out-of-plane vorticity in Figure 7.47.

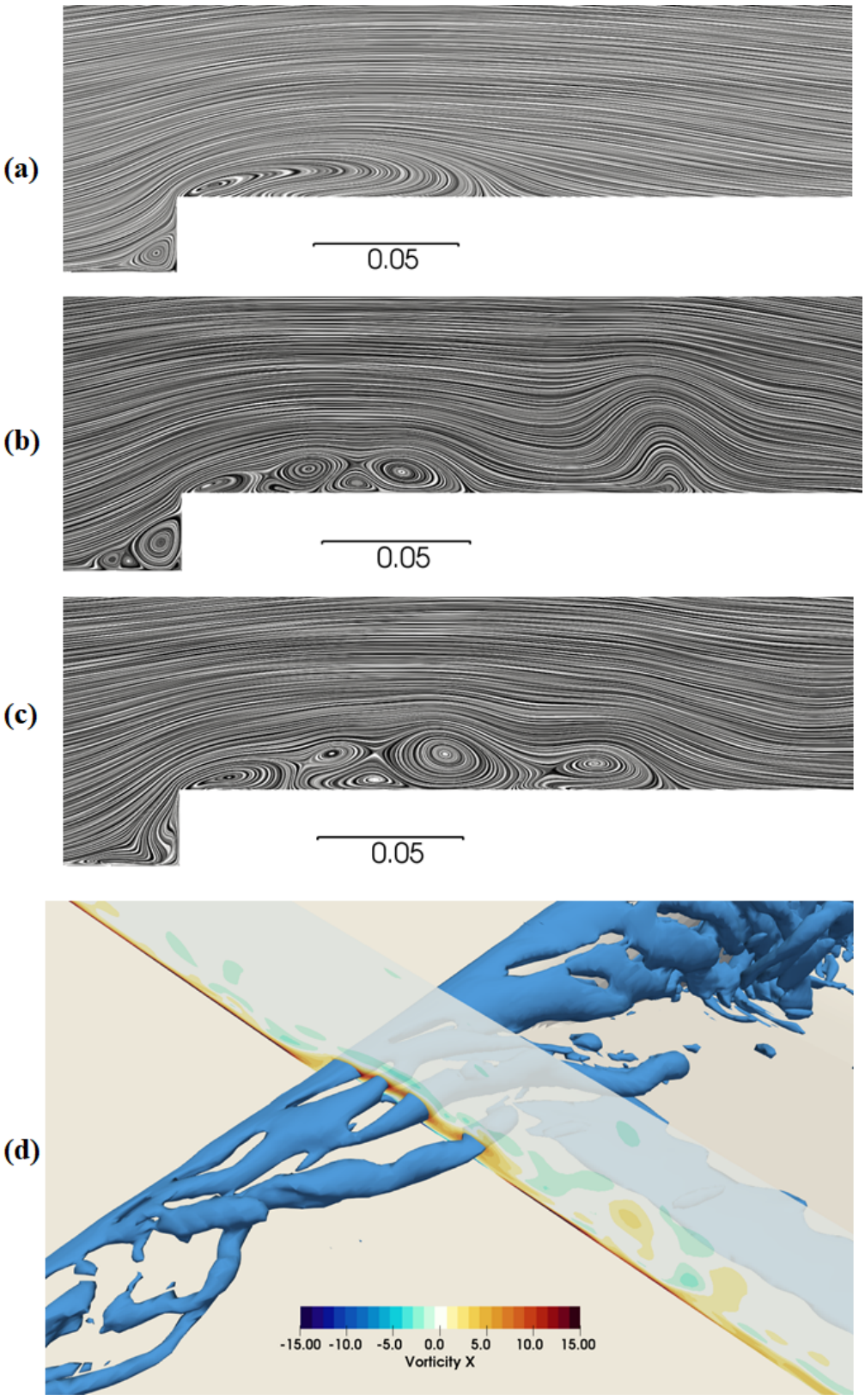

Figure 7.40: *Surface streamlines, isosurfaces of Q-criterion and Vorticity at Section D: (a) time averaged, (b) and (c) instantaneous surface streamlines and (d) instantaneous isosurfaces of Q-criterion and vorticity.*

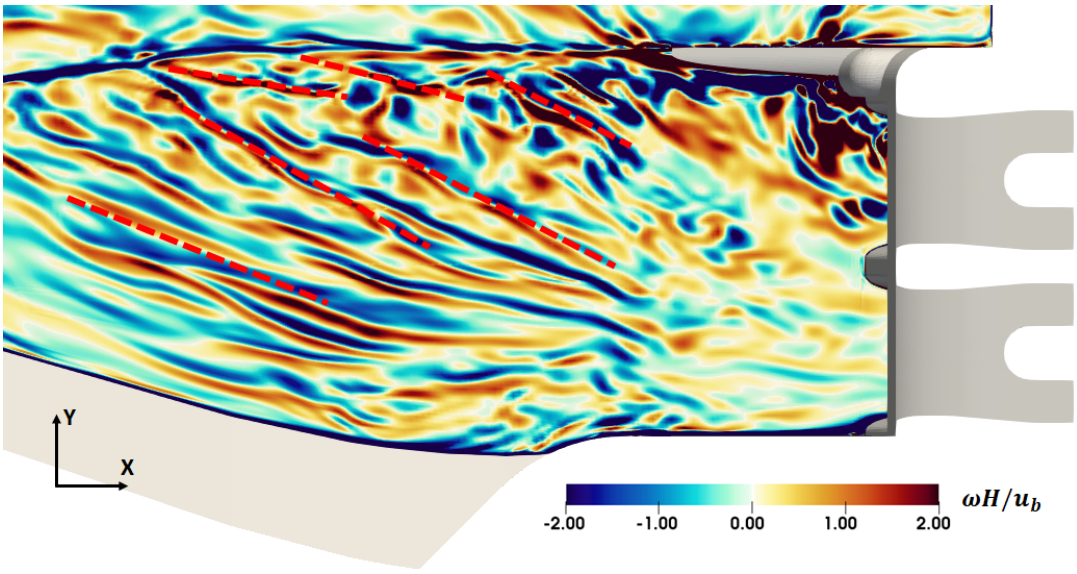

Figure 7.41: *Instantaneous vorticity magnitudes close to the bottom of the forebay.*

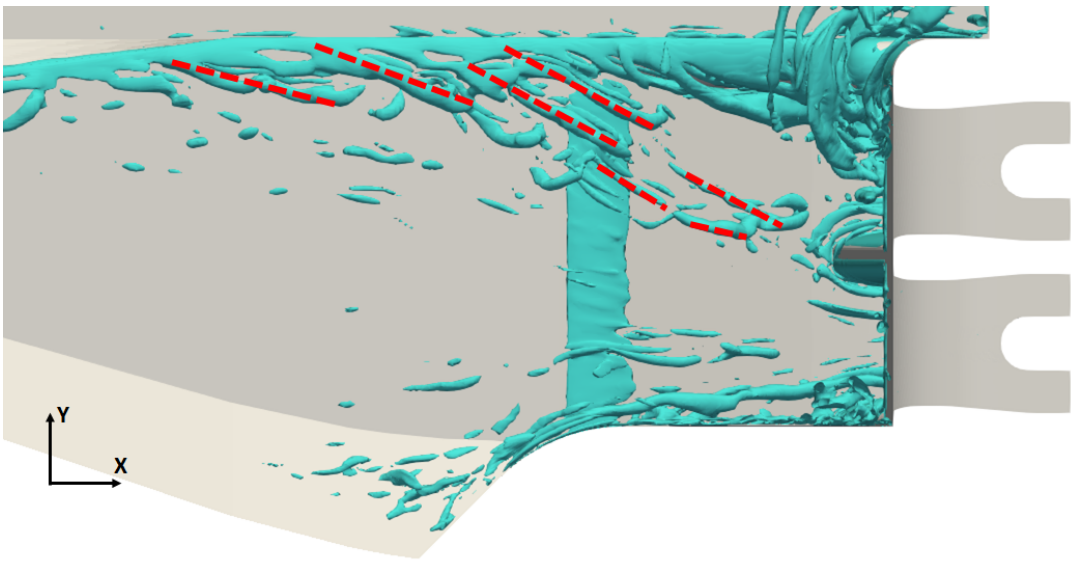

Figure 7.42: *Instantaneous vortical structures at the forebay visualized using isosurfaces of Q-criterion.*

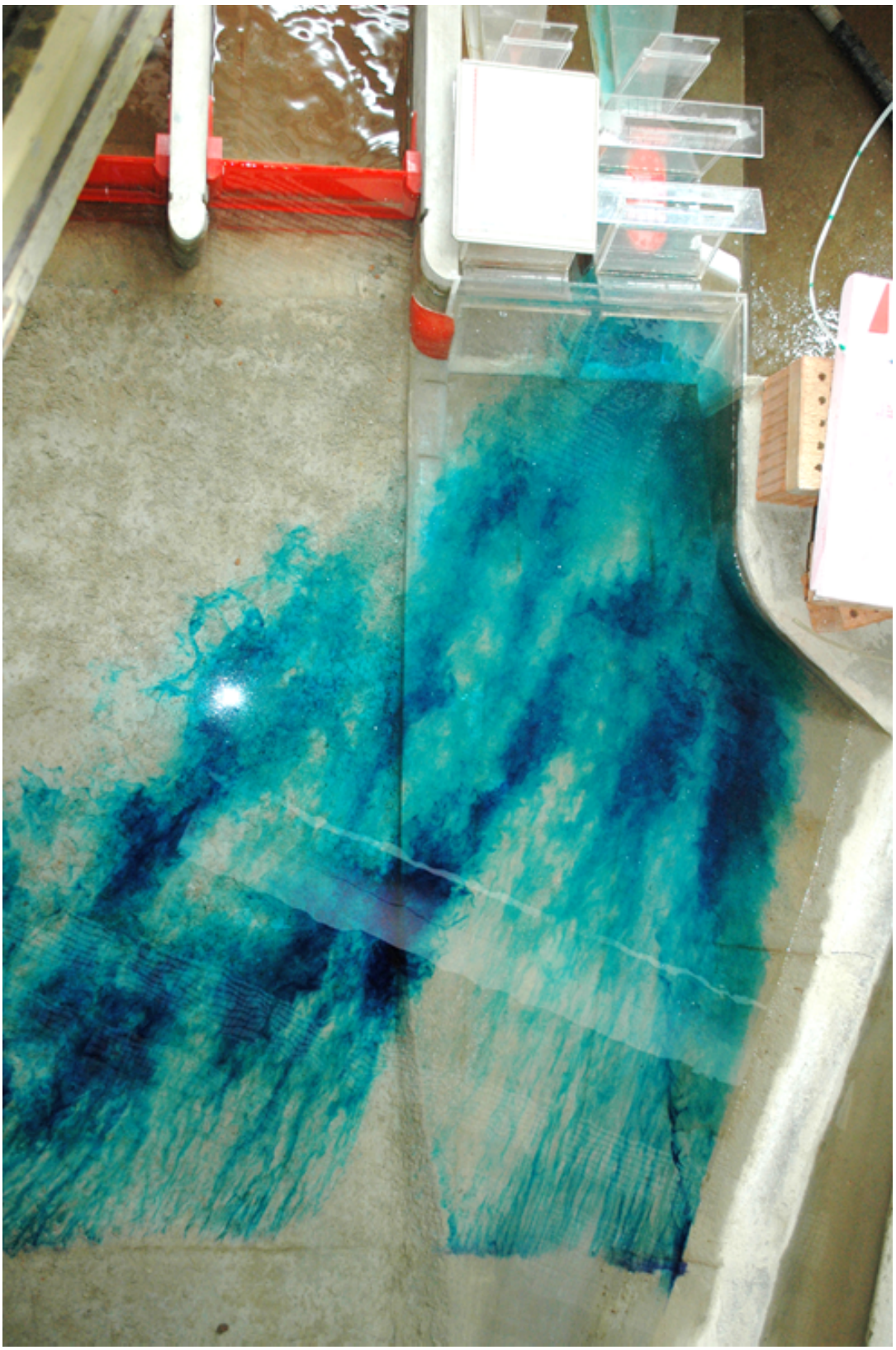

Figure 7.43: *Visualization of the flow pattern by injection of dye in the physical model study.*

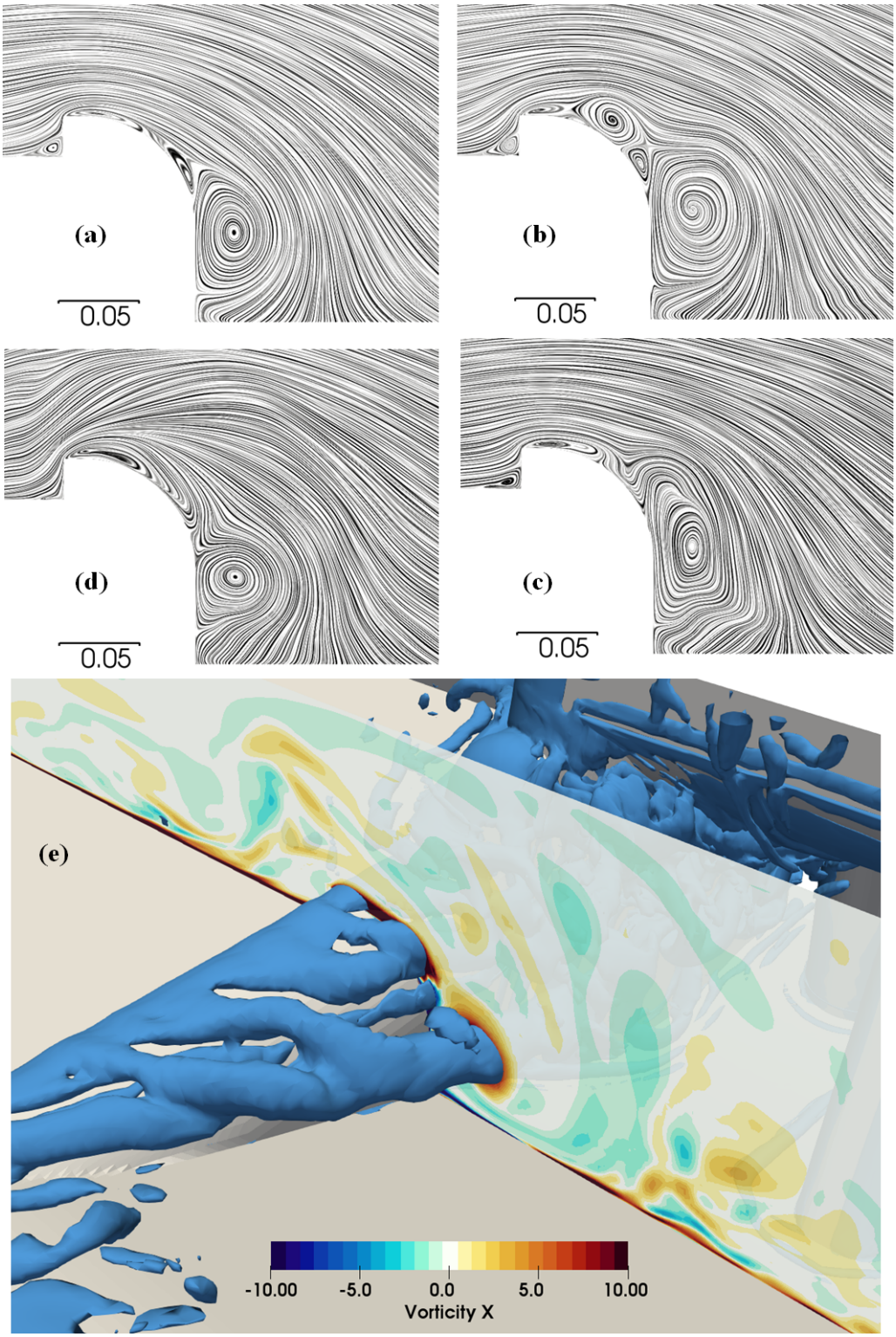

Figure 7.44: *Surface streamlines, isosurfaces of Q-criterion and vorticity at Section B: (a) time averaged, (b,c and d) instantaneous surface streamlines and (e) instantaneous isosurfaces of Q-criterion and vorticity.*

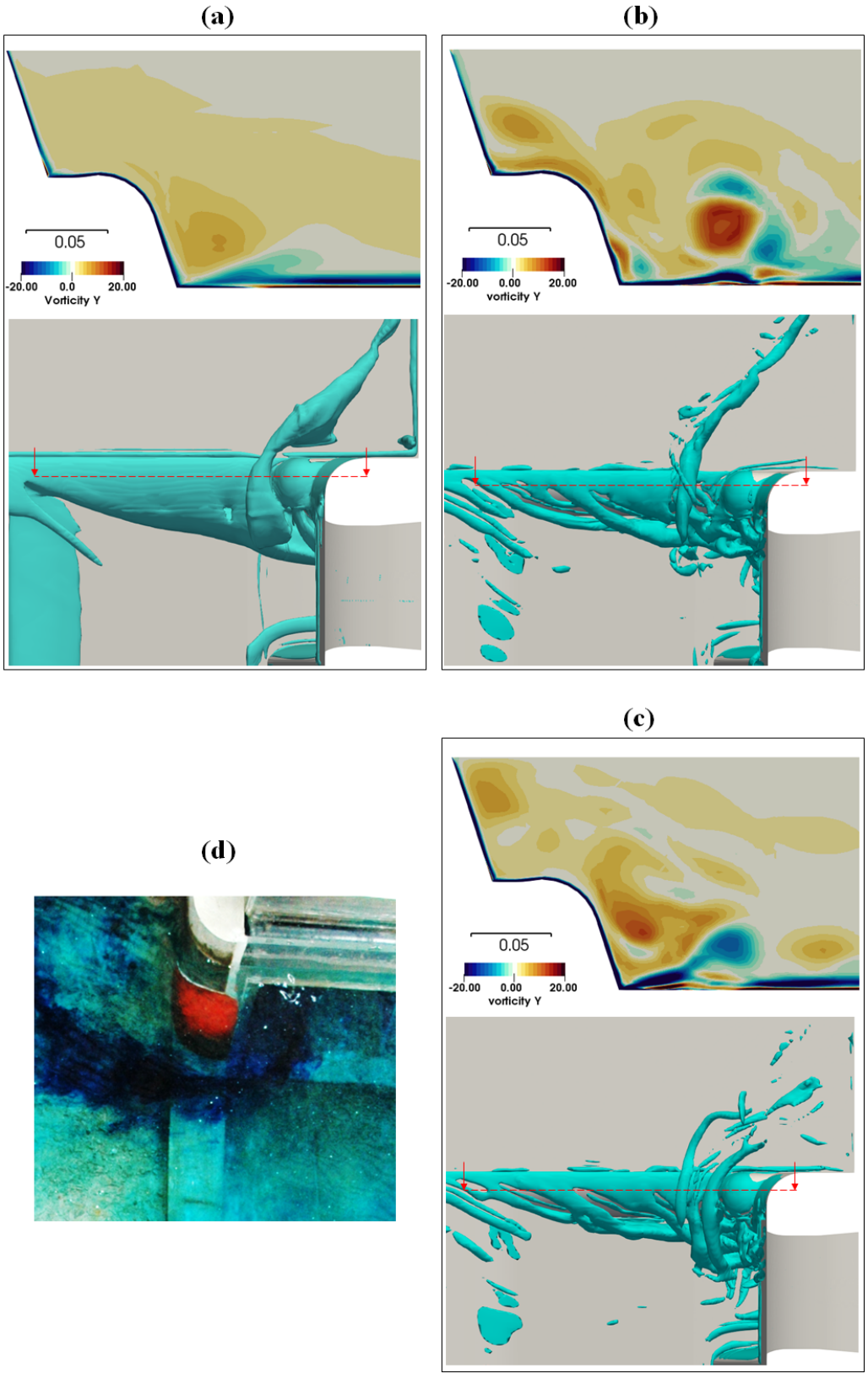

Figure 7.45: *Isosurfaces of Q-criterion and Vorticity at a vertical section across the length of the divider wall: (a) time averaged, (b and c) instantaneous and (e) visualization of the flow using dye in the experiment.*

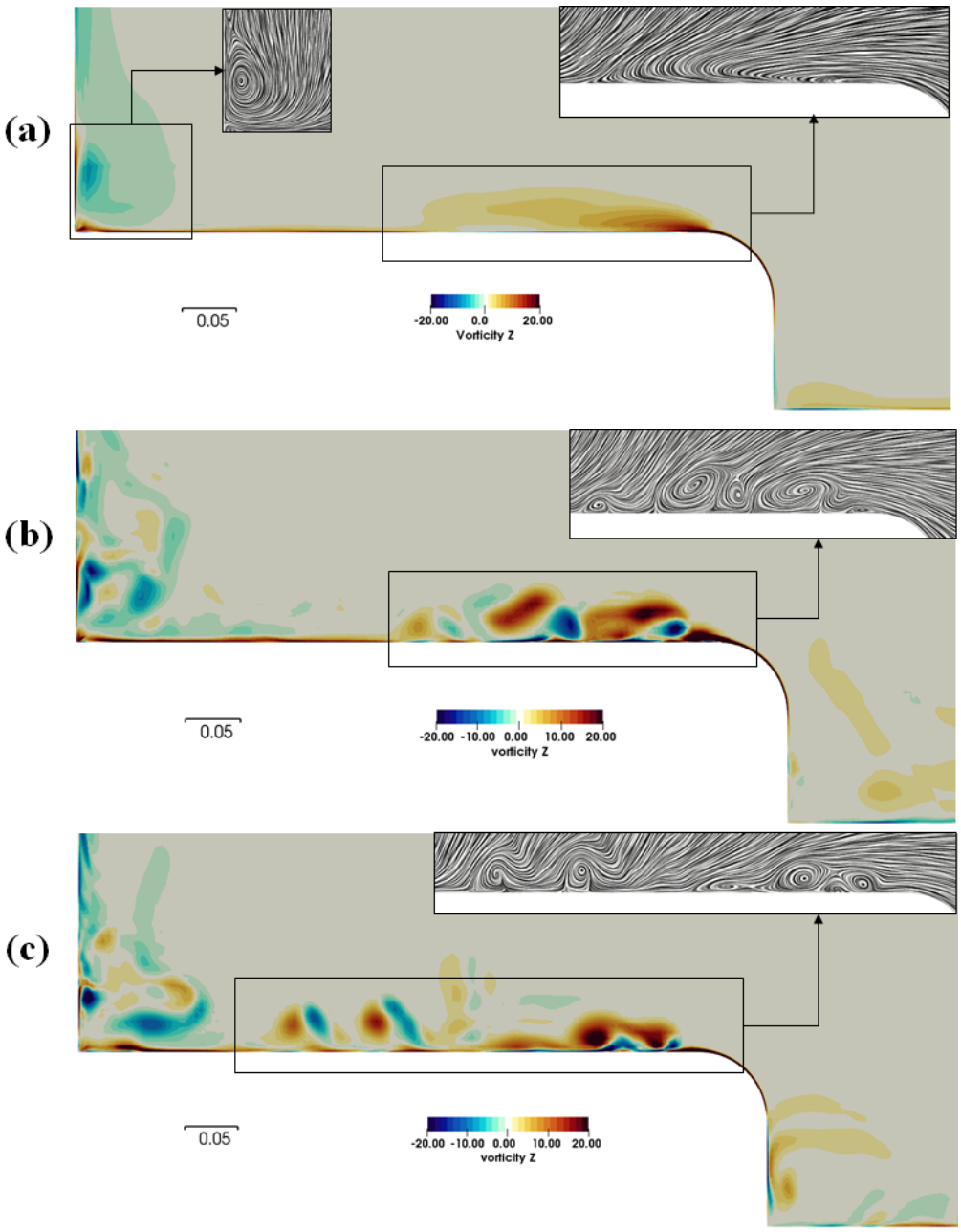

Figure 7.46: *Out-of-plane vorticity and surface streamlines at the water surface: (a) time averaged, (b and c) instantaneous.*

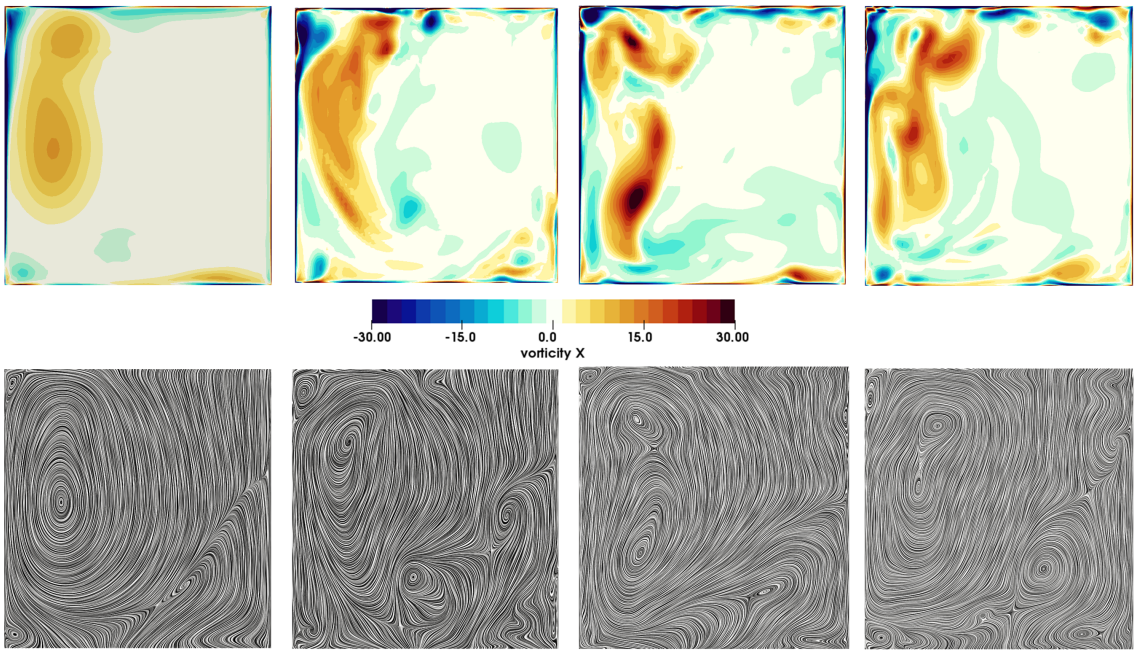

Figure 7.47: *Out-of-plane vorticity (upper row) and surface streamlines (lower row) at Section A. First column: time averaged, second, third and fourth: instantaneous.*

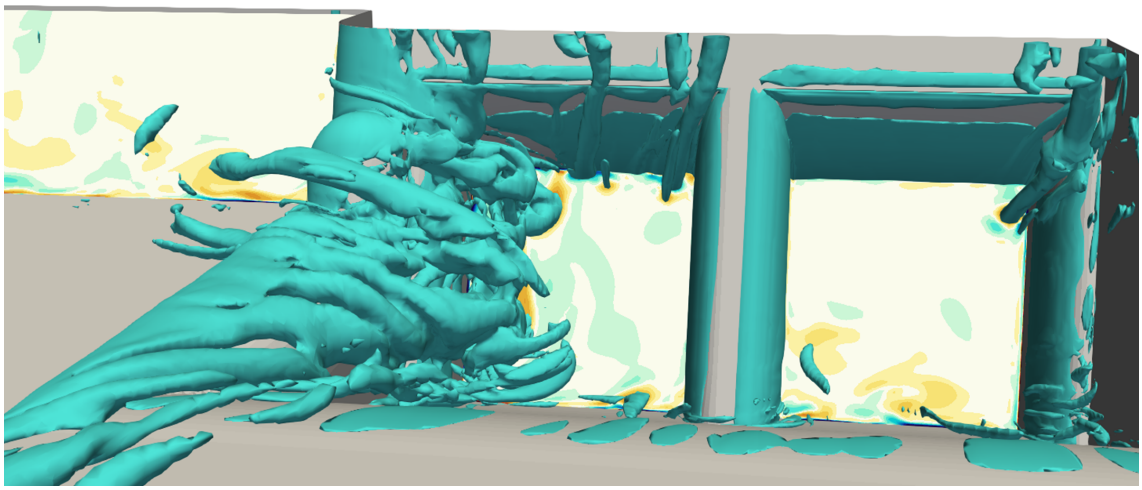

Figure 7.48: *Instantaneous isosurfaces of Q-criterion.*

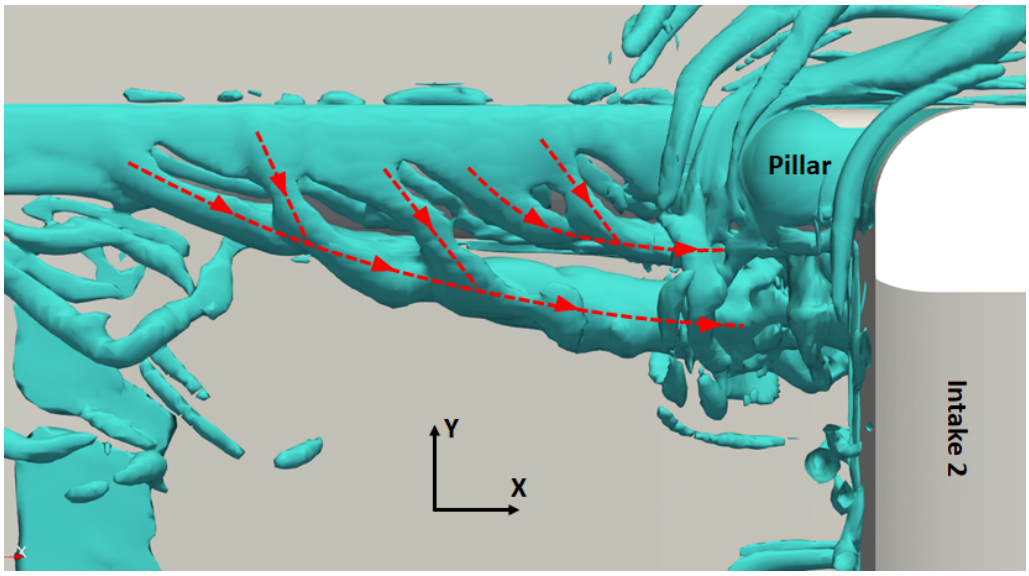

Figure 7.49: *Visualization of vortical structures at the divider wall and the separation pier by isosurfaces of Q-criterion.*

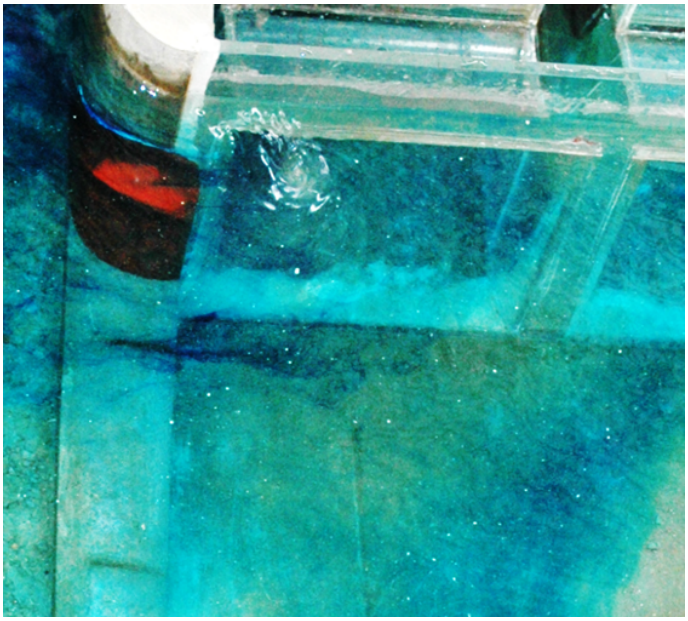

Figure 7.50: *Free surface vortex observed in the experimental study.*

8 SUMMARY AND CONCLUSION

The main objective of this study was to evaluate the application and the capability of numerical methods in modelling approach flows of the Run-of-River plants. This study is divided into four main parts. In the first part, an overview over the key components and design consideration of approach channel and intake structures are given. In the second part, the physical model study, the measurement strategy and measured values are described. In the third part, a RANS parameter study has been carried out, firstly, to identify the key parameters which are directly affecting the computed fields and, secondly, to evaluate the capability of this method for this particular application. In the final part, a detailed numerical study has been performed using Eddy-resolving method. In order to reduce the computational time, an explicit solver based on Runge-Kutta and fractional method has been implemented and validated. It is shown that this method may reduce computation time significantly. In the following sections, a brief summary and conclusion are presented.

8.1 Physical model test

A physical model test of a run-river plants has been carried out. This model was chosen due to its similarities to several other ROR projects. This project is also modelled numerially in the other chapters. The model was scaled based on Froude similarity law with 1:40 scale. It consists of an approach channel, two intakes and weirs. The measurement of the velocities has been performed for a load case, where the weirs are closed and the plant is operating in its full capacity (both turbines are running at their full capacity). The measurement has been carried out using ADV techniques inside the intakes. The data is then subjected to filtering and velocities as well as turbulence parameters have been computed and presented. These results have been used later on for comparison and validation of the numerical model results. Additionally, evaluation of the flow based on the Fisher-Franke's criteria has been carried out. It is found that the flow did not fulfilled several of the conditions. However, later it is found that this is due to the location of the measured section and shifting the measurement section downstream, significantly improve the conditions.

8.2 OpenFOAM

In this study, all the computations are carried out using OpenFOAM. The code is available as an open source and allows a user to model hydraulic problems from single phase pressurized system to open channel flows. A wide range of solvers and numerical schemes provide several choices depending on the problem. Furthermore, high level programming language facilitates understanding the underlying algorithm as well as implementation

of a new algorithm. These features make the code appealing for industrial and research problems. It is also shown that the code performs very well in high performance computing environment. Additionally, the post-processing tool ParaView, which is included as a third party tool, was shown to be powerful and sufficient for post-processing and visualization. Nevertheless additional tools like Python seem necessary to accomplish the high quality presentation of the results.

Despite OpenFOAM's advantages and superiority over many other codes (specially other open-source codes), there are a few shortcomings. In this study, it is found that the grid generators, which are a part of the code, namely blockMesh and snappyHexMesh, are not suitable for complex geometries, despite the fact that computation on a high quality grid is extremely important for accuracy and convergence. Therefore, ANSYS ICEM was used in this study to generate the computational grid. Furthermore, absence of a graphical user interface make this code not appealing for new users.

8.3 Explicit solver

Large Eddy Simulations and Eddy-resolving methods are transient and computationally demanding. Furthermore, the Courant number must be kept below 1 for accuracy and stability. Also, low order methods in time are too diffusive. In OpenFOAM, for transient problems, several implicit first or second order time integration schemes are available in conjunction with PISO or PIMPLE solvers. However, it is discussed that using explicit RK family of methods in combination with the fractional-step method can increase the accuracy and more importantly the speed of the computation, hence, make these methods more affordable for engineering purposes. In this study 4th and 3rd order explicit RK in combination with fractional step method implemented in OpenFOAM. Emphasis was given especially to the 3rd order method due to its speed compared to PISO algorithm. Series of numerical tests have been carried out to verify and validate the code via two relatively simple numerical test cases; fully developed turbulent channel flow and flow over two-dimensional dunes.

In the first case, LES of a fully developed turbulent channel flow for two different friction Reynolds numbers have been carried out. The results are then compared with the DNS data and it is shown that the results are in good agreement with the DNS data. Furthermore, it is found that the 3rd order variant of the solver is approximately 40% faster than PISO. Additionally, an IDDES simulation carried out on the same case and it shown that the solver in combination with IDDES performs very well even when a uniform grid is used.

The classical turbulence channel flow is relatively a simple case. In order to evaluate the numerical performance of the solver along with IDDES model in a more challenging case, the flow over two-dimensional dune is modelled due to availability of experimental as well as LES results. The number of elements in this study was at least 10 times lower than in previous LES studies. It is shown that the solver performs well and results are in good agreement with the experimental and LES results. Furthermore, it is found that the solver, is again, 40% faster than PISO solver. However, it must be noted that the speed up must be considered with care since the performance of the solver may depend on many factors including linear solvers, scalability of the solver and complexity of the case. In conclusion, the solver's verified and validated via two cases, hence, this solver is used in

the study where IDDES model is used.

8.4 RANS study

In practical hydraulic engineering problems, RANS is still considered a pragmatic choice. This is due to its robustness, efficiency and simple use. Hence, via series of parameter studies using RANS approach and SKE as a base turbulence model, several questions have been answered. Furthermore, in all the studies the focus is on the flow, in particular velocity distribution inside the intake, where the measurement carried out, as this section is considered to be important in the evaluation of the flow in intakes. The investigation began by grid convergence study on prototype scale to identify suitable grid size. In the second part, it is confirmed that the results from the scaled model are almost identical to the prototype and wall roughness does not affect the flow, especially in the scaled model. The third part of the investigation was focused on the effect of the inflow condition in two aspects: prescribed inflow values and the location of the domain's inlet. This study then followed by comparing the results from three RANS turbulence models. It is found that SST model provides a better insight based on the comparison with the physical model test results and subsequently this model is used for the rest of the study. In a separate study, two simplified model generated to study flow condition with minimum influence of the upstream features. Finally, a new section is proposed for flow evaluation further downstream because it is found that in previous section the flow is not developed sufficiently and effect of intakes walls is not fully imposed. In the following, the outcome of these studies is summarized:

1. Grid convergence study was shown that for preliminary analysis and/or optimization, a coarse grid can be used. This is confirmed by computation of GCI for several points via two different techniques: one based on Richardson extrapolation and the other Approximate Error Spline. It is found that all the GCI values are less than 5% with majority being significantly lower. Furthermore, it is found that Approximate Error Spline performs relatively better in two aspects; first, in computing true values and second, in estimating the GCI values. However, it must be noted that GCI is not always the true indicator of grid convergence and grid related errors.

2. The scale effect is investigated using two models assuming smooth walls. In the first model, the prototype scale is modelled. This is similar to the model which was previously computed in grid convergence study with medium grid size. Additionally, the scaled model (based on physical model study scale of 1/40) is modelled. The results are compared at the intake and it is found that the velocity values are almost identical. It must be noted that in a single phase models, several physical parameters i.e. surface tension and variation of water level specially for the scaled model are ignored. In the second part, effect of wall roughness is studied on the prototype as well as the scaled model with realistic values for concrete. In reality and in prototype the roughness may vary significantly from approach channel to the intakes. It is found that the wall roughness has negligible effects especially in the scaled model due to low Reynolds number. The most noticeable change is observed at the prototype scale where high roughness values lead to decrease of the flow velocities adjacent to the walls.

3. In single phase internal flows, it is common that the boundary conditions are velocity inlet and pressure outlet. In this set up, the pressure at the outlet is defined and the velocity along with turbulence parameters are defined for the inlet. Usually the values are defined as constant using empirical formulas or they are obtained via precursor analysis for accuracy. In this investigation, all the values are computed using precursor simulations through periodic channels and they imposed on the inlet of the domain. In order to investigate how the location of the inlet in the numerical models impacts the results inside intakes, three numerical models are compared. The inlet placed immediately before the forebay in the first model and in second and third models the approach channel is extended upstream of the forebay by eight and sixteen times the channel's water depth respectively. It is found that as far as the velocity inside the intakes is f concern, the inlet can be located as close as the beginning of the forebay, hence, reducing the model size and the computation time. However, if the flow at the forebay and upstream of the intakes are important, the inlet must be located further upstream.

4. It was shown that as far as the distribution of the velocity in the intake is of concern, the results are not significantly affected by grid refinement, scale and roughness effects, and the location of the inlet. Furthermore, SKE model is used as the base turbulence model for previous investigation. In this part, the effects of RANS turbulence models on the computed velocities at the intake are investigated. This is done using three commonly used RANS models: SKE, SA and SST turbulence models. The results from these three models were compared with the results from the physical model study. The simulations have been carried out on the scaled model with smooth walls. It is found that:

    - In intake 1 (right intake), similar velocity distributions are estimated by all the models. The results are also in good agreement with the physical model test.
    - In intake 2, significant difference can be observed between the models, especially between SST and other two models. The differences are considerably bigger on the left side compared to the right side of intake 2.
    - All models agreed upon presence of a swirling flow on the left side of intake 2 due to the separation wall and significant amount of flow from the left side.
    - Although the results from the SST model is closer to the measured values, this model predicted extra swirling flow at the left corner of intake 2 which was not observed in the physical model study.
    - SST model predicted two additional free surface vortices, one on the right side of intake 1 and one at the left side of intake 2. These were not observed in the results from SA-RANS and SKE.
    - The inflow condition criteria are evaluated for all the models. It is shown that only criterion C6 at the intake 1 and criterion C3 at both intakes are fulfilled. Although criterion C5 is not fulfilled, however, the results are very close to the Fisher-Franke's boundaries.
    - Finally, good convergence was achieved by three models. However, obtaining convergence with SST model is found to be difficult with SKE model was the most robust among the models.

5. In previous studies, a complex system of the approach flow is modelled and investigated. In order to study the flow characteristics in a simple geometry free from complex upstream geometrical features, two simplified versions of the full model were generated. The models were identical except that the slope to the intakes has been reduced in one. Furthermore, due to good performance of SST, this turbulence model was used for the simulations. The following conclusions are made through this study:

    - The computed velocity distribution in the intakes for both models are very similar to the intake 2 of the full model.
    - Reducing the approach slope is significantly improving the overall flow at the investigated section.
    - It is shown that even in the most simple form, the flow is not satisfying all the conditions. This means that perhaps this section is not suitable for the evaluation according to the Fisher-Franke conditions.

6. In previous studies, it is shown that even for the simplest case, not all the criteria can be full-filled. This indicates that the chosen section may be too close to the entrance of the intakes and the flow is still under influence of the entrance shape and not fully developed. Therefore the evaluation section is shifted further downstream and flow is evaluated using Fisher-Franke's criteria one again. This was done for two simplified models as well as for the full models where SST turbulence model is used. It is found that:

    - The flow conditions improved dramatically based on the evaluation criteria.
    - It is recommended that in a numerical model, the evaluation shall be carried out using a cloud of points instead of the numerical grid of the entire section.

8.5 DES study

Hybrid RANS-LES approaches in particular DES is a relatively new technique with promising capabilities to model complex flow problems accurately. Hence the approach flow to the run-of-river is modelled using IDDES, an improved version of the original DES. The computation was carried out using the third-order explicit solver which was implemented and validated. The main objectives were:

- To evaluate the capability and accuracy of IDDES in modelling complex hydraulic problems.
- To provide insight into the complex hydrodynamic processes at the intakes.

The inflow condition for the main domain was computed using a precursor analysis using a periodic trapezoidal channel. The length of the channel in periodic direction was chosen to be eight times the water depth. The flow parameters were stored at the outlet in order to be prescribed at the inlet of the main domain. The accuracy of the computed values were checked by comparing results with theoretical and empirical expressions. It

was shown that the vertical velocity profile at the center of the channel precisely follows the logarithmic profile. Similarly, the turbulence intensities and kinetic energy were in excellent agreement with the measured values and the empirical expression developed for open channel flows. Additionally, it was shown that the computed secondary flows were predicted accurately and they were in a good agreement with the experimental observations from the other studies. Finally, the normalized spatial two-point autocorrelations of the velocity components in streamwise direction for several points were computed. It was found that the values are decreasing rapidly and reaching well below 0.1 at the middle of the channel. Therefore it was concluded that the chosen periodic distance was sufficient.

Simulation of the main domain carried out using the inflow condition which has been computed using a period channel. Due to computational limitation, 16 flow passes have been simulated. The first and second order statistics are computed and presented. It is found that the approach flow is divided into two parts. The flow on the right side follows the forebay and the rest takes a longer path from the left and joins the flow approximately with 90 degree angle near the intakes.

In order to evaluate the accuracy of the model, the mean velocities and turbulence intensities contour plots are illustrated for the section where the measurements have been performed. The results have shown to be in a good agreement with the physical model test. Additionally, individual components of the velocities along the vertical measured lines are plotted against the measured values. It is found that DES predicted the streamwise velocities very well. Similar conclusion have been made when other components of velocities were compared at intake 1. On the other hand, in the intake 2, results differs especially close to the left and right side walls.

Plots of surface streamlines and the streamwise vorticity inside the intakes revealed two swirling flow structures on the left side of the intake 2. Although the flow significantly improved downstream, the swirling flow is found to be present further downstream. The source of this horizontal swirling flow, similar to RANS, is found to be the high velocity flow perpendicular to the intake where it passes over the divider wall and joins the streamwise flow. It is also shown that almost the entire forebay's flow is directed toward the right intake, whereas, the entire flow of left intake is supplied by the perpendicular flow from the left. This gave rise to two additional swirling flow structures in front and on the top of the submerged pier. On the right side, a free surface vortex is present, similar to what SST model has predicted. Additionally, due to the slope effect, additional rotating flow is present at the intake 1 extending from the beginning of the slope to the intake. This is similar to what have been observed in the RANS study on the simplified model.

One of the advantages of DES over RANS, beside accuracy, is the possibility of visualization of the instantaneous flow field and coherent flow structures. Hence, the instantaneous flow field is investigated to reveal more details about the hydrodynamical processes. The investigation was started off from upstream of the intakes at the forebay. The forebay is raised from the channel bed and created a step. It is shown that due to the flow from the channel toward the forebay, a separation occurs, which is very similar to the hydrodynamical process in a forward-step case, where the separation and reattachment occurs after the step. However, due to slight angle of the flow related to step as well as the influence of the streamwise flow in the forebay, the separated layer is angled toward the intakes. This continues until the beginning of the slope to the intakes. Moreover, it is also seen that the

entire flow of the forebay and significant portion of the flow in the channel is adopting a path toward the right intake.

Perhaps the most important process occurs at the right side of the divider wall where the high velocity flow from the left passes over the wall and generate a massive separation. The separated flow elongated in horizontal direction toward the left intake giving rise to the observed clockwise swirling flow inside the intake 2. It is found that this process is highly dynamic and transient where different layers in horizontal and vertical directions are generated and joined frequently. This is not the only dynamic process which has been observed at this zone. Further downstream, the flow passes around the pier and consequently it gave a rise to the vortices behind the pier. These vortices then extended partially to the top left corner of intake 2. Instantaneous fields at vertical sections downstream have shown that these complex hydrodynamical processes continued though the left intake. These highly unstable and complex flow fields inside the intake 2 explain the difficulty of RANS turbulence models to estimate a correct velocity fields and their poor performances in comparison with DES approach.

Finally, in the physical model study, a free surface vortex has been observed on the left side of the intakes. The numerical study revealed that the vortex is generated due to the high velocity flow from the left side, where it passes over the pier with 90 degree turn and generates a separation layer. This separated layer gives a rise to a free surface vortex at that location. It is found that this vortex is highly transient and shallow, meaning that it does not extend significantly below the water level and the location is highly variable in spanwise direction. Furthermore, an additional vortex is present at the right side where the core, unlike the left vortex, extends downstream inside the intake 1. This is also predicted by RANS, when SST model is used.

8.6 Final remarks

Approach flow in run-of-river plants is complex, especially in block types where the approach channel is widened via forebay structure to accommodate intakes. In this study, several numerical simulations have been carried out using OpenFOAM to evaluate the capability of the numerical models. It was found that with careful selection of numerical parameters, RANS can be used to model the approach flow as far as the flow inside the intakes are of concern. It may be used alone or in combination with physical models to investigate the approach flow. Furthermore, it is shown that methods like DES also can provide valuable insight into the hydrodynamical processes and they are capable of modelling flow fields accurately with moderate computational costs. The additional cost can be reduced by utilizing faster solvers similar to the explicit solver which is implemented, validated and used in this study. In conclusion, the numerical models along with the experimental studies can be used to investigate the flow in more details and optimize the flow. This in return leads to lower hydraulic losses and maintenance costs.

8.7 Further studies

Given the complexity of the approach flow of Run-of-River plants and several key parts which are affecting the flow directly, the focus of the future studies can be on the specific aspects of such hydraulic structures as follows:

- Carrying out measurement in the prototypes and comparing the results to the hydraulic laboratory models and the numerical models.
- Run-of-River plants often operate not in their full capacity, hence, different load cases may lead to different flow fields. This can be investigated via numerical models.
- Numerical models can be used to optimize the upstream structures to achieve optimum flow. This can be done on a generic model and then it can be applied to the new or old but similar real world intake structures.
- The trashrack can significantly change the flow downstream, hence, numerical as well as experimental study must be carried out to understand the effect of this structure on the flow.
- The sedimentation process can be investigated numerically and experimentally for optimum sediment management and protection of the turbines.
- The approach flow may be investigated and optimized by numerical models for fish protection.
- The current design criteria (known as Fisher and Franke) for low head intakes have to be updated based on the numerical and physical models in cooperation with turbine manufacturers.

BIBLIOGRAPHY

Åkerstedt, H. O., S. Eller, and T. S. Lundström
2017. Numerical investigation of turbulent flow through rectangular and biconvex shaped trash racks. *Engineering*, 9(05):412.

Andersson, A. and S. F. Daly
1992. Laboratory investigation of trash rack freezeup by frazil ice. Technical report, COLD REGIONS RESEARCH AND ENGINEERING LAB HANOVER NH.

Annandale, G. W., G. L. Morris, and P. Karki
2016. *Extending the life of reservoirs*. Washington, DC: World Bank.

Ansari, K.
2011. *Boundary shear stress distribution and flow structures in trapezoidal channels*. PhD thesis, University of Nottingham.

Balachandar, R., B.-S. Hyun, and V. Patel
2007. Effect of depth on flow over a fixed dune. *Canadian Journal of Civil Engineering*, 34(12):1587–1599.

Basson, G.
2008. Reservoir sedimentation an overview of global sedimentation rates, sediment yield and sediment deposition prediction. In *International Workshop on Erosion, Transport and Deposition of Sediment Berne*, Pp. 28–30.

Basson, G.
2009. Sedimentation and sustainable use of reservoirs and river systems. ICOLD Bulletin 147, International Commission on Large dams, 61, avenue Kleber, 75116, Paris, France.

Batuca, D. G. and J. Jordaan Jr
2000. *Silting and desilting of reservoirs*. CRC Press.

Benigni, H., J. Schiffer-Rosenberger, S. Höller-Litzlhammer, and H. Jaberg
2018. Improvement of intake structures with numerical simulation. In *World Congress ICOLD 2018*, Pp. 2252–2263. Verlag der Technischen Universität Graz.

Blazewicz, A., M. Bull, and R. Kelso
2007. Characteristics of flow regimes for single plates of rectangular cross-section.

BMLFUW
2014. Hydrographisches Jahrbuch. Technical report, The Austrian Federal Ministry of

Agriculture, Forestry, Environment and Water Management. https://www.bmlfuw.gv.at/.

Calhoun, R. J.
1998. *Numerical investigations of turbulent flow over complex terrain.* dissertation, Stanford University, Stanford, California.

Canuto, C., M. Y. Hussaini, A. Quarteroni, and T. A. Zang
2007. *Spectral methods: evolution to complex geometries and applications to fluid dynamics*. Springer Science & Business Media.

Cea, L., J. Puertas, and L. Pena
2007. Velocity measurements on highly turbulent free surface flow using adv. *Experiments in fluids*, 42(3):333–348.

Celik, I., J. Li, G. Hu, and C. Shaffer
2005. Limitations of richardson extrapolation and some possible remedies. *Journal of Fluids Engineering*, 127(4):795–805.

Celik, I. B., U. Ghia, P. J. Roache, et al.
2008. Procedure for estimation and reporting of uncertainty due to discretization in {CFD} applications. *Journal of fluids {Engineering-Transactions} of the {ASME}*, 130(7).

Chang, K., G. Constantinescu, and S.-O. Park
2007. Assessment of predictive capabilities of detached eddy simulation to simulate flow and mass transport past open cavities. *Journal of Fluids Engineering*, 129(11):1372–1383.

Chanson, H.
2004. *Hydraulics of open channel flow*. Elsevier.

Chorin, A. J.
1968. Numerical solution of the navier-stokes equations. *Mathematics of computation*, 22(104):745–762.

Clark, S. P., J. M. Tsikata, and M. Haresign
2010. Experimental study of energy loss through submerged trashracks. *Journal of Hydraulic Research*, 48(1):113–118.

Constantinescu, G., M. Koken, and J. Zeng
2011. The structure of turbulent flow in an open channel bend of strong curvature with deformed bed: Insight provided by detached eddy simulation. *Water Resources Research*, 47(5).

Constantinescu, G., S. Miyawaki, B. Rhoads, and A. Sukhodolov
2012. Numerical analysis of the effect of momentum ratio on the dynamics and sediment-entrainment capacity of coherent flow structures at a stream confluence. *Journal of Geophysical Research: Earth Surface*, 117(F4).

Constantinescu, G. and V. Patel
2000. Role of turbulence model in prediction of pump-bay vortices. *Journal of Hydraulic Engineering*, 126(5):387–391.

Constantinescu, G. S. and K. D. Squires
2003. Les and des investigations of turbulent flow over a sphere at re= 10,000. *Flow, Turbulence and Combustion*, 70(1-4):267–298.

Crandall, S., S. Vigander, and P. March
1975. Destructive vibration of trashracks due to fluid-structure interaction. *Journal of Engineering for Industry*, 97(4):1359–1365.

Cuchet, M.
2014. *Fish Protection and Downstream Migration at Hydropower Intakes*. PhD thesis, Technische Universität München.

Daly, S. F.
1991. Frazil ice blockage of intake trash racks. Technical report, COLD REGIONS RESEARCH AND ENGINEERING LAB HANOVER NH.

De Villiers, E.
2007. *The potential of large eddy simulation for the modelling of wall bounded flows*. PhD thesis, University of London Doctoral Thesis, London, UK.

Demny, G., K. Rettenmeier, C. Forkel, and J. Koengeter
1998. Verification and application of a 3d-numerical model for the flow through the intakes of run of the river power plants. In *Modelling, testing and monitoring for hydro powerplants III*, Pp. 273–283. The international journal on hydropower and dams.

Dendy, F., W. Champion, and R. Wilson
1973. Reservoir sedimentation surveys in the united states. *Washington DC American Geophysical Union Geophysical Monograph Series*, 17:349–357.

Denny, D. and G. Young
1957. *The prevention of vortices and swirl at intakes*. British Hydromechanics Research Association.

Dorfmann, C., G. Harb, and G. Zenz
2012. Simulation of hydrodynamic and sediment transport processes–two austrian case studies. In *Proceedings of the XIXth TELEMAC-MASCARET User Conference 2012, 18 to 19 October 2012, St Hugh's College, Oxford*, Pp. 45–50.

Dorfmann, C., M. Redtenbacher, and G. Zenz
2015. Investigating the sediment transport processes in a river meander. In *Proceedings of the XXII TELEMAC-MASCARET Technical User Conference October 15-16, 2029*, Pp. 8–8.

DZS
2015. Statistical yearbook of the republic of croatia. Technical report, Croatian Bureau Of Statistic.

E-Control
2016. Statistiken für den elektrizitäts-, erdgas- und ökostrombereich.

Einstein, H. A. and H. Li
1951. Steady vortex flow in a real fluid. *Proc. Heat Transfer and Fluid Mechanics Institute, Stanford University*, Pp. 33–43.

Erlebacher, G., M. Y. Hussaini, C. G. Speziale, and T. A. Zang
1992. Toward the large-eddy simulation of compressible turbulent flows. *Journal of fluid mechanics*, 238:155–185.

Ferziger, J. H. and M. Peric
2012. *Computational methods for fluid dynamics*. Springer Science & Business Media.

Feynman, R.
1964. The Feynman lectures on physics (by feynman, leighton and sands, addison-wesley, redwood city).

Fisher, R. K. and G. F. Franke
1987. The impact of inlet flow characteristics on low head hydro projects. In *Water Power'87*, Pp. 1673–1680. ASCE.

Fluent, A.
2018. Ansys fluent. *Academic Research. Release*, 18.

Fošumpaur, P. and F. Čihák
2005. Design and optimization of a turbine intake structure. *Acta Polytechnica*, 45(3).

Fröhlich, J., C. P. Mellen, W. Rodi, L. Temmerman, and M. A. Leschziner
2005. Highly resolved large-eddy simulation of separated flow in a channel with streamwise periodic constrictions. *Journal of Fluid Mechanics*, 526:19–66.

Fureby, C., A. Gosman, G. Tabor, H. Weller, N. Sandham, and M. Wolfshtein
1997. Large eddy simulation of turbulent channel flows. *Turbulent shear flows*, 11:19–30.

Gabl, R., D. Innerhofer, S. Achleitner, M. Righetti, and M. Aufleger
2018. Evaluation criteria for velocity distributions in front of bulb hydro turbines. *Renewable Energy*, 121:745–756.

Gebre, S., K. Alfredsen, L. Lia, M. Stickler, and E. Tesaker
2013. Review of ice effects on hydropower systems. *Journal of Cold Regions Engineering*, 27(4):196–222.

Georgiadis, N. J., D. P. Rizzetta, and C. Fureby
2010. Large-eddy simulation: current capabilities, recommended practices, and future research. *AIAA journal*, 48(8):1772–1784.

Ghamry, H. and C. Katopodis
2012. Numerical investigation of turbulent flow through bar racks in closed conduits. In *Proceedings of the 9th International Symposium on Ecohydraulics, Vienna*, Pp. 17–21.

Giesecke, J., S. Heimerl, and E. Mosonyi
2014. *Wasserkraftanlagen: Planung, Bau und Betrieb*. Springer-Verlag.

Godde, D.
1994. *Experimental investigations on the impingement of tube turbines: a contribution to the optimization of the turbine inlet*. na.

Goring, D. G. and V. I. Nikora
2002. Despiking acoustic doppler velocimeter data. *Journal of Hydraulic Engineering*, 128(1):117–126.

Greenshields, C. J.
2015. *OpenFOAM® Version 3.0.1 Programmer's Guide*. OpenFOAM Foundation Ltd.

Grigoriadis, D., E. Balaras, and A. Dimas
2009. Large-eddy simulations of unidirectional water flow over dunes. *Journal of Geophysical Research: Earth Surface*, 114(F2).

Gritskevich, M. S., A. V. Garbaruk, J. Schütze, and F. R. Menter
2012. Development of ddes and iddes formulations for the k-ω shear stress transport model. *Flow, turbulence and combustion*, 88(3):431–449.

Harb, G.
2013. *Numerical modeling of sediment transport processes in alpine reservoirs*. na.

Harb, G., C. Dorfmann, H. Badura, and J. Schneider
2013. Numerical analysis of the flushing efficiency of an alpine reservoir. In *Proceedings of the 2013 IAHR World Congress*.

Harb, G., C. Dorfmann, S. Haun, H. Badura, and J. Schneider
2012. Numerical analysis of sediment transport processes in a reservoir. In *International Conference on Fluvial Hydraulics*, Pp. 859–865. Taylor & Francis Group.

Harb, G., S. Haun, N. R. Olsen, and J. Schneider
2014. Numerical analysis of synthetic granulate deposition in a physical model study. *International Journal of Sediment Research*, 29(1):110–117.

Harb, G., S. Haun, S. Ortner, C. Dorfmann, J. Schneider, et al.
2011. The influence of secondary currents on reservoir sedimentation-experimental and numerical studies. In *Proceedings of the 34th World Congress of the International Association for Hydro-Environment Research and Engineering: 33rd Hydrology and Water Resources Symposium and 10th Conference on Hydraulics in Water Engineering*, P. 1733. Engineers Australia.

Haun, S., C. Dorfmann, G. Harb, and N. R. B. Olsen
2012. 3d numerical modelling of the reservoir flushing of the bodendorf reservoir, austria. In *IAHR European Conference, Munich, Germany*.

Heller, V.
2007. scale effects in the hydraulic model. *water energy air*, 99(2):153–159.

Heller, V.
2011. Scale effects in physical hydraulic engineering models. *Journal of Hydraulic Research*, 49(3):293–306.

Hermann, F., P. Billeter, and R. Hollenstein
1998. Investigations on the flow through a trashrack under different inflow conditions. *Hydroinformatics, Balkema, Rotterdam*, Pp. 121–128.

Hirsch, C.
2007. *Numerical computation of internal and external flows: The fundamentals of computational fluid dynamics*. Elsevier.

Holmén, V.
2012. Methods for vortex identification. *Master's Theses in Mathematical Sciences*.

Huebsch, W., B. Munson, T. Okiishi, and D. Young
2009. *Fundamentals of fluid mechanics*, sixth edition. John Wiley & Sons.

Issa, R. I.
1986. Solution of the implicitly discretised fluid flow equations by operator-splitting. *Journal of computational physics*, 62(1):40–65.

Iwamoto, K., N. Kasagi, and Y. Suzuki
2005. Direct numerical simulation of turbulent channel flow at reτ= 2320. In *Proc. 6th Symp. Smart Control of Turbulence*, Pp. 327–333.

Jackson, R. G.
1976. Sedimentological and fluid-dynamic implications of the turbulent bursting phenomenon in geophysical flows. *Journal of Fluid Mechanics*, 77(3):531–560.

Jameson, A., W. Schmidt, and E. Turkel
1981. Numerical solution of the euler equations by finite volume methods using runge kutta time stepping schemes. In *14th fluid and plasma dynamics conference*, P. 1259.

Jarrin, N., R. Prosser, J.-C. Uribe, S. Benhamadouche, and D. Laurence
2009. Reconstruction of turbulent fluctuations for hybrid rans/les simulations using a synthetic-eddy method. *International Journal of Heat and Fluid Flow*, 30(3):435–442.

Jasak, H.
1996. Error analysis and estimation for finite volume method with applications to fluid flow.

Jiménez Sendín, J., S. Hoyas, M. P. Simens, and Y. Mizuno
2010. Turbulent boundary layers and channels at moderate reynolds numbers. *Journal of Fluid Mechanics*, 657:335–360.

Kadota, A. and I. Nezu
1999. Three-dimensional structure of space-time correlation on coherent vortices generated behind dune crest. *Journal of Hydraulic Research*, 37(1):59–80.

Karatekin, O.
1997. Numerical experiments on application of richardson extrapolation with nonuniform grids.

Khan, L. A., E. A. Wicklein, M. Rashid, L. L. Ebner, and N. A. Richards
2004. Computational fluid dynamics modeling of turbine intake hydraulics at a hydropower plant. *Journal of Hydraulic Research*, 42(1):61–69.

Kim, J., P. Moin, and R. Moser
1987. Turbulence statistics in fully developed channel flow at low reynolds number. *Journal of fluid mechanics*, 177:133–166.

Kirkil, G., S. Constantinescu, and R. Ettema
2008. Coherent structures in the flow field around a circular cylinder with scour hole. *Journal of Hydraulic Engineering*, 134(5):572–587.

Knauss, J.
2017. *Swirling flow problems at intakes*. Routledge.

Koken, M. and G. Constantinescu
2009. An investigation of the dynamics of coherent structures in a turbulent channel flow with a vertical sidewall obstruction. *Physics of Fluids*, 21(8):085104.

Kostic, T.
2016. Numerical studies on bulb turbine intakes. Master's thesis, Graz University of Technology,Faculty of Civil Engineering, Institute for Hydraulic Engineering and Water Management.

Launder, B. and D. Spalding
1974. The numerical computation of turbulent flows. *Computer Methods in Applied Mechanics and Engineering*, 3:269–289.

Lund, T. S., X. Wu, and K. D. Squires
1998. Generation of turbulent inflow data for spatially-developing boundary layer simulations. *Journal of computational physics*, 140(2):233–258.

Matsumoto, M., H. Ishizaki, C. Matsuoka, Y. Daito, Y. Ichikawa, and A. Shimahara
1998. Aerodynamic effects of the angle of attack on a rectangular prism. *Journal of Wind Engineering and Industrial Aerodynamics*, 77:531–542.

Menter, F.
1993. Multiscale model for turbulent flows. In *24th Fluid Dynamics Conference, Orlando, FL, July*, Pp. 6–9.

Menter, F. and M. Kuntz
2004. Adaptation of eddy-viscosity turbulence models to unsteady separated flow behind vehicles. In *The aerodynamics of heavy vehicles: trucks, buses, and trains*, Pp. 339–352. Springer.

Menter, F., M. Kuntz, and R. Langtry
2003. Ten years of industrial experience with the sst turbulence model. *Turbulence, heat and mass transfer*, 4(1):625–632.

Menter, F. R.
1994. Two-equation eddy-viscosity turbulence models for engineering applications. *AIAA journal*, 32(8):1598–1605.

Meusburger, H.
2002. *Energieverluste an Einlaufrechen von Flusskraftwerken*. PhD thesis, ETH Zurich.

Meusburger, H., P. Volkart, and H.-E. Minor
2001. A new improved formula for calculating trashrack losses. In *PROCEEDINGS OF THE CONGRESS-INTERNATIONAL ASSOCIATION FOR HYDRAULIC RESEARCH*, Pp. 804–809.

Moin, P. and J. Kim
1982. Numerical investigation of turbulent channel flow. *Journal of fluid mechanics*, 118:341–377.

Möller, G.
2013. *Vortex-induced air entrainment rate at intakes*. PhD thesis, ETH Zurich, ZÃ¼rich.

Möller, G., M. Detert, and R. M. Boes
2015. Vortex-induced air entrainment rates at intakes. *Journal of Hydraulic Engineering*, 141(11):04015026.

Morris, G. L. and J. Fan
1998. *Reservoir sedimentation handbook: design and management of dams, reservoirs, and watersheds for sustainable use*. McGraw Hill Professional.

Moser, R. D., J. Kim, and N. N. Mansour
1999. Direct numerical simulation of turbulent channel flow up to re τ= 590. *Physics of fluids*, 11(4):943–945.

Mosonyi, E.
1987. *Water Power Development: Volume One: Low Head-power Plants*. Akademiai Kiado.

Mukha, T. and M. Liefvendahl
2015. Large-eddy simulation of turbulent channel flow with openfoam.

Nakamura, Y., Y. Ohya, and H. Tsuruta
1991. Experiments on vortex shedding from flat plates with square leading and trailing edges. *Journal of Fluid Mechanics*, 222:437–447.

Nascimento, L., J. Silva, and V. Di Giunta
2006. Damage of hydroelectric power plant trash-racks due to fluid-dynamic exciting frequencies. *Latin American Journal of Solids and Structures*, 3(3):223–243.

Naudascher, E.
2017. *Flow-induced Vibrations: an Engineering Guide: IAHR Hydraulic Structures Design Manuals 7*. Routledge.

Naudascher, E. and Y. Wang
1993. Flow-induced vibrations of prismatic bodies and grids of prisms. *Journal of Fluids and Structures*, 7(4):341–373.

Nezu, I. and H. Nakagawa
1993. Turbulence in open-channel flows. *IAHR/AIRH Monograph*.

Nguyen, T. D. and E. Naudascher
1991. Vibration of beams and trashracks in parallel and inclined flows. *Journal of Hydraulic Engineering*, 117(8):1056–1076.

Nicoud, F. and F. Ducros
1999. Subgrid-scale stress modelling based on the square of the velocity gradient tensor. *Flow, turbulence and Combustion*, 62(3):183–200.

Nikora, V. and D. Goring
2000. Flow turbulence over fixed and weakly mobile gravel beds. *Journal of Hydraulic Engineering*, 126(9):679–690.

Nortek, A.
2009. Vectrino velocimeter user guide. *Nortek AS, Vangkroken, Norway*.

Ohya, Y., Y. Nakamura, S. Ozono, H. Tsuruta, and R. Nakayama
1992. A numerical study of vortex shedding from flat plates with square leading and trailing edges. *Journal of Fluid Mechanics*, 236:445–460.

Omidyeganeh, M.
2013. *Large-eddy simulation of unidirectional turbulent flow over dunes*. dissertation.

Ott, R. F.
1995. Guidelines for design of intakes for hydroelectric plants. Technical report, American Society of Civil Engineers, New York, NY (United States).

Papillon, B., J. Kirejczyk, and M. Sabourin
2000. Atmospheric air admission in hydroturbines. *HydroVision 2000 (Charlotte, North Carolina, USA)*.

Patankar, S.
1980. Numerical heat transfer and fluid flow. *Washington, DC, Hemisphere Publishing Corp., 1980. 210 p.*, 1.

Polatel, C.
2006. *Large-scale roughness effect on free-surface and bulk flow characteristics in open-channel flows*. PhD thesis, University of Iowa Iowa, USA.

Poletto, R., T. Craft, and A. Revell
2013. A new divergence free synthetic eddy method for the reproduction of inlet flow conditions for les. *Flow, turbulence and combustion*, 91(3):519–539.

Pope, S. B.
2001. Turbulent flows.

Pugh, C. A., Engineering, and R. C. (U.S.).
1983. *Hydraulic model studies on bulb turbine intakes [microform] / by Clifford A. Pugh*. Hydraulics Branch, Division of Research, Engineering and Research Center ; Available from the National Technical Information Service, Operations Division, [distributor] Denver, Colo.

Raynal, S., L. Chatellier, L. David, D. Courret, and M. Larinier
2013. Numerical simulations of fish-friendly angled trashracks at model and real scale.

Reynolds, O.
1895. On the dynamical theory of incompressible viscous fluids and the determination of the criterion. *Philosophical Transactions of the Royal Society of London. A*, 186:123–164.

Richardson, L. F.
1911. The approximate arithmetical solution by finite differences of physical problems involving differential equations, with an application to the stresses in a masonry dam. *Philosophical Transactions of the Royal Society of London. Series A, Containing Papers of a Mathematical or Physical Character*, 210:307–357.

Roache, P. J.
1998. *Verification and validation in computational science and engineering*, volume 895. Hermosa Albuquerque, NM.

Rodi, W., G. Constantinescu, and T. Stoesser
2013. *Large-eddy simulation in hydraulics*. Crc Press.

Roth, U.
2018. Velocity measurements of approach flow to low head run-off hydropower plant intakes in the laboratory. Master's thesis, Institute of Hydraulic Engineering and Water Resources Management, Graz University of Technology.

Schneider, J., G. Harb, and S. Shahriari
2018. Modelltechnische Untersuchungen für die Neuerrichtung des Kraftwerkes Töging sowie der Wehranlage Jettenbach. *WasserWirtschaft*.

Schneider, J., C. Sindelar, R. Feldbacher, and H. Knoblauch
2011. Die Auswirkungen eines Geschiebe fÃ¼hrenden Zubringers auf die Verlandungssituation im Unterwasser eines Laufkraftwerkes. *WasserWirtschaft*, (07-08):70–75.

Schneider, J., S. Zechner, H. Schimpf, and G. Puchner
2012. Hydraulische Untersuchungen eines geplanten Flusskraftwerkes - KW Stegenwald. In *Wasserbau Symposium 2012 Wasser - Energie Global denken - lokal handeln*, Pp. 361–370, Graz/Austria.

Schneider, J., G. Zenz, and M. Knoll
2009. Theodorawehr - Hydraulischer Modellversuch. Technical Report 328, Eigenverlag.

Shur, M. L., P. R. Spalart, M. K. Strelets, and A. K. Travin
2008. A hybrid rans-les approach with delayed-des and wall-modelled les capabilities. *International Journal of Heat and Fluid Flow*, 29(6):1638–1649.

Slater, J. W.
2006. Examining spatial (grid) convergence. *Public tutorial on CFD verification and validation, NASA Glenn Research Centre, MS*, 86.

Smagorinsky, J.
1963. General circulation experiments with the primitive equations: I. the basic experiment. *Monthly weather review*, 91(3):99–164.

Spalart, P., W. Jou, M. Strelets, and S. Allmaras
1997. Comments of feasibility of les for wings, and on a hybrid RANS/LES approach. In *International Conference on DNS/LES, Aug. 4-8, 1997, Ruston, Louisiana.*

Spalart, P. R.
1988. Direct simulation of a turbulent boundary layer up to r θ= 1410. *Journal of fluid mechanics*, 187:61–98.

Spalart, P. R., S. Deck, M. L. Shur, K. D. Squires, M. K. Strelets, and A. Travin
2006. A new version of detached-eddy simulation, resistant to ambiguous grid densities. *Theoretical and computational fluid dynamics*, 20(3):181.

Stoesser, T., C. Braun, M. Garcia-Villalba, and W. Rodi
2008. Turbulence structures in flow over two-dimensional dunes. *Journal of Hydraulic Engineering*, 134(1):42–55.

Strelets, M.
2001. Detached eddy simulation of massively separated flows. In *39th Aerospace sciences meeting and exhibit*, P. 879.

Suerich-Gulick, F., S. Gaskin, M. Villeneuve, G. Holder, and E. Parkinson
2006. Experimental and numerical analysis of free surface vortices at a hydropower intake.

Suerich-Gulick, F., S. J. Gaskin, M. Villeneuve, and É. Parkinson
2013. Characteristics of free surface vortices at low-head hydropower intakes. *Journal of Hydraulic Engineering*, 140(3):291–299.

SURS
2000. Rivers, longer than 25 km, and their catchment areas. Technical report, Statistical Office of the Republic of Slovenia. http://www.stat.si/StatWeb/doc/letopis/2000/01_00/01-10-00.htm.

Taghvaei, S., R. Roshan, K. Safavi, and H. Sarkardeh
2012. Anti-vortex structures at hydropower dams. *International Journal of Physical Sciences*, 7(28):5069–5077.

Teisson, C.
1991. Cohesive suspended sediment transport: feasibility and limitations of numerical modeling. *Journal of Hydraulic Research*, 29(6):755–769.

Temmerman, L.
2004. *Large eddy simulation of separating flows from curved surfaces*. PhD thesis.

Tokyay, T. and S. Constantinescu
2006. Validation of a large-eddy simulation model to simulate flow in pump intakes of realistic geometry. *Journal of hydraulic Engineering*, 132(12):1303–1315.

Tominaga, A., I. Nezu, K. Ezaki, and H. Nakagawa
1989. Three-dimensional turbulent structure in straight open channel flows. *Journal of hydraulic research*, 27(1):149–173.

Tsikata, J. M., C. Katopodis, and M. F. Tachie
2009a. Experimental study of turbulent flow near model trashracks. *Journal of Hydraulic Research*, 47(2):275–280.

Tsikata, J. M., M. F. Tachie, and C. Katopodis
2009b. Particle image velocimetry study of flow near trashrack models. *Journal of Hydraulic Engineering*, 135(8):671–684.

Tsitaka, J., M. Tachie, C. Katopodis, E. Teklemariam, H. Ghamry, K. Sydor, and B. Shumilak
2007. A particle image velocimetry study turbulent through model trash rack. In *Proceedings of the 18th Hydrotechnical Conference, Winnipeg*, Pp. 22–24.

USBR
2016. Design standards no. 6-hydraulic and mechanical equipment-chapter 12: Trashracks and trashrack cleaning devices.

Van Dyke, M.
1982. *An album of fluid motion*. Parabolic Press, Stanford, CA.

Verbund
2017. https://www.verbund.com. Accessed: 2017-07-10.

Versteeg, H. K. and W. Malalasekera
2007. *An introduction to computational fluid dynamics: the finite volume method*. Pearson Education.

Vuorinen, V., A. Chaudhari, and J.-P. Keskinen
2015. Large-eddy simulation in a complex hill terrain enabled by a compact fractional step openfoam® solver. *Advances in Engineering Software*, 79:70–80.

Vuorinen, V., J.-P. Keskinen, C. Duwig, and B. Boersma
2014. On the implementation of low-dissipative runge–kutta projection methods for time dependent flows using openfoam®. *Computers & Fluids*, 93:153–163.

Vuorinen, V., M. Larmi, P. Schlatter, L. Fuchs, and B. Boersma
2012. A low-dissipative, scale-selective discretization scheme for the navier–stokes equations. *Computers & Fluids*, 70:195–205.

Wahl, T. L.
1992. *Trash control structures and equipment: A literature review and survey of bureau of reclamation experience*. US Bureau of Reclamation.

Wahl, T. L.
2000. Analyzing adv data using winadv. In *Building partnerships*, Pp. 1–10.

Wahl, T. L.
2003. Discussion of despiking acoustic doppler velocimeter data by derek g. goring and vladimir i. nikora. *Journal of Hydraulic Engineering*, 129(6):484–487.

Wickenhäuser, M.
2008. *Zweiphasenströmung in Entlüftungssystemen von Druckstollen*. PhD thesis, ETH Zurich.

Wilcox, D. C. et al.
1998. *Turbulence modeling for CFD*, volume 2. DCW industries La Canada, CA.

Wright, N., A. Crossley, H. Morvan, and T. Stösser
2004. Detailed validation of cfd for flows in straight channels. In *River Flow*, volume 2, Pp. 1041–1048.

Yue, W., C.-L. Lin, and V. C. Patel
2006. Large-eddy simulation of turbulent flow over a fixed two-dimensional dune. *Journal of Hydraulic Engineering*, 132(7):643–651.

Zenz, G., A. Hammer, S. Zechner, M. Knoll, and M. Kovacs
2015. *Erweiterung Kraftwerk Kirchbichl*, 342.01. Eigenverlag. Reportnr.: 342.01.

Zenz, G., J. Schneider, G. Harb, and M. Redtenbacher
2016a. *Hydraulischer Modellversuch - Murkraftwerk Gratkorn*. Eigenverlag.

Zenz, G., J. Schneider, G. Harb, S. Shahriari, and F. Lazar
2016b. *Erweiterung und Effizienzsteigerung des Innkraftwerks Jettenbach/Töging, Erneuerung KW Töging, Hydraulischer Modellversuch Kraftwerk Töging*. Eigenverlag.

Zenz, G. and S. Shahriari
2014. *Kraftwerk Rothleiten - Zuströmung Turbineneinlauf*. Eigenverlag. Reportnr.: Gutachten Februar 2014.

Zenz, G. and S. Shahriari
2019. Hydro power plant kirchbichl hydraulic simulation: Bericht kw kirchbichl. Technical report, Institute of Hydraulic Engineering and Water Resources Management, TU Graz, Stremayrgasse 10/II, 8010, Graz , Austria.

List of Figures

List of Tables